Westinghouse Non-Proprietary Class 3

WCAP-16747-NP
Revision 0

March 2007

POLCA-T: System Analysis Code with Three-Dimensional Core Model

WCAP-16747-NP
Revision 0

POLCA-T: System Analysis Code with Three-Dimensional Core Model

Authors:

Ulf Bredolt
Dobromir Panayotov
Mats Thunman
Camilla Rotander
Staffan Söderholtz

March 2007

Prepared by:

*M. Riggs, Principal Engineer
Fuel Engineering Licensing

*R. B. Sisk, Manager
Fuel Engineering Licensing

*Electronically approved records are authenticated in the electronic document management system.

Westinghouse Electric Company LLC
P.O. Box 355
Pittsburgh, PA 15230-0355

© 2007 Westinghouse Electric Company LLC
All Rights Reserved

TABLE OF CONTENTS

LIST OF TABLES vii

LIST OF FIGURES ix

ACRONYMS xi

1 INTRODUCTION AND OBJECTIVES 1-1
2 BASIS OF POLCA-T 2-1
2.1 REFERENCES 2-2
3 POLCA-T SUMMARY DESCRIPTION 3-1
3.1 THE THERMAL HYDRAULIC MODEL 3-3
3.2 COMPONENT MODELS 3-4
3.3 THE THERMAL MODEL 3-5
3.4 POWER GENERATION MODELS 3-5
3.5 NUMERICAL METHODS 3-6
4 CODE STRUCTURE 4-1
4.1 INTERACTION OF THERMAL-HYDRAULICS AND NEUTRON KINETICS 4-1
4.2 POLCA-T STRUCTURE 4-2
4.3 REFERENCES 4-2
5 GEOMETRICAL MODELLING ASSUMPTIONS 5-1
6 PRIMARY VARIABLES – STATE VECTOR CONCEPT 6-1
7 HYDRODYNAMIC MODEL 7-1
7.1 VOLUME CELL 7-2
7.1.1 Mass Conservation Equations 7-3
7.1.2 Energy Conservation Equations 7-7
7.2 FLOW PATH 7-11
7.2.1 Momentum Conservation Equation 7-11
7.3 REFERENCES 7-17
8 POWER GENERATION MODEL 8-1
8.1 3-D KINETICS 8-1
8.2 DECAY POWER GENERATION 8-1
8.2.1 By Tables 8-1
8.2.2 By Equations 8-1
8.3 REFERENCES 8-2
9 CONSTITUTIVE MODELS 9-1
9.1 DRIFT FLUX EQUATION 9-1
9.1.1 The DF01 Drift Flux Correlation 9-2
9.1.2 The DF02 Drift Flux Correlation 9-3
9.2 WALL FRICTION AND SINGULAR IRREVERSIBLE LOSSES 9-4
9.2.1 Single-Phase Friction Factors 9-4
9.2.2 Irreversible Losses Due to Contraction/Expansion 9-5
9.3 COUNTERCURRENT FLOW LIMITATION CORRELATION 9-6
9.3.1 CCFL Correlation 9-6
9.3.2 Mass Drift Flux 9-8
9.4 HEAT AND MASS TRANSFER BETWEEN PHASES 9-9
9.5 HEAT TRANSFER TO HEAT STRUCTURES 9-11

TABLE OF CONTENTS (Cont'd)

9.6 HEAT TRANSFER BETWEEN THE PHASES IN THE BULK 9-11
9.6.1 Bulk Evaporation/Condensation, Low Void 9-12
9.6.2 Bulk Condensation/Evaporation, High Void 9-13
9.6.3 Near Wall Condensation 9-16
9.7 WALL CONDENSATION 9-16
9.7.1 Mass Transfer 9-16
9.8 REFERENCES 9-17
10 HEAT STRUCTURE MODELS 10-1
11 CONVECTIVE HEAT TRANSFER MODELS 11-1
11.1 HEAT TRANSFER REGIMES 11-2
11.1.1 Two-Phase Subcooled, Nucleate and Flow Boiling Regime (H5) 11-4
11.1.2 Laminar and Turbulent Natural Convection Regime (H1 or H6) 11-5
11.1.3 Steam Condensation (H4) 11-6
11.1.4 Turbulent Forced Convection Regime (H3 or H8) 11-7
11.1.5 Post-Dryout Heat Transfer Regime 11-7
11.1.6 Transition Boiling 11-9
11.2 REFERENCES 11-12
12 DRYOUT AND DNB CORRELATIONS 12-1
12.1 FLOW BOILING CRITICAL HEAT FLUX CORRELATION 12-1
12.2 FLOW BOILING CRITICAL QUALITY 12-1
12.3 DNB-CORRELATION 12-2
12.4 POOL BOILING CRITICAL HEAT FLUX 12-3
12.4.1 Rod Critical Temperature 12-3
12.4.2 Slab Critical Temperature 12-4
12.5 REFERENCES 12-4
13 HEAT CONDUCTION MODELS 13-1
13.1 CYLINDRICAL ROD CONDUCTION MODEL 13-1
13.2 SLAB CONDUCTION MODEL 13-4
13.3 REFERENCES 13-6
14 FUEL ROD MODEL 14-1
14.1 GAS GAP MODEL 14-1
14.1.1 Radiation Heat Transfer 14-1
14.1.2 Gas Gap Heat Conduction, Solid Cylinder Pellet 14-2
14.1.3 Gas Gap Heat Conduction, the Cracked Pellet 14-6
14.1.4 Conduction Heat Transfer by Fuel-Cladding Contact Area 14-6
14.2 PELLET MODEL 14-9
14.2.1 Pellet Conductivity 14-10
14.2.2 Pellet Volume Change 14-12
14.2.3 Pellet Thermal Expansion 14-15
14.2.4 Model of Fission Gas Production 14-16
14.3 CLADDING MODEL 14-18
14.3.1 Thermal Expansion 14-19
14.3.2 Zircaloy Cladding Elastic Moduli 14-19
14.3.3 Poisson's Ratio 14-21
14.3.4 Creep Deformation 14-21
14.3.5 Elastic Deformation 14-21
14.4 METAL – WATER REACTION MODEL 14-23

TABLE OF CONTENTS (Cont'd)

14.5 CLADDING RUPTURE MODEL 14-24
14.5.1 Cladding Creep Model 14-25
14.6 REFERENCES 14-30
15 SPECIAL PROCESS MODELS 15-1
15.1 CRITICAL FLOW MODEL 15-1
15.2 PRESSURE RELIEF VALVE SYSTEM 15-2
15.3 REFERENCES 15-2
16 CONTROL SYSTEM MODEL 16-1
16.1 DIGITAL CONTROL SYSTEM SIMULATION PACKAGE 16-1
16.2 IMPLICIT CONTROL SYSTEM 16-1
17 SUPPORTING METHODS 17-1
17.1 TIME STEP CONTROL AND ACCURACY 17-1
17.2 REFERENCES 17-1
18 COMPONENT MODELS 18-1
18.1 PUMPS 18-1
18.1.1 Turbo Pumps 18-1
18.1.2 Jet Pumps 18-5
18.2 STEAM SEPARATOR 18-7
18.2.1 Definition of Carryover and Carryunder 18-7
18.2.2 Mechanistic Separator Model 18-8
18.3 DRIVE DEVICE 18-11
18.3.1 Asynchronous Motor 18-11
18.4 REFERENCES 18-13
19 SOLUTION METHOD 19-1
19.1 NUMERICAL SOLUTION 19-1
19.2 REACTOR KINETICS SOLUTION 19-3
19.3 HYDRAULIC MODEL SOLUTION 19-3
19.4 HEAT CONDUCTION AND TRANSFER SOLUTION 19-7
19.4.1 Coupling between Rod Heat Transfer and Hydraulic 19-7
19.5 REFERENCES 19-10
20 MATERIAL PROPERTIES 20-1
20.1 STEAM-WATER PROPERTIES 20-1
20.2 PROPERTIES OF SOLIDS 20-2
20.3 PROPERTIES OF GASES 20-3
20.4 REFERENCES 20-5
21 MODELING CAPABILITY 21-1
21.1 VALIDITY RANGE OF EQUATION FORMULATION 21-1
21.2 VALIDITY OF CORRELATIONS 21-1
21.2.1 Drift Flux Correlation 21-1
21.2.2 Heat Transfer Correlations 21-2
21.3 EQUATION OF STATE 21-2
21.4 REFERENCES 21-2
22 THE POTENTIAL ENERGY AND DISSIPATION TERMS 22-1
23 NOMENCLATURE, SUBSCRIPTS AND SUPERSCRIPTS, AND DIMENSIONLESS GROUPS 23-1

TABLE OF CONTENTS (Cont'd)

23.1 NOMENCLATURE 23-1
23.2 SUBSCRIPTS AND SUPERSCRIPTS 23-3
23.3 DIMENSIONLESS GROUPS 23-4

LIST OF TABLES

Table 14.2-1 [ ]^{a,b,c} 14-11

Table 14.5-1 Table of Constants for the Parabolic Rate Law, Equation 14-108 14-30

Table 20-1 Thermal Conductivity of Gases: $k = a \cdot T + b$ 20-4

Table 20-2 Molecular Weights and Sutherland Constants for Gases 20-4

Table 20-3 Viscosity of Pure Gases: $\mu = a \cdot T + b$ 20-5

Table 20-4 Accommodation Coefficients, α 20-5

Table 21-1 [ ]^{a,b,c} 21-2

LIST OF FIGURES

Figure 2-1 Codes Providing Models and Methodological Input to POLCA-T 2-1

Figure 3-1 Typical Nodalization of a BWR Reactor Pressure Vessel for POLCA-T 3-2

Figure 3.5-1 Time Integration Schematic Illustration (advancing from time step n-1 to n) 3-6

Figure 4.1-1 [ ]^{a,c} ..4-1

Figure 4.2-1 Overview of POLCA-T Structure 4-3

Figure 6-1 Primary Variables for Volume Cells 6-1

Figure 7.1-1 A Volume Cell in POLCA-T with State Variables 7-3

Figure 7.1-2 Volume Cell with Mass Flow Paths 7-4

Figure 7.1-3 [ ]^{a,c} 7-8

Figure 7.2-1 [ ]^{a,c} 7-11

Figure 7.2-2 Volume Cells with Flow Junctions 7-14

Figure 9.1-1 Definitions of Velocities 9-1

Figure 9.3-1 CCFL Curve Together with Mass Drift Flux G_d 9-9

Figure 9.4-1 Interfacial Heat Flow and Mass Flow Paths in a Volume Cell 9-10

Figure 10-1 Volume Cell With Heat Structure 10-1

Figure 11.1-1 Heat Transfer Regime Maps Used in POLCA-T 11-3

Figure 11.1-2 Heat Flux versus Surface Temperature 11-10

Figure 12.2-1 Principles of Computation of Critical Heat Flux 12-2

Figure 13.1-1 Typical Subdivision of a Cylindrical Heat Structure 13-2

Figure 13.2-1 Typical Subdivision of a Slab Heat Structure 13-4

Figure 14.1-1 Fuel Rod with Definition of Pressures and Other Characteristic Variables 14-9

Figure 14.2-1 Pellet with Cracks 14-10

Figure 14.2-2 The Porosity Correction Factor to Thermal Conductivity *P* of UO_2 Fuel, as a Function of Fuel Density (as can be seen, the factor is normalized to one for 95-percent dense fuel.) 14-11

Figure 14.2-3 Temperature Dependence of the Linear Thermal Expansion of UO_2 14-16

Figure 14.3-1 The Elastic Moduli of Zircaloy as a Function of Temperature for Unirradiated Material with Δ=0 ppm and ζ=0 14-20

Figure 14.3-2 Fuel Tube, Geometrical Dimensions 14-21

Figure 18.1-1 Frictional Torque Versus Shaft Speed 18-3

LIST OF FIGURES (Cont'd)

Figure 18.1-2 Outline of a Jet Pump 18-5
Figure 18.2-1 Principles of Steam Separation in a BWR 18-8
Figure 18.2-2 [ ]^{a,c} 18-9
Figure 18.2-3 [ ]^{a,c} 18-10
Figure 18.3-1 Principal Drive Equipment for a Pump 18-11
Figure 18.3-2 Torque Versus Rev Rate for Asynchronous Motor 18-12
Figure 19.1-1 Simplified Flow Chart of the Calculation Sequence 19-2
Figure 19.4-1 Slab Heat Transfer to Hydraulics 19-8
Figure 20.1-1 Saturation Line and Metastable Lines for Water 20-2

ACRONYMS

Acronyms	Definition
ADS	automatic depressurization system
ANS	American Nuclear Society
ATWC	anticipated transients without (crediting) control rods
ATWS	anticipated transient without scram
BCC	body centered cubic
BWR	boiling water reactor
CCFL	countercurrent flow limitation
CHF	critical heat flux
CO	carryover
CPR	critical power ratio
CRDA	control rod drop accident analysis
CU	carryunder
DNB	departure from nucleate boiling
DNBR	departure from nucleate boiling ratio
ECCS	emergency core cooling system
FGR	fission gas release
HCP	hexagonal closed pack
LOCA	loss-of-coolant accident
LWR	light water reactor
NRC	Nuclear Regulatory Commission
PM	process model
PI	proportional integrator
QMS	Quality Management System
RIA	reactivity initiated accident
1-D	one dimensional
2-D	two dimensional
3-D	three dimensional

1 INTRODUCTION AND OBJECTIVES

This report describes Westinghouse Electric Company methodology and methods for analyzing boiling water reactor (BWR) transients using POLCA-T. POLCA-T is an advanced dynamic system analysis code with the three-dimensional (3-D) core physics described by the nodal code POLCA presented in the topical report CENPD-390-P-A Revision 0, "The Advanced PHOENIX and POLCA Codes for Nuclear Design of Boiling Water Reactors," December 2000. Once approved, Westinghouse intends to use the methodology presented here for BWR licensing analyses.

POLCA-T is a computer code for transient thermal-hydraulic and neutron-kinetic analysis of BWRs. It can be used as a general tool for advanced simulation of single- and two-phase flow systems including non-condensable gases. The code has a full 3-D neutronic model where each fuel assembly in the reactor core may be represented in the thermal-hydraulic model. The reactor pressure vessel, external pump loops, steam system, feedwater system, emergency core cooling systems, and steam relief system can be modeled in detail. Basic information about the physical models, numerical methods, and BWR specific system models, that are implemented in the POLCA-T code, are described herein.

The POLCA-T general code description is provided in the main topical with applications described in Appendix A and B. Additional Appendices C and D will be submitted later. The general code description section provides basic information about the physical models, BWR process system models, and numerical methods that are implemented in the POLCA-T code. It also provides an overview of the code structure and how POLCA-T connects to other codes in typical analyses. Details on the use of the codes, including their interactions, are presented in the application specific appendices. The applications will be introduced in a staged process and will include Control Rod Drop Accident (CRDA) Analysis, Stability Analysis, Transient Analysis, and Anticipated Transient without Scram (ATWS) Analysis. The first two applications are included as Appendix A and B. Subsequent applications (including Transient Analysis and ATWS) will be submitted prior to their use. Each application is included as an appendix which contains the evaluation model and the qualification of the code for performing the intended analysis.

Appendix A, "Control Rod Drop Accident Analysis," presents the evaluation model for performing control rod accident licensing analysis and the qualification of the evaluation model. An Organization for Economic Co-Operation and Development (OECD) rod ejection benchmark problem and representative SPERT-III-E cases are analyzed. The CRDA, as modeled by the current RAMONA-3 licensed methodology, is compared to the CRDA as modeled by POLCA-T.

Appendix B, "Stability Analysis," presents the evaluation model for performing stability licensing evaluations and the qualification of the evaluation model. Only determination of a stable operating domain and the exclusion zones are considered. The qualification is performed against plant stability measurements and FRIGG loop stability measurements.

Additional application appendices will be submitted later as supplements to this POLCA-T topical report.

Appendix C, "Transient Analysis," will include the evaluation model and its qualification for transient analysis and the determination of the plant operating limits.

Appendix D," Anticipated Transients Without Scram Analysis," will include the evaluation model and its qualification for ATWS analysis.

2 BASIS OF POLCA-T

The POLCA-T code utilizes or incorporates codes/models developed and used in other Westinghouse codes that have been and still are used for design and licensing analysis of BWRs. Many of these codes/models have been reviewed and approved by the NRC. Others have been used in European applications for licensing basis analyses. This section will provide an overview of the POLCA-T code. Subsequent sections will provide details of the individual codes/models. Figure 2-1 provides clarification of the structure of POLCA-T.

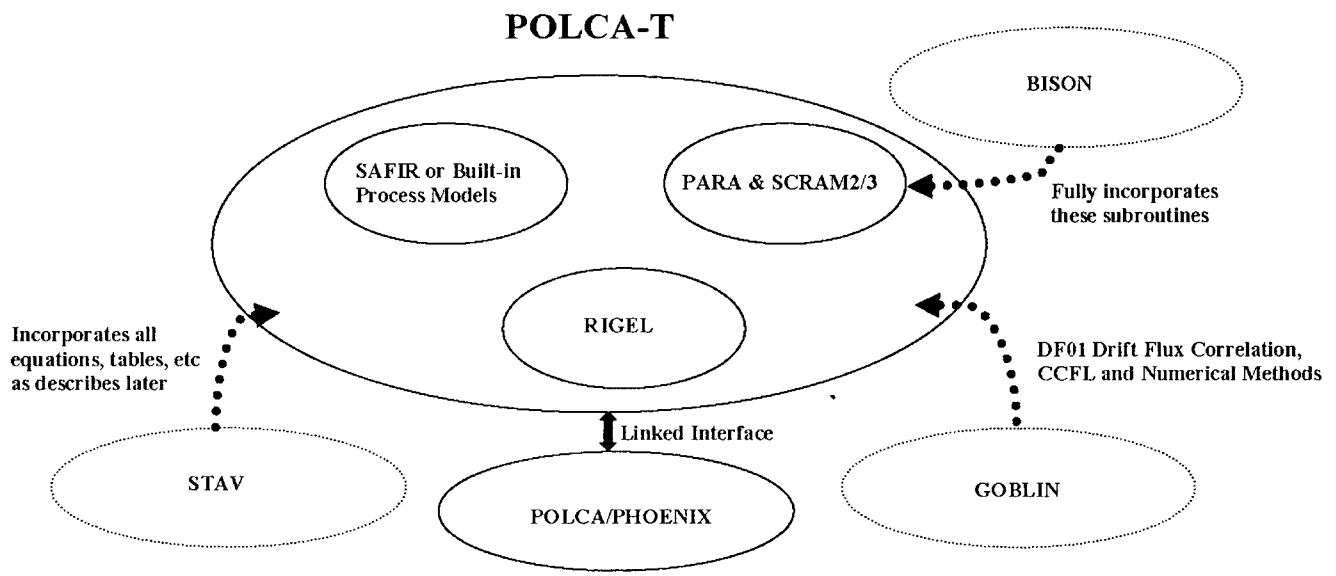

Figure 2-1. Codes Providing Models and Methodological Input to POLCA-T

The PHOENIX/POLCA (Reference 2.1) code suite is the static core simulator where cell data are created for each fuel assembly type in the core. POLCA also is used to calculate the fission power distributions in the core. POLCA-T incorporates the kinetics terms used for transient calculations and iterates with POLCA to solve the two-group diffusion equations with a number of delayed neutron families determined by the code user. As described in this topical, POLCA-T was developed with PHONEIX4/POLCA7 (Reference 2.1) as the static core simulator. However, any latter versions of the static core stimulator that are licensed by the NRC can be used with POLCA-T.

POLCA-T's thermal-hydraulics model (RIGEL – an advanced 3-D thermal-hydrualics code developed and used in Europe) models each fuel assembly in the core, including intra- and inter-assembly bypass regions. This model has been fully incorporated into the POLCA-T code and interacts with the neutron kinetics (POLCA/PHOENIX) through arrays that store data structure for communication between the two codes.

POLCA-T includes two different control and safety system modules (SAFIR or built-in process models). These modules model a series of relief, safety, and controlled depressurization valves that can be located on the steam lines of a BWR. Several of these valves may be associated with the automatic depressurization system (ADS). The valve model includes the capability to simulate delay times in

opening and closing, force open and force close signals, low power close interlocks, and a programmed controlled opening, as in the control depressurization valves. The application of SAFIR will be described and validated in subsequent application appendices (not required for Appendices A and B).

The entire PARA and SCRAM2/3 codes have been fully incorporated in POLCA-T for compatibility with BISON simulation of the behavior of the steam lines and the scram system during pressurization events. The application of these routines will be described and validated in subsequent application appendices (not required for Appendices A and B).

The GOBLIN code provides the bases for the solution formulation and several models for thermal-hydraulic and heat transfer simulations. The DF01 drift flux correlation is used with the same validity range as in the loss-of-coolant-accident (LOCA) Evaluation Model (EM). The mass, momentum, energy, and state equations along with the pump speed equations are solved simultaneously using Newton's method. The Jacobian matrix includes all derivatives and is inverted using a sparse matrix technique.

All of the equations, tables, and so forth specified in Section 14 are from the STAV code. These equations, tables, and so forth have been directly incorporated into POLCA-T.

All code modifications comply with Westinghouse's Appendix B Quality Assurance Program.

2.1 REFERENCES

2.1 "The Advanced PHOENIX and POLCA Codes for Nuclear Design of Boiling Water Reactors," CENPD-390-P-A, December 2000.

3 POLCA-T SUMMARY DESCRIPTION

POLCA-T is a computer code for transient thermal-hydraulic and neutron kinetic analysis of BWRs. It can be used also as a general tool for advanced simulation of single- and two-phase flow systems including non-condensable gases. The code incorporates a full 3-D neutronics model of the reactor core and each fuel assembly in the core, including in- and inter-assembly bypass regions, may be represented in the thermal-hydraulic model. The reactor pressure vessel, external pump loops, steam system, feedwater system, emergency core cooling system (ECCSs) and steam relief system can be modeled to the desired detail. Control and safety systems are modeled using the SAFIR code package, which is an integral part of the code.

The application areas of the POLCA-T cover:

1. Anticipated operational transients

2. Core stability

3. Reactivity initiated accidents (RIA)

4. Anticipated transients without scram (ATWS) and anticipated transients without (crediting) control rods (ATWC)

5. LOCAs without uncovering of the core

The POLCA-T code is specifically adapted to the analysis of transient events where the 3-D power generation phenomena in the core become important. The code also contains models for boron transport, which makes it possible also to analyze different types of boron shutdown scenarios (ATWS and ATWC).

The models implemented in the code allow for flexibility in the description of the primary system and secondary systems to accommodate various plant designs.

The reactor is divided into a user-specified number of volume cells and flow paths connecting volume cells. Figure 3-1 shows a sample geometric representation for the POLCA-T code.

The POLCA-T code models can be divided into four main sections:

1. The thermal-hydraulic model includes thermal non-equilibrium between phases and has full geometric flexibility. The model solves the mass and energy conservation equations for each phase and for each volume cell. The momentum conservation equation is solved for each flow path. Constitutive equations are included for calculating the fluid properties and their derivatives. Empirical correlations are implemented for the calculation of pressure drops, fluid properties, solubility of non-condensable gases, phase flows (drift flux), and critical flow rate.

2. The system models contain models of the various reactor components. They include the steam separators and dryers, reactor water level measurement, reactor trip system, depressurization systems, and recirculation and jet pumps.

a,b,c

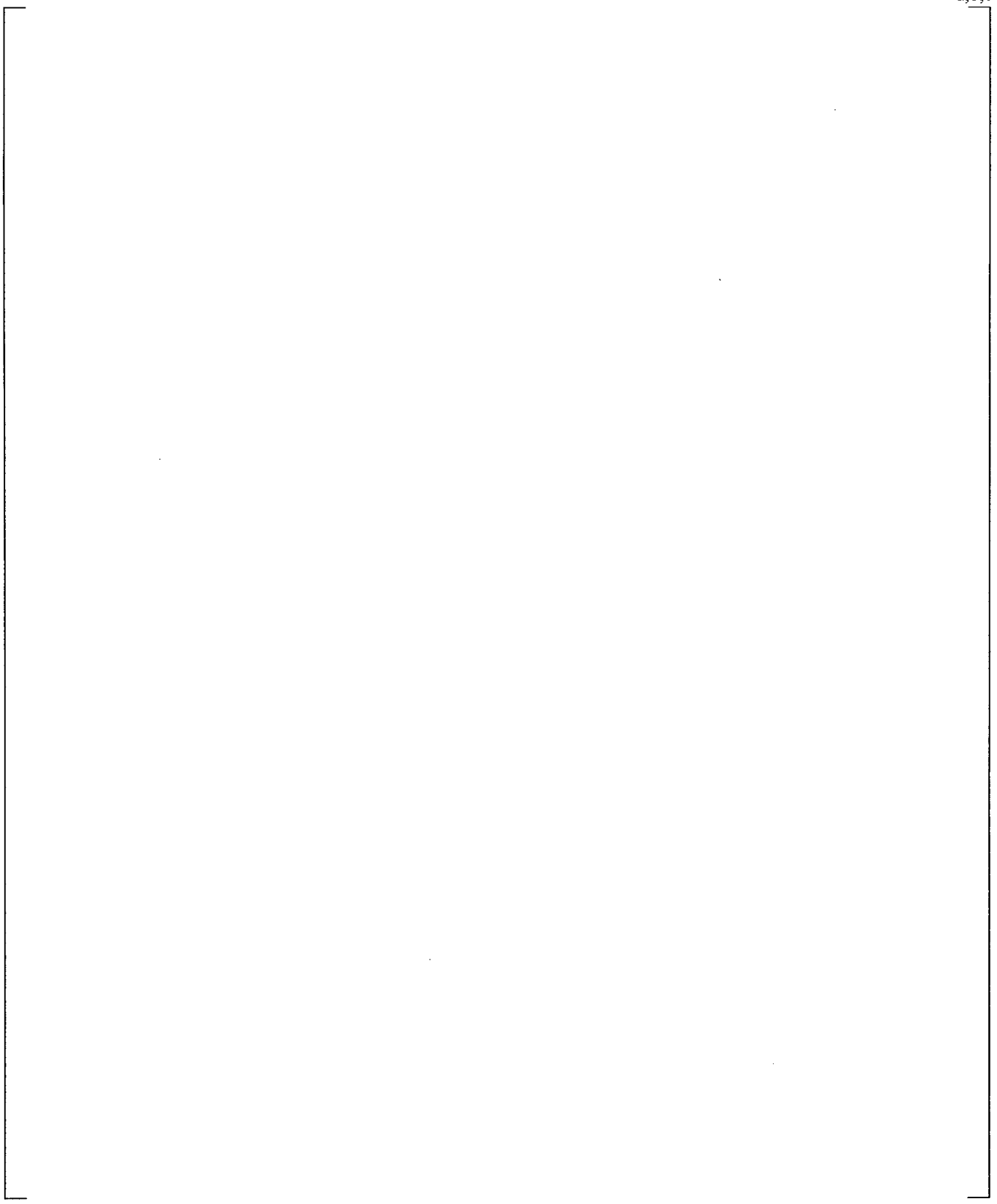

Figure 3-1. Typical Nodalization of a BWR Reactor Pressure Vessel for POLCA-T

3. The thermal model solves the heat conduction equation for the heat structures (fuel rods, pressure vessel, and internals) using heat transfer boundary conditions. The result is the heat transfer to the coolant. A complete range of convective heat transfer regimes is included in the code.

4. The power generation models calculate the heat generation due to fission in the fuel, direct heat released in the coolant, and decay heat. A two group 3-D neutron kinetics model determines fission power. The neutronics models in the code are the same as those that are used in the static nuclear core analyzer POLCA7 with the addition of proper kinetic terms for transient use.

The user has the option to use a fully implicit numerical method or a semi-implicit method to solve the hydraulic model and the simultaneous heat transfer and thermal conduction equations.

The following provides a summary description of the main POLCA-T models. A more detailed description of each model is given in separate sections that follow.

3.1 THE THERMAL HYDRAULIC MODEL

The hydraulic model solves the governing equations for the coolant flow, as follows:

[

]^{a,c}

The mass conservation equations for boron and non-condensable gases are solved if the user has requested such models.

The above set of equations (together with the necessary secondary relations and constitutive correlations, and boundary conditions) form a complete system of equations for calculating the fluid flow conditions.

The mass and energy conservation equations for the fluid flow are integrated over the volume cells, and the resulting set of equations are cast into finite-difference form using a fully or semi-implicit scheme.

---

1. Gas may be a mixture of vapor and non-condensable gases.

The momentum balance is integrated between the centers of the volume cells connected by the flow path as shown later in Figure 7.2-2.

For each volume cell, values of pressure, phase temperatures, void content, and average phase velocities are determined by the solution of the conservation equations. Properties such as steam qualities, void fractions, fluid temperatures, velocities, etc., are calculated using secondary relations and constitutive correlations.

Several constitutive equations and empirical correlations are necessary to complete the formulation of the basic fluid equations. The most important correlations in the hydraulic model of the POLCA-T code are:

[

]^{a,c}

A relation based on drift flux and countercurrent flow limitation (CCFL) correlations calculates the phase velocities in the flow paths and is also the basis for calculating the two-phase energy transport in these flow paths. The CCFL correlation is a general formulation applicable to different flow geometries.

Choked flow is treated using correlations for critical flow valid for a wide range of coolant states.

3.2 COMPONENT MODELS

POLCA-T includes specific models for the following boiling water reactor systems and components:

[

]^{a,c}

The speed of the main circulation pumps is determined from the solution of the angular momentum balance for the pump impeller. This equation is solved simultaneously with the fluid conservation equations. The applied torque represents the net torque from all sources, i.e., the hydraulic interaction between the fluid and the pump impeller (usually referred to as the "hydraulic torque"), frictional losses in the rotating machinery, and torque supplied by the pump motor. The pump head and hydraulic torque are determined from user supplied homologous curves which are functions of pump speed, volumetric flow rate, and void fraction. The user can, instead of using the homologous pump curves, use pump performance data for positive flow and head as input to the pump model, which in some cases could be very advantageous.

The jet pump model modifies the 1-D momentum equation to account for the spatial and temporal acceleration due to the significant momentum exchange occurring between the jet pump drive and suction flows.

Models describing the efficiency of the steam separators are included. The model determines the separation efficiency expressed by the carryover fraction (water entrained by the steam to the steam dome) and carryunder fractions (steam entrained by the water to the downcomer).

The steam line flow and moisture content can be specified as a function of time. The feedwater system flow and enthalpy can also be specified versus time.

Loss-of-offsite power can be modeled to occur at any time during the transient with the subsequent diesel start, pump start, and valve actuation delays. The steam pressure relief/safety valve system including the automatic depressurization system (ADS) can be modeled in the desired detail to account for opening and reset delays. The control logic and controllers are modeled by the SAFIR package.

The ECCSs for both core spray and injection can be modeled using tables of flow rates as a function of differential pressure between the reactor and the containment wetwell if the condensation pool is the source of the water. Other ways to model the flow are available if the ECCS uses water from other sources.

3.3 THE THERMAL MODEL

The thermal model in the POLCA-T code calculates the heat transferred from the fuel rods, reactor vessel, and internals to the coolant (to steam and water phases separately), and the energy interchange between phases. The surface heat transfer and material heat conduction problems are solved simultaneously to determine the rate at which total heat is transferred to the coolant.

The heat transfer coefficient couples the hydraulic solution to the thermal conduction solution through the coolant state and surface temperature. Empirical heat transfer coefficient correlations are included for single-phase liquid and vapor, two-phase non-dryout, transition boiling, and post-dryout heat transfer regimes.

The radial heat conduction equation is solved for the fuel rods (axial conduction is neglected) using an implicit finite-difference technique and the appropriate heat transfer coefficients as boundary conditions.

Detailed models for heat transfer from the reactor vessel and the internals are also included. These components are referred to as "slabs" or in general as "heat structures." The user can specify any number of heat transferring heat structures, which can be in contact with coolant on both sides or isolated on either side. The 1-D heat conduction equation is solved for a user-specified nodal subdivision of each heat structure using a finite difference technique. Each heat structure can be composed of several layers, each of them made from different material.

3.4 POWER GENERATION MODELS

The power generation part of POLCA-T calculates the fission power and decay power. A 3-D two-group kinetics model allowing for up to six delayed neutron groups calculates the fission power generation in the core. Reactivity feedback is included for moderator (coolant) temperature, fuel temperature, boron concentrations and reactor control rods. The power fraction deposited directly in the coolant is modeled as a function of coolant density.

The decay power generation is calculated by specification of fractions of slow and fast decaying parts of decay power, together with its time constants, simulating the decay of Uranium-239 and Neptunium-239. A second option is to provide a table as decay power versus time to simulate the decay power generation.

3.5 NUMERICAL METHODS

The mass and energy equations for the phases (liquid and gas), the momentum equation, and the drift flux correlation for each flow path along with the pump speed equations are solved simultaneously using Newton's method. The Jacobian matrix includes all derivatives and is inverted using a sparse matrix technique.

The heat structure conduction equations are solved by Gaussian elimination and back substitution. The conduction equation and the surface heat transfer are solved iteratively for the surface temperature.

The 3-D-kinetics model, POLCA7, is solved using an iterative method and is then iterated in an outer loop including the thermal-hydraulic equations until convergence is reached.

The hydraulic model can be solved using a fully implicit or semi-implicit method. The thermal conduction and heat transfer models are solved using a method that is implicit in time. The hydraulic and conduction solutions are coupled through the surface heat transfer. The hydraulic fluid conditions are treated implicitly in the heat conduction and heat transfer solutions. The surface heat transfer, however, is treated explicitly in the hydraulic solution. Figure 3.5-1 shows the outline of the computational procedure in POLCA-T.

Figure 3.5-1 illustrates schematically the time integration of the models.

a,b,c

Figure 3.5-1. Time Integration Schematic Illustration (advancing from time step n-1 to n)

4 CODE STRUCTURE

4.1 INTERACTION OF THERMAL-HYDRAULICS AND NEUTRON KINETICS

The POLCA-T kinetics is based on the static neutronics version of POLCA7 (Reference 4.1), with some additions due to the time dependencies. The POLCA7 part of POLCA-T solves the two-group diffusion equations with a number of delayed neutron families determined by the code user.

[

]^{a,c}

a,b,c

[

]

Figure 4.1-1. [**]^{a,c}**

[

]^{a,c}

4.2 POLCA-T STRUCTURE

The physical system is nodalized, i.e., divided into a number of nodes. The nodes are of two basic types: volume cells and flow paths. Volume cells and flow paths alternate in a network to form a staggered mesh.

Volume cells represent physical volumes with capacities to contain things such as a fluid mass or heat energy. **Flow paths** (junctions) represent boundaries between volume cells, with characteristic variables "velocities," "energy flows," etc. A flow path has two volume cell neighbors. Neighbors to the volume cells do not need to be specified; a network is completely determined by the flow paths and the volume cells they connect.

The spatial variation of physical properties inside any volume cell is assumed to be uniform. Hence, the nodalization is a special kind of spatial discretization, allowing the physical system to be represented by a set of ordinary differential equations.

$$\dot{y}_i = f_i(y) \tag{4-1}$$

for the "primary variables" y_i, where the dot denotes time derivative. The primary variables defining the state vector $\vec{y}$ with relatively few components can group the equations of the system (4-1).

[

]^{a,c}

4.3 REFERENCES

4.1 "The Advanced PHOENIX and POLCA Codes for Nuclear Design of Boiling Water Reactors," CENPD-390-P-A, December 2000.

a,b,c

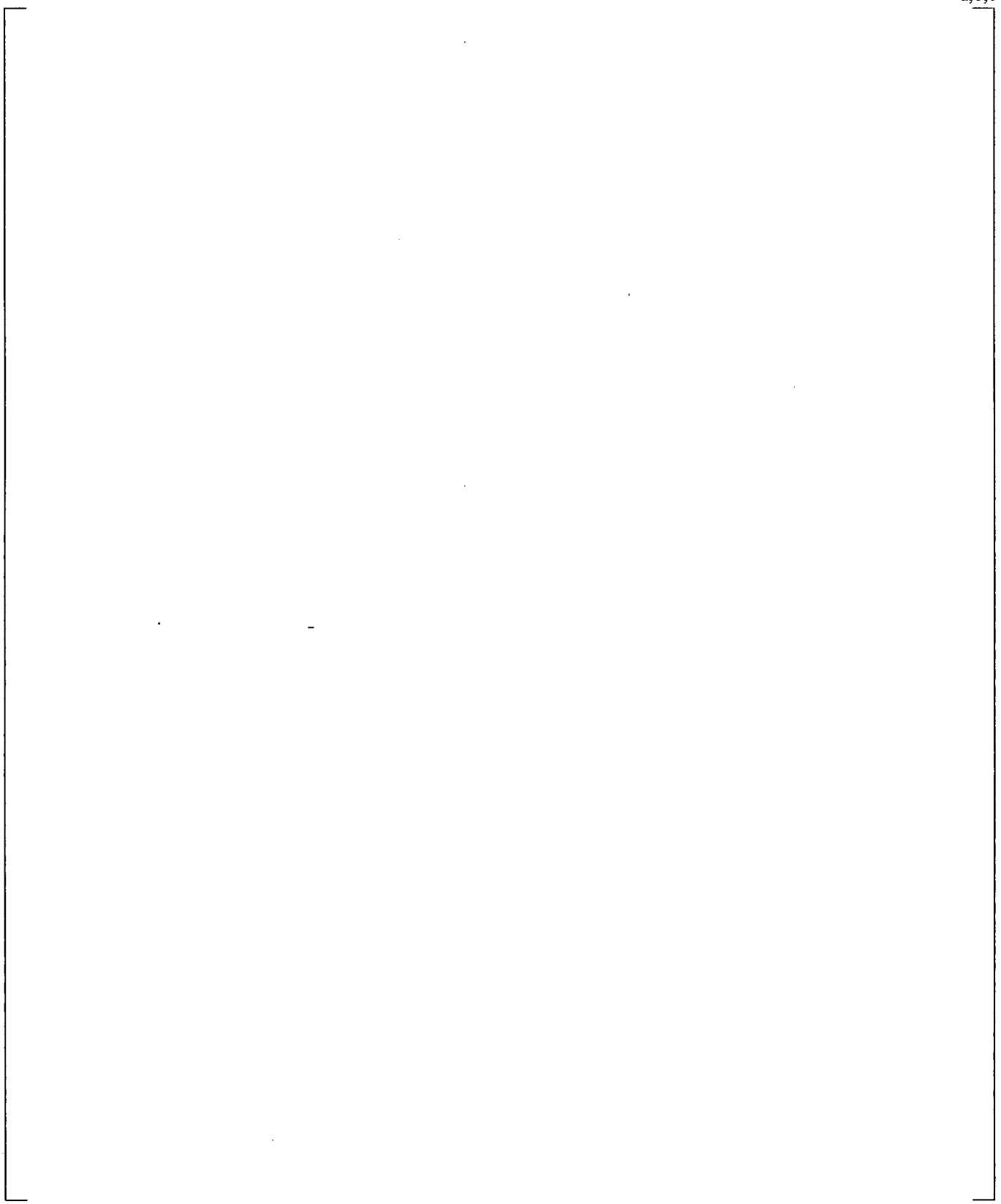

Figure 4.2-1. Overview of POLCA-T Structure

5 GEOMETRICAL MODELLING ASSUMPTIONS

This section describes the geometrical modeling assumptions for the hydraulic model in the POLCA-T code.

The primary circulation system of the reactor is subdivided into a number of volume cells connected by flow paths. The volume cells may have more than one inlet or outlet flow paths. The total number of volumes and flow paths is determined by the user, based on experience gained in the application of the code. The boundaries between the volumes, as well as the sizes of them, are mainly determined by the requirement of spatial resolution in the results considering the physical processes that will take place during the event that will be analyzed.

Furthermore, the subdivision into volumes is governed by the assumptions inherent in the hydraulic models. One typical such assumption is that of a spatially constant fluid temperature within a volume, which for instance means that, a control volume boundary should be placed immediately above the feedwater inlet to the pressure vessel.

The geometrical models for fuel rods and internal or bounding structures are closely related to the geometrical model for the hydraulic models. The state in the hydraulic model's volume cells is used as boundary condition to the heat transfer and conduction models for those elements. At the same time, the heat transfer rates to or from the fuel rods and structures are supplied as source terms in the energy balances for the hydraulic volume cells.

Normally, the fuel rods and structures are subdivided so that there is only one volume cell bounding the individual pieces of a rod or structure (there may be one volume cell at each side of a two-sided structure).

A number of boundary cells/flow paths with pre-specified (potentially time dependent) fluid conditions may also be used with POLCA-T modeling. They can be useful in simulating an interaction with out-of-vessel systems (feed water, core spray) especially when simulating experimental loops.

6 PRIMARY VARIABLES – STATE VECTOR CONCEPT

The basic equations are formulated (see Section 7) for the volume cells and flow paths by integrating the space-dependent equations over the volumes and introducing macroscopic variables (such as mass content and mass flow rates) instead of microscopic variables (such as density and velocity). The momentum balance equation is integrated between the centers of the volume cells connected by the flow path. The resulting basic equations, which now are in the form of ordinary differential equations, are formulated as functions of the primary variables.

The primary variables for the volume cell (Figure 6-1) are collectively the state vector for that volume cell. They are:

- Volume averaged total pressure (p)
- Void content (void) (volume fraction of gas[2])
- Liquid temperature (T_{liq})
- Gas temperature (T_{gas})
- Partial pressure of non-condensable gas (P_{nc})
- Boron concentration (C_{bor})
- Average velocity for liquid (U_{liqm})
- Average gas velocity (U_{gasm})

For the flow paths the velocities of liquid and gas are chosen as primary variables making up the state vector for a flow path:

- Liquid velocity (U_{liq})
- Gas velocity (U_{gas})

a,b,c

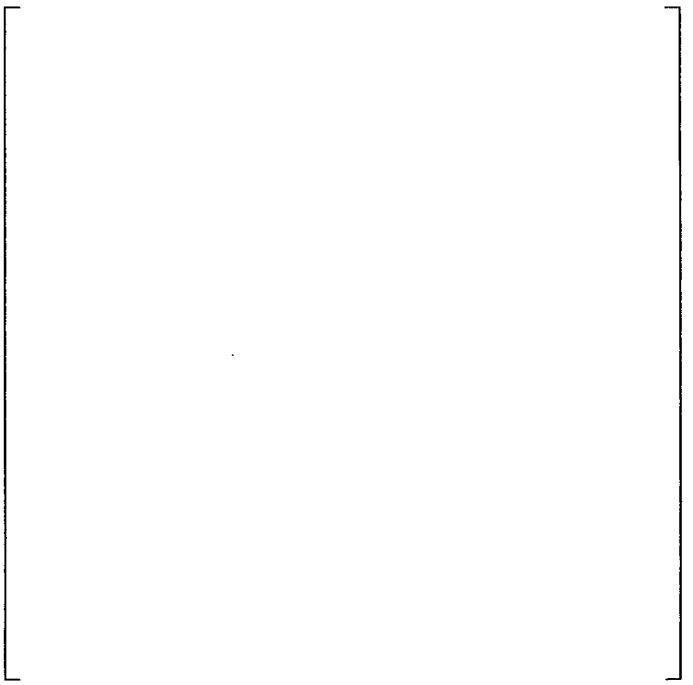

Figure 6-1. Primary Variables for Volume Cells

2. Wherever the word gas is used it means the mixture of vapor and non-condensable gas (if present).

The equations are kept in their conserving form (i.e., conserving masses and energy for each phase and momentum for the mixture of gas and liquid). Secondary variables are introduced in order to simplify the solution procedure. These variables describe the results from the constitutive equations and empirical correlations (such as energy flow rates, mass flow rates, pressure drop, and so forth) and are functions of the primary variables.

[

]^{a,c}

[

]a,c

7 HYDRODYNAMIC MODEL

The hydraulic models in the POLCA-T code are based on the following main principles and assumptions.

A geometrical model of the primary system uses flow paths to connect volume cells. The code user determines the number of volume cells and flow paths as well as the layout of them, which is based on the user's experience or stated in application-specific topical reports and qualification reports. The volumes of each volume cell are fixed, the water level in each cell is calculated both as a condensed level or as a two-phase level as a secondary variable calculation. The basic equations determine the fluid state in each volume cell and the mass flow rates of the phases through each flow path. The basic equations are the mass, energy, and momentum conservation equations. They are derived for 1-D flow. The mass and energy equations are separate for each phase – gas and liquid – while the momentum equation is formulated for the mixture of liquid and gas.

The main assumptions used in this derivation considering the two-phase flow are:

1. The phases may be in thermal non-equilibrium (i.e., have different temperatures).

2. The individual phase velocities can be determined from empirical correlations.

The non-equilibrium model is based on the formulation of two mass balances (one for the liquid and one for the gas/steam phase), two energy balances (one for the liquid and one for the gas phase), and one momentum balance for the mixture.

The equations of state supplemented by empirical correlations for the fluid properties support the basic equations.

Empirical correlations are used to determine the interfacial heat and mass (solubility of non-condensable gases) transfer, heat transfer to heat structures, the pressure drop for the flowing fluid due to friction and local flow obstacles, critical flow, and the flow of the individual phases in the case of two-phase flow.

The basic (conservation) equations result in ordinary differential equations for each volume cell and flow path. The solution of these equations describes the time variation of a set of basic (conserved) variables for each volume and each flow path. All other variables describing the state in a volume cell or the flows in a flow path, the primary variables, can be derived from these basic variables using the constitutive models (empirical relations and equations of state). The basic variables for the volume cells are the liquid mass (M_l), the gas mass (M_g), the energy of the liquid (E_l) and the energy of gas (E_g). For flow paths, the basic variable is the mixture mass flow rate (w). In addition to these equations, algebraic equations are set up for each volume cell to determine the average velocities of the phases.

Water (two-phase) levels may be tracked as a secondary variable in vertical columns of control volumes. In this case, the basic equation is a correlation describing the movement of the level and the associated basic variable is the level position.

The steady-state conditions are calculated by the code using the same set of equations as for transient analysis but with time derivatives equal to zero. A minimum set of boundary conditions are used to

specify the initial steady-state condition. These boundary conditions are the power generation and its distribution, given by POLCA7, the feedwater temperature, the steam line pressure, the pump revolution rate, and the water level in the downcomer in the case of simulating a BWR.

The hydraulic models interact with the thermal conduction and/or heat transfer models for fuel rods and internal structures to bounding the primary system. Furthermore, the hydraulic models interact through mass, energy, and momentum source terms with the system models (steam separators, pumps, emergency cooling water systems, etc.).

The constitutive models that are used are described in Section 9. The application of the models to the volume cell and flow path approach that is used in the code is explained in the rest of this section.

7.1 VOLUME CELL

This section describes the basic equations that are used in the thermal-hydraulic model for each volume cell. The basic equations are:

Mass Balances

- A mass balance for the gas phase in the volume
- A mass balance for the liquid phase in the volume

As an option, and in addition, to these two mass balances, the following two mass balances of boron and non-condensable gas can be added to the set of equations for specified volume cells:

- A mass balance for the boron in the volume
- A mass balance for the non-condensable gas in the volume

Energy Balances

- An energy balance for the gas phase in the volume
- An energy balance for the liquid phase in the volume

[

]^{a,c}

a,b,c

Figure 7.1-1. A Volume Cell in POLCA-T with State Variables

7.1.1 Mass Conservation Equations

Hereafter, the theoretical basis for the mass conservation equations is given. Then the formulation of the equations in the POLCA-T code is derived and described.

Theoretical Basis

The mass conservation equation for the phases/components (References 7.1 and 7.2) is:

$$\frac{\partial \rho_i}{\partial t} = -\nabla(\rho_i u_i) \tag{7-1}$$

Integrating (7-1) over a control volume (volume cell) as shown in Figure 7.1-2 results in the following formulation:

$$\frac{\partial M}{\partial t} = \sum j \, Wj \cdot Sj + Wsrc + \Gamma \tag{7-2}$$

where:

W_j is the mass flow rate through flow path number j,
W_{src} accounts for external mass source and sink terms, and
Γ is the interfacial mass transfer rate, j, between phases/components.

The summation extends over all flow paths connected to the volume and the number of flow paths is unlimited with practically no restriction.

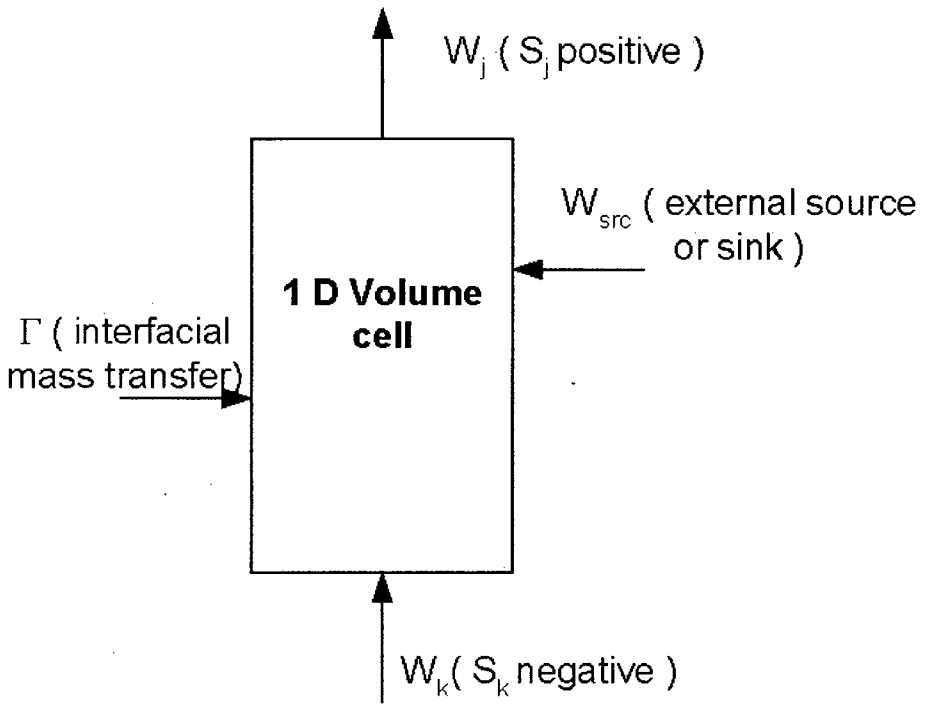

Figure 7.1-2. Volume Cell with Mass Flow Paths

Furthermore,

$$S_j = \begin{cases} +1 \text{ if positive flow through flow path j is directed into the volume} \\ -1 \text{ otherwise} \end{cases}$$

The external mass source W_{src} and sink terms account for:

Wbr = Break flow rate from control volume,

Wecc = Coolant flow into control volume from various systems (e.g., feedwater, spray),

Wsep = Coolant flow into control volume from separator outlets,

Wcond = Coolant flow into control volume from steam dryer outlets, and

Γ = The contribution in mass transfer rate from interfacial flow accounts for evaporation and condensation interfacial mass flow and for solution/dissolution of non-condensable gases in the liquid phase.

Application in the POLCA-T Code

The integrated mass conservation equation is written in finite difference form using a fully implicit to semi-implicit finite difference scheme method as specified by the user. Hence equation (7-2) becomes for the phases:

Liquid Phase Mass Conservation Equation

$$\frac{M_{liq,i}^{n+1} - M_{liq,i}^{n}}{\Delta t} - \sum_{j} W_{liq,j}^{n+1} S_j - \Gamma_i^{n+1} - W_{liq,src,i}^{n+1} = 0 \qquad (7\text{-}3)$$

where superscripts n and n+1 denote time t_n and t_{n+1}, respectively, the subscript i denotes fluid volume cell number and subscript j denotes flow path number. The summation is extended over all flow paths connected to volume i.

$M_{liq,i}$ = liquid mass in volume cell i,

$W_{liq,j}$ = liquid mass flow rate through flow path number j,

Γ_i = liquid generation rate in volume cell i due to condensation/evaporation, and

$W_{liq,src,i}$ = liquid flow in to or out from volume cell i due to external sources or sinks (cf. Wsrc above).

The conserved quantity M_{liq} is a function g_{liq} of the primary variables (p, void, Tliq):

$$M_{liq} = g_{liq}(p, void, T_{liq}) \qquad (7\text{-}4)$$

Gas Phase Mass Conservation Equation

The gas mass conservation equation is derived in the same manner as the liquid mass conservation equation:

$$\frac{M_{gas,i}^{n+1} - M_{gas,i}^{n}}{\Delta t} - \sum_{j} W_{gas,j}^{n+1} S_j - \Gamma_i^{n+1} - W_{gas,src,i}^{n+1} = 0 \qquad (7\text{-}5)$$

where:

Mgas,i = vapor mass in volume cell i,

Wgas,j = vapor mass flow rate through flow path number j,

Γ_i = vapor generation rate in volume cell i due to evaporation/condensation + generation of non-condensable gas (dissolution or generation from other sources), and

Wgas,src,i = vapor flow into or out of volume cell i due to external sources or sinks (cf. Wsrc above).

The conserved quantity M_{gas} is a function g_{gas} of the primary variables (p, void, Tgas):

$$M_{gas} = g_{gas}(p, v, H) = \alpha \cdot V/v_{gas} \tag{7-6}$$

where:

α = volume fraction of vapor (is a function of the primary variables (p v, H)), and
v_{gas} = specific volume of vapor (also a function of the primary variables (p, v, H)).

The same equation set up is used for component of non-condensable gases and for boron mass calculation.

For a non-condensable gas it will be:

$$\frac{M^{n+1}_{ncgas,} - M^{n}_{ncgas,}}{\Delta t} - \sum_j W^{n+1}_{ncgas,} S_j - \Gamma_i^{n+1} - W^{n+1}_{ncgas,src,i} = 0 \tag{7-7}$$

where:

Mncgas,i = mass of non-condensable gas in volume cell i,

Wncgas,j = mass flow rate of non-condensable gas through flow path number j,

Γi = non-condensable gas generation rate in volume cell i due to solution/dissolution of non condensable gases (or other sources), and

Wncgas,src,i = non-condensable gas flow in to or out from volume cell i due to external sources or sinks (cf. Wsrc above).

The conserved quantity M_{gas} is a function g_{gas} of the variables (p_{nc}, Tgas):

$$M_{gas} = g_{gas}(P_{nc}, Tgas) \tag{7-8}$$

For mass balance of boron it will be:

$$\frac{M^{n+1}_{bor,i} - M^{n}_{bor,i}}{\Delta t} - \sum_j W^{n+1}_{bor,j} S_j - W^{n+1}_{bor,src,i} = 0 \tag{7-9}$$

The conserved quantity M_{bor} is a function g_{bor} of the primary variables (C_{bor}, W_{liq}).

$$M_{bor} = g_{bor}(C_{bor}, W_{liq}) \tag{7-10}$$

7.1.2 Energy Conservation Equations

This section describes the derivation and application of the energy balance equation that is applied to each phase in the POLCA-T code.

Theoretical Basis

The general form of the energy conservation equation (References 7.1 and 7.2) is:

$$\frac{\partial(e\rho)}{\partial t} + \nabla(e\rho\,\underline{u}) + \nabla\,\underline{q}'' - q''' - \nabla(\underline{\underline{\tau}}\,\underline{u}) = 0 \tag{7-11}$$

where:

$$e = eint + ekin + epot = \text{total specific energy} \tag{7-12}$$

eint = internal energy,
ekin = kinetic energy,
epot = potential energy,
ρ = density,
u = velocity field vector,
q" = heat flux,
q''' = internal heat generation per unit volume, and
$\underline{\underline{\tau}}$ = stress tensor,

The specific enthalpy h is introduced,

$$h = e_{int} + p/\rho \tag{7-13}$$

and the stress tensor is divided into a normal and shear stress

$$\sigma_{ij} = -\,p\,\delta ij + \bar{\tau}_{ij} \tag{7-14}$$

where ∂_{ij} is the Kronecker delta, defined by

$$\partial ij = \begin{cases} 0 & \text{if } \begin{cases} i \neq j \\ i = j \end{cases} \\ 1 \end{cases} \tag{7-15}$$

ρ = local static pressure, and

$$\overline{\tau_{ij}} = \delta ij - \left\{\sum_{k=1}^{3} \frac{\tau_{kk}}{3}\right\} \cdot \delta ij \tag{7-16}$$

The stress deviator term τ_{ij} represents the part of the forces in the fluid, due to relative motion of nearby particles in the fluid.

Equation (7-11) can be now rewritten as:

$$\frac{\partial(h\rho - p)}{\partial t} + \nabla \cdot (h\rho\underline{u}) + \nabla \cdot q'' - q''' =$$

$$-\frac{\partial}{\partial t}(\rho(e_{kin} + e_{pot}) - \nabla \cdot (\rho(ekin + epot)\, u + \nabla \cdot (\underline{\underline{\tau}}\ \underline{u}) \qquad (7\text{-}17)$$

The right hand side of equation (7-17) represents the contributions from kinetic and potential energy and dissipation due to stress. Below it is demonstrated that some terms of the right hand side of equation (7-17) can be neglected, hence the energy equation used in the POLCA-T code is:

$$\frac{\partial((h + e_{kin})\rho - p)}{\partial t} + \nabla \cdot (h\rho u + e_{kin}\, \rho u) + \nabla \cdot q'' - q''' = 0 \qquad (7\text{-}18)$$

The potential energy and dissipation terms are omitted in equation (7-18). Section 22 demonstrates that these terms are negligible.

Finite Difference Formulation of the Energy

Equation (7-18) is integrated over the volume cell shown in Figure 7.1-3.

[ ]^{a,c}

a,b,c

[

]

Figure 7.1-3. [ ]^{a,c}

The first term is

$$\int_V \frac{\partial((h + e_{kin})\rho - p)}{\partial t} dV = \frac{d}{dt}\int_V ((h + e_{kin})\rho - p)dV = \frac{d}{dt}(M_{phase,i} \cdot H0_{phase,i} - V_i \cdot P_i) \quad (7\text{-}19)$$

where for each phase/component *phase* (liquid or gas):

$$\int_{V_i} \rho_{phase,i} dV = \text{The mass of phase n in the volume cell}$$

$$H0_{phase,i} = \frac{1}{M_{phase,i}} \int_{V_i} \rho_{phase}(h_{phase} + u^2_{phase}/2)dV = \text{Average total enthalpy of phase n in the volume cell}$$

$$P_i = \frac{1}{V}\int_V pdV = \text{Mean pressure of the control volume}$$

The second term, applying the divergence theorem, gives

$$\int_V \nabla \cdot \rho_n \cdot (h_n + e_{kin\,n}) \cdot \mathbf{u}_n \cdot dV = \int_S \rho_n \cdot (h_n + e_{kin\,n}) \cdot \mathbf{u}_n \cdot \vec{n} \cdot dS$$

Since u = 0 on the rigid boundaries, the surface integral reduces to

$$\int_V \nabla \cdot \rho_n \cdot (h_n + e_{kin\,n}) \cdot \mathbf{u}_n \cdot dV = \sum_j \left(\int_{A_j} \rho_n (h_n + e_{kin\,n}) \cdot \mathbf{u}_n \cdot \vec{n} \cdot dA \right) + \int_{A_{src}} \rho_n h \cdot \mathbf{u} \cdot \vec{n} \cdot dA$$

$$= \sum_j \left[W_{phase,j} \cdot (h_{phase,j} + e_{kin_{phase,j}}) \cdot S_j \right] - Wh_{src_{phase,i}} \quad (7\text{-}20)$$

where the summations are performed over all flow paths connected to the volume (note that Wh and $(Wh)_{src}$ have positive direction into the volume).

The term $Wh_{src_{phase,i}}$ is the enthalpy flow source of phase due to external sources or sinks connected to the volume cell i.

The third term, applying the divergence theorem, gives

$$\int_V \nabla \cdot \underline{q}'' \cdot dV = \int_S \underline{q}'' \cdot \vec{n} \cdot dS = Q_A \quad (7\text{-}21)$$

where Q_A is heat transfer through the surface. The conduction over the fluid surfaces (A_j and A_k) have been neglected[3].

The fourth term,

$$\int_V q''' \, dV = Q_V = Q_V$$

The term Q_V consists of internal heat generation due to neutron slowing down, gamma absorption and scattering in the fluid, and the interfacial heat transfer rate $Q_{\Gamma g}$ between phases/components in the cell. The term Q_V is lumped together with Q_A and $Q_\Gamma = Q_{\Gamma g} + Q_{\Gamma w}$ and the sum is the net heat source to each phase.

$$Q_i = Q_A + Q_V + Q_\Gamma \tag{7-22}$$

The integrated energy equation can now be written

$$\frac{d}{dt}(M_{phase\,j} \cdot H0_{phase\,j} - V_i \cdot P_i) + \sum_j \left(Wh_{phase,j} \cdot S_{phase\,j}\right) + (W_{phase} e_{kin,phase})_i - wh_{src_{phase,j}} -$$

$$Q_{phase\,j} = 0 \tag{7-23}$$

The fully implicit finite difference or a semi-implicit form of equation (7-23) is used is POLCA-T for each phase. The fully implicit formulation is:

$$\frac{\left|(M_{phase\,j} \cdot H0_{phase\,j})^{n+1} - (V_i \cdot P_i)^{n+1}\right| - \left|(M_{phase\,j} \cdot H0_{phase\,j})^{n} - (V_i \cdot P_i)^{n})\right|}{\Delta t} +$$

$$\sum_j (Wh^{n+1}_{phase,j} \cdot S_{phase\,j} + (W_{phase} e_{kin,phase})^{n+1}_i - Wh^{n+1}_{src,phase} - Q^{n+1}_{phase\,j} = 0 \tag{7-24}$$

The energy of the fluid phases/components in volume cell i is defined as

$$E_{cell,i} = \sum_{phase} M_{phase} H0_{phase} - V_i P_i$$

---

3. The heat flux due to conduction within the fluid clearly can be neglected for most transient analysis when comparing the magnitude of terms two and three. The fluid conduction is of the order

   $$q'' = -k \cdot dT/dx = -(0.7\ W/m,K) \cdot (10\ K/m) = 7\ W/m^2$$

   or less, which is clearly negligible when compared to the energy transported by the fluid of the order 10^9 - 10^{10}, W/m^2.

and the mass flow rate

$$W_{phase} = A_{phase}\, u_{phase}\, \rho_{phase}$$

for each *phase* (=liquid or gas).

The primary variable from energy equation is the temperatures of each phase/component, T_{liq}, T_{gas}. The temperatures of non condensable gas and vapor are equal; i.e., they are in thermodynamic equilibrium.

7.2 FLOW PATH

[

]^{a,c} a,b,c

Figure 7.2-1. [ ]^{a,c}

7.2.1 Momentum Conservation Equation

In this subsection, the momentum conservation equation is described including the application in the POLCA-T program. The momentum equation is set up for the mixture gas and liquid.

Theoretical Basis

The general formulation for the momentum equation (References 7.1 and 7.2) is:

$$\frac{\partial}{\partial t}(\rho \cdot \underline{u}) = -\nabla\rho \cdot \underline{u}\underline{u} - \nabla p + \nabla \underline{\underline{\tau}} + \rho g \qquad (7\text{-}25)$$

where the terms in (7-25) are:

$\frac{\partial}{\partial t}(\rho \cdot \underline{u})$ = Rate of momentum change,

$-\nabla\rho \cdot \underline{u}\underline{u}$ = Rate of momentum gain by convection,

∇p = Pressure force,

$\nabla \underline{\underline{\tau}}$ = Rate of momentum gain due to viscous stress, and

ρg = Gravitational force.

Equation (7-25) is integrated over a fixed control volume V with solid surfaces S,

$$\int_V \frac{\partial}{\partial t}(\rho \cdot \underline{u})dV = \int_V \{-\nabla\rho \cdot \underline{u}\underline{u} - \nabla p + \nabla \underline{\underline{\tau}} + \rho g\}dV \tag{7-26}$$

The Gauss divergence theorem is applied to the first and third terms on the right-hand side of equation (7-26) giving

$$\int_V \nabla \rho \underline{u}\underline{u} dV = \int_S \rho \underline{u}\underline{u}\ \underline{n}\, dS \tag{7-27}$$

$$\int_V \nabla \underline{\underline{\tau}}\, dV = \int_S \underline{\underline{\tau}}\ \underline{n}\, dS \tag{7-28}$$

where $\underline{n}$ is the outward normal vector of surface element dS.

Substituting (7-27) and (7-28) into (7-26) yields

$$\int_V \frac{\partial}{\partial t}(\rho \cdot \underline{u})dV = -\int_S \rho \underline{u}\underline{u}\ \underline{n}\, dS - \int_V p dV + \int_S \underline{\underline{\tau}}\ \underline{n}\, dS + \int_V \rho g\, dV \tag{7-29}$$

This equation is applied to 1-D pipe flow by integrating the component of the vector equation, which is parallel to the pipe over a short section of the pipe (x_1 to x_2). The coordinate along the pipe's x and the pipe area, A(x), is a function of x. The evaluation is done term by term in equation (7-29) by taking the scalar product of it and unit vector ($\underline{n}x$) along the pipe and integrating:

$$\underline{n}_x \bullet \int_V \frac{\partial}{\partial t}(\rho \cdot \underline{u})dV = \frac{\partial}{\partial t}\int_{x1}^{x2}\left[\int_{A(x)} \rho \underline{u} dA\right]dx = \frac{\partial}{\partial t}\int_{x1}^{x2} W(x)dx \tag{7-30}$$

where the mass flow rate (W) has been introduced and where u for convenience denotes the component of the velocity in the x-direction i.e., $u=\underline{n}x \cdot \underline{u}$.

The momentum flux term of (7-29) is zero on the rigid wall of the pipe and hence it can be written:

$$\underline{n}_x \bullet \int_S \rho \underline{u}\underline{u}\ \underline{n}\, dS = \int_{A_2} \rho u^2 dA - \int_{A_1} \rho u^2 dA = (Wu)_2 - (Wu)_1 = \tag{7-31}$$

$$\int_{x1}^{x2} \frac{\partial Wu}{\partial x} dx$$

The pressure gradient can directly be integrated:

$$\underline{n}_x \bullet \int_V p dV = \int_{x1}^{x2} \left[\int_{A(x)} \frac{\partial p}{\partial x} dA \right] dx = \int_{x1}^{x2} A(x) \frac{\partial p}{\partial x} dx \tag{7-32}$$

The third term on the right-hand side of equation (7-29) is the unrecoverable friction loss term which is zero except on the rigid surfaces. It can be written:

$$\underline{n}_x \bullet \int_S \underline{\underline{\tau}}\, \underline{n}\, dS = \int_{x1}^{x2} - \tau P_w dx \tag{7-33}$$

where P_W is the wetted perimeter and τ is the wall shear stress defined to be positive for positive flow.

The gravity term of equation (7-29) is treated in similar way to the pressure gradient term:

$$\underline{n}_x \bullet \int_V \rho g dV = g_x \int_{x1}^{x2} A(x)\, \rho\, dx \tag{7-34}$$

where g_X is the component of gravity vector in the x direction given by $g_X = -g \cdot dz/dx$.

At this stage $\partial p/dx$ and ρ represent area averaged values as does u in equation (7-30).

Substituting equations (7-30) through (7-34) into (7-29), dividing by Δx, taking the limit as Δx goes to zero and dividing by the area yields the 1-D momentum equation use as a base for discretization in POLCA-T:

$$\frac{1}{A}\frac{\partial W}{\partial t} = -\frac{1}{A}\frac{\partial}{\partial x}\left(\frac{W^2}{\rho A}\right) - \frac{\partial p}{\partial x} - \frac{\tau P_w}{A} - \frac{\partial}{\partial x}(\rho g z) \tag{7-35}$$

Finite Difference Formulation of the Momentum Equation

In this section the mathematical formulation of the momentum equation will be written in the finite difference form used in POLCA-T.

Consider the flow path j shown in Figure 7.2-2. Equation (7-35) is integrated between points x_i and x_{i+1} to give

$$\int_{x_i}^{x_{i+1}} \frac{1}{A}\frac{\partial W}{\partial t} dx = -\int_{x_i}^{x_{i+1}} \frac{1}{A}\frac{\partial}{\partial x}\left(\frac{W^2}{\rho A}\right) dx - \int_{x_i}^{x_{i+1}} \left(\frac{\partial p}{\partial x}\right) dx - \int_{x_i}^{x_{i+1}} \frac{\tau P_w}{A} dx - \int_{x_i}^{x_{i+1}} \frac{\partial}{\partial x}(\rho g z) dx \tag{7-36}$$

a,b,c

Figure 7.2-2. Volume Cells with Flow Junctions

Temporal Acceleration Term

[

]^{a,c}

[

]^{a,c}

Unrecoverable Pressure Losses

The unrecoverable pressure losses are divided into a wall friction term, ΔP_{fric}, and a term corresponding to unrecoverable pressure losses, ΔP_{loc}, due to area changes.

$$-\int_{x_i}^{x_{i+1}} \frac{\tau P_w}{A} dx = -\Delta p_{fric} - \Delta p_{loc} \tag{7-40}$$

The wall friction term corresponds to each half of the momentum equation control cell. The expression for the friction pressure drop, valid for both co-current flow and counter current flow over a length l, can be written as:

$$\Delta p_{fric} = \Delta p_{fric,liq} \cdot \Gamma_{liq} + \Delta p_{fric,gas} \cdot \Gamma_{gas} \tag{7-41}$$

where Γ_{liq} represents the liquid wetted fraction of the perimeter in the volume cell and Γ_{gas} is the non wetted fraction, ($\Gamma_{liq} + \Gamma_{gas} = 1$).

$$\Delta P_{fric,liq} = \frac{L \cdot f(\mathrm{Re}_{liq}, \kappa)}{D_h} \cdot \frac{\rho_{liq} u_{liq}^2}{2} \cdot F(\alpha(\rho_{gas} / \rho_{liq})) \tag{7-42}$$

The void correction factor is used to take into account the velocity distribution in the channel when void, α, occurs. The correction factor has the form below:

$$F(\alpha(\rho_{gas} / \rho_{liq})) = 1 + \sqrt{1 - \frac{\rho_{gas}}{\rho_{liq}}} \cdot (\alpha^2 C_2 + \alpha C_1) \tag{7-43}$$

and for the gas part;

$$\Delta p_{fric,gas} = \frac{L \cdot f(Re_{gas}, \kappa)}{D_h} \cdot \frac{\rho_{gas} u_{gas}^2}{2} \tag{7-44}$$

and the relative surface roughness by:

$$\kappa = \varepsilon / D_h \tag{7-45}$$

In the application of equation (7-43) in the code the friction loss from x_i to x_{i+1} in Figure 7.2-2 is calculated as the sum of the friction in each of the two volume cells that are connected by the flow path. Actual cell densities and viscosities are used in both volumes cells together with flow area, hydraulic diameter, and surface roughness for each cell. The velocities, u_{liq}, u_{gas}, are taken as the primary variables from the volume cells connected by the flow path.

The area change pressure loss is calculated in the similar way to the friction pressure loss. In both co-current and countercurrent flow:

$$\Delta P_{loc} = \Delta p_{loc,liq} \cdot (1-\alpha) + \Delta p_{loc,gas} \cdot \alpha \tag{7-46}$$

$$\Delta p_{loc,phase} = \xi(Re_{phase}, \text{direction}) \cdot \frac{\rho_{phase} u_{phase}^2}{2} \tag{7-47}$$

Spatial Acceleration

The momentum flux term

$$\int_{x_i}^{x_{i+1}} \frac{1}{A} \frac{\partial}{\partial x} \frac{W^2}{\rho A} dx = -\Delta p_{flux} \tag{7-48}$$

is formulated by considering spatial acceleration due to gradients in mass flow rate, density and area separately. The integral in equation (7-48) can developed into three terms:

$$\int_{x_i}^{x_{i+1}} \frac{1}{A} \frac{\partial}{\partial x} \frac{W^2}{\rho A} dx = I_1 + I_2 + I_3 \tag{7-49}$$

with:

$$I_1 = \frac{1}{A^2 \rho} \int_{x_i}^{x_{i+1}} \frac{\partial}{\partial x} W^2 dx \qquad \text{(velocity gradients)} \tag{7-50}$$

$$I_2 = \frac{W^2}{A^2}\int_{x_i}^{x_{i+1}} \frac{\partial}{\partial x}\frac{1}{\rho}dx \qquad \text{(density gradients)} \qquad (7\text{-}51)$$

$$I_3 = \frac{W^2}{A\rho}\int_{x_i}^{x_{i+1}} \frac{\partial}{\partial x}\frac{1}{A}dx \qquad \text{(area gradient)} \qquad (7\text{-}52)$$

The integration of these three terms for each phase, liquid and gas, is performed from x_i to x_{i+1} using the mean value theorem of integrals and appropriate approximations:

$$I_1 = \frac{1}{A_i^2 \rho_i}\cdot(W_j^2 - \overline{W_i}^2) + \frac{1}{A_{i+1}^2 \rho_{i+1}}\cdot(W_{i+1}^2 - \overline{W_j}^2) \qquad (7\text{-}53)$$

$$I_2 = \begin{cases} \dfrac{W_j^2}{2}\cdot\left(\dfrac{1}{A_i^2}+\dfrac{1}{A_{i+1}^2}\right)\cdot\left(\dfrac{1}{\rho_{i+1}}-\dfrac{1}{\rho_i}\right) \\ \text{If } W_j\cdot(\rho_i - \rho_{i+1}) \le 0 \\ 0. \end{cases} \qquad (7\text{-}54)$$

$$I_3 = \frac{W_j^2}{4}\left(\frac{1}{A_{i+1}}+\frac{1}{A_i}\right)\left(\frac{1}{A_{i+1}^2}-\frac{1}{A_i^2}\right) \qquad (7\text{-}55)$$

Finally inserting equations (7-37) through (7-55) into (7-36) yields

$$I_j\frac{\partial W}{\partial t} = p_i - p_{i+1} - \Delta p_{fric} - \Delta p_{loc} - \Delta p_{grav} - \Delta p_{flux} + \Delta p_{pump} \qquad (7\text{-}56)$$

A fully implicit finite difference scheme or a semi-implicit method can be used to represent the momentum equation. The time derivative is approximated by

$$\frac{\partial W_j}{\partial t} = \frac{W_j^{n+1} - W_j^n}{\Delta t} \qquad (7\text{-}57)$$

where the upper index denotes time step number (Δt apart). In the fully implicit formulation, all other state variables in equation (7-57) are calculated at time step n+1 (i.e., at $t+\Delta t$).

7.3 REFERENCES

7.1 R. B. Bird, W. E. Stewart, E. N. Ligthfoot, "Transport Phenomena" John Wiley & Sons, 1960.

7.2 "Water Reactor Emergency Core Cooling System Evaluation Model: Code Description and Qualification," RPB 90-93-P-A (Proprietary), October 1990.

8 POWER GENERATION MODEL

The volumetric heat generation in the fuel and coolant are calculated in POLCA-T. The heat sources for the fuel appear in the heat conduction equation as the volumetric heat generation term, q''', in equation (13-1). The heat sources for the direct nuclear heat to coolant appear as the volumetric heat generation term, Q_v in the energy equation (see equation (7-22)).

Heat generation due to reactor power and decay power is modeled as the sum of heat generated from three basic sources – prompt fission power, fission product decay, and actinide decay. The total prompt fission power is the sum of the power generated in the fuel and direct heating fission power generated in the coolant. The total power is distributed axially and radially throughout the core based from calculation by a neutron 3-D-kinetics model.

The fission products and actinide decay power can be calculated by the code it self or by reading user-supplied files. Finally, it can be calculated by using the built-in function for end of cycles cores for decay power generation in a typical BWR core.

8.1 3-D KINETICS

The POLCA7 portion of POLCA-T solves the two-group diffusion equation with arbitrary number of delayed neutron families, for each thermal-hydraulic iteration performed until convergence is reached, named herein as "power – void iterations."

A full description of the 3-D-neutron kinetics model can be found in Reference 8.1.

8.2 DECAY POWER GENERATION

The decay power generation of the core can be simulated either by tables or by a set of equations where the user can take into account the increase or decrease of fission power depending on the behavior of the transient.

8.2.1 By Tables

The user can supply files describing the power decay coast down during a certain event or use built-in functions for decay power according to American Nuclear Society - ANS79 standard. This built-in function for decay power is based on conditions that envelope BWR core designs with a possibility to add any number of sigma uncertainties.

8.2.2 By Equations

The reactor kinetics equations include effects arising only from the direct fission power. The user must provide the decay of fission products and actinides. The total power generation is the sum of the fission and decay power.

$$Q(t) = Q_{fiss}(t) + Q_{decay}(t) \qquad (8.2\text{-}1)$$

The decay based on the total power given by

$$Q_{decay}(t) = f_d Q(t) \tag{8.2-2}$$

The total decay heat generation rate is

$$Q_{decay}(t) = \sum_{i=1}^{m} f_{d,i} Q(t) \tag{8.2-3}$$

Where $f_{d,i}$ is the decay power fraction at steady-state and τ_i is the decay power time constant for decay group i.

Combining equation 11-1 to 11-3 gives the decay power as function of fission power

$$Q_{decay} = \frac{f_{d,i}}{1 - \sum_{i=1}^{m} f_{d,i}} Q_{fiss}(t) \tag{8.2-4}$$

[

]^{a,c}

The number of groups m is a user input and the model can be applied for different fuel bundle burnups also defined by the user. The time constants and effective energy fractions for the number of selected groups can be based on a fit to the proposed ANS Standard 5.1 of 1971 Reference 8.2. The decay time constants and effective energy fractions can also be based on Reference 8.3. The user, via input, can add to the resultant fission product power generation an uncertainty of 20 percent as required by Appendix K of 10CFR50.

8.3 REFERENCES

8.1 "The Advanced PHOENIX and POLCA Codes for Nuclear Design of Boiling Water Reactors," CENPD-390-P-A, December 2000.

8.2 American Nuclear Society, "American National Standard for Decay Heat Power in Light Water Reactors," ANSI/ANS-5.1-2005, Approved April 1, 2005.

8.3 ISO 10645, "Nuclear Energy – Light Water Reactors - Calculation of the Decay Heat Power in Nuclear Fuels, First Edition, March 1992."

9 CONSTITUTIVE MODELS

9.1 DRIFT FLUX EQUATION

The relationship between the velocities of the gas and liquid phases is given by the drift flux equation. This drift flux equation is the sixth basic equation in the hydraulics model. The definitions of the velocities are shown in Figure 9.1-1.

The drift-flux equation includes a countercurrent flow limitation correlation of the form defined by Wallis (Reference 9.2).

The drift flux formulation for relative motion between two phases (Reference 9.2) is

$$j_{gas} = \alpha C_0 (j_{gas} + j_{liq}) + \alpha V_{gj} \tag{9-1}$$

where the superficial velocities are defined as;

$$j_{liq} = V_{liq}/(A_{liq} + A_{gas}) = u_{liq}(1 - \alpha) \tag{9-2}$$

for the liquid phase

$$j_{gas} = V_{gas}/(A_{liq} + A_{gas}) = u_{gas}\alpha \tag{9-3}$$

for the gas phase

where j_g and j_l are superficial velocities of gas and liquid and the concentration coefficient, C_0, slip velocity S. and the drift velocity V_{gj} are defined by empirical correlations.

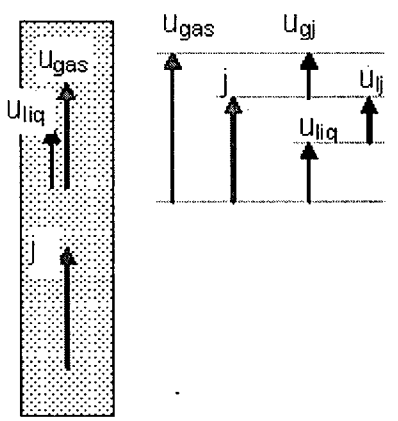

Figure 9.1-1. Definitions of Velocities

[

]^{a,c}

Where the slip ratio and the relative velocity are defined as:

$$\text{The relative velocity } u_{rel} = u_{gas} - u_{liq} \tag{9-5}$$

The relative velocity can also be related to the drift velocity according to:

$$u_{rel} = \frac{V_{gj}}{(1-\alpha)} = \varsigma(\alpha) \cdot V_{\infty} \tag{9-6}$$

and

$$\varsigma(\alpha) = (1-\alpha)^{n+1},$$

n = 1-3 depending on the flow regime.

where V_{∞} is the terminal velocity of a single bubble in quiescent liquid.

The slip ratio

$$S = \frac{u_{gas}}{u_{liq}} = \frac{x}{1-x}\frac{\rho_{liq}}{\rho_{gas}}\frac{(1-\alpha)}{\alpha} \tag{9-7}$$

9.1.1 The DF01 Drift Flux Correlation

The relation between the phase velocities for two-phase flow is determined from a drift flux correlation developed from the work of Holmes (Reference 9.1) and includes a countercurrent flow limitation correlation of the form defined by Wallis (Reference 9.2).

Concentration Coefficient Correlation

[

]^{a,c}

[

]^{a,c}

To be used together with the formulation of the drift flux equation (9-4), the relative velocity and the slip ratio is:

$$S(\alpha, p) = \frac{u_{gas}}{u_{liq}} = \frac{1-\alpha}{\frac{1}{C_0} - \alpha} \tag{9-12}$$

and the relative velocity is:

$$u_{rel}(\alpha, p) = \frac{C_0 K_u V_c}{1 - \alpha C_0 \left(1 - \sqrt{\frac{\rho_{gas}}{\rho_{liq}}}\right)} \tag{9-13}$$

The drift flux correlation of the Holmes type given above was derived from a regression analysis of data from void measurement – equations (9-6) and (9-7). The values of correlation parameters from this study are implemented in the DF01 correlation.

9.1.2 The DF02 Drift Flux Correlation

Based on the void measurement data from tests performed at Westinghouse's FRIGG Test Loop, a new regression analysis was made for a different formulation of the drift flux correlation.

[

]^{a,c}

[

]^{a,c}

The characteristic velocity is based on the Laplace length according to following formulation:

$$Vcl = \sqrt{g\, L_p \left(\frac{\rho_l - \rho_g}{\rho_l} \right)} \tag{9-15}$$

and for the gas phase

$$Vcg = Vcl / \sqrt{\frac{\rho_g}{\rho_l}} \tag{9-16}$$

The Kutateladze number is calculated for each phase k and is depending on the amount of void in cell i as;

$$Ku_k = \{j_k\} \sqrt{\frac{\rho_k}{g\sigma\sqrt{\rho_l - \rho_g}}} \tag{9-17}$$

j_k is the superficial velocity of phase k.
σ is the surface tension.
ρ is the density of liquid respective gas.

During the regression analysis of the measured data, constants for low void and high void were determined, as well as transition values for void parameters, for flow function calculation.

9.2 WALL FRICTION AND SINGULAR IRREVERSIBLE LOSSES

The frictional pressure drop in co-current flow is calculated from Equation (7-41). The friction factor correlations are described in the following subsections.

9.2.1 Single-Phase Friction Factors

The single-phase friction factors is calculated for turbulent flow in fuel bundles by (Reference 9.4):

$$f_i = C1 \cdot Re^{-C2} \tag{9-18}$$

where

$$[C1 = 0.2$$

$$C2 = 0.2$$

$$Re = \frac{W D_{hyd}}{A \eta} \quad]^{a,c}$$

For turbulent flow in other parts of the flow loop, the Colebrook's correlation (Reference 9.5), is used by default.

$$f_i = 5.5 \cdot 10^{-3} \left[1 + \left(2 \cdot 10^4 \frac{\varepsilon}{D_{hyd}} + \frac{10^6}{Re} \right) \right]^{1/3} \tag{9-19}$$

where ε is the surface roughness.

Optionally, the user can specify that the Blasius formulation shall be used instead or by mixed correlations.

$$f = \frac{0,316}{Re^{0,25}} \tag{9-20}$$

For laminar flow the friction factor is:

$$f_i = 64 / Re \tag{9-21}$$

The transition between laminar and turbulent flow occurs at the Reynolds number when the friction factor for turbulent flow is equal to the one at laminar flow.

Optionally, the flow can be modeled as friction-free or a constant friction factor can be specified for selected parts of the geometry model.

9.2.2 Irreversible Losses Due to Contraction/Expansion

The local momentum losses (implemented in equation (7-47) are modeled by use of irreversible loss coefficients. These coefficients are functions of the geometric details of the flow channel or pipe and sometimes the actual flow direction. Irreversible losses associated with flow through a sharp-edged expansion or contraction is calculated according to the following formulas, if the values for the loss coefficients are not given by the user.

Sudden expansion, Carnot-Borda loss:

$$\zeta = \left(1 - \frac{A_1}{A_2}\right)^2 \tag{9-22}$$

Sudden contraction:

$$\zeta = 0.4\left(1 - \left(\frac{A_1}{A_2}\right)^2\right) \tag{9-23}$$

9.3 COUNTERCURRENT FLOW LIMITATION CORRELATION

[

]^{a,c}

First the CCFL correlation to be used in POLCA-T is described, then an expression for G_d above is derived. Refer to the following subsection.

9.3.1 CCFL Correlation

In the countercurrent flow region, there is a physical limit to the downward water flow for a given upward stem flow. Countercurrent flow limitation has been described by Wallis (Reference 9.2) for flow in vertical tubes, with the dimensionless relationship:

$$\frac{j_g^{1/2}}{\left[\frac{g\,D\,(\rho_f - \rho_g)}{\rho_g}\right]^{1/4}} + \frac{K_1\,(-j_f)^{1/2}}{\left[\frac{g\,D\,(\rho_f - \rho_g)}{\rho_f}\right]^{1/4}} = K_2 \tag{9-26}$$

[ ]^{a,c}

Defining the characteristic length as:

$$D_L = \left[\frac{\sigma}{g\Delta\rho}\right]^{1/2} \tag{9-27}$$

and dividing both sides by $D_L^{1/4}$ and multiplying by $D^{1/4}$ gives:

$$\frac{j_g^{1/2}}{\left[\frac{\sigma g \Delta\rho}{\rho_g^2}\right]^{1/8}} + \frac{K_1 (-j_f)^{1/2}}{\left[\frac{\sigma g \Delta\rho}{\rho_f^2}\right]^{1/8}} = \frac{K_2 D^{1/4}}{\left[\frac{\sigma}{g\Delta\rho}\right]^{1/8}} = K_u^{1/2} \tag{9-28}$$

[

]^{a,c}

Holmes (Reference 9.1) reported a geometry dependence of CCFL as a function of the dimensionless pipe diameter D^* in the form $(D^*-2)/(D^*+2.5)$ where:

$$D^* = \left[\frac{g\Delta\rho}{\sigma}\right]^{1/2} \cdot D = \frac{D}{D_L} \tag{9-29}$$

and D is the pipe diameter.

[

]^{a,c}

The above relation is applicable at $0.45 < \alpha < 1.0$ and the other relation is applicable at $0 < \alpha < 0.18$. This latter relation, given by Holmes, has been modified to include the geometry dependencies. Thus

$$Ku_2 = \frac{2.55}{C_0} \cdot \frac{\frac{D_h}{D_L} - 2}{\frac{D_h}{D_L} + 2.5} \tag{9-31}$$

where D_h is the hydraulic diameter.

[

]^{a,c}

9.3.2 Mass Drift Flux

Now the mass drift flux, G_d, can be calculated from the CCFL correlation. Using the following definitions:

$$jg = \frac{G_g}{\rho g} \qquad jf = \frac{G_f}{\rho f} \qquad V_c = \left(\frac{g\,\Delta\rho}{\rho f^2}\right)^{1/4} \tag{9-33}$$

in equation (9-24) give:

$$\left[\frac{G_g\sqrt{\frac{\rho f}{\rho g}}}{\rho f \cdot Ku \cdot V_c}\right]^{1/2} + \left[\frac{-G_f}{\rho f \cdot Ku \cdot V_c}\right]^{1/2} = 1 \tag{9-34}$$

For the countercurrent flow regime, and for void fractions greater than 0.45, the drift flux relation, equation (9-4) gives lines of constant α which are tangential to the CCFL curve, equation (9-34). This relationship is shown in Figure 9.3-1. The resultant expression is

$$G_d = \frac{X^*(1-X^*)\,\rho f\, Ku\, V_c}{1 - X^* + X^*\sqrt{\frac{\rho f}{\rho g}}} \tag{9-35}$$

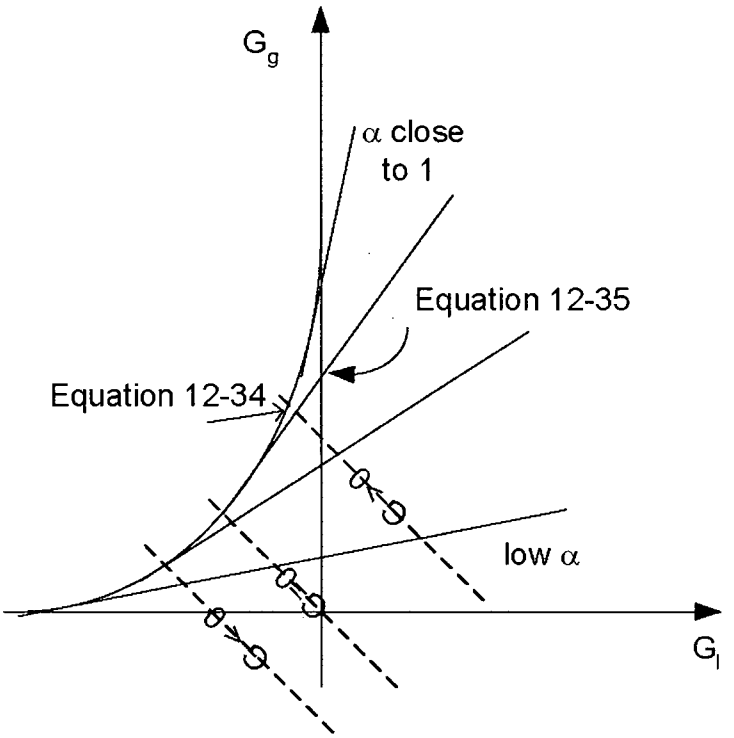

Figure 9.3-1. CCFL Curve Together with Mass Drift Flux G_d

9.4 HEAT AND MASS TRANSFER BETWEEN PHASES

The steam generation in POLCA-T, or more generally the mass and energy transfer between the liquid and gaseous phases, is modeled as a combination of surface and bulk processes.

In a boiling channel with subcooled conditions at the inlet, the heat flux from the heated surfaces will heat the water and the water temperature near the surfaces will be higher than in the bulk. As soon as the temperature at the surface becomes higher than the saturation temperature, steam will start to form while the bulk of the water is still subcooled. Steam that is formed at the surface will migrate to the bulk and condense. Thus, the amount of steam in the channel will be determined by a balance between formation of steam at the surface and condensation of steam in the bulk. Along the channel, the bulk water temperature will increase and condensation will gradually reduce and become zero at the point where the bulk water reaches saturation.

The heat and mass transfer models are used together with the mass balance equations, equations (7-3 and 7-5) for the liquid and gas phase and the energy equations for the phases, equation (7-23). Appropriate heat transfer coefficients etc depend on actual flow regime and possible mode of heat transfer.

The interfacial mass transfer rate of fluid – liquid to gas or gas to liquid - is divided into two parts:

$$\Gamma = \Gamma_{lg} + \Gamma_w \tag{9-36}$$

where:

Γ is the total mass transfer rate at the phase interface and at the wall,
Γ_{lg} is the interfacial mass transfer rate between the two phases in the bulk, and
Γ_w is the condensation/evaporation mass transfer rate, which is a function of the wall temperature.

The heat transfer is also divided into two parts. One part takes into account the heat transfer between the fluid and the heat structure, $q_{\Gamma w}$, described in Section 11 regarding the convective heat transfer models.

The second part takes care of the bulk heat transfer between the phases, the interfacial heat transfer $\dot{S}_{\Gamma lg}$.

Heat transfer between fluid and heat structure,

$$q_{\Gamma w} = q_{liq} + q_{gas} + q_{nc} \tag{9-37}$$

with the partial contributions to the wall heat flow,

q_{liq} heat flux to surface from liquid phase
q_{gas} heat flux to surface from gas/vapor phase
q_{nc} surface heat flux due to near wall condensation

The second part, $\dot{S}_{\Gamma lg}$, that are the heat flow per unit volume in the bulk between the phases,

$$\dot{S}_{\Gamma lg} = \dot{S}_{\Gamma liq} + \dot{S}_{\Gamma gas} \tag{9-38}$$

Figure 9.4-1 is schematic view of the heat and mass transfer process in a volume cell with a connected heat structure.

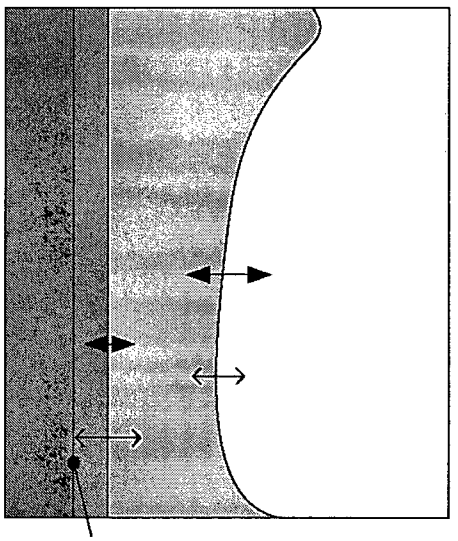

Figure 9.4-1. Interfacial Heat Flow and Mass Flow Paths in a Volume Cell

9.5 HEAT TRANSFER TO HEAT STRUCTURES

The components in the heat transfer between the fluid phases and the heat structure are calculated as shown below. See Section 11 for the description of convective heat transfer models.

Heat flux to liquid phase:

$$q_{liq} = h_{liq} \cdot (T_w - T_{liq}) \tag{9-39}$$

Heat flux to the gas/vapor phase:

$$q_{gas} = h_{gas} \cdot (T_w - T_{gas}) \tag{9-40}$$

Phase change heat flux that generates or condensate steam:

$$q_{lg} = h_{lg} \cdot (T_w - T_{sat}) \tag{9-41}$$

Appropriate heat transfer coefficients are calculated based on the actual flow regime, actual heat transfer regime map and phase. See Section 11 for the description of the convective heat transfer.

[

]^{a,c}

9.6 HEAT TRANSFER BETWEEN THE PHASES IN THE BULK

The phase change processes in the bulk are driven by the difference between the liquid temperature and saturation and by the difference between the gas temperature and saturation.

[

]a,c

9.6.1 Bulk Evaporation/Condensation, Low Void

If the liquid temperature is higher than the saturation temperature, then liquid will be evaporated in the fluid. In that case, POLCA-T assumes that the interfacial heat transfer coefficient for the liquid is h_{il}.

The interfacial area and heat transfer terms in the low void fraction region are given by:

Interfacial heat flow per unit volume to liquid phase:

$$\dot{S}_{illow} = A_i h_{il} (T_{liq} - T_{sat}) \tag{9-43}$$

Interfacial heat flow to gas phase:

$$\dot{S}_{iglow} = (A_i h_{ig} + k_{gstrong})(T_{gas} - T_{liq}) \tag{9-44}$$

[

]a,c

[

]a,c

9.6.2 Bulk Condensation/Evaporation, High Void

At high-void contents, the heat transfer is based on heat transfer to drops and to the film layer. A film thickness is calculated and used to select appropriate heat transfer coefficients. For the drops, an estimation of the drops are made and then the heat transfer to the drops is calculated. Selected models for heat transfer coefficients are based also on the values of T_{liq}, T_{gas}, and T_{sat}.

Minimum film thickness is calculated from:

$$d_{film0} = \left(\frac{18\sigma\eta_{liq}^2}{g^2\rho_{liq}^3} \right)^{1/5} \tag{9-49}$$

Liquid volume fraction is:

$$\beta = (1-\alpha)$$

and the liquid fraction based on the minimum film thickness;

$$\beta_0 = d_{film0}\frac{4\gamma_{liq}}{D_{hyd}} \tag{9-50}$$

where the fraction of surfaces that are wetted is γ_{liq}.

The volume fraction of film is:

$$\beta_{film} = \begin{cases} \beta_0\left(1-\left(1-\dfrac{\beta}{2\beta_0}\right)^2\right) & if \quad \beta < 2\beta_0 \\ \beta_0 \quad if \quad \beta \geq 2\beta_0 \end{cases} \tag{9-51}$$

The volume fraction of drops is:

$$\beta_{drop} = \beta - \beta_{film}$$

Interfacial area gas to film is calculated as:

$$A_{ifilm} = \frac{4\gamma_{liq}}{D_{hyd}} \tag{9-52}$$

Interfacial area of drops to gas is calculated as:

$$A_{idrop} = \begin{cases} 6\dfrac{\beta_{drop}}{d_{drop}} & if\ \Delta T_{gas} > 0 \\ 6\dfrac{\beta_{drop}+0.0001}{d_{drop}} & if\ \Delta T_{gas} \leq 0 \end{cases} \tag{9-53}$$

And the heat transfer terms for the high void fraction region are given by:

$$\dot{S}_{ilhigh} = (A_{ifilm}h_{igfilm} + A_{idrop}h_{igdrop} + k_{lstrong})(T_{liq} - T_{sat}) \tag{9-54}$$

$$\dot{S}_{iglow} = (A_{ifilm}h_{igfilm} + A_{idrop}h_{igdrop})(T_{gas} - T_{sat}) \tag{9-55}$$

[

]^{a,c}

[

]^{a,c}

9.6.3 Near Wall Condensation

Vapor condensation takes place also close to the heated wall if the wall temperature is higher than the saturation temperature while the liquid temperature is lower than the saturation temperature; this condition can also be referred to as sub cooled boiling. Near wall condensation is modeled in POLCA-T by using the Hancox-Nicoll correlation for the Nusselt number, i.e., $Nu = 0.1 \times Re_l^{0.662} \times Pr_l$. Similar to the case of bulk condensation, the heat transfer coefficient for the near-wall condensation, h_{nc}, is calculated.

9.7 WALL CONDENSATION

Condensation when the heat structure surface temperature is below the saturation temperature is calculated by the appropriate heat transfer coefficients from the heat transfer coefficient map.

9.7.1 Mass Transfer

The mass transfer rate during condensation or evaporation between the phases when heat is transferred to a heat structure is calculated from:

$$\Gamma_w = \frac{h_{lg} \cdot (T_{surf} - T_{sat}) - h_{nc} \cdot (T_{sat} - T_{liqs})}{i_{gas\_sat} - i_{liq\_sat}} \tag{9-61}$$

where:

i_{gas_sat} = vapor enthalpy at saturation and
i_{liq_sat} = liquid enthalpy at saturation
h_{nc} = near wall condensation heat transfer coefficient, subsection 9.6.3

When bulk vaporization or condensation of the fluid takes place it is calculated from following equation can be set up, $\dot{S}_{\Gamma lg}, \dot{S}_{\Gamma liq}$, and $\dot{S}_{\Gamma gas}$ as described in Section 9.3.

$$\Gamma_{lg} = \frac{\dot{S}_{\Gamma lg}}{i_{gas\_sat} - i_{liq\_sat}} = \frac{\dot{S}_{\Gamma liq} + \dot{S}_{\Gamma gas}}{i_{gas\_sat} - i_{liq\_sat}} \tag{9-62}$$

9.8 REFERENCES

9.1 J. A. Holmes, "Description of the Drift Flux Model in the LOCA Code RELAP-UK," Conference in Heat and Fluid Flow in Water Reactor Safety, I Mech E, Manchester, 1977.

9.2 G. B. Wallis, "One-dimensional Two-phase Flow," New York, McGraw Hill, Inc., 1969.

9.3 R. T. Lahey and F. J. Moody, "The Thermal-hydraulics of a Boiling Water Nuclear Reactor," ANS Monograph, 1977.

9.4 "Water Reactor Emergency Core Cooling System Evaluation Model: Code Description and Qualification" RPB 90-93-P-A (Proprietary), October, 1991.

9.5 F. Colebrook, Turbulent Flow in Pipes with Particular Reference to the Transition Region between the Smooth and Rough Pipes, J. Inst. Civil Engineers, No. 4, 1938.

10 HEAT STRUCTURE MODELS

The thermal model in the POLCA-T code calculates the heat transferred from the fuel rods, reactor vessel, and internals to the coolant. This is used for the hydraulic transient calculation. The surface heat transfer and material heat conduction problems are solved simultaneously to determine the total heat transfer to the coolant.

The heat transfer coefficient couples the hydraulic solution to the thermal conduction solution through the coolant state and surface temperature, as shown Figure 10-1. Empirical heat transfer coefficient correlations are modeled for: single-phase liquid heat transfer, two-phase non-dryout heat transfer, transition boiling, two-phase post-dryout heat transfer, single-phase vapor and surface to surface radiation heat transfer.

The models are described in more detail in Section 13.

The radial heat conduction equation is solved for the fuel rods (axial conduction is neglected) or the slab heat conduction equation is solved for slabs using an implicit finite-difference technique in combination with the appropriate boundary conditions.

Detailed models for heat transfer from the pressure vessel and the internals are also included. These components are referred to as "heat structures."

The user can specify an arbitrary number of heat structures, which can be in contact with coolant on both sides or isolated on either side. The 1-D heat conduction equation is solved for a user-specified nodal subdivision of each heat structure using a finite difference technique. Each heat structure can be composed of several different materials.

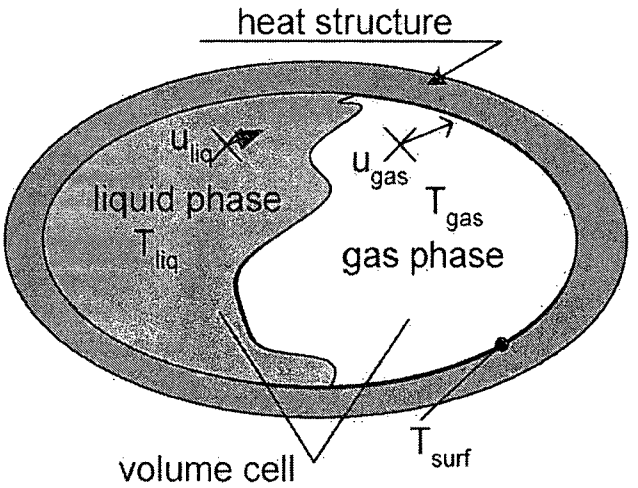

Figure 10-1. Volume Cell With Heat Structure

11 CONVECTIVE HEAT TRANSFER MODELS

The coupling between the hydraulic and thermal model is through the surface to fluid heat transfer. The surface heat transfer appears in the energy conservation equation (7-17) as the component Q_A (defined in equation (7-22)) of the term Q. The total surface heat transfer is divided into convective components based on liquid and gas phase heat transfer.

$$Q_A = Q_{Cliq} + Q_{Cgas} \tag{11-1}$$

The convective heat transfer to water and gas/steam (Q_{Cliq} and Q_{Cgas}, respectively) is calculated separately for each phase that has been specified to be in convective contact with heating surface and is defined by:

$$Q_{Cliq} = h_l \cdot Aht_l \cdot (T_{surf} - T_{liq}) \tag{11-2}$$

$$Q_{Cgas} = h_g \cdot Aht_v \cdot (T_{surf} - T_{gas}) \tag{11-3}$$

where:

T_{surf}	=	surface temperature,
T_{liq}, T_{gas}	=	temperature of water and steam phase, respectively,
h_l, h_g	=	heat transfer coefficients to water and steam phase, respectively, and
Aht_l, Aht_g	=	heat transfer area (contact area) to water and steam phases, respectively.

The convective heat transfer is calculated using an empirical correlation, which is primarily a function of fluid properties, flow, surface material, and surface temperature.

In POLCA-T, modeling the interfacial heat transfer between water and steam phases is also accounted for as described in the Section 9.4 description of heat and mass transfer.

In many heat transfer regimes, the heat transfer coefficient is surface temperature dependent. The solution method used in POLCA-T accounts for this dependency by solving the heat transfer and heat conduction problems simultaneously.

This section describes the heat transfer regimes, convective heat transfer correlations, dryout correlation, Leidenfrost temperature, and transition boiling correlation.

Distribution of energy transferred from structures to water and steam is calculated separately from chosen correlations. The logic matrix of heat transfer regimes is presented in the next section.

11.1 HEAT TRANSFER REGIMES

The various heat transfer regimes modeled in POLCA-T are shown in Figure 11.1-1:

Pre-dryout Heat Transfer ($T_{surf} > T_{sat}$, Boiling or Steam cooling)

Heat Transfer to Water

- Boiling according to Chen (H5)

Heat Transfer to Steam

- Turbulent natural convection (H6)
- Turbulent forced convection (H8)

Pre-dryout Heat Transfer ($T_{surf} \leq T_{sat}$, Single-phase Water or Steam)

Heat Transfer to Water

- Turbulent natural convection (H1)
- Turbulent forced convection (H3)
- Condensation of steam (H4)

Heat Transfer to Steam

- Turbulent natural convection (H6)
- Turbulent forced convection (H8)

Post-Dryout Heat Transfer

Heat Transfer to Water

- Forslund-Rohsenow (H11)

(Direct wall to liquid heat transfer in dispersed flow)

Heat Transfer to Steam

- Forced convection to steam with (H10)

Two-phase enhancement factor for dispersed flow

- Modified Bromley (H12)

a,b,c

Figure 11.1-1. Heat Transfer Regime Maps Used in POLCA-T

[

]a,c

11.1.1 Two-Phase Subcooled, Nucleate and Flow Boiling Regime (H5)

For nucleate and non-dryout flow boiling, the Chen's correlation (Reference 11.1) is used:

$$h = 0.023 \cdot \frac{k_f}{D_h} Re^{0.8} Pr^{0.4} \cdot F$$

$$+ 0.00122 \cdot \frac{k_f^{0.79} \cdot c_{pf}^{0.45} \cdot \rho_f^{0.49}}{\sigma^{0.5} \cdot \mu_f^{0.29} \cdot h_{fg}^{0.24} \cdot \rho_g^{0.24}} \qquad (11\text{-}4)$$

$$\cdot (T_{surf} - T_{sat})^{0.24} \cdot (p_w - p)^{0.75} \cdot S$$

where:

$Re = G_f D_h / \mu_f$,
$Pr = \mu_f c_{pf} / k_f$,
$T_w = \max\{T_{surf}, T_{sat}+23\}$, and
$p_w = p_{sat}(T_w)$.

The two-phase Reynolds number factor F is

$$F = \begin{cases} 1.0 \text{ for } X_{tt}^{-1} \le 0.1 \\ 2.3511447 \cdot (X_{tt}^{-1} + 0.213)^{0.736} \text{ for } X_{tt}^{-1} > 0.1 \end{cases}$$

where

$$X_{tt}^{-1} = \left(\frac{X}{1-X}\right)^{0.9} \cdot \left(\frac{\rho_f}{\rho_g}\right)^{0.5} \cdot \left(\frac{\mu_g}{\mu_f}\right)^{0.1}$$

and X is the steam quality, which is limited to less than 0.981.

The subcooling suppression factor S is:

$$S = \begin{cases} 1/(1+0.012 \cdot Re_{TP}^{1.14}) \text{ for } Re_{TP} < 32.5 \\ 1/(1+0.042 \cdot Re_{TP}^{0.78}) \text{ for } 32.5 \le Re_{TP} < 70 \\ 0.1 \text{ for } Re_{TP} \ge 70 \end{cases} \quad \text{where}$$

$$Re_{TP} = 10^{-4} \cdot |G| \cdot (1-x) D_h / \mu_f \cdot F^{1.25}$$

11.1.2 Laminar and Turbulent Natural Convection Regime (H1 or H6)

The heat transfer coefficient for natural convection of steam or water is from M. Jakob (Reference 11.2) for vertical plates.

$$Nu = C \cdot (Gr \cdot Pr)^n$$

$$h = k_{flm} \cdot Nu / L \qquad (11\text{-}5)$$

where L is the film length

$$Pr = \frac{\mu_{flm} \cdot c_{pflm}}{k_{flm}}$$

and

$$Gr = g \cdot \beta_{flm} \cdot L^3 \cdot |T_{surf} - T_c| \cdot \left(\frac{\rho_{flm}}{\mu_{flm}}\right)^2$$

The subscript "c" is for the water regime (H1) and g is for the steam regime (H6).

The subscript "flm" means that properties shall be evaluated at film temperature T_{flm}

$$T_{flm} = (T_{surf} + T_c) \cdot 0.5$$

and β_{flm} is the thermal expansion coefficient

$$\beta_{flm} = \frac{1}{v} \cdot \left(\frac{\partial v}{\partial T}\right)_p = \frac{1}{v} \cdot \frac{\partial^2 g}{\partial T \partial p}$$

where:

v = specific volume, and
g = Gibb's free enthalpy.

The coefficients C and n for laminar natural convection, are:

$C = 1.35;\ n = 0.15$ for $1 < Gr \bullet Pr < 5554$

$C = 0.57;\ n = 0.25$ for $5554 \le Gr \cdot Pr \le 1.057 \cdot 10^8$

and for turbulent natural convection:

$C = 0.13;\ n = 0.333$ for $1.057 \cdot 10^8 < Gr \cdot Pr$

11.1.3 Steam Condensation (H4)

Near Wall Condensation

According to Hancox-Nicoll (Reference 11.4) the near wall condensation is calculated as:

$$h_{NWcond} = k_{liq} Nu / D_{hyd} \tag{11-6}$$

together with

$$Nu = 0.1 Re_{liq}^{0.662} Pr_{liq}$$

Bulk Condensation

For prediction of condensation in turbulent flow inside of horizontal tubes, the general technique from Shah (Reference 11.5) is used. This correlation is good for all flow patterns as long as both the liquid film and vapor core is turbulent. That means following basic three conditions must be considered:

$$u_g > 3 m/s, Re_l > 350, Re_g > 3500$$

$$h_{TP}/h_f = 1 + 3.8/Z^{0.95} \tag{11-7}$$

The parameter Z is defined as:

$$Z = \left(\frac{1}{x} - 1\right)^{0.8} \cdot Pr^{0.4}$$

The superficial heat transfer coefficient h_j is calculated as:

$$h_f = h_L (1 - x)^{0.8}$$

h_L is the heat transfer coefficient, assuming all mass to be flowing as liquid, and is calculated by Dittus-Boelter equation (Reference 11.3) as:

$$h_L = 0.023 \left(\frac{GD}{\mu_f}\right)^{0.8} Pr_f^{0.4} \frac{k_f}{D_{hyd}} \tag{11-8}$$

For $Re_G < 35000$.

The condensation heat transfer coefficient is calculated in accordance with (Reference 11.6) as:

$$h_{TP} = F_s \cdot h_{Nu} \tag{11-9}$$

Where h_{Nu} is calculated from:

$$h_{Nu} = 0.725 \cdot \left[\frac{k_f^3 h_{fg} \rho_g (\rho_f - \rho_g) g}{D_{hyd} \mu_f \Delta T_{sat}} \right]^{\frac{1}{3}} \quad \text{and } F_s = 0.77 \text{ according to (Reference 11.6).}$$

11.1.4 Turbulent Forced Convection Regime (H3 or H8)

Dittus-Boelter correlation (Reference 11.3) is used for turbulent forced convection of steam and water.

$$Nu = 0.023 \cdot Re_c^{0.8} \cdot Pr_c^{0.4}$$

$$h = k_c \cdot Nu/D_h \qquad (11\text{-}10)$$

where again subscript "c" is for the water regime (H3) and g is for the steam regime (H8).

$$Re_f = \frac{|G_f| D_h}{\mu_f (1-\alpha)}$$

$$Pr_f = \frac{\mu_f \cdot c_{pf}}{k_f}$$

$$Re_g = \frac{|G_g| D_h}{\mu_g \alpha}$$

$$Pr_g = \frac{\mu_g \cdot c_{pg}}{k_g}$$

11.1.5 Post-Dryout Heat Transfer Regime

11.1.5.1 Direct Wall to Liquid Heat Transfer (H11)

Direct wall to liquid heat transfer at wall temperature above T_{min} (Leidenfrost temperature) is calculated using the Forslund-Rohsenow equation (Reference 11.7):

$$h_{wd} = 0.2 \frac{\pi}{4} \left(\frac{6}{\pi} \right)^{2/3} \cdot (1 - \alpha)^{2/3} \qquad (11\text{-}11)$$

$$\cdot \left[\frac{g \rho_f \rho_V h_{fg} k_V^3}{(T_{surf} - T_{sat}) \mu_V \left(\frac{\pi}{6} \right)^{1/3} D_d} \right]^{1/4} \cdot (T_{surf} - T_{sat})$$

where D_d is a drop diameter calculated as described in Reference 11.5.

11.1.5.2 Forced Convection to Steam with Two-Phase Enhancement Factor for Dispersed Flow (H10)

The dispersed flow film boiling heat flux is used when $\alpha > 0.9$ and $T_{surf} > T_{min}$.

$$H = \psi h_{spv} \tag{11-12}$$

where:

h_{spv} = turbulent heat transfer coefficient to steam (H8), and
ψ = enhancement factor for dispersed flow.

This two-phase enhancement factor for dispersed flow, ψ is approximated by an extension of analogy between wall shear stress and heat transfer, as follows:

$$\psi = \frac{H_{2\Phi}}{H_{spv}} = \sqrt{\frac{\tau_{2\Phi}}{\tau_w}} = \left(1 + \frac{\tau_d}{\tau_w}\right)^{1/2}$$

$$\tau_d = \frac{3\,\alpha_d\,\rho_v\,C_{Dd}\,(U_v - U_d)^2}{4\,D_d}$$

$$\tau_w = \frac{1}{2}\,\rho_v\,f_w\,\frac{U_v^2}{D_h}$$

where:

τ_d = interfacial shear due to droplets,

τ_w = vapor-wall shear stress,

$\tau_{2\Phi}$ = total shear stress for 2Φ dispersed flow = $\tau_w + \tau_d$,

f_w = wall friction factor,

f_w = $0.0791 \cdot Re_v^{-0.25}$,

C_{Dp} = drop drag coefficient,

C_{Dd} = $\frac{24}{Re_D}\,(1 + 0.1\,Re_D^{0.75})$

D_d = drop diameter,

α_d = volume fraction of entrained drops,

Re_D = Reynolds number for vapor over drops, and

$$Re_D = \frac{D_d \rho_V (U_V - U_d)}{\mu_V}$$

11.1.5.3 Low Flow Film Boiling Regime (H12)

For the inverted annular regime, a modified Bromley correlation is used

$$h = Nu \cdot k_g / L_H \tag{11-13}$$

The Nusselt number is given by:

$$Nu = 0.62 \cdot \left(\frac{Ra \cdot h_{fg}}{c_{pg} \cdot \Delta T_w} \right)^{1/4}$$

where:

ΔT_w = $T_{surf} - T_{sat}$, and

$$Ra = \frac{L_H^3 \cdot g \cdot \rho_g \cdot (\rho_f - \rho_g) \cdot Pr_g}{\mu_g^2}$$

and the L_H is the Helmholtz instability length is

$$L_H = 16.24 \cdot \left(\frac{\sigma^4 h_{fg}^3 \mu_g^5}{\rho_g (\rho_f - \rho_g)^5 g^5 k_g^3 \Delta T^3} \right)^{1/11}$$

11.1.6 Transition Boiling

Transition boiling, or unstable boiling, occurs when the surface temperature is above the critical temperature, T_{crit}, but below the Leidenfrost temperature, T_{Leid} (see Figure 11.1-2). This regime is some times called the unstable dryout regime.

The heat flux in the unstable dryout regime is calculated by weighting of the heat transfer correlations from forced convection, H10, direct wall to liquid heat transfer, H11, and low flow film boiling regime, H12.

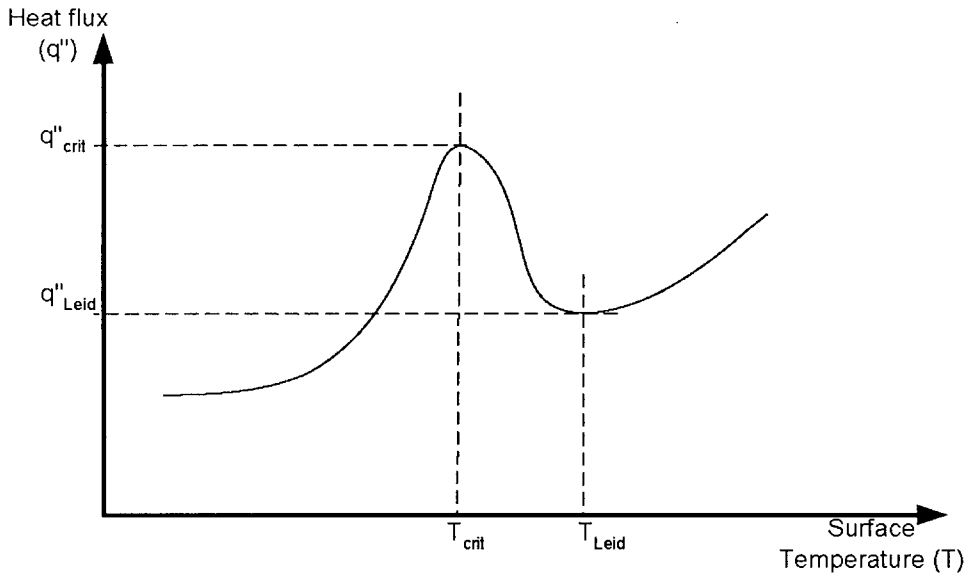

Figure 11.1-2. Heat Flux versus Surface Temperature

The heat transfer coefficients to the phases for temperatures between the critical and the Leidenfrost temperatures is approximated by the interpolation relationship:

$$h_l = f_1 \cdot h_{lH10} + f_2 \cdot h_{lH11} + f_3 \cdot h_{lH12} \tag{11-14}$$

$$f_1 = \frac{\alpha - 0.6}{0.3}$$

$$f_2 = \frac{\alpha - 0.6}{0.3}$$

$$f_3 = 1 - \frac{\alpha - 0.6}{0.3} \cdot 0.75$$

and

$$h_g = f_1 \cdot h_{gH10} + f_2 \cdot h_{gH11} + f_3 \cdot h_{gH12} \tag{11-15}$$

$$f_1 = \frac{\alpha - 0.6}{0.3}$$

$$f_2 = \frac{\alpha - 0.6}{0.3}$$

$$f_3 = 1 - \frac{\alpha - 0.6}{0.3} \cdot 0.25$$

11.1.6.1 Leidenfrost Temperature

It is assumed that the minimum film boiling temperature is the wall temperature that results in an instantaneous contact temperature equal to the homogenous nucleation temperature, T_{HN}. Using a contact temperature correction to include the effects of surface thermal properties, the minimum film boiling temperature is (Reference 11.8):

$$T_{Leid} = T_{HN} + (T_{HN} - T_l) \cdot \left(\frac{(k \rho C_p)_l}{(k \rho C_p)_{surf}} \right)^{1/2} \tag{11-16}$$

where the homogenous nucleation temperature is given as a function of pressure by a simple curve fit:

$$T_{HN} = (673.44 - 4.722 \cdot 10^{-2} \cdot DP + 2.3907 \cdot 10^{-5} \cdot DP^2 - 5.8193 \cdot 10^{-9} \cdot DP^3) \cdot 5/9 \tag{11-17}$$

where $DP = 3203.6 - 14.5038 \cdot 10^{-5} \cdot p$.

The minimum film boiling temperature is specified as the larger of either equation (11-1) or that given by Henry's modification of the Berenson correlation:

$$T_{Leid} = T_B + 0.42 (T_B - T_l) \cdot \left\{ \left[\frac{(k \rho C_p)_l}{(k \rho C_p)_{surf}} \right]^{1/2} \cdot \left[\frac{h_{fg}}{C_{psurf} (T_B - T_f)} \right] \right\}^{0.6} \tag{11-18}$$

where

$$T_B = T_{sat} + 0.127 \cdot \frac{\rho_v h_{fg}}{k_v} \cdot \left[\frac{g (\rho_f - \rho_g)}{(\rho_f + \rho_g)} \right]^{2/3} \cdot \left[\frac{\sigma}{g (\rho_f - \rho_g)} \right]^{1/2} \cdot \left[\frac{\mu_v}{(\rho_f - \rho_g)} \right]^{1/2} \tag{11-19}$$

There are limits on maximum and minimum values of T_{Leid} predicted by the above correlations.

[

]^{a,c}

11.2 REFERENCES

11.1 J. C. Chen, "A Correlation for Boiling Heat Transfer of Saturated Fluids in Convective Flow" ASME paper 63-HT-34, 1963.

11.2 M. Jakob, "Heat Transfer," Vol. 1, Wiley, 1949, pg. 529.

11.3 F. W. Dittus and L. M. K. I. Boelter, Pub. Eng. 2, Univ. of Calif., Berkeley, 1930, pg. 433

11.4 Hancox W. T, Nicoll W.B., "Prediction of Time Dependent Diabatic Two-Phase Water Flows, Progress of Heat and Mass Transfer, Vol. 6, Pergamon Press, 1972, pp.119-135.

11.5 Shah, M. M, "A General Correlation for Heat Transfer during Film Condensation Inside Pipes," Int. J. Heat Mass Transfer, Vol. 22, pp. 547-556, 1979.

11.6 Chato, J. C., "Laminar Condensation Heat Transfer Inside Horizontal Tubes," ASHRAE J., Vol. 4, No. 2, pp 52-60, 1962.

11.7 R.P. Forslund and W. M. Rohsenow, "Thermal Non-Equilibrium in Dispersed Flow Film Boiling in a Vertical Tube," MIT Heat Transfer Lab, Rep 75317-44, 1966.

11.8 L. E. Hochreiter, "Interfacial Heat and Mass Transfer Models for GOBLIN-BE SED-LEH-87-107," November 16, 1987.

12 DRYOUT AND DNB CORRELATIONS

The boiling transition between non-dryout heat transfer and post-dryout heat transfer is determined from critical heat flux (CHF) correlations.

The critical power ratio (CPR) is evaluated in BWRs. The CPR is a measure of the margin to dryout, for a given CHF correlation. The CPR at an axial location is defined as the ratio of the integrated bundle power from the inlet to the dryout location, to the actual integrated bundle power over the same length. CPR correlations appropriate for each unique assembly type in the core are included in POLCA-T. One example of CPR correlations for Westinghouse BWR fuel is found in Reference 12.1.

The departure from nucleate boiling (DNB) is a local quantity that describes when bubble formation is rapid enough to cause a continuous vapor film to form at the tube wall.

The critical heat flux used is the maximum between a flow boiling and a pool boiling correlation:

$$q''_{crit} = \max \{ q''_{fb} , q''_{pb} \} \quad (12\text{-}1)$$

The calculation of CPR or DNB for all fuel bundles during steady-state and transient conditions are performed by its fuel-specific correlation which is chosen by the user depending on the fuel type. The CPR correlation developed for each new fuel type is submitted for NRC review and approval as a part of the fuel type licensing activities. Once approved, the new correlation is added to the dryout correlation library.

12.1 FLOW BOILING CRITICAL HEAT FLUX CORRELATION

One of the CHF correlation of the Φ/x-type in POLCA-T is the AA-74 correlation This correlation is developed from ASEA-ATOM 8x8 fuel assembly CHF test data, as shown later in Figure 12.2-1. [

]^{a,c}

Other Φ/x-correlations for POLCA-T are available via a common library, which is linked to POLCA-T.

12.2 FLOW BOILING CRITICAL QUALITY

Another type of flow boiling critical quality correlation available in POLCA-T is correlations of the type of critical quality versus boiling length, correlation of type x/L-correlation, as shown in Figure 12.2-1.

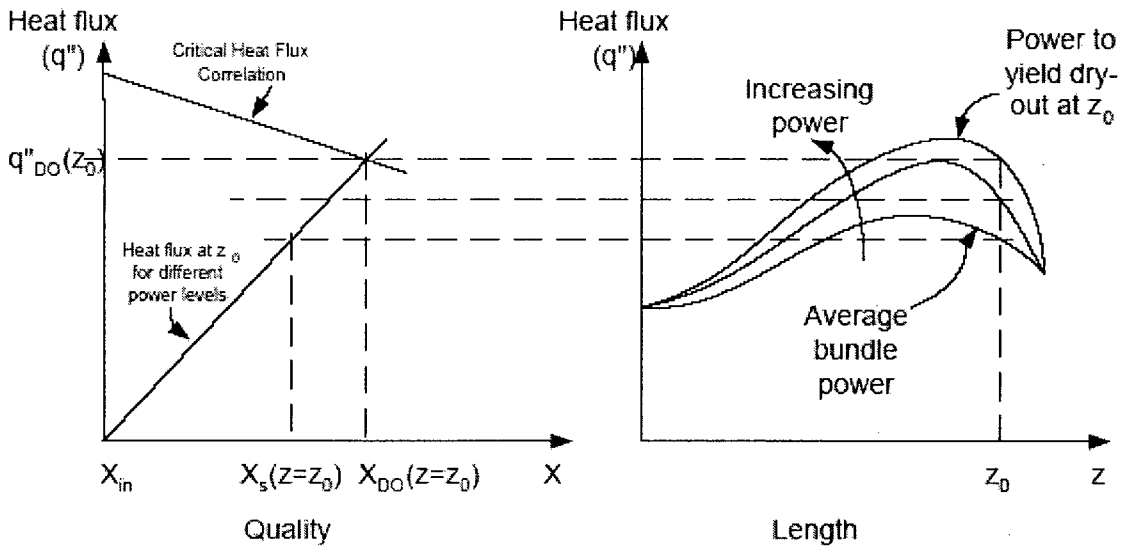

Figure 12.2-1. Principles of Computation of Critical Heat Flux

[

]^{a,c}

Other x/L-correlations for POLCA-T are available via a common library, which is linked to POLCA-T.

12.3 DNB-CORRELATION

The correlation for calculating the DNB in POLCA-T is based on a lookup table for CHF, Reference 12.2. The correlation for the CHF is of the form:

$$CHF_{actual} = CHF_8(p,G,x)*k_1*k_2*k_3*k_4*k_5*k_6 \qquad (12\text{-}3)$$

where:

p	=	local pressure,
G	=	mass flux,
x	=	thermodynamic quality, and
k_i	=	factors for local peaking pattern and fuel bundle geometry, etc.

And the heat flux ratio, the DNB ratio (DNBR) is:

$$DNBR = CHF_{actual}/\Phi \quad (12\text{-}4)$$

where:

Φ = actual heat flux, and
CHF_{actual} = critical heat flux at actual position.

12.4 POOL BOILING CRITICAL HEAT FLUX

The critical heat flux in pool boiling is calculated from a modified Zuber (Reference 12.3) correlation. The original Zuber correlation was

$$q''_{pc,Z} = \frac{\pi}{24} \cdot hfg \cdot \rho g \cdot \left(\frac{\sigma\, g\, (\rho f - \rho g)}{\rho g^2}\right)^{1/4} \cdot \left(\frac{\rho f}{\rho f + \rho g}\right)^{1/2} \quad (12\text{-}5)$$

This correlation is derived and tested for a heated wire. When applied to a rod bundle the correlation is multiplied by a factor, FRB, to account for the differences.

$$F_{RB} = \frac{F_D}{10 + F_D}$$

$$F_D = \frac{D_{heat}}{\left(\frac{\sigma}{g\,(\rho f - \rho g)}\right)^{1/2}}$$

According to Griffith (Reference 12.4) the correlation should be modified for two-phase mixtures by multiplying by (1-α), where α is the void fraction. Hence, the final correlation for the critical heat flux in pool boiling is:

$$q''_{pc} = F_{RB} \cdot (1-\alpha) \cdot \frac{\pi}{24} \cdot hfg \cdot \rho g \cdot \left(\frac{\sigma\, g\, (\rho f - \rho g)}{\rho g^2}\right)^{1/4} \cdot \left(\frac{\rho f}{\rho f + \rho g}\right)^{1/2} \quad (12\text{-}6)$$

12.4.1 Rod Critical Temperature

The critical temperature is calculated from:

$$T_{crit} = \frac{q''_{crit}}{H_{crit}(T_{crit})} + T_{coolant} \quad (12\text{-}7)$$

where:

q''_{crit} = maximum heat flux (equation (12-1), and
H_{crit} = heat transfer coefficient in the two-phase boiling regime.

Since H_{crit} depends on T_{crit}, an iterative solution is necessary.

12.4.2 Slab Critical Temperature

The critical temperature for the reactor vessel and internals (metal slabs) is calculated from Reference 12.4

$$T_{crit} = T_{sat} + 23\ ^{\circ}C \tag{12-8}$$

where T_{sat} is the saturation temperature.

12.5 REFERENCES

12.1 10x10 SVEA Fuel Critical Power Experiments and CPR Correlation: SVEA-96 Optima2, WCAP-16081-P-A, March 2006.

12.2 HTFS Handbook, Volume 2, BM24, Tabular method for predicting critical heat flux for water in vertical tubes, Harwell, N.E.L. Chalk River, 1985.

12.3 N. Zuber, M. Tribus, J. W. Westwater, The Hydrodynamic Crisis in Pool Boiling of Saturated and Subcooled Liquids, International Developments in Heat Transfer Part II, 1961, pg. 230-236.

12.4 P. Griffith, K. T. Avedisian, J. F. Walkush, Countercurrent Flow Critical Heat Flux, National Heat Transfer Conference San Francisco, Aug. 1975.

13 HEAT CONDUCTION MODELS

The thermal model in POLCA-T consists of a 1-D conduction model. Cylindrical coordinates are used to model the fuel rods and shell structures and models while cartesian coordinates are used to model the reactor vessel and internals. The thermal properties of the structural materials are also considered.

The heat conduction model accounts for the influence of a moving two-phase water level on the heat transfer. This is done by subdividing any rod or slab into a portion above and below the water level and performing separate heat conduction calculations for each subdivision.

13.1 CYLINDRICAL ROD CONDUCTION MODEL

In POLCA-T, the coolant conditions are specified by the hydraulic model and the heat transfer coefficient is solved implicitly with the heat conduction solution. The POLCA-T can also handle hot rod models of the average fuel rod for each fuel bundle. The hot rod model has a thermal-hydraulic environment, which is equal to the same state conditions as the average rod. The hot rod model have either a user-specified internal power peak factor, Fint, or a Fint that is calculated by the POLCA7 for the entire core running with the pin-power reconstruction mode activated.

Heat transfer in a fuel rod during, for example, a LOCA can be characterized as a multi-region, transient, 2-D conduction problem with volumetric heat generation and general boundary conditions. Since the axial temperature gradients in the fuel rod and cladding are much smaller than the radial temperature gradients, axial conduction is assumed to be negligible, and is not modeled.

With these assumptions, the time-dependent heat conduction equation may be written (in cylindrical coordinates) as:

$$\rho c \frac{\partial T}{\partial t} = q''' + \frac{1}{r}\frac{\partial}{\partial r}\left(kr\frac{\partial T}{\partial r}\right) \qquad (13\text{-}1)$$

The fuel rod or fuel rod simulator is divided into N radial rings characterized by material type, inner radius, outer radius and volumetric heat generation rate, as shown in Figure 13.1-1. The material types include UO_2 and Zircaloy among others. Also gas gaps are treated as radial rings.

Equation (13-1) is multiplied with r and integrated over a ring from r_a to r_b,

$$\frac{r_b^2 - r_a^2}{2}\left(\rho c \frac{\partial T}{\partial t} - q'''\right) = \left(kr\frac{\partial T}{\partial r}\right)_{r_b} - \left(kr\frac{\partial T}{\partial r}\right)_{r_a} \qquad (13\text{-}2)$$

The upper bar denotes a ring average value. Introducing the temperatures at r_a and r_b (T_a and T_b) and the temperature at the radial midpoint of the ring (T_m) the spatially discretized form of equation (13-2) is written:

$$\frac{r_b^2 - r_a^2}{2}\left(\frac{\rho c T_m}{4}\frac{d\left(T_a + 2T_m + T_b\right)}{dt}\right) - q''' \tag{13-3}$$

$$= \frac{2\cdot k(T_m)}{r_b - r_a}\left(r_b(T_b - T_m) + r_a(T_a - T_m)\right) = f(T_a, T_m, T_b)$$

This equation is further discretized in time to read:

$$\frac{(r_b^2 - r_a^2)}{2}\cdot$$

$$\left(\frac{\rho\{\Theta c(T_m^{n+1}) + (1-\Theta)c(T_m^n)\}\cdot\{(T_a+2T_m+T_b)^{n+1} - (T_a+2T_m+T_b)^n\}}{4\cdot\Delta t}\right) = \tag{13-4}$$

$$= \Theta\cdot f(T_a^{n+1}, T_m^{n+1}, T_b^{n+1}) + (1-\Theta)\cdot f(T_a^n, T_m^n, T_b^n)$$

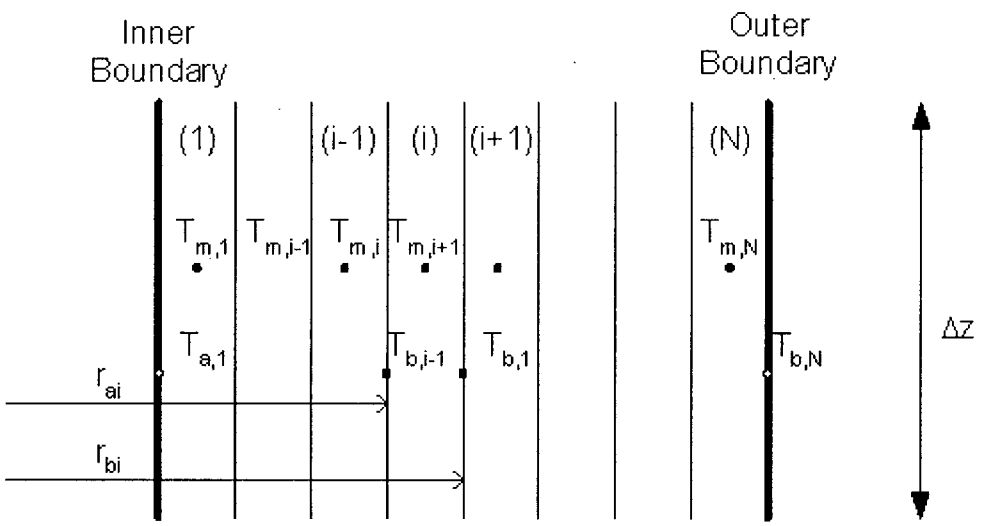

Figure 13.1-1. Typical Subdivision of a Cylindrical Heat Structure

The upper index is used here as usual to denote the time step number. The equation can be looked upon as an energy balance for a ring where q''' now represents the time step average volumetric heat generation rate. The implicitness factor Θ is zero for a fully explicit numerical scheme and unity for a fully implicit numerical scheme. In order to use the equation in POLCA-T for a cylindrical rod divided into rings, conditions must be specified on the interfaces between the rings and also on the boundary of the rod.

Inner Boundary

The inner boundary is either the center line (zero radius) or at some finite radius. In both cases, the radial temperature gradient is assumed to be zero:

$$T_{a1} = T_{m1} \tag{13-5}$$

Interfaces Between Rings

The heat flux on each side of an interface must be equal:

$$\frac{2\cdot k(T_{m,i})\cdot(T_{m,i}-T_{b,i})}{r_{b,i} - r_{a,i}} = \frac{2\cdot k(T_{m,i+1})\cdot(T_{m,i+1}-T_{b,i+1})}{r_{b,i+1} - r_{a,i+1}} \tag{13-6}$$

Of course, $r_{b,i}=r_{a,i+1}$ and $T_{b,i}=T_{a,i+1}$.

Outer Boundary

On the outer boundary of the rod, either the total heat flux is known or the heat flux is given as the sum of radiate and convective components to water and steam. The equations corresponding to the two cases are:

$$\frac{2\cdot k(T_{m,N})\cdot(T_{m,N} - T_{b,N})}{r_{b,N} - r_{a,N}} = q_{tot} \tag{13-7a}$$

or

$$\frac{2\cdot k(T_{m,N})\cdot(T_{m,N} - T_{b,N})}{r_{b,N} - r_{a,N}} = h_l\cdot(T_{b,N} - T_l) + h_v\cdot(T_{b,N} - T_v) + q_{rad} \tag{13-7b}$$

where:

T_l, T_v = temperature of water and steam, respectively, and

h_l, h_v = heat transfer coefficient of water and steam, respectively.

Equation (13-5) with (13-4) repeated N times and (13-6) repeated N-1 times with (13-7a or 13-7b) to form a three-diagonal, almost linear, system of equations for $[T_{a,1}, (T_{m,i}, T_{b,i}, i=1,2,...,N)]$. The coefficient matrix depends on the temperatures through the material properties (k(T) and c(T)). The system is solved by direct Gaussian elimination, which is iterated until convergence requirements have been met.

After elimination phase the derivative

$$\frac{dT_{b,N}}{dq} = \frac{2\cdot\pi\cdot rbN\cdot\Delta z}{C_2N + 1,2} \tag{13-8}$$

can be calculated, where $C_{2N+1,2}$ is the diagonal element of equation (13-7a or 13-7b). This derivative is used in solving the coupling between conduction and heat transfer phenomena.

The conductivity of a gas gap is calculated from:

$$k = h_{gap} \cdot (r_b - r_a) \cdot (r_b + r_a)/(2 \cdot r_b) \tag{13-9}$$

where h_{gap} is calculated as described in Section 14.1. The specific heat of a gas gap is set to zero.

The implicitness parameter, Θ, has a value of 0.5 which gives the Crank-Nicolson method (Reference 13.1). The volumetric heat generation rate is determined from the total heat generation in the reactor and power distribution for channel to channel, rod section to rod section, and radial ring to radial ring. The power generation includes fission power, decay power, and power due to metal-water reaction.

13.2 SLAB CONDUCTION MODEL

POLCA-T can model any number of heat-transferring slabs (simulating parts of the vessel or the internals) which are in contact (cooled) with coolant on both sides or insulated on either side. The 1-D heat conduction equation is solved using a finite difference technique and a user-specified nodal subdivision of each slab. Each slab has one conduction area (A_C) and also heat transfer areas on each side (A_L, A_R), which in turn can be liquid (A_{lL}, A_{lR}) or in the gas phase (A_{vL}, A_{vR}). It can be composed of different materials.

The 1-D heat conduction equation

$$\rho c \frac{\partial T}{\partial t} = \frac{\partial}{\partial x} \left[k(T) \frac{\partial T}{\partial x} \right] \tag{13-10}$$

is integrated over the conduction nodes (see Figure 13.2-1).

For node i equation 13-10 is:

$$\rho_i c_i \Delta x_i \frac{\partial T_i}{\partial t} = - k_{i-1,i} \cdot \left. \frac{\partial T}{\partial x} \right|_{i-1,i} + k_{i,i+1} \cdot \left. \frac{\partial T}{\partial x} \right|_{i+1,i} \tag{13-11}$$

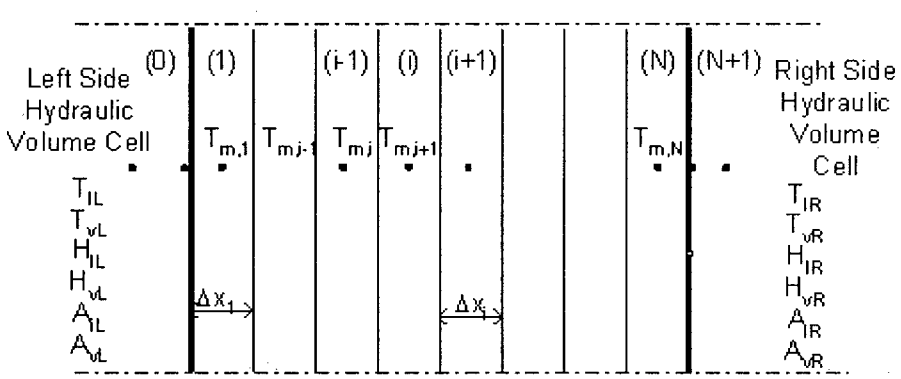

Figure 13.2-1. Typical Subdivision of a Slab Heat Structure

The partial derivatives are approximated by the following differences:

$$\frac{\partial T_i}{\partial t} = \frac{T_i^{n+1} - T_i^n}{\Delta t} \tag{13-12}$$

$$\left.\frac{\partial T}{\partial x}\right|_{i-1,i} = \frac{T_i - T_{i-1}}{0.5 \cdot (\Delta x_i + \Delta x_{i-1})} \tag{13-13}$$

$$\left.\frac{\partial T}{\partial x}\right|_{i,i+1} = \frac{T_{i+1} - T_i}{0.5 \cdot (\Delta x_i + \Delta x_{i+1})} \tag{13-14}$$

$$\left.\frac{\partial T}{\partial x}\right|_{L,1} = \frac{T_1 - T_0}{0.5 \cdot \Delta x_1} \tag{13-15}$$

$$\left.\frac{\partial T}{\partial x}\right|_{N,R} = \frac{T_{N+1} - T_N}{0.5 \cdot \Delta x_N} \tag{13-16}$$

The thermal conductivity at the boundaries of the nodes is calculated using the requirement of a continuous heat flux across the node boundaries.

$$k_{i,i+1} = \frac{k(T_i)\, k(T_{i+1}) \cdot (\Delta x_i + \Delta x_{i+1})}{k(T_i)\, \Delta x_{i+1} + k(T_{i+1})\, \Delta x_i} \tag{13-17}$$

Equation (13-11) is written in the finite difference form using the method developed by Crank and Nicolson (Reference 13.1):

$$\rho_i \Delta x_i\, c_i(T_i^n) \cdot \frac{T_i^{n+1} - T_i^n}{\Delta t} =$$

$$- \frac{k_{i-1,i}^n}{0.5\,(\Delta x_i + \Delta x_{i-1})} \cdot \left(\Theta\, T_i^{n+1} + (1-\Theta)\, T_i^n - \Theta\, T_{i-1}^{n+1} - (1-\Theta)\, T_{i-1}^n\right) \tag{13-18}$$

$$+ \frac{k_{i,i+1}^n}{0.5\,(\Delta x_i + \Delta x_{i+1})} \cdot \left(\Theta\, T_{i+1}^{n+1} + (1-\Theta)\, T_{i+1}^n - \Theta\, T_i^{n+1} - (1-\Theta)\, T_i^n\right)$$

where Θ is the implicitness.

On the outer boundaries of the plate, either total heat fluxes are known or the heat transfer components are given as the sum of the convective components.

For the left boundary, the following equation is used:

$$-k\,T_1^n \cdot \frac{T_0^{n+1} - T_1^{n+1}}{0.5\,\Delta x_1} \cdot A_C = A_{lL} \cdot H_{lL} \cdot (T_0^{n+1} - T_{lL}^{n+1}) + A_{vL} \cdot H_{vL} \cdot (T_0^{n+1} - T_{vL}^{n+1}) + A_L \cdot q_{radL}^n + Q_{distL} \quad (13\text{-}19)$$

and for the right boundary:

$$k\,T_N^n \cdot \frac{T_N^{n+1} - T_{N+1}^{n+1}}{0.5\,\Delta xN} \cdot A_C = A_{lR} \cdot H_{lR} \cdot (T_{N+1}^{n+1} - T_{lR}^{n+1}) + A_{vR} \cdot H_{vR} \cdot (T_{N+1}^{n+1} - T_{vR}^{n+1}) + A_R \cdot Q_{distR} \quad (13\text{-}20)$$

where $Qdist_L$ and Q_{distR} are the disturbances introduced to calculate derivatives,

$$\frac{dT_0}{dQ_L}, \frac{dT_0}{dQ_R}, \frac{dT_{N+1}}{dQ_L}, \frac{dT_{N+1}}{dQ_R} \quad (13\text{-}21)$$

used to solve coupling between heat conduction and transfer.

The heat conduction problem for the slabs is solved using equations above. These form a three-diagonal linear system of equations with three right-hand sides (undisturbed, disturbed on left or right side) with the unknown temperatures (Tk,i=0,1,..,N+1). The system is solved using a Gaussian elimination technique accounting for the structure of the matrix.

13.3 REFERENCES

13.1 J. Crank and P. Nicolson, "A Practical Method for Numerical Evaluations of Solutions of Partial Differential equations of the Heat Conduction Type," Proc. Cambridge Phil. Soc., Vol. 43, 1947.

14 FUEL ROD MODEL

In POLCA-T, all fuel assembles can be modeled. Each fuel assembly can consist of an average fuel rod, part length rods, and water rods. The number of rods is determined by the user. In addition to this model, a hot rod fuel rod can be simulated. This simulation only uses the thermal-hydraulic environment for the average rod to calculate maximum temperatures when an internal peaking factor is set for this hot rod. The internal peaking factor can be constantly user-specified, or be taken from POLCA7 as the internal peaking factor calculated from pin-power reconstruction.

All of the equations, tables, etc. stated in this section and used in POLCA-T are from the STAV code (Reference 14.1) for completeness of the section, except for a few equations that are explicitly referenced.

14.1 GAS GAP MODEL

Gas phase heat conduction (h_g), as well as thermal radiation (h_{rad}), carry out the heat transfer across the pellet-cladding gap. In the case of a fuel-cladding surface contact, a third term (h_{cont}) might contribute to the overall gap heat conductance which furthermore enhances the heat transfer.

The overall heat transfer coefficient across the gap is the sum of the items mentioned above.

$$h = h_{rad} + h_g + h_{cont} \tag{14-1}$$

The mathematical formulation and implementation of these mechanisms in the POLCA-T code is presented in the following subsections.

14.1.1 Radiation Heat Transfer

Lambert's and Stefan-Boltzmann's laws govern the thermal radiation between fuel and cladding. It may be represented by the following equation:

$$h_{rad} = C_{f,c} \cdot \frac{T_f^4 - T_c^4}{T_f - T_c} = C_{f,c} \cdot (T_f + T_c) \cdot (T_f^2 - T_c^2) \tag{14-2}$$

where:

$$C_{f,c} = \frac{\sigma}{\frac{1}{\varepsilon_f} + \frac{\phi}{\varepsilon_c} - \phi} \tag{14-3}$$

and

σ = Stefan-Boltzman constant = $5.67032 \cdot 10^{-8}$ W m^{-2} K^{-4}
ε = emissivity
T = surface temperature, K
ϕ = ratio of pellet to cladding radius

The subscripts f and c stand for the fuel and cladding, respectively. The amount of heat transfer by the radiation term is significant only during the LOCA, where the surface temperatures of the fuel and cladding become high.

14.1.2 Gas Gap Heat Conduction, Solid Cylinder Pellet

The pellet-cladding gap is usually filled with helium gas and fission gases, which are produced during the fuel life cycle. The heat transfer ability of the gap depends primarily upon the thermodynamic properties of the gas mixture in the gap. The heat transfer coefficient of the gas mixture, h_g, is given by:

$$h_g = \sum_{i=1}^{n} h_{g,i} \tag{14-4}$$

where $h_{g,i}$ is the heat transfer coefficient of the gas constituent i in the gas mixture.

On the other hand, the heat transfer coefficient of a single pure gas is given as:

$$h_{g,i} = K_i \; / \; G_{i,eff} \tag{14-5}$$

in which K_i represents the effective gas thermal conductivity of component i in the gas mixture and $G_{i,eff}$ is the effective gap size.

The effective thermal conductivity of a single pure gas in a gas mixture is calculated, based on the thermal conductivity of pure gases making up the mixture, according to the following equation:

$$K_i = \frac{k_i x_i}{\sum_{j=1}^{n} A_{ij} \cdot x_j} \tag{14-6}$$

where:

k_i = thermal conductivity of pure gas i, W m-1 K-1,
xi = mole fraction of gas i in the mixture,
Aij = Sutherland weighting factor for the gas species i, in the gas mixture, and
n = number of gas constituents in the mixture.

The Sutherland weighting factor can be obtained from the following equation:

$$A_{ij} = \frac{1}{4} \cdot \left\{ 1 + \left[\frac{\mu_i}{\mu_j} \cdot \left(\frac{M_j}{M_i} \right)^{3/4} \cdot \frac{T + S_i}{T + S_j} \right]^{1/2} \right\}^2 \cdot \frac{T + \sqrt{S_i \cdot S_j}}{T + S_j} \tag{14-7}$$

where:

μ = viscosity of pure gas,
M = molecular weight,
T = temperature in degrees Kelvin, and
S = Sutherland constants for gas species (given in Table (20-2) for some common gases).

The temperature profile across the fuel rod is discontinuous at the boundaries to the solid surfaces (fuel and cladding). In order to make the heat transfer continuous over boundaries, the real gap size should be extended into the solid surfaces by an additional distance called temperature jump distance. Therefore, the thermal gap size for each gas constituent in the mixture can be expressed as:

$$G_{Ti} = G_0 + R_e + g_{i,jump} \tag{14-8}$$

where:

G_{Ti} = thermal gap size for gas species I,
G_0 = nominal design gap size,
R_e = roughness equivalence, and
$g_{i,jump}$ = temperature jump distance for gas species i.

The temperature jump distance of gas i is calculated according to the gas kinetics theory formula:

$$g_{i,jump} = \left(\frac{1}{\alpha_f} + \frac{1}{\alpha_c} - 1\right) \cdot \frac{4}{1+\gamma_i} \cdot \frac{k_i}{\mu_i c_{pi}} \cdot \lambda_i \tag{14-9}$$

where:

k_i, μ_i, c_{pi} = conductivity, viscosity and heat capacity of the gas i,

α_f, α_c = accommodation coefficients for the pellet and cladding,

λ_i = mean free path of the molecules i in the mixture, and

γ_i = cv/cp = ratio of specific heat at constant volume and constant pressure respectively.

The accommodation coefficients for fuel and cladding surfaces are given in Table 20-4.

According to the thermodynamics of gases:

$$\frac{k_i}{\mu_i c_{pi}} \approx \frac{9 - 5\gamma_i}{4} \tag{14-10}$$

and mean free path of the gas molecules is given by:

$$\lambda_i = C \cdot \frac{\mu_{i,eff}}{p \cdot \sqrt{\frac{T}{M_i}}} \tag{14-11}$$

where:

p, T	are pressure and temperature of gas,
M_i, $\mu_{i,eff}$	are molar weight and effective viscosity of species i in the gas mixture, and
C	constant = 114.5.

The effective viscosity of gas in the mixture is calculated from the following expression:

$$\mu_{i,eff} = \frac{\mu_i \cdot x_i}{\sum_{j=1}^{n} A_{ij} \cdot x_j} \tag{14-12}$$

Combining theses equations and solving for $g_{i,jump}$ will result in:

$$g_{i,jump} = C \cdot \frac{9 - 5\gamma_i}{1 + \gamma_i} \cdot \left(\frac{1}{\alpha_f} + \frac{1}{\alpha_c} - 1\right) \cdot \frac{\mu_{i,eff}}{p \cdot \sqrt{\frac{T}{M_i}}} \tag{14-13}$$

The effective gap size is calculated by the following equation:

$$\frac{1}{G_{i,eff}} = \int \frac{w(r)}{G_{Ti} + r} dr \tag{14-14}$$

where w(r) is distribution function for the roughness with the following properties:

$$\int w(r)\, dr = 1, \text{ and, } \int r\, w(r)\, dr = 0 \tag{14-15}$$

Assuming w(r) to be a parabolic distribution function of the following form:

$$w(r) = \frac{3}{4 \cdot R_e} \cdot \left[1 - \left(\frac{r}{R_e}\right)^2\right] \tag{14-16}$$

where $R_e = \sqrt{5} \cdot \sqrt{R_f^2 + R_c^2}$ and $w(r) = 0$ if $|r| > R_e$.

As a result, the effective gap size G_{eff} can be calculated as:

$$\frac{1}{G_{i,eff}} = \frac{3}{4 \cdot R_e} \cdot \left\{ 2Q + (1 - Q^2) \cdot \ln\left(\frac{Q+1}{Q-1}\right) \right\} \tag{14-17}$$

where $Q = \quad Q = \frac{G_{Ti}}{R_e}$

To speed up the execution time of POLCA-T, a simplification of the modeling is made, without loss of simulation accuracy. In particular, temperature jump distance, $g_{i,jump}$ has been replaced by a mean value $\overline{g}_{jump}$, which is calculated based on the mole fractions of gases in the mixture.

$$\overline{g}_{jump} = \sum_{i=1}^{n} x_i \cdot g_{i,jump} \tag{14-18}$$

This simplification, in turn, implies a mean thermal gap size to be defined by the following relationship:

$$\overline{G}_T = G_0 + R_e + \overline{g}_{jump} \tag{14-19}$$

and consequently the ratio:

$$\overline{Q} = \frac{\overline{G}_T}{R_e} = 1 + \frac{G_0 + \overline{g}_{jump}}{R_e} \tag{14-20}$$

implying that $\overline{Q} \geq 1$ is always true.

The mean value of effective gap size is expressed as:

$$\overline{G}_{eff} = \overline{G}_T \cdot F(\overline{Q}) \tag{14-21}$$

where:

$$F(\overline{Q}) = \frac{4}{3 \cdot \overline{Q} \cdot \left\{ 2\overline{Q} + (1 - \overline{Q}^2) \cdot \ln\left(\frac{\overline{Q}+1}{\overline{Q}-1}\right) \right\}} \tag{14-22}$$

and finally:

$$h_g = \frac{\overline{K}_{eff}}{\overline{G}_{eff}} = \frac{\overline{K}_{eff}}{\overline{G}_T \cdot F(\overline{Q})} \tag{14-23}$$

The constants R_e and G_0 are input values in POLCA-T input data file.

14.1.3 Gas Gap Heat Conduction, the Cracked Pellet

Upon sufficient rise in rod power, large temperature gradient develops across the fuel pellet. This produces cracks in the pellet. These cracks expend some of the free area of the gap, meaning that they cause the fuel perimeter to increased and the occurrence of pellet relocation. Pellet relocation changes the gas heat transfer coefficient and thus needs to be included in the gap heat transfer modeling.

The effective gap, $\overline{G}_T$, is modified to incorporate the effect of relocation. This has been done by modifying the mean plane gap by:

$$\overline{G}_T = G_0 + R_{eq} + (1-\Gamma)\Re \tag{14-24}$$

where Γ denotes the fraction of pellet fragments which emanates from azimuthal "misfitting", $(1-\Gamma)$ represents the corresponding quantity for the radial misfitting, and $\Re$ is the radial displacement of the pellet due to relocation.

Since locally the pellet fragments are assumed to be distributed statistically, the local heat transmission coefficient h_g^{loc} becomes a stochastic variable with a generalized mean value defined by:

$$\langle h_g^{loc} \rangle = E_f(h_g^{loc}) \tag{14-25}$$

where $E_f(h_g^{loc})$ is a generalized mean value for any monotonic continuous function f, its exact mathematical definition is given in STAV.

$$f(h_g^{loc}) = \frac{1}{h_g^{loc} + C\kappa / a} \tag{14-26}$$

where κ is the fuel pellet conductivity, a is the pellet radius, and C=15.0 is an empirical constant.

14.1.4 Conduction Heat Transfer by Fuel-Cladding Contact Area

The heat transfer occurs by solid-solid conduction mechanism when the fuel pellet comes into contact with the cladding surface.

A model assuming cylindrical area of contact between pellet and cladding calculates gap conductance according to the following expression:

$$h_{cont} = F \cdot \left(\frac{P_c}{H}\right)^n \tag{14-27}$$

where:

F = represents physical properties of the surfaces in contact,
P_c = interfacial pressure,
H = Meyer hardness (T-dependent), and
n = 1/2 if $P_c/H < 0.001$ else n=1.

The parameter F is calculated from the expression:

$$F = C \cdot k_m / R_m \tag{14-28}$$

and

$$C = 77.4 \cdot R_f^{0.528}$$

$$R_m = \sqrt{R_f 2 + R_c 2}$$

$$K_m = \frac{2\, k_f k_c}{k_f + k_c}$$

where k_f and k_c are the conductivity of fuel pellet and cladding.

Meyer hardness is the measure of material hardness and is defined as the load divided by the area, i.e., $H = 4P/(\pi d)2$ where P is the applied load and d is the diameter of area idented the metal surface with a solid ball. The dependence of Meyer hardness on temperature is expressed by the following equation:

$$H = \exp(A + B \cdot T + C \cdot T2 + D \cdot T3) \tag{14-29}$$

where T is temperature in degrees Kelvin and

A = 2.6034·10+1
B = - 2.6394·10-2
C = 4.3502·10-5
D = -2.5621·10-8

As shown by the equation, Meyer hardness decreases rapidly with temperature.

14.1.4.1 Gas Gap Pressure

For the POLCA-T calculations, the fuel rods are axially divided into a number of segments (as current standard 25 axial segments per rod). Knowing volume and temperature within each segment as well as the total number of moles of gas in the gap, the pressure can be calculated as follows:

$$P = \frac{n_{tot}}{\frac{K}{\sum_{k=1} \frac{V_k}{T_k}}} \tag{14-30}$$

where n_{tot} is the total number of gas moles and V_k and T_k are volume and temperature in segment k. The calculated pressure is used afterwards to update the value of g_{jump}.

The number of moles of gas in each rod is calculated from fission gas release models and the initial number of moles of helium the rods are filled with. The gas volume for each axial rod segment is calculated when pellet and cladding displacement are calculated as described below. This calculation of the rod pressure is updated only after each time step.

Figure 14.1-1 presents a fuel rod with its pellets. The pressure is equal in the entire rod p_{gas}, but the pressure on the outside is changing with the axial level. The volume for each segment is calculated as below when the gas gap for each segment is calculated.

$$V_k = \pi \cdot \left[(r_{ci} + \Delta)^2 - (r_{po} + \delta)^2 \right] \cdot l_k \tag{14-31}$$

where:

- Δ is the displacement of the cladding inner radius,
- δ is the displacement of the pellet outer radius,
- r_{ci} is the nominal cladding inside radius,
- r_{po} is the nominal pellet outside radius, and
- l_k is the length of the segment.

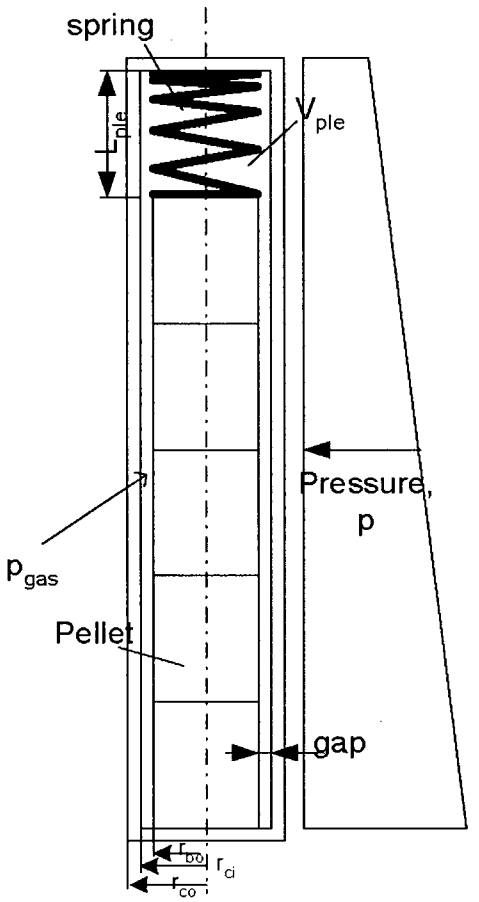

Figure 14.1-1. Fuel Rod with Definition of Pressures and Other Characteristic Variables

Figure 14.1-1 is an outline drawing of a fuel rod with definition of pressures and characteristic geometrical quantities to calculate the displacement of the cladding. According to the figure:

Pressure p	is the pressure distribution along the rod.
p_{gas}	is the gas gap pressure for the entire rod.
gap	is the gas gap distance.
r_{ci} and r_{co}	is the inner and outer radius, respectively.
L_{ple}	is the length of the rod plenum.

14.2 PELLET MODEL

Fuel pellet can be either be made of UO_2 or (U, Gd)O_2 material. The fuel models apply to normal operation of light water reactor fuel.

The fuel pellet is treated as a stiff body, which interacts with elastic and plastic Zircaloy cladding. Pellet cracking is not considered explicitly. However, the effect of cracking on thermal expansion and pellet-cladding gap reduction (pellet relocation) is taken into account. Fuel restructuring is not presently treated in the code. Figure 14.2-1 shows a pellet with possible cracks.

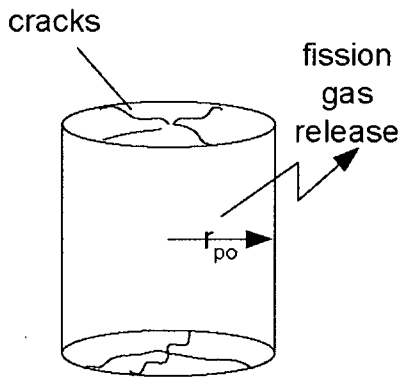

Figure 14.2-1. Pellet with Cracks

14.2.1 Pellet Conductivity

The heat conduction inside the pellet and the power generation inside the pellet is treated as a 1-D problem and the temperature field is calculated as described in Section 13.1 regarding cylindrical rod conduction model for heat structures.

In POLCA-T with the STAV option, the thermal conductivity of UO_2 fuel is temperature and burnup dependent using the built in function of the form k = f(T,D_f,G_f, Bu).

where:

k is the thermal conductivity (W/mK),
T is the temperature (C),
D_f is the density fraction due to cracking up,
G_f is the Gadolinium fraction, and
Bu is the average burn up of pellet (MWd/kg).

The function used in POLCA-T, which is applied for each radial zone in the fuel pellet model at a volumetric average temperature for each elevation of the fuel rod:

$$k = P\left[\frac{K_1}{K_2 + K_1 b(u) + \min(T,1650)} + K_3 e^{K_4 T}\right] \text{ for } 0 \le T \le T_m \text{ [°C]} \qquad (14\text{-}32)$$

where:

k = thermal conductivity in [W/m °C],
P = porosity correction factor (see equation 14-33),
T = temperature [°C],
b(u) = fuel burnup dependent term (see equation 14-36),
T_m(u) = burnup dependent melting temperature [°C], and
u = local burnup.

The melting temperature for UO_2 fuel is:

$$T_m(u) = 2805–3.2u \quad (14\text{-}33)$$

here u is in [MWd/kgU]. [

]^{a,c}

a,b,c

[

]

Table 14.2-2 shows the values of constants used in equation (14-32).

The porosity correction factor appearing in equation (14-32) is given by:

$$P = \frac{1 - \beta(1 - D_T)}{1 - \beta(1 - 0.95)} \quad (14\text{-}34)$$

where D_T is the fraction of theoretical density and β is a porosity coefficient given by:

$$\beta = 2.58 - 5.8 \times 10^{-4} T \quad (14\text{-}35)$$

Figure 14.2-2 shows the plot of P as a function of fraction of theoretical density for temperatures 500°C and 1500 °C.

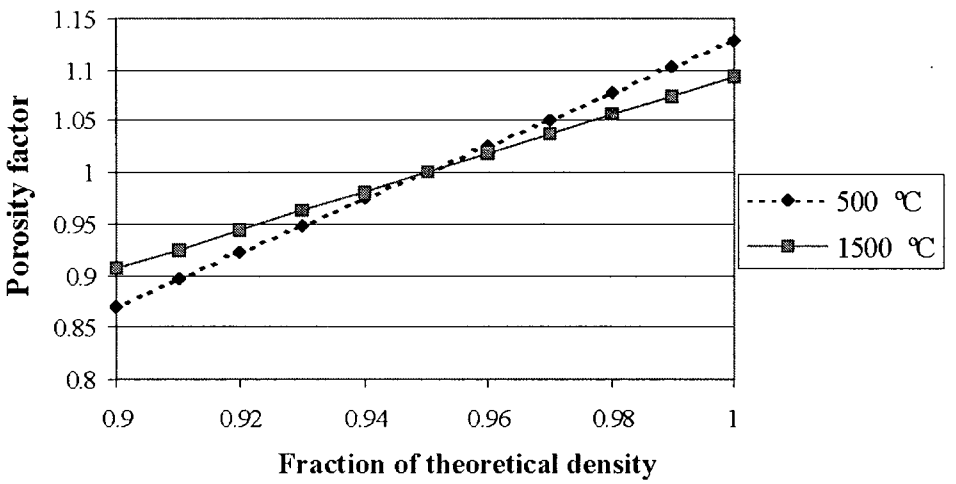

Figure 14.2-2. The Porosity Correction Factor to Thermal Conductivity P of UO_2 Fuel, as a Function of Fuel Density (as can be seen, the factor is normalized to one for 95-percent dense fuel.)

[

{

]a,c

Gadolinium Fuel Thermal Conductivity

Thermal conductivity of unirradiated gadolinium-uranium has been a subject of several measurements. The thermal conductivity correlation used for $(U,Gd)O_2$ in POLCA-T is the extension of the UO_2 correlation described in subsection 9.3.1:

$$k_g = P\left[\frac{K_1}{K_2 + K_1 b(u) + K_5 w_g + \boldsymbol{min(T,1650)}}\right] + K_3 \ell^{K_4 T}$$

for $0°C \le T \le T_m(u,w_g)$ [°C]

$$0 \le w_g \le 0.1 \qquad (14\text{-}37)$$

where

$$T_m(u,w_g) = T_m(u) - 375\, w_g \qquad (14\text{-}38)$$

where k_g is the $(U,Gd)O_2$ thermal conductivity in [W/mK], w_g is the weight fraction of gadolinium in $(U,Gd)O_2$, K_5=4670, P is given by equation (14-33), $b(u)$ by equation (14-36), $T_m(u)$ by (14-33), and K_1 through K_4 are listed in Table 14.2-1.

14.2.2 Pellet Volume Change

The volume change of UO_2 fuel is the sum of the volume changes due to thermal expansion, densification, and fuel swelling. These phenomena are treated in the POLCA-T code.

The swelling is defined as the increase in fuel volume caused by the replacement of heavy atoms by fission products in the fuel. However, due to the porous structure of ceramic nuclear fuel, the crystal lattice accommodates a sizeable portion of fission products during irradiation without a significant deformation of the pellet. The swelling is to be distinguished from the total volume changes during irradiation of the fuel, which includes also fuel densification, as a volume decreasing mechanism, as well as fuel relocation and crack formation and healing as volume increasing mechanism. The total fuel volume change can either be positive or negative. However, the swelling is always positive.

Swelling mechanism can be subdivided into two parts: swelling due to solid fission products, and swelling caused by gaseous and volatile fission products such as cesium which can be in a liquid state at operating fuel temperatures. The gaseous fission products diffuse to the grain boundaries and form into bubbles at fuel temperatures above 1000°C. These bubbles can dominate the swelling behavior of fuel at high temperatures and burnup, and their interlinkage leads to fission gas release.

The total fuel swelling is obtained by adding different contributions of swelling types and densification, i.e.:

$$(\Delta V / V)_{total} = (\Delta V / V)_D + (\Delta V / V)_{solid} + (\Delta V / V)_A + (\Delta V / V)_G \quad (14\text{-}39)$$

where $(\Delta V/V)$ designates fraction of change in fuel volume and the subscripts, total, solid, D, A, G, denote the contributions of the total swelling, solid swelling, densification, swelling accommodation, and gaseous swelling, respectively.

14.2.2.1 Pellet Solid Swelling

The solid swelling rate is assumed to be directly proportional to the local burnup. A correlation provided from STAV for solid swelling is:

$$D_{PS} = \max\left[0{,}0; \frac{0{,}836 \cdot \rho_F}{10520{,}0 \cdot (Bu - 13{,}8)}\right] \quad (14\text{-}40)$$

where:

D_{PS} is the pellet swelling (μm),
ρ_F is the pellet density (kg/m^3), and
Bu is the pellet average burnup (MWd/kgU).

14.2.2.2 Pellet Densification

Fuel densification is caused by the shrinkage of submicron size pores during irradiation. Densification of UO_2 fuel has been studied extensively. The main results of these investigations show that:

- In-pile densification is correlated to the out-of-pile isothermal resintering tests, for example at 1700°C, for 24 h under argon-8% H_2 atmosphere.

- The densification saturates after a rather low burnup, which ranges between 1 to 7 MWd/kgU.

Thus, the negative contribution of the densification to swelling is given by:

$$D_{PD} = \frac{10,2 \cdot \Delta\rho}{0,75 \cdot \left(1 - e^{\frac{-Bu}{2,71}}\right)} \tag{14-41}$$

where:

D_{PD} is the pellet densification (mm) rod internal free volume,
$\Delta\rho$ is the thermal stability (%), and
Bu is the pellet average burnup (MWd/kgU).

Same correlations as for UO_2 fuel for densification and swelling are used for $(U,Gd)O_2$ fuel.

14.2.2.3 Pellet Relocation Model

A raise in fuel rod power produces cracks in the pellets due to thermal stress induced by the radial temperature gradients across the fuel pellet. The pellet-cladding gap area accommodates the spacing area developed by these cracks inside the pellet. This gap size reduction, or alternatively, increase in apparent pellet diameter due to pellet cracking is referred to pellet relocation.

Based on an analysis similar to that of Oguma's the following pellet relocation model has been devised for STAV:

$$R = 0 \text{ for } Q < Q_c$$

$$R = C_1 a F(E)\left[1 - e^{0.154(Q_c - Q)}\right] \quad \text{for } Q \geq Q_c \tag{14-42}$$

with

$$F(E) = C_2 + (1 - C_2)e^{-0.15E} \tag{14-43}$$

where:

R pellet relocated radius [m],
a pellet outer radius [m],
E local burnup [MWd/kgU],
Q linear heat generation rate [kW/m],
Q_c critical power for pellet cracking (onset of relocation) = 4 kW/m,
C_1 = 4.0×10^{-3}, and
C_2 = 1.51.

The relocation effect is an irreversible function of power, which varies with time. During transients the relocation can be treated constant throughout the run, but as an option, the relocation can be calculated after each time step when the gas pressure in the rods is recalculated.

14.2.3 Pellet Thermal Expansion

The stress state in the pellet and its effect on pellet dimensions is not calculated by POLCA-T. Since there is a great temperature gradient along the pellet radius, an integral of pellet thermal expansion coefficient over pellet radius is necessary. A simple linear thermal expansion model for a solid pellet with an infinite number of radial cracks is considered:

$$(\alpha_T)_{pellet}^{radial} = \frac{\int_0^{R_0} \alpha_T(r)dr}{\int_0^{R_0} dr} = \frac{1}{R_0}\int_0^{R_0} \alpha_T(r)dr \qquad (14\text{-}44)$$

where:

$(\alpha_T)_{pellet}^{radial}$ radial pellet thermal expansion, dimensionless,

$\alpha_T(r) = \alpha_T\left(T(r)\right)$ UO_2 thermal expansion coefficient at temperature $T(r)$ and radius r, and

R_0 pellet outer radius.

The linear thermal expansion coefficient is defined by:

$$\alpha_T = \frac{1}{L}\frac{dL}{dT} \qquad (14\text{-}45)$$

where L is the length, and dL/dT its derivative with respect to temperature. For temperatures below melting, the fractional linear thermal expansion is expressed by:

$$\frac{\Delta L}{L}(T) = -4.972\times10^{-4} + 7.107\times10^{-6}T + 2.581\times10^{-9}T^2 + 1.140\times10^{-13}T^3 \qquad (14\text{-}46)$$

where, $\Delta L / L$ is the fractional linear thermal expansion T is temperature [°C]. Figure 14.2-3 shows the plot of $\Delta L/L$ versus temperature.

The axial pellet thermal expansion is calculated as:

$$(\alpha_T)_{pellet}^{axial} \equiv \alpha_T(T_{av})$$

where T_{av} is the radial average pellet temperature.

Measurements of the coefficient of thermal expansion of $(U,Gd)O_2$ fuel indicate that, for gadolinium concentrations less than 12 wt %, the UO_2 coefficient of thermal expansion is applicable.

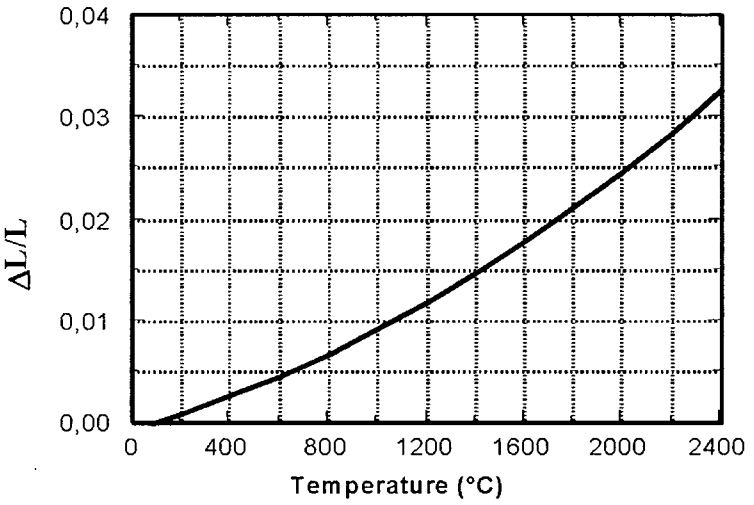

Figure 14.2-3. Temperature Dependence of the Linear Thermal Expansion of UO_2

14.2.4 Model of Fission Gas Production

[

]^{a,c}

[

]^{a,c}

[

]^{a,c}

14.3 CLADDING MODEL

The cladding is made of Zircaloy and is treated as a long, thin tube. The material is considered to be isotropic except for the thermal expansion, which is taken to be different in the radial and axial direction. The cladding temperature model includes thermal conductivity and specific heat. The cladding deformation models include thermal expansion, elasticity and plasticity, creep, and growth.

14.3.1 Thermal Expansion

The thermal expansion model for Zircaloy cladding in POLCA-T is from STAV. Thermal expansion varies linearly with temperature in the alpha phase ($300<T<1073\ K$) according to:

$$\frac{\Delta L}{L_0} = 4.44 \times 10^{-6} T - 1.24 \times 10^{-3} \tag{14-60}$$

and

$$\frac{\Delta D}{D_0} = 6.72 \times 10^{-6} T - 2.07 \times 10^{-3} \tag{14-61}$$

where:

$\frac{\Delta L}{L_0}$ = linear axial strain caused by thermal expansion (-),

L_0 = length at a reference temperature (m),

$\frac{\Delta D}{D_0}$ = diametric strain caused by thermal expansion(-),

D_0 = diameter of cladding at a reference temperature (m), and

T = temperature (K)

14.3.2 Zircaloy Cladding Elastic Moduli

Zircaloy cladding elastic moduli mainly depends on temperature, the fast neutron fluence, the amount of cold work, and the oxygen content. The following relations are selected for the STAV code.

[

]^{a,c}

[

]^{a,c}

The relationships used for calculations of C_{E1}, C_{G1}, C_2 and C_3 are:

$$C_{E1} = (6.61\times10^{11} + 5.912\times10^{8}\,T)\Delta \tag{14-66}$$

$$C_{G1} = (7.07\times10^{11} - 2.315\times10^{8}\,T)\Delta \tag{14-67}$$

$$C_2 = 1 \text{ or } \Phi < 1.0\times10^{22} \text{ [n/m}^2\text{]}$$

$$C_2 = 0.88 + 0.12\exp\left(-\frac{\Phi}{10^{25}}\right) \text{ for } \Phi \geq 1.0\times10^{22} \text{ [n/m}^2\text{]} \tag{14-68}$$

$$C_3 = -2.6\times10^{10}\,Ç \quad (3.23)$$

where:

Δ = kg oxygen/kg Zircaloy, is the average oxygen concentration minus oxygen concentration of as-received cladding and is default 0,

Φ = fast neutron fluence, ≥1 MeV [neutrons/m^2], and

$Ç$ = cold work [dimensionless ratio of areas], is default 0.

The standard error for Young's modulus is 6.4×10^9 Pa and for the shear modulus is 9×10^9 Pa.

Using these correlations, the temperature dependence of elastic moduli are plotted in Figure 14.3-1.

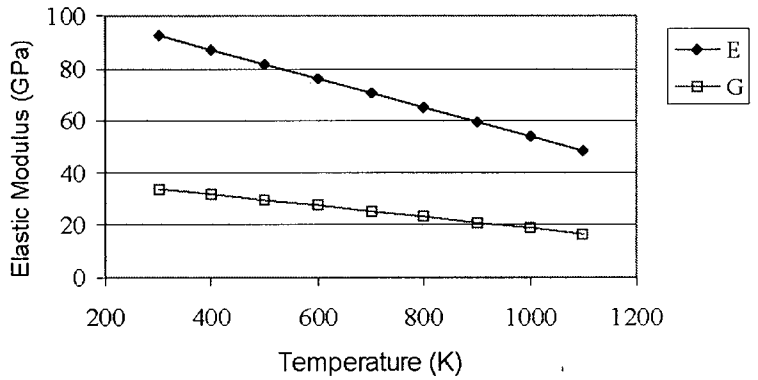

Figure 14.3-1. The Elastic Moduli of Zircaloy as a Function of Temperature for Unirradiated Material with Δ=0 ppm and $Ç$=0

14.3.3 Poisson's Ratio

Poisson's ratio for isotropic cladding, μ, is given by:

$$\mu = \frac{E}{2G} - 1 \tag{14-69}$$

where:

μ Poisson's ratio for isotropic cladding,
G Shear modulus for Zircaloy with random texture [Pa], and
E Young's modulus for Zircaloy with random texture [Pa].

and

$C_{E1}=C_{G1}=C_3=0$ in the equations for elastic moduli above.

14.3.4 Creep Deformation

[

]^{a,c}

14.3.5 Elastic Deformation

For a pipe cross-section, see Figure 14.3-2 for geometrical conditions.

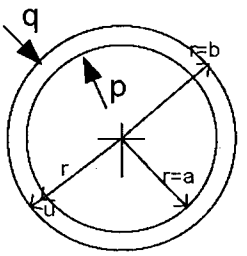

Figure 14.3-2. Fuel Tube, Geometrical Dimensions

Figure 14.3-2 Fuel Tube Geometrical Dimensions can be determined to be:

$$\frac{d}{dr}(r\sigma_r) - \sigma_\varphi = 0 \tag{14-71}$$

Together with a compatibility relationship as:

$$\varepsilon_\varphi + r\frac{d\varepsilon_\varphi}{dr} - \varepsilon_r = 0 \tag{14-72}$$

and together with Hooks general constitutive equations:

$$\varepsilon_r = \frac{1}{E}(\sigma_r - \upsilon\sigma_\varphi) \tag{14-73}$$

$$\varepsilon_\varphi = \frac{1}{E}(\sigma_\varphi - \upsilon\sigma_r) \tag{14-74}$$

The following differential equation can be set up:

$$r^2 \cdot \frac{d^2\sigma_r}{dr^2} + 3r\frac{d\sigma_r}{dr} = 0 \tag{14-75}$$

With the general solution:

$$\sigma_r = A + Br^{-2} \tag{14-76}$$

And boundary conditions as:

r=a then σ_r = p and r=b σ_r = -q

$$\sigma_r(r) = \frac{p\cdot(b^{-2} - r^{-2}) - q\cdot(a^{-2} - r^{-2})}{a^{-2} - b^{-2}} \tag{14-77}$$

$$\sigma_\varphi(r) = \frac{p\cdot(b^{-2} + r^{-2}) - q\cdot(a^{-2} + r^{-2})}{a^{-2} - b^{-2}} \tag{14-78}$$

And, finally, the displacement of the radius can be calculated (in the hoop direction there is no displacement due to symmetry in load), the radial displacement is:

$$u(r) = r\cdot\varepsilon_\varphi(r) \tag{14-79}$$

which is used for calculating the volume of the gas gap and the displacement of the inner radius of the cladding due to the pressure difference.

14.4 METAL – WATER REACTION MODEL

The reaction of zirconium a steam is treated using the correlation suggested by Baker and Just (Reference 14.2). The metal-water reaction model is coupled with the fuel rod deformation model. In case of rupture of the cladding the inside of the cladding can react. The metal-water reaction can occur in different fuel bundles for different rods depending on the actual core model.

The metal-water reaction model calculates the oxide thickness on the cladding surfaces. However, it does not alter the thermal properties of the cladding as the oxide layers develop. The model calculates the amount of hydrogen feed from each surface undergoing metal-water reaction, this hydrogen does not get included into POLCT-T hydraulic equations, nor does the steam being consumed get withdrawn from the steam mass balance.

The reaction rate between zirconium and steam is expressed as:

$$Zr + 2H_2O \rightarrow ZrO_2 + 2H_2 + \Delta E \tag{14-80}$$

The isothermal heat evolved, ΔE, for this reaction is about 6510 kJ/kg Zr reacted. There are two broad types of rate-limiting phenomena that can represent the mechanism for the oxidation of zirconium in a steam environment. They are:

- The gas-phase diffusion of steam from the bulk stream toward the cladding surface, through gaseous hydrogen which must diffuse away from the zirconium dioxide product layer.
- The solid-state diffusion of various ionic species through the zirconium dioxide product layer and into the base metal, a phenomena quantitatively expressed as the parabolic rate law.

In POLCA-T, the reaction is conservatively considered not to be steam limited. The parabolic rate law expressing the solid-state diffusion is taken as suggested by Reference 14.7. The power generated per unit length of rod is the energy released per mass reacted times the rate of cladding oxidation.

$$Q_{MWR} = \frac{\Delta E \rho_{Zr} \left(V_{Zr} / \Delta z \right)}{\Delta t} \tag{14-81}$$

where the zirconium density is 6560 kg/m^3 and the oxidation heat:

$\Delta E = 6.669 \cdot 10^6 - 257 \cdot T$ (J/kg) and temperature T in Kelvin.

The reacted cladding volume is calculated from the oxidation rate equation:

$$\frac{dr}{dt} = \frac{C1}{r} \cdot \exp\left[\frac{-C2}{T} \right] \tag{14-82}$$

Integrating the equation above gives the radius oxidized over time Δt. The volume per unit length oxided cladding is thus:

$$\frac{V_{Zr}}{\Delta z} = \left[2\pi \frac{2r_0}{r_1 + r_2} - 1\right] C_1 \cdot \exp\left[\frac{-C_2}{T}\right] \cdot \Delta t \quad (m^2) \qquad (14\text{-}83)$$

where r_0, r_1 and r_2 are respectively the outer cladding radius, initial oxidation front radius and final radius in time Δt. The default values of the constants are chosen to match the Baker-Just correlation. $C_1 = 3.937\ 10^{-5}\ m^2/s$, $C_2 = 2298.84$ K. The constants for Cathcart-Powel correlation $C_1 = 0.1126\ 10^{-5}$ and $C_2 = 18062.41$ K.

The power calculated by equation (14-81) is added in the cladding conduction calculation for the nodes between radius r_1 and r_2 depending where the oxidation front is located.

14.5 CLADDING RUPTURE MODEL

The criterion for rupture of a cladding tube is formulated as a burst stress which is compared with the true stress (from equation (14-78)). The burst stress is temperature dependent but also influenced by the thickness of the double layer of oxide and oxygen stabilized a-phase zircaloy and the oxygen concentration. The base formulation is taken from Reference 14.3.

$$\sigma_{B1} = a \cdot \exp(-b \cdot T) \qquad (14\text{-}84)$$

where:

a and b are temperature-dependent parameters.

For $T < T_\alpha$:

a = 705600 MPa
b = 0.00793 K^{-1}

At T = $T_{\alpha\beta}$ (= $1/2 \cdot (T_\alpha + T_\beta)$):

a = 3000 MPa
b = 0.003 K-1

For $T > T_\beta$:

a = 2300 MPa
b = 0.003 K^{-1}

The transition temperatures (T_α and T_β) are given by equations (14-89) and (14-90). The values for a and b in equation (14-84) are taken from Reference 14.8, except in the α region where a fit to data has been made.

Linear interpolation in ln(a) and b is used in the lower and upper halves of the α+β region.

The burst stress used in POLCA-T takes into account oxygen effects through a multiplier that is considered to account for the reduction in burst stress for the main metal, and through an additive term that accounts for the strength of the double layer.

$$\sigma_B = \sigma_{B1} \frac{\delta - \delta_{x\alpha}}{\delta} \cdot \exp\left(-C_s \cdot X^m\right) + \sigma_{x\alpha} \cdot \frac{\delta_{x\alpha}}{\delta} \tag{14-85}$$

where:

C_s	=	temperature dependent coefficient,
m	=	temperature dependent exponent,
X	=	total oxygen concentration defined by equation 14-103,
σx_α	=	burst stress of the double layer (oxide plus oxygen stabilized α-phase),
δ	=	actual cladding thickness (m), and
δx_α	=	thickness of the double layer (oxide plus oxygen stabilized α-phase).

The following relations are used for the parameters:

$$C_s = \begin{cases} 0. & T < T_\alpha \\ 95. \left(T - T_\alpha\right) / \left(T_\beta - T\right)_\alpha & T_\alpha \le T < T_\beta \\ 95. & T \le T \end{cases} \tag{14-86}$$

$$m = \begin{cases} 1. & T \lhd T_\beta \\ 1 \Big/ \left(1 + \left(T / T_\beta - 1\right)\right) \cdot 0.5 & T_\beta \le T \end{cases} \tag{14-87}$$

$$\sigma x_\alpha = 8577 \cdot \exp(-0.003 \cdot T) \quad \text{MPa} \tag{14-88}$$

The burst stress for the double layer has been determined from a data point in Reference 14.4 that implicitly gives the value 113 MPa at 1170 °C and assuming the same decay constant (b) as for β-phase zircaloy.

The burst stress and true stress are evaluated at each time step and compared in order to detect a rod burst.

14.5.1 Cladding Creep Model

The cladding creep is usually given by an (empirical) equation determining the creep rate (tangential strain rate). The creep rate is affected mainly by:

- Tangential stress in the cladding
- Temperature of the material
- Material properties

The material properties are temperature dependent and also dependent on the crystal structure of the cladding material. Furthermore, the properties are affected by the oxygen uptake (by oxidation and diffusion) that occurs at high temperatures.

Zircaloy cladding material exhibits two distinct crystal structures corresponding to two allotropic phases. At relatively low temperatures (less than approximately 800°C), the equilibrium phase corresponds to an anisotropic hexagonal-closed-packed (hcp) crystal structure. This phase is called the α-phase. At higher temperatures (approximately greater than 975°C), the equilibrium phase corresponds to an isotropic body centered cubic (bcc) crystal structures. This phase is called the the β-phase.

At high temperatures in steam atmosphere, the zircaloy cladding will oxidize. Furthermore, oxygen will diffuse into the zircaloy material. The zirconium oxide is brittle and may crack, especially if the cladding tube is strained. Oxygen that diffuses into the zircaloy will be present as interstitial defects. The effect of this is called an oxidation hardening, i.e., the cladding will be less prone to creep deformation. Diffusion of oxygen into the zircaloy will also cause a stabilization of the α-phase, i.e., it will exist even at temperatures higher than the aforementioned transformation temperature.

The model in POLCA-T for cladding burst gives a burst stress as a function of material properties and temperature. The influence of surface oxide and oxygen that has diffused into the zircaloy is accounted for. The burst stress is compared to the true actual stress to detect a rupture. The true actual stress is calculated as a function of the pressures inside and outside of the rod and the strained dimensions of the rod.

A comprehensive background to the area of high temperature deformation and failure of zircaloy tubes is given in Reference 14.5. There the evolution from methods based on correlations for engineering burst stress or burst strains to more mechanistic models are described.

The validation of the cladding strain model and comparison with the numerous experimental data can be found in Reference 14.4.

14.5.1.1 Basic Creep Model

The original formulation of the creep law in Reference 14.6 reads:

$$\dot{\varepsilon}_c = A\,\sigma^n \exp(-Q/RT) \qquad (14\text{-}89)$$

where:

$\dot{\varepsilon}_c$ = tangential strain rate = $d\varepsilon_c/dt$

σ = true tangential stress (based on actual dimensions)

A,n,Q = correlation parameters according to Reference 17.7

T = absolute cladding temperature (K)

R = general gas constant (8.31441 J/mol,K)

The values of the correlation parameters (A, n and Q) depends on the structural phase of the zircaloy. The structure or phase can be α, α+β, or β depending on the temperature. The transition temperature between α and α + β is:

$$T_\alpha = 1085.15 + 14.28\,(dT/dt)^{0.28} \quad (K) \tag{14-90}$$

and the transition temperature between α +β and β is:

$$T\beta = 1248.15 \quad (K) \tag{14-91}$$

In the α-phase (i.e. for $T< T_\alpha$), the material is anisotropic and the following parameter values are used in equation (14-89):

$$\begin{aligned} &A = 11616\ MPa^{-5.89}/s \\ &n = 5.89 \\ &Q = 321000 + 24.69\,(T-923.15)\ J/mol \end{aligned} \tag{14-92}$$

In the β -phase (i.e. for $T>T\beta$), the material is isotropic and the following parameter values are used in equation (14-89):

$$\begin{aligned} &A = 8.719\ MPa^{-3.78}/s \\ &n = 3.78 \\ &Q = 141919\ J/mol \end{aligned} \tag{14-93}$$

In the α +β region (i.e. $T_\alpha \leq T \leq T\beta$), two different methods of interpolation are used to calculate A, n, and Q depending on a formal strain rate:

$$d\varepsilon_O/dt = 0.24 \cdot 0.6194 \cdot \sigma^{2.33} \cdot \exp(-102366/(RT)) \tag{14-94}$$

If $d\varepsilon_O/dt \leq 0.003$, then a two-region linear interpolation is made for ln (A), n, and Q from T_α to $T_{\alpha\beta}$ and from $T_{\alpha\beta}$ to $T\beta$ where $T_{\alpha\beta}$ is:

$$T_{\alpha\beta} = 1/2 \cdot (T_\alpha + T\beta) \tag{14-95}$$

and at $T_{\alpha\beta}$:

$$\begin{aligned} &A = 0.24 \cdot 0.6194\ MPa^{-2.33} \cdot s^{-1} \\ &n = 2.33 \\ &Q = 102366\ J/mol \end{aligned} \tag{14-96}$$

If $d\varepsilon_O/dt > 0.003$, then a two-region linear interpolation is made for ln(A) whereas n and Q are calculated through linear interpolation from T_α to $T\beta$. At $T_{\alpha\beta}$:

$$A = 29.2 \cdot 1.2497\ MPa^{-4.835}\ s^{-1} \tag{14-97}$$

14.5.1.2 Calculation of True Stress

The true stress used in equation (14-89) is based on the actual strained dimensions of the cladding taking into account both creep and thermal deformation. Given the creep and thermal strains and also the thickness of the oxide scale (ε_c, ε_t and δ_{ox}), the cladding inside radius, cladding thickness and cladding outside radius are calculated from:

$$r_{co} = (1 + \varepsilon_c + \varepsilon_t) r_{cio} \tag{14-98}$$

$$\delta = \left(\frac{1}{1+\varepsilon_c} + \varepsilon_t\right) \cdot \left(\delta_o - \frac{\delta_{ox}}{1.477}\right) + \frac{\delta_{ox}}{1+\varepsilon_c} \tag{14-99}$$

$$r_{co} = r_{ci} + \delta \tag{14-100}$$

where:

r_{cio} = nominal cladding inside radius, and
δ_o = nominal cladding wall thickness.

The true tangential stress is obtained from a force balance on half of the cladding tube:

$$\sigma = (P_i \cdot r_{ci} - P_o \cdot r_{co}) / \delta \tag{14-101}$$

or more exact by equation (14-78).

14.5.1.3 Modified Creep Law

The creep law just described has been modified to account for the effect of oxidation that is apparent when the model is compared to data from high temperature creep tests in steam atmosphere. When zircaloy comes into contact with steam at high temperature (above 800-900°C), a scale of zirconium oxide is formed on the surface and also a layer of oxygen-rich α-phase metal is formed beneath the oxide. This layer does not change the crystallic structure when it is heated above T_α but, instead, it retains the α-phase structure at all temperatures. The α-phase is said to be oxygen stabilized. Some oxygen will also be dissolved in the main metal body beneath the stabilized layer.

The presence of oxygen in the material markedly reduces the creep rate. To account for this, it has been assumed that both the thickness of the double layer of oxide and stabilized α-phase and the oxygen concentration in the main metal affects the rate of strain. The double layer is assumed to have a hardening effect only for a combined thickness greater than 15 μm in accordance with experimental observations in Reference 14.8 of the crack pattern. The concentration of oxygen in the main metal is assumed to influence the creep rate at all levels of concentration.

The modification of the equation (14-88) is made by substituting the true stress with an effective stress, which is equal the true stress divided by a correction factor:

$$\sigma_{eff} = \sigma / (1 + C_c \cdot X^{n_c} + C_\alpha \cdot (\delta_{x\alpha} / \delta_O)^{n_\alpha}) \quad (14\text{-}102)$$

where

X	=	mass concentration of oxygen in the cladding.
C_c	=	temperature dependent coefficient.
n_c	=	temperature dependent exponent.
$\delta_{x\alpha}$	=	thickness of the double layer (oxygen stabilized plus oxide) minus 15 μm i.e.:
$\delta_{x\alpha}$	=	max (δ_{ox} + δ_α - 15 μm, 0).
C_α	=	hardening coefficient (temperature dependent).
n_α	=	temperature dependent exponent.

The following relations are used for the parameters in equation (14-102):

$$X = \frac{G_{tot}}{\delta \cdot \rho_{zr}} - 0.0012 \quad (14\text{-}103)$$

where:

G_{tot}	-	total oxygen uptake (kgm^{-2}),
ρ_{zr}	-	zirconium density (6490 kgm^{-3}), and
δ	-	actual cladding thickness (m).

$$C_c = \begin{cases} 34 & T \le T_\alpha \\ 34 + (145-34)\cdot(T-T_\alpha)/(T_{\alpha\beta}-T_\alpha) & T_\alpha \le T < T_{\alpha\beta} \\ 145 + (390-145)\cdot(T-T_{\alpha\beta})/(T_\beta-T_{\alpha\beta}) & T_{\alpha\beta} \le T < T_\beta \\ 390 / (1+4\cdot(T/T_\beta-1)^{0.5}) & T_\beta \le T \end{cases} \quad (14\text{-}104)$$

$$n_c = \begin{cases} 0.85 / (1 + 6\cdot(1-T/T_\alpha)) & T < T_\alpha \\ 0.85 + 0.15\cdot(T-T_\alpha)/(T_\beta-T_\alpha) & T_\alpha \le T < T_\beta \\ 1 & T_\beta \le T \end{cases} \quad (14\text{-}105)$$

$$C_\alpha = \begin{cases} 25 & T < T_\beta \\ 25 + (T/T_\beta-1)\cdot(-69.2308+(T/T_\beta-1)\cdot 133.136) & T_\beta \le T \end{cases} \quad (14\text{-}106)$$

$$n_\alpha = \begin{cases} 0.5 & T < T_\beta \\ 0.5 + (T/T_\beta - 1)\cdot 3 & T_\beta \le T \end{cases} \qquad (14\text{-}107)$$

The functional relations for C_c and n_c has been determined from data in Reference 14.7 up to the β-transition. Above that temperature, some data from internal overpressure transients in Reference 14.8 have been used in the development.

14.5.1.4 Steam – Metal Reaction Kinetics

Calculation of the cladding creep strain and the rupture stress require the calculation of oxygen uptake by the zircaloy both by oxidation and by diffusion (see Sections 14.5.1 and 14.5 about cladding creep and the cladding rupture model).

The growth of the oxide-layer, the growth of the oxygen stabilized α-layer and the rate of total oxygen uptake are all calculated using parabolic rate laws:

$$\tau \cdot d\tau/dt = C_1 \cdot \exp(-C_2/T) \cdot (1 + C_3 \cdot \varepsilon_c)^2 \qquad (14\text{-}108)$$

Here τ represents any of the quantities in Table 14.5-1 which also specifies the numerical values of the constants C1, C2, and C3. They are taken from Reference 14.3.

Table 14.5-1. Table of Constants for the Parabolic Rate Law, Equation 14-108

Quantity τ	C_1	C_2	C_3
Oxygen uptake (kgm^{-2}) (G_{tot})	26.21 $kg^2m^{-4}s^{-1}$	20962 K	1.208
Oxide layer (m) (δ_{ox})	$3.92 \cdot 10^{-6}$ m^2s^{-1}	20214 K	0
Oxygen stabilized α-layer (m) ($\delta\alpha$)	$25.4 \cdot 10^{-6}$ m^2s^{-1}	21922 K	0

14.6 REFERENCES

14.1 "Fuel Rod Design Methods for Boiling Water Reactors," CENPD-285-P-A (proprietary), CENPD-285-NP-A (non-proprietary), July 1996.

14.2 L. Baker, L. C. Just, "Studies of Metal-Water Reactions at High Temperatures: III Experimental and Theoretical Studies of the Zirconium Water Reaction," ANL-6548, 1962.

14.3 S. Leistikow, G. Schantz, "Oxidation Kinetics and Related Phenomena of Zircaloy-4 Fuel Cladding Exposed to High Temperature Steam and Hydrogen-Steam Mixtures Under PWR Accident Conditions," Nuclear Engineering and Design 103 (1987) 65-84.

14.4 ABB ATOM Report RPB 88-108, 89-05-30, "Models for Zircaloy Cladding Tube Creep and Rupture Following a Loss-of-Coolant Accident in a BWR".

14.5 Y. R. Rashid, "Transient Failure of Zircaloy Cladding, Nuclear Engineering and Design 101" (1987) 305-313.

14.6 F. J. Erbacher, H. J. Neitzel, H. Rosinger, H. Schmidt, H. Wiehr, "Burst Criterion of Zircaloy Fuel Claddings in a Loss-of-Coolant Accident," Zirconium in the Nuclear Industry; Fifth Conf. ASTM STP 754.

14.7 M. E. Markiewicz, F. J. Erbacher, "Experiments on Ballooning in Pressurized and Transiently Heated Zircaloy-4 tubes," KfK 4343, February 1988.

14.8 T. Jonsson, Y. Haag, C. Wikström, "Kapslingsbeteende vid LOCA-transienter upp till 1300, C," Studsvik report NF(P) - 81/64.

15 SPECIAL PROCESS MODELS

15.1 CRITICAL FLOW MODEL

The POLCA-T code is based on the Moody critical flow model for two-phase break flow with frozen mixture between phases and homogenus flow conditions. The slip between phases is equal to unity.

The break mass flow rate is calculated for a given coolant state (pressure, p_0, enthalpy, h_0, and if applicable, water level) at the break, receiver (downstream) pressure, break area, and flow loss coefficient. For guillotine pipe breaks, the two break locations are specified and the flow path connecting the two pipe sections is closed off.

Critical flow checks may also be specified for any flow path. For a flow path being checked, the evaluated mass flow rate is compared to the mass flow rate calculated by the critical flow model and limited to this value if warranted.

Critical Flow

This model is described in References 15.1 and 15.2.

The assumptions used in the model, which includes friction in the pipe, are:

1. Straight pipe with constant flow area and adiabatic walls
2. Steady flow, isentropic flow
3. Annular flow without entrainment and liquid in contact with the wall
4. Liquid and vapor in thermodynamic equilibrium at any section, homogenus flow conditions for the two-phase flow
5. Uniform and linear velocities of each phase
6. No phase transfer, frozen flow

Subcritical Flow

For receiver pressures, p_B, greater than the pipe exit pressure base on critical flow, p_2, the mass flow rate is calculated from:

$$G = \frac{2\,(p_0 - p_B)\;\rho_0(p_0,h_0)}{1 \div \xi} \qquad (15\text{-}1)$$

where ξ is the flow resistance of the pipe (i.e., the subcritical flow is calculated by the regular momentum equation between volume cells.) If the vessel pressure is less than the receiver pressure, p_B, it is assumed than saturated steam is entering the vessel from the surroundings.

15.2 PRESSURE RELIEF VALVE SYSTEM

A series of relief, safety, and controlled depressurization valves can be located on the steam lines of a BWR. Several of these valves may be associated with the ADS. All these valves can be simulated in POLCA-T (together with SAFIR), or by the built-in control functions in POLCA-T, the PM09xx models. The valve model includes the capability to simulate delay times in opening and closing, force open and force close signals, low-power close interlocks, and a programmed controlled opening, as in the control depressurization valves.

15.3 REFERENCES

15.1 F. S. Moody, "Maximum Flow Rate of a Single Component, Two-Phase Mixture" ASME Paper 64-HT-35, August, 1964.

15.2 F. J. Moody, "Introduction to Unsteady Thermofluid Mechanincs" Wily-Interscience, ISBN-0-471-85705-X, 1990.

16 CONTROL SYSTEM MODEL

In POLCA-T, there are different ways to add and use a control system to a computational model. Essentially, one can distinguish between explicit control system and implicit control system functions.

16.1 DIGITAL CONTROL SYSTEM SIMULATION PACKAGE

Digital control system simulation is available with POLCA-T. The package SAFIR simulates a digital control system and is implemented in POLCA-T for explicit control system evaluation. The overall control logic, algorithms, structure of control blocks, and logic, etc. in SAFIR is similar to most industrial digital control systems. That means that control systems buildup in the plants can be well simulated with the code package.

16.2 IMPLICIT CONTROL SYSTEM

The implicit control system in POLCA-T is mainly used to simulate minor control system and a system that is used to create steady state. In that case, the controllers are automatically discarded after steady state has been reached, if the user opts for it.

The term implicit control system implies that the control equation used is a part of the entire equation system and is solved simultaneously together with the state vectors for the computational problem.

The building blocks for control are limited to the following functions:

- Proportional integrator (PI) controller
- Mathematical measurement of state variables

PI Controller

$$\Im = (\text{SETPNT} - y)\cdot G - \tau\frac{\partial y}{\partial t} \qquad (16\text{-}1)$$

where:

SETPNT	=	is the setpoint value output signal,
y	=	is the in signal,
G	=	is the gain factor, and
τ	=	is time constant

in addition, the derivatives of each signal with respect to its dependency, (i.e., the Jacobian) is required.

[

]a,c

17 SUPPORTING METHODS

17.1 TIME STEP CONTROL AND ACCURACY

A variety of checks on solution acceptability are used to control the time step. These include material Courant limit checks, material properties out of defined ranges, and water steam gas property error and ranges. Checks are also made for very fast disturbances so the code is able to follow the disturbance.

Time Step

The time steps in a transient are calculated by the code and set within the bounds specified by the user. Start time step is also specified by the user as well as final time of the simulation.

In some cases, it can be useful to have the time step selected so it follows a disturbance exactly. The user can opt for this automatic adjustment to disturbance knots. The time step decreases if the accuracy within a specified number of allowed iterations are not fulfilled for each state variable.

Accuracy

[

]^{a,c}

Time Integration Method

By default, the time integration method for the state variables is fully implicit, theta factor equal to unity, which is a first order method to integrate in time. However, the practice in using the code is to use second order time integration by specifying the theta factor close to 0.5 (References 17.1 and 17.2).

17.2 REFERENCES

17.1 D. A. Anderson, John C. Tannehill, Richard H Pletcher, "Computional Fluid Mechanics and Heat Transfer," Mc Graw-Hill Book Company, 1984.

17.2 U. Bredolt, On the Time Integration Method an Its Impact on Prediction of Hydraulic Stability by the POLCA-T Code," International Conference on Nuclear Engineering, ICONE 15, 2007 (to be published).

18 COMPONENT MODELS

This chapter describes the models of different plant components.

18.1 PUMPS

18.1.1 Turbo Pumps

The behavior of the main recirculation line reactor coolant pumps is modeled for single- and two-phase flow conditions under normal operation and coastdown conditions.

Pump Speed and Torque

The behavior of the main recirculation pump is modeled by the conservation of angular momentum

$$I\frac{d\omega}{dt} = T \tag{18-1}$$

where:

ω = angular velocity,
t = time,
T = net torque on the shaft, and
I = mass momentum of inertia.

The difference formulation of equation (18-1) is:

$$\frac{\omega^{n+1} - \omega^{n}}{\Delta t} - \frac{T^{n+1}}{I} = 0 \tag{18-2}$$

The pump equation is solved at every time step simultaneously with the basic conservation equations.

The net torque, T, is calculated as,:

$$T = T_m - T_{hyd} + T_{fric} \tag{18-3}$$

The torque T represents the net torque on the pump impeller. It consists of three components:

- The hydraulic component of torque, T_{hyd}, due to the interaction between the fluid and the pump impeller
- The friction component of the torque, T_{fric}, due to friction losses in the bearing and rotating machinery
- The third component, the pump motor torque or drive torque, T_m

The pump motor torque is evaluated at the initial time, when the pump speed is constant and there is no net torque on the pump impeller (See equation (18-1)). Thus:

$$T_m(t) = T_{hyd}(t=0) - T_{fric}(t=0) \quad (18\text{-}4)$$

This value for $T_m(t)$ is maintained until the pumps are disturbed at a time specified by the user.

The user inputs homologous curves for hydraulic torque as four tables of dimensionless hydraulic torque versus the ratio between dimensionless flow and speed (or its reciprocal). The tabulated curves are:

Table	Independent Variable	Dependent Variable	Usage Criteria
1	ν/α	β/α^2	$\lvert\alpha\rvert \geq \lvert\nu\rvert$, $\alpha \geq 0$
2	a/ν	β/ν^2	$\lvert\alpha\rvert < \lvert\nu\rvert$, $\nu < 0$
3	ν/α	β/α^2	$\lvert\alpha\rvert \geq \lvert\nu\rvert$, $\alpha < 0$
4	a/ν	β/ν^2	$\lvert\alpha\rvert < \lvert\nu\rvert$, $\nu \geq 0$

where

β = T_{hyd} / T_{hydref} (torque ratio)

T_{hydref} is the hydraulic reference torque.

ν = Q / Q_{ref} (flow ratio)

Q_{ref} is the volumetric flow reference.

α = ω / ω_{ref} (speed ratio)

ω_{ref} is the speed reference value.

For a specified volume flow, Q, through the pump and a specified pump speed, ω, the dimensionless hydraulic torque is calculated by quadratic interpolation from the appropriate table.

The absolute hydraulic torque is then calculated from:

$$T_{hyd} = \beta \cdot T_{hydref} - \left(\frac{\rho}{\rho_{ref}}\right) \quad (18\text{-}4)$$

where

ρ = density of fluid in the pump, and
ρ_{ref} = reference pump fluid density.

The friction torque, T_{fric}, is calculated by:

$$T_{fric} = \begin{cases} HC_2 \cdot (\omega^{n+1})^2 \cdot \psi \text{for} \mid \omega^{n+1} \mid > HC_3 \\ HC_4 \cdot \psi \text{for} \mid \omega^{n+1} \mid = HC_3 \end{cases} \quad (18\text{-}5)$$

where

$$\psi = = \begin{cases} +1 \text{ for } \omega^n < 0 \\ -1 \text{ for } \omega^n \geq 0 \end{cases} \quad (18\text{-}6)$$

The constants HC_2, HC_3, HC_4, and HC_5 are user-specified constants and represent the friction torque coefficient (HC_2) at angular speeds greater than HC_3 and the friction torque (HC_4) when the angular speed is less than HC_3. The constant HC_5 is the friction torque that must be overcome to start the pump from zero speed, as shown in Figure 18.1-1.

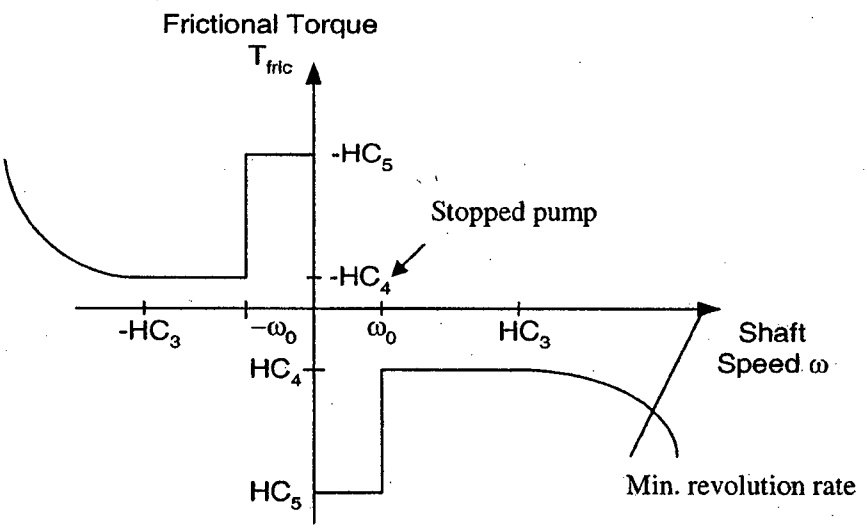

Figure 18.1-1. Frictional Torque Versus Shaft Speed

If the pump speed at the earlier time step (ω^n) was less than a user-specified value (ω_0), the pump will stop. Only if the hydraulic torque is greater than the maximum friction torque at rest (HC_5), will the pump start running again.

The friction torque as a function of the pump speed is shown in the Figure 18.1-1.

Pump Hydraulic Head

The momentum equation of the control volume containing the pump includes a term for the pump head (see equation (7-56)). The user inputs homologous curves for head as four tables of dimensionless pump head versus ratio between dimensionless flow and speed (or its reciprocal). The tabulated curves are:

Table	Independent Variable	Dependent Variable	Usage Criteria
1	ν/α	h/α^2	$\lvert\alpha\rvert \geq \lvert\nu\rvert,\ \alpha \geq 0$
2	α/ν	h/ν^2	$\lvert\alpha\rvert < \lvert\nu\rvert,\ \nu < 0$
3	ν/α	h/α^2	$\lvert\alpha\rvert \geq \lvert\nu\rvert,\ \alpha < 0$
4	α/ν	h/ν^2	$\lvert\alpha\rvert < \lvert\nu\rvert,\ \nu \geq 0$

where:

$h = H / H_{ref}$ (head ratio)

H_{ref} is the hydraulic reference head.

$\nu = Q / Q_{ref}$ (flow ratio)
$\alpha = \omega / \omega_{ref}$ (speed ratio)

For a specified volume flow, Q, and pump speed, ω, the dimensionless hydraulic head is calculated by quadratic interpolation from the appropriate table.

The absolute pump head is then calculated from:

$$\Delta p_{pump} = g \cdot \rho_{pump} \cdot (h \cdot H_{ref} - HC_{10} \cdot Q \cdot |Q|) \quad (18\text{-}7)$$

where HC_{10} is the pump diffuser head loss coefficient.

Two-Phase Pump Behavior

A user-specified set of homologous differential head curves and a two-phase multiplier determine the pump head under two-phase flow conditions, which is a function of void fraction. The two-phase dimensionless head is then calculated from:

$$h_{2\Phi} = h_{1\Phi} - M(\alpha) \cdot h_D \quad (18\text{-}8)$$

where $M(\alpha)$ is the tabulated multiplier and h_D is the difference between the single and two-phase pump head at a reference void fraction. The single-phase head, $h_{1\Phi}$ is calculated as described in the previous section. This formulation is adapted from Reference 18.1.

The two-phase pump head is then calculated from equation (18-8).

18.1.1.1 Simplified Turbo Pump Model

A simplified turbo pump model is available in the POLCA-T code. The simplification is mainly the input to the model. Instead of providing a full set of homologous data, a set of data for the first quadrant of pump characteristics is enough. The pump performance, flow rate, pump head and torque for the other quadrants are calculated by the model (Reference 18.2).

18.1.2 Jet Pumps

Figure 18.1-2 is an outline of a jet pump where a definition of the main parts are made.

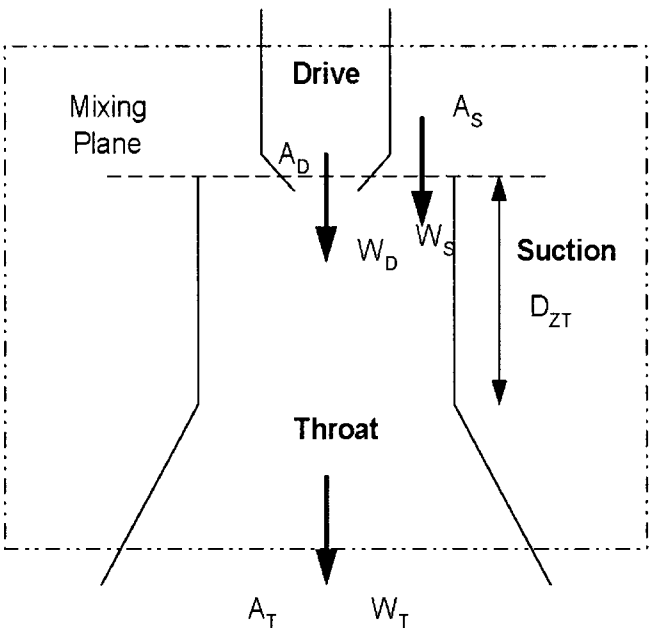

Figure 18.1-2. Outline of a Jet Pump

The main parts are:

- Drive is the nozzle where the drive mass flow rate, W_D, is injected from the drive pumps, and can be characterized by an area A_D.
- In the mixing plane where the recirculation mass flow rate, W_S starts to mix with the drive flow, an area is defined with an area A_S.
- The suction part of the pump is defined by its length, D_{ZT}.
- The throat of the pump where a pressure recovery is made is defined by the area A_T and the mass flow rate W_T.

The momentum equation for the jet pump drive and suction flow paths are modified to account for the momentum exchange between the two flow paths (Reference 18.1), as shown in Figure 18.1-2.

The temporal acceleration term in equation (7-37) for the drive flow path is:

$$\int_{x_D}^{x_T} \frac{1}{A}\frac{dW}{dt}\,dx = \int_{x_D}^{x_M} \frac{1}{A}\frac{dW}{dt}\,dx + \int_{x_M}^{x_T} \frac{1}{A}\frac{dW}{dt}\,dx \tag{18-9}$$

$$= \frac{dW_D}{dt}\cdot\int_{x_D}^{x_M}\frac{1}{A_{DN}}\,dx + \frac{dW_D}{dt}\cdot\int_{x_M}^{x_T}\frac{1}{A_D}\,dx + \frac{dW_S}{dt}\cdot\int_{x_M}^{x_T}\frac{1}{A_S}\,dx$$

$$= I_D\cdot\frac{dW_D}{dt} + I_S\cdot\frac{dW_S}{dt} \tag{18-10}$$

[

]^{a,c}

For the drive and suction flows, the spatial acceleration term, equation (7-48), is also modified to account for the increased mixing losses in the throat region when a density difference exists between the drive and suction fluids. The spatial acceleration term for the drive flow is:

$$\int_{x_D}^{x_T}\frac{1}{A}\cdot\frac{\partial}{\partial x}\left(\frac{W^2}{\rho A}\right)dx = \int_{x_D}^{x_M}\frac{1}{A}\cdot\frac{\partial}{\partial x}\left(\frac{W^2}{\rho A}\right)dx + \int_{x_M}^{x_T}\frac{1}{A}\cdot\frac{\partial}{\partial x}\left(\frac{W^2}{\rho A}\right)dx$$

$$= \frac{W^2}{\rho_D}\cdot\left(\frac{1}{A_D{}^2} - \frac{1}{A_{DN}{}^2}\right)\frac{1}{A_T}\cdot\left(\frac{W_T{}^2}{\rho_T A_T} - \frac{W_S{}^2}{\rho_S A_S} - \frac{W_D{}^2}{\rho_D A_D}\right)\cdot f_1\cdot f_2 \tag{18-13}$$

where

$$f_1 = \begin{cases} 1 & W_D > 0 \\ 0 & W_D \leq 0 \end{cases} \tag{18-14}$$

and the factor f_2 accounts for the additional mixing losses due to the density difference between the suction and drive flow. The factor f_2 has been calculated by solving the momentum equation in the jet pump throat for two adjacent streams of differing density. This analytical result has been correlated, for a range or jet pump flow and density differences, by

$$f_2 = \begin{cases} \dfrac{a_1 (1+a_2) \cdot (\rho_D/\rho_S)}{a_2 + (\rho_D/\rho_S)} & \text{for } \rho_D/\rho_S > 1 \\ \dfrac{a_1 (1+a_2) \cdot (\rho_S/\rho_D)}{a_2 + (\rho_S/\rho_D)} & \text{for } \rho_D/\rho_S \leq 1 \end{cases} \tag{18-15}$$

where $a_1 = 0.933$ and $a_2 = 0.78$.

The spatial acceleration for the suction flow path is analogous to equation (18-16).

18.2 STEAM SEPARATOR

Figure 18.2-1 shows an outline of a steam-water separator.

18.2.1 Definition of Carryover and Carryunder

For a known inlet steam and water flow rates and user-specified water carryover, CO, and steam carryunder, CU, fractions, the phase separation can be calculated.

The carryover and carryunder are defined as:

The carryover

$$CO = \frac{W_{liq,s}}{W_{gas,s}} = \text{water flow / total upward steam flow} \tag{18-16}$$

The carryunder

$$CU = \frac{W_{gas,p}}{W_{liq,p}} = \text{steam flow / total downward water flow} \tag{18-17}$$

where the subscript s is secondary flow path and p is primary flow path, as shown in Figure 18.2-1.

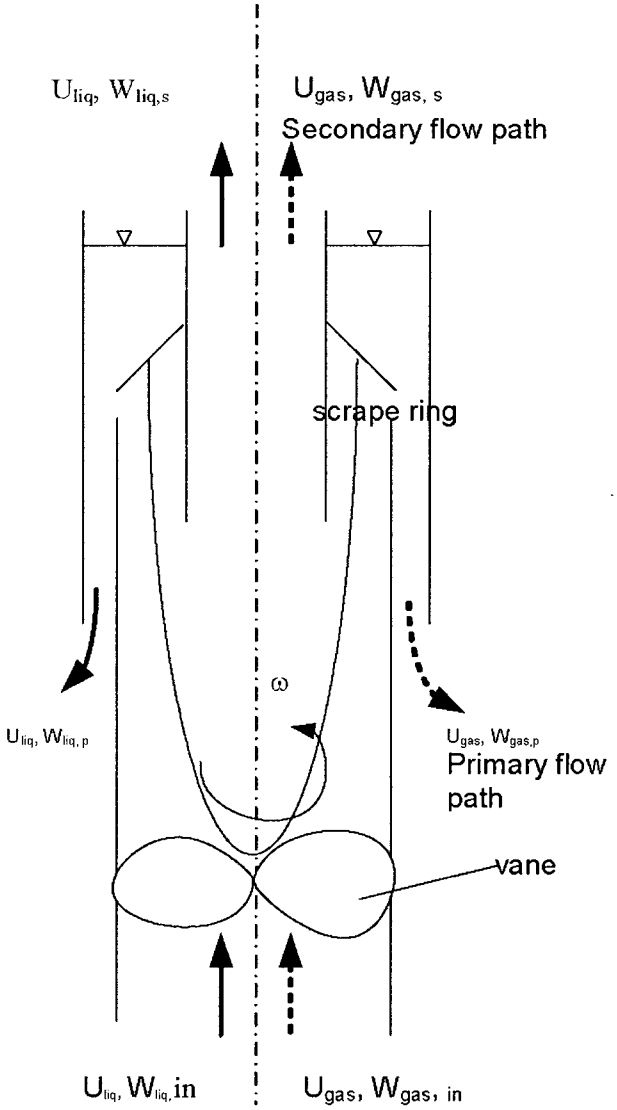

Figure 18.2-1. Principles of Steam Separation in a BWR

18.2.2 Mechanistic Separator Model

[

]^{a,c}

[

]^{a,c}

a,b,c

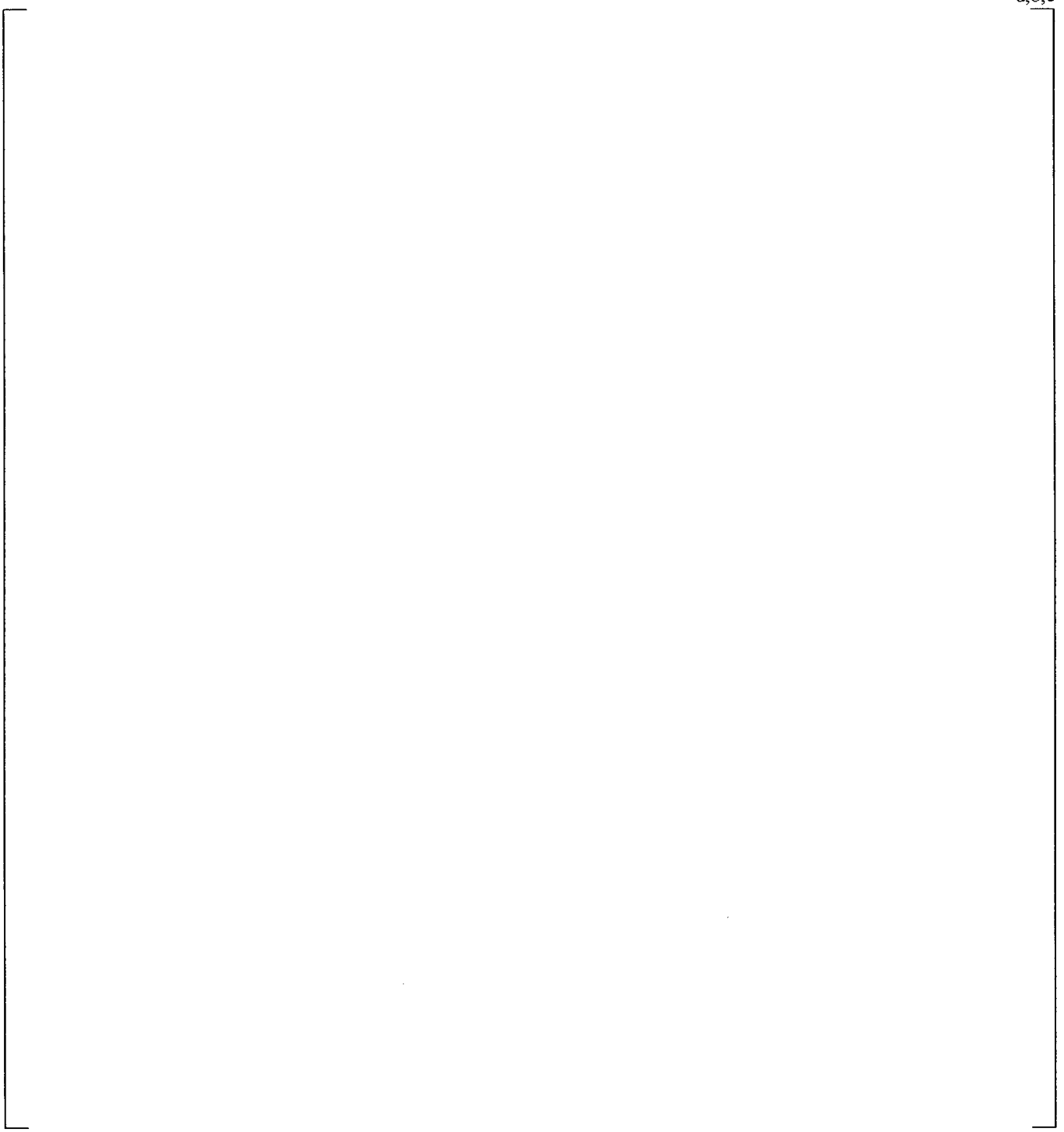

Figure 18.2-2. [ ]^{a,c}

a,b,c

[

]

Figure 18.2-3. [ ][a,c]

[

]

]

[

]^{a,c}

18.3 DRIVE DEVICE

18.3.1 Asynchronous Motor

Figures 18.3-1 and 18.3-2 show the characteristic view of an asynchronous electrical motor torque versus frequency or revolution rate.

Close to zero slip, the drive torque is almost linear. For a large asynchronous motor, a good approximation of the drive torque is equal to (Reference 18.2):

$$T = T_{max} \cdot \frac{2 s s_m}{s_m^2 + s^2} \tag{18-21}$$

where:

s = slip,

s_m = motor constant, small for large motors < 0.1,

$$s_m = \frac{R_2}{X_{20}} \propto \frac{R_2}{f}$$

T = torque, and
T_{max} = maximal torque.

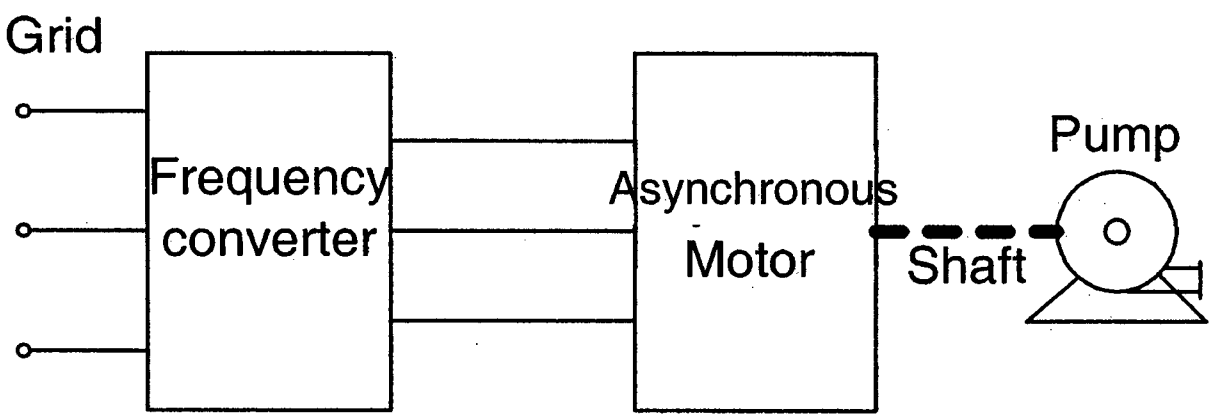

Figure 18.3-1. Principal Drive Equipment for a Pump

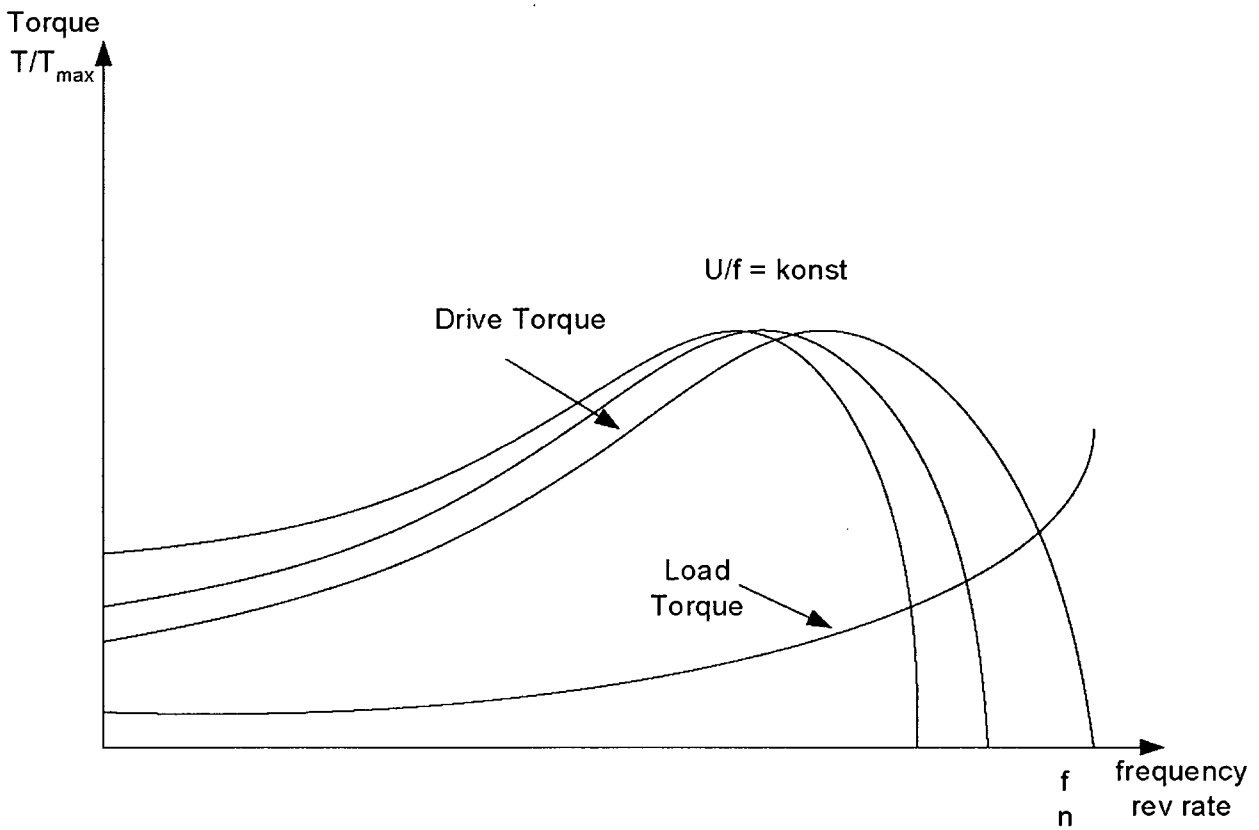

Figure 18.3-2. Torque Versus Rev Rate for Asynchronous Motor

$$T_{max} = k\frac{U^2}{f^2} \tag{18-22}$$

U	grid voltage
X_{20}	reactance for the core bobbin at frequency f
R2	rotor resistance for each phase

Within the normal operational area for the motor is the slip s small compared to motor constant s_m, $s^2 << s_m^2$.

The slip dependency on the controlling frequency can be written as:

$$s = 1 - \frac{\omega}{\omega_0}\frac{f_0}{f} \tag{18-23}$$

$$T = C \cdot \frac{U^2}{f^2} \cdot \frac{2 s s_m}{s_m^2 + s^2} = C_{motor} \cdot \frac{U^2}{f} \cdot s \tag{18-24}$$

where:

C_{motor} is a constant for each motor type and size,
f is the converter frequency,
U is the voltage from converter, and
T is the torque from the motor.

18.4 REFERENCES

18.1 "Water Reactor Emergency Core Cooling System Evaluation Model: Code Description and Qualification RPB 90-93-P-A (Proprietary), October, 1991."

18.2 D. Babala, "A Fast Semi-Implicit Integration Method for Thermohydraulic Networks." Trans. Am. Soc., 47, 295-7, 1984."

19 SOLUTION METHOD

The mass, momentum, energy, and state equations along with the pump speed equations are solved simultaneously using Newton's method. The Jacobian matrix includes all derivatives and is inverted using a sparse matrix technique (Reference 19.1).

The rod and slab conduction equations are solved by Gaussian elimination and back substitution. The conduction equation and the surface heat transfer are solved iteratively for the surface temperature. The kinetics model is solved using a second order integration method.

The hydraulic model is solved at different grades of implicitness, ranging from 1,0 to 0,5, defined by the user, with time. Thermal conduction and heat transfer models are also solved implicitly with time. The hydraulic and conduction solutions are coupled through the surface heat transfer. The hydraulic fluid conditions are treated implicitly in the heat conduction and heat transfer solution. The surface heat transfer, however, is treated explicitly in the hydraulic solution.

19.1 NUMERICAL SOLUTION

Several numerical methods are employed in POLCA-T to solve the power generation, hydraulic, and heat conduction/transfer models. A simplified flow chart of the calculation sequence is shown in Figure 19.1-1.

After initialization of the problem, the first quantities evaluated for each calculation time step are the boundary conditions (e.g., ECCS flow rates) and power generation. The reactor kinetics model, used in evaluating the power generation, is solved by an improved Gauss-Seidel iteration method, NEU3.

Next the hydraulic model is solved iteratively for the primary variables. The hydraulic problem is solved by a simultaneous solution of the conservation equations and pump speed equations using methods described in Sections 7 and 6.

The primary variables are pressure, p, void, α, temperatures, T_{gas}, T_{liq}, of the phases, gas and liquid velocities, u_{gas}, u_{liq}, boron concentration, C_{bor}, and partial pressure p_{nc} of the non-condensable gases, if any. Secondary variables are calculated from supporting expression where the primary variables can be a part of, which is normally made after each completed and accepted time step. Variable transient time step logic based on the transient hydraulics is used to optimize the computational time. If the hydraulic problem does not converge the time step is reduced and the calculation restart from the last accepted time step.

The heat transfer is solved together with the linearized heat conduction. Once the hydraulic problem is solved, the coolant state is used in finding the solution of the rod and the heat structure heat conduction problems. The convective and radiate heat fluxes are then calculated from the known temperatures and heat transfer coefficient.

The calculation procedure is outlined in Figure 19.1-1.

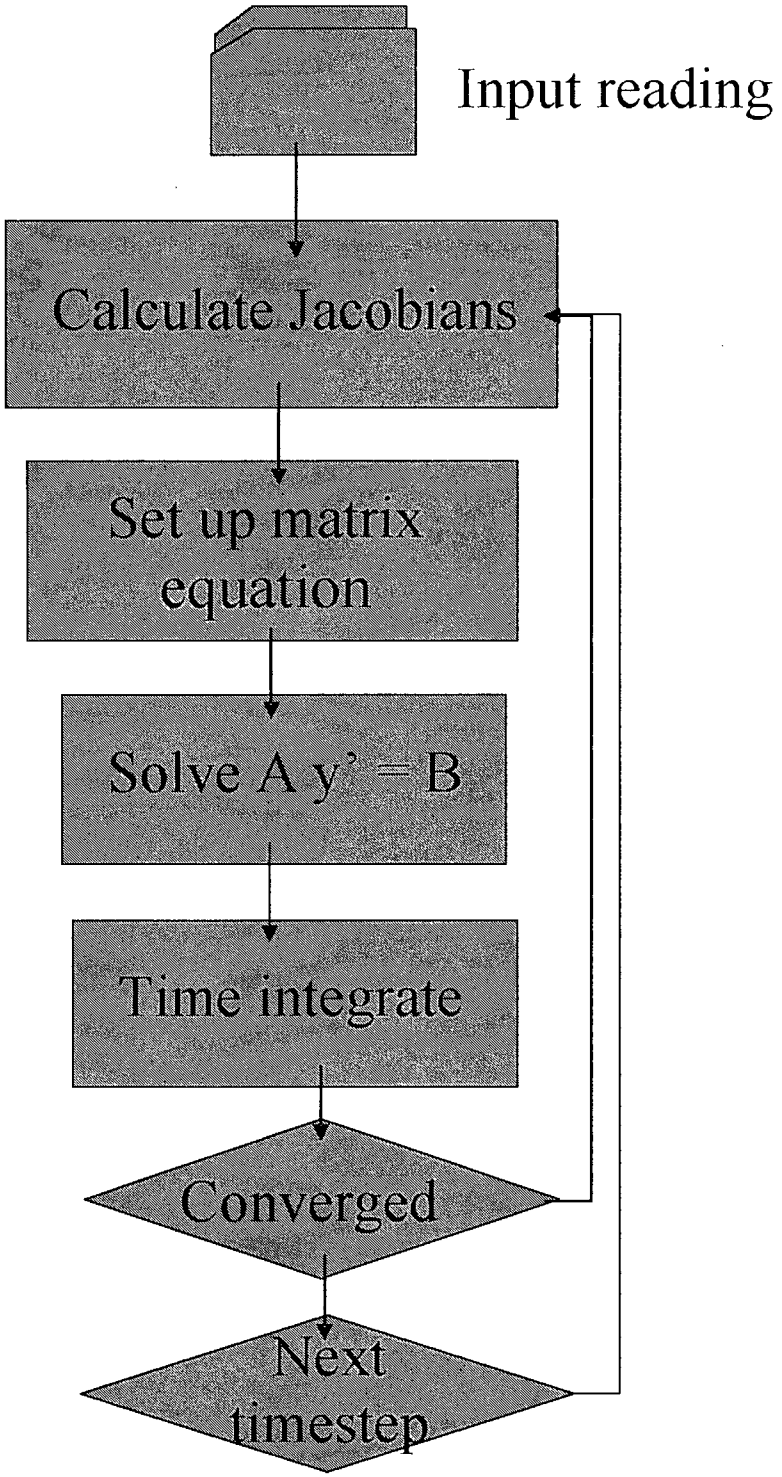

Figure 19.1-1. Simplified Flow Chart of the Calculation Sequence

19.2 REACTOR KINETICS SOLUTION

The numerical solution of the two-group kinetic model in POLCA7 is well described in Reference 19.2.

19.3 HYDRAULIC MODEL SOLUTION

[

]^{a,c}

[

]^{a,c}

[

]^{a,c}

[

]^{a,c}

[

]^{a,c}

19.4 HEAT CONDUCTION AND TRANSFER SOLUTION

The heat conduction equations (as described in Section 3) are solved with the boundary condition for surface heat flux q:

$$q_{surf} = q_l + q_v \tag{19-18}$$

where:

q_l = heat flux to water, and
q_v = heat flux to steam.

When setting up and solving heat conduction equations for heat structures the derivatives in the form dT_{surf}/dq_{surf} are calculated. These derivatives are used subsequently in linearization of conduction problem when solving hydraulic equations.

19.4.1 Coupling between Rod Heat Transfer and Hydraulic

The heat conduction equation can be looked upon as a linear relation between surface heat flux and surface temperature:

$$q_{surf} = (A + T_{surf}) / k \tag{19-19}$$

where $k = \frac{\partial T_{surf}}{\partial q_{surf}}$

The convective heat fluxes can be expressed as:

$$q_l = a_l + b_l(T_{surf} - T_l) \tag{19-20}$$

$$q_v = a_v + b_v(T_{surf} - T_v) \tag{19-21}$$

Finding surface temperature T_{surf} from equation (19-20) and substituting to (19-20 and 19-21), one obtains:

$$q_l (1\text{-}k\, b_l) .. - q_v\, k\, b_l = a_l - b_l \cdot (A + T_l) \tag{19-22}$$

$$- q_l\, k\, b_v + q_v\, (1\text{-}k\, b_v) = a_v - b_v \cdot (A + T_v)$$

The convective heat fluxes q_l and q_v can now be determined from equation (19-22).

$$q_l = \frac{(1 - k\, b_v)\,(a_l - b_l\,(A+T_l)) + k\, b_l\,(a_v - b_v\,(A+T_v))}{1 - k\,(b_l + b_v)} \tag{19-23a}$$

$$q_v = \frac{k\, b_v\,(a_l - b_l\,(A+T_l)) + (1 - k\, b_l)\,(a_v - b_v\,(A+T_v))}{1 - k\,(b_l + b_v)} \tag{22-23b}$$

The constant A is calculated after the solution of heat conduction equation is found:

$$A = (q_{0l} + q_{0v})\, k - T_{0surf}$$

Coupling between slab heat transfer and the hydraulic.

The convective heat transfer at the slab surfaces is (see Figure 19.4-1):

$$Q_{Ll} = A_L \cdot h_{Ll} \cdot (T_L - T_{Ll}) \tag{19-24}$$

$$Q_{Lv} = A_L \cdot h_{Lv} \cdot (T_L - T_{Lv}) \tag{19-25}$$

$$Q_{Rl} = A_R \cdot h_{Rl} \cdot (T_R - T_{Rl}) \tag{19-26}$$

$$Q_{Rv} = A_R \cdot h_{Rv} \cdot (T_R - T_{Rv}) \tag{19-27}$$

where subscripts L and R refer to the left and right side respectively and subscripts l and v refer to water and gas phase, respectively.

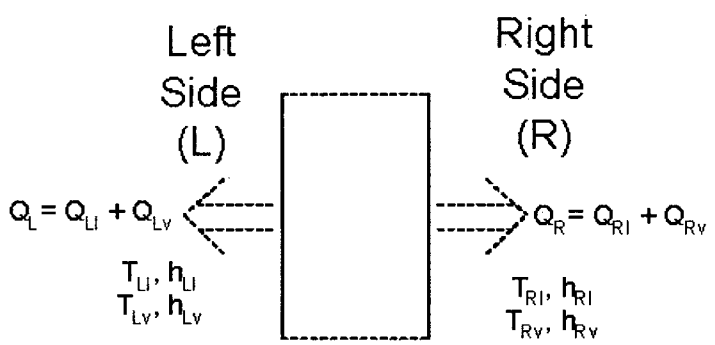

Figure 19.4-1. Slab Heat Transfer to Hydraulics

On the other hand, the conductive heat fluxes can be expressed in linearized form as,

$$Q_L = Q_{L0} + \frac{\partial Q_L}{\partial T_L}\cdot(T_L - T_{L0}) + \frac{\partial Q_L}{\partial T_R}\cdot(T_R - T_{R0}) \quad (19\text{-}28)$$

$$Q_R = Q_{R0} + \frac{\partial Q_R}{\partial T_L}\cdot(T_L - T_{L0}) + \frac{\partial Q_R}{\partial T_R}\cdot(T_R - T_{R0}) \quad (19\text{-}29)$$

where the subscript 0 denotes instant when conduction equation is solved.

Equations (22-24) through (22-29) can be solved together to give:

$$T_L = (C_L \cdot S_R + C_R \cdot \frac{\partial Q_L}{\partial T_R}) / J \quad (19\text{-}30)$$

$$T_R = (C_R \cdot S_L + C_L \cdot \frac{\partial Q_R}{\partial T_L}) / J \quad (19\text{-}31)$$

where:

$$S_L = (h_{LI} + h_{Lv})\cdot A_L - \frac{\partial Q_L}{\partial T_L}$$

$$S_R = (h_{RI} + h_{Rv})\cdot A_R - \frac{\partial Q_R}{\partial T_R}$$

$$C_L = Q_{L0} - T_{L0}\cdot\frac{\partial Q_L}{\partial T_L} - T_{R0}\cdot\frac{\partial Q_L}{\partial T_R} + A_L\cdot(h_{LI}\cdot T_{LI} + h_{Lv}\cdot T_{Lv})$$

$$C_R = Q_{R0} - T_{L0}\cdot\frac{\partial Q_R}{\partial T_L} - T_{R0}\cdot\frac{\partial Q_R}{\partial T_R} + A_R\cdot(h_{RI}\cdot T_{RI} + h_{Rv}\cdot T_{Rv})$$

$$J = S_L \cdot S_R - \frac{\partial Q_L}{\partial T_R}\cdot\frac{\partial Q_R}{\partial T_L}$$

The derivatives:

$$\frac{\partial T_L}{\partial Q_L}, \frac{\partial T_L}{\partial Q_R}, \frac{\partial T_R}{\partial Q_L} \text{ and } \frac{\partial T_R}{\partial Q_R}$$

are calculated by simultaneous solution of the equation system with the right hand sides with boundary conditions undisturbed and disturbed on the left and right sides.

One can say that surfaces temperatures are the function of the surface heat fluxes:

$$T_L = T_L(Q_L, Q_R)$$

$$T_R = T_R(Q_L, Q_R)$$

and the reverse derivatives can be expressed as:

$$\frac{\partial Q_L}{\partial T_L} = \frac{1}{E} \cdot \frac{\partial T_R}{\partial Q_R}$$

$$\frac{\partial Q_R}{\partial T_L} = -\frac{1}{E} \cdot \frac{\partial T_R}{\partial Q_L}$$

$$\frac{\partial Q_L}{\partial T_R} = -\frac{1}{E} \cdot \frac{\partial T_L}{\partial Q_R}$$

$$\frac{\partial Q_R}{\partial T_R} = \frac{1}{E} \cdot \frac{\partial T_L}{\partial Q_L}$$

where

$$E = \frac{\partial T_L}{\partial Q_L} \cdot \frac{\partial T_R}{\partial Q_R} - \frac{\partial T_L}{\partial Q_R} \cdot \frac{\partial T_R}{\partial Q_L}$$

19.5 REFERENCES

19.1 "Water Reactor Emergency Core Cooling System Evaluation Model: Code Description and Qualification," RPB 90-93-P-A (Proprietary), October, 1991.

19.2 "The Advanced PHOENIX and POLCA Codes for Nuclear Design of Boiling Water Reactors," CENPD-390-P-A, December 2000.

20 MATERIAL PROPERTIES

This section presents methods for calculating the material properties.

Section 20.1 describes the calculation of steam-water data used in evaluation of thermal-hydraulic models.

Sections 20.2 and 20.3 describe calculation of properties such as thermal conductivity, heat capacity, and density of solids. This data are applied in solving heat conduction problems.

Section 20.3 also provides tables with correlations for properties of gases used in modeling of gas gap.

20.1 STEAM-WATER PROPERTIES

Steam-water data are calculated using an interpolation method with bicubic B-splines in rectangular temperature-pressure mesh. Mesh data have been generated from a formulation presented in Reference 20.1.

The critical point data resulting from this formulation are:

Temperature	T_{crit} = 373.976 °C = 647.126 K	
Pressure	P_{crit} = 22.055 MPa	
Density	ρ_{crit} = 322 kg/m^3	(20-1)
Free enthalpy	g_{crit} =-767.44 kJ/kg	
Entropy	s_{crit} = 4.409 kJ/kg K	

The saturation line position $p_{sat} = p(T)$ has been determined from base equation of formulation by stating the Gibbs conditions:

$$T_{liquid} = T_{vapor}$$

$$p_{liquid} = p_{vapor} \qquad (20\text{-}2)$$

$$g_{liquid} = g_{vapor}$$

The spinodal limits (border of the metastable state) for water Tml(p) and steam Pmv(T) have been found from base equation of the formulation.

The evaluation of the steam-water data is performed by the set of FORTRAN 95 routines. The data base consists of the eight tables stored in rectangular (t, p) mesh. From this data base, all thermodynamic parameters and derivatives can be calculated.

The water mesh data cover a range of pressure from $p=p_{sat}(0°C)=612$ Pa up to a critical pressure P_{crit} and the temperature range from 0°C up to $\min(T_{crit},T_{ml}(p))$, where $T_{ml}(p)$ is the temperature of the spinodal (metastable) limit for a given pressure.

The steam mesh data cover a range of temperature from 0 up to 2000°C and a range of pressure from 200 Pa up to min (P_{crit}, $P_{mv}(T)$), where $P_{mv}(T)$ is the pressure of the spinodal limit for a given temperature.

Figure 20.1-1 shows the saturation line and spinodal limit lines for water and steam.

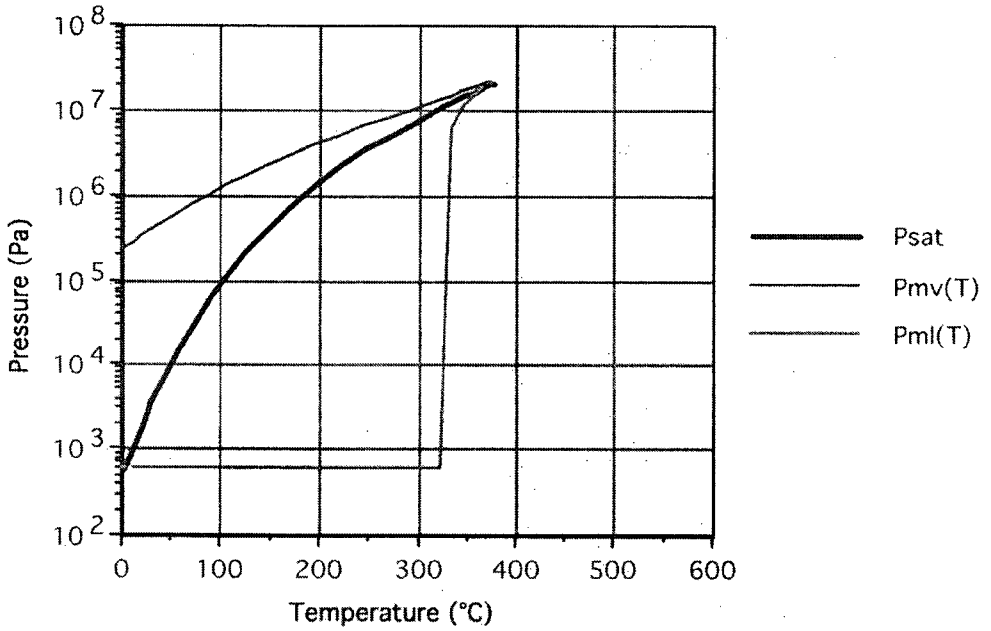

Figure 20.1-1. Saturation Line and Metastable Lines for Water

20.2 PROPERTIES OF SOLIDS

Only a few material property equations, as a function of temperature, are incorporated into POLCA-T.

The material properties of most interest are thermal conductivity, heat capacity, and density. The user must provide the data as tables to POLCA-T. The values in tables are linearly interpolated and integrated by the trapezoid rule from the first pair of data.

Temperature	T in °C.
Conductivity	k in W/m,K.
Heat capacity	c in J/kg,K.
Density	ρ in kg/m_3.

20.3 PROPERTIES OF GASES

Evaluation of some properties of gases is necessary in POLCA-T. It concerns mainly fission gases encountered in the gas gap.

Thermal conductivity of pure gases is approximated with the formula:

$$k = a \cdot T + b \tag{20-3}$$

where coefficients a and b are shown in Table 20-1.

The effective thermal conductivity of a single pure gas in a gas mixture is calculated, based on the thermal conductivity of pure gases making up the mixture, according to the following equation:

$$K_i = \frac{k_i x_i}{\sum_{j=1}^{n} A_{ij} \cdot x_j} \tag{20-4}$$

where:

k_i = thermal conductivity of pure gas i, W m^{-1} K^{-1},
x_i = mole fraction of gas i in the mixture,
A_{ij} = Sutherland weighting factor for the gas species i, in the gas mixture, and
n = number of gas constituents in the mixture.

The Sutherland weighting factor can be obtained from the following equation:

$$A_{ij} = \frac{1}{4} \cdot \left\{ 1 + \left[\frac{\mu_i}{\mu_j} \cdot \left(\frac{M_j}{M_i} \right)^{3/4} \cdot \frac{T + S_i}{T + S_j} \right]^{1/2} \right\}^2 \cdot \frac{T + \sqrt{S_i \cdot S_j}}{T + S_j} \tag{20-5}$$

where:

μ = viscosity of pure gas,
M = molecular weight,
T = temperature in degree Kelvin, and
S = Sutherland constants for gas species.

Table 20-1. Thermal Conductivity of Gases: $k = a \cdot T + b$		
Gas	**a**	**b**
Helium	$2.693 \cdot 10^{-3}$	0.7085
Argon	$2.986 \cdot 10^{-4}$	0.7224
Xenon	$4.351 \cdot 10^{-5}$	0.8616
Krypton	$8.241 \cdot 10^{-5}$	0.8363
Nitrogen	$5.314 \cdot 10^{-4}$	0.6898
Hydrogen	$1.097 \cdot 10^{-3}$	0.8785
Oxygen	$1.853 \cdot 10^{-4}$	0.8729
CO	$1.403 \cdot 10^{-4}$	0.9090
CO_2	$9.460 \cdot 10^{-6}$	1.3120
H_2O	$8.720 \cdot 10^{-6}$	1.3401

Molecular weights and Sutherland constants for some common gases are shown in Table 20-2.

Table 20-2. Molecular Weights and Sutherland Constants for Gases		
Gas	**Molecular Weight**	**Sutherland Constant**
Helium	4.003	70.0
Argon	39.994	142.0
Xenon	131.300	252.0
Krypton	83.700	188.0
Nitrogen	28.060	110.6
Hydrogen	2.016	93.4
Oxygen	32.000	127.0
CO	28.010	118.0
CO_2	44.010	274.0
H_2O	18.020	650.

Viscosity of pure gases is approximated with $\mu = a \cdot T + b$ where coefficients a and b are given in Table 20-3.

Table 20-3. Viscosity of Pure Gases: $\mu = a \cdot T + b$

Gas	a	b
Helium	$0.47632 \cdot 10^{-6}$	0.65752
Argon	$0.57621 \cdot 10^{-6}$	0.65417
Xenon	$0.46019 \cdot 10^{-6}$	0.71428
Krypton	$0.30786 \cdot 10^{-6}$	0.76293
Nitrogen	$0.16851 \cdot 10^{-6}$	0.69647
Hydrogen	$0.46667 \cdot 10^{-6}$	0.64550
Oxygen	$0.51638 \cdot 10^{-6}$	0.65601
CO	$0.44641 \cdot 10^{-6}$	0.65304
CO_2	$0.23544 \cdot 10^{-6}$	1.74008
H_2O	$0.13470 \cdot 10^{-7}$	1.15010

The accommodation coefficients for fuel and cladding surcaces (α) are shown in Table 20-4.

Table 20-4. Accommodation Coefficients, α

Gas	Gas-cladding Zircaloy	Gas-fuel
Helium	0,33	0,35
Argon	0,86	0,84
Xenon	1,03	1,03
Krypton	0,808	0,80

20.4 REFERENCES

20.1 L. Haar, J. S. Gallagher, G. S. Kell, "NBS/NRC Steam Tables." Hempshire Publishing Corporation, 1984.

21 MODELING CAPABILITY

This section discusses the valid formulation range of the basic equations, the applicability of the correlations and finally the range of the steam water tables used in POLCA-T.

The code it self can be used to model a BWR at system level down to component level or specific parts of such a nuclear power plant.

The POLCA-T code can also be used as a pure thermal-hydraulic tool to simulate non-nuclear plants or phenomena in single-to two-phase flow conditions.

21.1 VALIDITY RANGE OF EQUATION FORMULATION

The basic 1-D thermal-hydraulic conservation equation, mass balances (4 equations) energy equations (2 equations), and mixture momentum equation (1 equation) are general and cover the flow range from stagnant flow/gravity driven flow up to supersonic flow via forced flow, in arbitrary flow direction and can handle reverse flow situations with counter current flow situations.

However, stratified flow in horizontal pipes with a free surface is not within the range for the code for now.

Validity for form losses, friction coefficients, etc, is method/user dependent.

The heat conduction is limited to one direction heat flow both in general heat structures and in fuel rod heat structures. Valid thermal properties data for heats structures, both general and fuel rod structures, are method/user dependent.

21.2 VALIDITY OF CORRELATIONS

21.2.1 [ ]^{a,c}

[

]^{a,c}

a,b,c

[

]

21.2.2 Heat Transfer Correlations

The heat transfer correlation package validity range and usage can be found in Section 9.4 heat transfer between phases and Section 11 for convective heat transfer and references to the correlations.

21.3 EQUATION OF STATE

See Section 20.1 regarding the validity range of steam water properties. Non-condensable gases are treated as ideal gases.

21.4 REFERENCES

21.1 "Water Reactor Emergency Core Cooling System Evaluation Model: Code Description and Qualification" RPB 90-93-P-A (Proprietary), October, 1991.

22 THE POTENTIAL ENERGY AND DISSIPATION TERMS

During a typical transient, the maximum values of e_{pot} are:

$$e_{pot} = g \cdot z = 9.81\ m/s^2 \cdot 10\ m \approx 100\ J/kg \tag{22-1}$$

One hundred J/kg corresponds to a change in water temperature of about 0.02°C. Hence, these terms are clearly negligible compared to the fluid internal energy.

In order to justify omission of dissipation effects, the dominating terms of $\nabla \cdot (\underline{\underline{\tau}} \cdot \underline{u})$, the dissipation term, must be examined.

$$\begin{aligned} \nabla \cdot (\underline{\underline{\tau}} \cdot \underline{u}) \quad &\approx \frac{\partial}{\partial t}(t_y \cdot u_x) \\ &= \frac{\partial}{\partial t}\bar{\tau}_{yy} \cdot u_X + \bar{\tau}_{yx}\frac{\partial u_X}{\partial y} \\ &\approx \bar{\tau}_{yx}\frac{\partial u_X}{\partial y} \end{aligned} \tag{22-2}$$

where x is the main flow direction and y is perpendicular to x. The term τ_{yx} can be estimated by an equation for pressure drop due to friction.

$$\tau_{wall} \cdot P_W = \Delta p_{fric} / \Delta x \cdot A \tag{22-3}$$

which for a typical rod bundle is:

$$\begin{aligned} \tau_{wall} \quad &= \frac{\Delta p_{fric}}{\Delta x}\frac{A}{P_W} = \frac{1}{4}\frac{\Delta P_{fric}}{\Delta x} \cdot D_h \\ &= 1/4 \cdot 5000 \cdot 0.01 = 10\ N/m^2 \end{aligned} \tag{22-4}$$

Furthermore:

$$\frac{\partial u_X}{\partial x} \approx \frac{u}{D_h} \approx \frac{15}{0.01} = 1500\ s^{-1} \tag{22-5}$$

substituting into equation (2) the dissipation term gives:

$$\nabla \cdot (\underline{\underline{\tau}} \cdot \underline{u}) \approx 10 \cdot 1500\ Nm/m^3 s = 0.015\ MW/m^3 \tag{22-6}$$

When compared to the power density of the core (per cubic meter coolant)

$$qv \approx (3000 \cdot 10^6 \text{ W}) / 24 \text{ m}^3 \approx 100 \text{ MW/m}^3 \quad (22\text{-}7)$$

the dissipation term is clearly negligible.

23 NOMENCLATURE, SUBSCRIPTS AND SUPERSCRIPTS, AND DIMENSIONLESS GROUPS

The following is a compilation of used nomenclature for different quantities, superscripts, and subscripts. A list of the most common used dimensionless groups can be found in the end of the section.

23.1 NOMENCLATURE

Quantity	Symbol	Coherent SI Unit
Absorptivity (radiation)	α	–
Absorption Coefficient (radiation)	κ	m^{-1}
Activation Energy of a Reaction		
Angle		
plane	$\alpha, \beta, \gamma, \theta, \varphi$	rad
solid	θ	sr
of contact		rad
Area		
cross-sectional	A_c , S	m^2
surface	A , A_s	m^2
Coefficient of Volume Expansion	$\beta = (1/v)\ (\partial v/\partial T)_p$	K^4
Compressibility Factor ($= \overline{pv} / \overline{R}\,T$)	Z	–
Density		
mass $\left(= M / V\right)$	ρ	kg/m^3
Coordinates		
Cartesian	x, y, z	m, m, m
cylindrical	r, φ, z	m, rad, m
spherical	r, θ, φ	m, rad, rad
Diffusion Coefficient	D	m^2/s
Diffusivity, Thermal ($= k/\rho c_p$)	α	m^2/s
Dryness Fraction (quality) of flow	x	–
	x^*	–
Emissive Power (radiation)	E	W/m^2
Emissivity (radiation)	ε	–
Energy	E	J=Nm
kinetic	E_k	J=Nm
potential	E_p	J=Nm
transfer per unit time (power)	$\dot{W}$	W=Nm/s=kg m^2/s^3
Enthalpy $\left(= U + pV\right)$	H	J
specific	h, i	J/kg
Entropy	S	J/K
specific	s	J/kg

Quantity	Symbol	Coherent SI Unit
Force	F	N=kg m/s^2
weight (force of gravity)	Mg	N=kg m/s^2
Fraction		
mass, of species i	x_i, y_i	–
void		
gas volume	α	–
liquid volume	β	–
Frequency	v, f	Hz=s^{-1}
circular	ω	rad/s
Gas Constant		
molar (universal)	R	J/kmol K
specific, of species i	R_i	J/kg K
Gibbs Function $(= H - TS)$	G	J
specific $(= h - Ts)$	g	J/kg
Gravitational Acceleration	g	m/s^2
Heat		
quantity of	Q	J
rate (power)	$\dot{Q}$	W=J/s
flux $(\dot{Q} / A)$	$\dot{q}$, q''	W/m^2
rate per unit volume	$\dot{S}$, q'''	W/m^3
Heat Capacity	C	J/K
specific (constant v or p)	c_v, c_p	J/kg K
ratio c_p/c_p	γ	–
Heat Transfer Coefficient	h, htc	W/m^{2}K
Helmholtz Function $(= U - TS)$	F	J
specific $(= u - Ts)$	f	J/kg
Intensity (radiation)	I	W/m^{2}sr
Internal Energy	U	J
specific	u	J/kg
Length	L	m
width	W	m
height	H	m
diameter	D	m
radius	R	m
distance along path	s	m
film thickness	δ	m
thickness	δ, Δ	m
Mass	M, m	kg
flow rate	$\dot{M}$, $\dot{m}$, w	kg/s
velocity of flux (flowrate per unit area = $\dot{M} / A_c$)	G, ρu	kg/m^2/s
Mass Transfer Coefficient	h_m, k_m	m/s

Quantity	Symbol	Coherent SI Unit
Mass Transfer Rate	Γ	kg/s
Mean Free Path	λ, l	m
Pressure	p	$Pa=N/m^2$
drop	Δp	Pa
partial	p_i	Pa
Reflectivity (radiation)	ρ	–
Scattering Coefficient radiation)	σ_s	m^{-1}
Shear Stress	τ	$Pa=N/m^2=kg/m\ s^2$
Surface Tension	σ	$N/m=kg/s^2$
Temperature	t	C
Temperature		
absolute	T	K
Thermal Conductivity	k	W/mK
Time	t	s
Velocity	u	m/s
components in Cartesian coordinates x, y, z	u, v, w	m/s
View Factor (geometric or configuration factor)	F_{ij}	–
Viscosity		
dynamic (absolute)	μ	$Pa\ s=N\ s/m^2=kg/m\ s$
kinematic (= μ/ρ)	ν	m^2/s
Volume	V	m^3
flow rate	$\dot{V}$	m^3/s
Work	W	J =Nm
rate (power)	$\dot{W}$	W = J/s=Nm/s

23.2 SUBSCRIPTS AND SUPERSCRIPTS

Quantity	Symbol
Bulk	b
Critical State	c
Fluid	f
Gas	g, gas
Liquid	l, liq
Hydraulic	hyd
Change of Phase	
evaporation	lg
Mass transfer quantity	m
Solid or Saturated Solid	s
Saturated conditions	sat
Wall	w

Quantity	Symbol
Free-stream	∞
Inlet	in, 1
Outlet	out, 2
At Constant Value of Property	*P, v, T,* etc
Stagnation (subscript)	0
Interface	i
Water film	film
Water drops	drop
Gas bubble	bub

23.3 DIMENSIONLESS GROUPS[4]

Quantity	Symbol
Biot Number	$Bi=hL/k$
Eckert Number	$Ec = u^2/c_p\Delta T$
Euler Number	$Eu = \Delta p / (\frac{1}{2}\rho u^2)$
Fourier Number	$Fo = \alpha t/L^2$
Fricton Factor, Darchy	$f = \tau_w /(\frac{1}{2}\rho u^2)$
Froude Number	$Fr = u^2/gl$
Grashof Number	$Gr = \beta g L^3 \Delta T / v^2$
Graetz Number	$Gz = (Re)(Pr)D/L$
Knudsen Number (λ = mean free path)	$Kn = \lambda / L$
Mach Number	$M = u / u_{sound}$ $= u /(\gamma RT / M)^{\frac{1}{2}}$ for perfect gas
Nusselt Number	$Nu = hL/k_f$
Péclet Number	$Pe = (Re)(Pr)$
Prandtl Number	$Pr = c_p\mu/k$
Rayleigh Number	$Ra = (Gr)(Pr)$
Reynolds Number	$Re = uL / v = \rho uL / \mu = mL / \mu$
Stanton Number	$St=(Nu)/(Re)(Pr)=h/\rho c_p u$
Strouhal Number	$Sr = vL/u$
Weber Number	$We=u^2\rho L/\sigma$

4. The symbol L in the dimensionless groups stands for a generic length, and is defined according to the particular geometry being described; i.e., it may be diameter, hydraulic diameter, plate length, etc.

APPLICATION APPENDICES

APPENDIX A
POLCA-T: CONTROL ROD DROP ACCIDENT ANALYSIS (CRDA)

ABSTRACT

This appendix describes the Westinghouse boiling water reactor (BWR) control rod drop accident (CRDA) methodology and provides qualification information demonstrating that the methodology is adequate for ensuring compliance to General Design Criterion (GDC) 28 and the Standard Review Plan (SRP) NUREG-800. The purpose of this appendix is to present an advanced CDRA methodology for use in performing BWR licensing analysis that is based on the three-dimensional (3-D) dynamic code POLCA-T instead of the RAMONA-3 code.

A complete cycle-specific analysis is fundamentally a two-step approach. The first step involves determination of possible candidates for the control rod that would cause the most severe consequences resulting from a CRDA. The second step is simulation of the dynamic response to the identified worst dropped control rod(s) and the subsequent consequences to the fuel. This evaluation is performed with the coupled 3-D neutron kinetics and thermal-hydraulics system transient code POLCA-T.

The Westinghouse strategy for a cycle-specific evaluation includes systematic review of existing results and the use of bounding calculations to envelope worst-case consequences of the CRDA for the subject cycle.

The examples of the Westinghouse CRDA methodology are provided in this appendix. It is demonstrated that the methodology described and justified in this report is practical and can be conveniently and accurately utilized for the CRDA evaluation on a cycle-specific or generic basis.

Appendix A

TABLE OF CONTENTS

ABSTRACT i

TABLE OF CONTENTS iii

A.1 SUMMARY AND CONCLUSIONS A-1
A.1.1 SCOPE A-1
A.1.2 OBJECTIVES A-2
A.1.3 NOT USED A-2
A.1.4 CONCLUSIONS A-2
A.2 CRDA MODEL REQUIREMENTS A-3
A.2.1 ACCIDENT DESCRIPTION A-3
A.2.2 CURRENT ANALYSIS METHOD A-4
A.2.3 DESIGN BASIS A-4
A.2.4 DESIGN BASIS ACCEPTANCE CRITERIA A-4
A.2.5 PARAMETER SENSITIVITIES AND PIRT TABLES A-5
A.3 ASSESSMENT DATA BASE A-11
A.3.1 SINGLE PARAMETER CONFIRMATION AND SEPARATE EFFECTS A-12
A.3.2 INTEGRAL EFFECTS A-19
A.3.3 CONCLUSIONS A-31
A.4 WESTINGHOUSE BWR CONTROL ROD DROP ACCIDENT ANALYSIS METHODOLOGY A-35
A.4.1 INTRODUCTION A-35
A.4.2 OVERVIEW A-35
A.4.3 DETERMINATION OF CANDIDATES FOR THE LIMITING CONTROL ROD A-37
A.4.4 DYNAMIC ANALYSIS TO DETERMINE ENERGY DEPOSITION IN FUEL A-44
A.4.5 EVALUATION OF PEAK SYSTEM PRESSURE DURING THE TRANSIENT METHODOLOGY A-55
A.4.6 CYCLE-SPECIFIC EVALUATIONS METHODOLOGY A-56
A.4.7 COMPARISON OF ANALYSIS RESULTS WITH EVALUATION CRITERIA A-56
A.5 EVALUATION MODEL ASSESSMENT A-58
A.5.1 POLCA-T SENSITIVITY STUDIES A-58
A.5.2 PEAK FUEL ENTHALPY A-70
A.5.3 ESTABLISHMENT OF THE POLCA-T UNCERTAINTY A-71
A.5.4 CONSERVATISM IN POLCA-T CRDA METHODOLOGY A-77
A.5.5 [ ]^{A,C} A-78
A.6 REFERENCES A-78

Appendix A

LIST OF TABLES

Table A.2-1 Control Rod Drop Accident Analysis PIRT A-7

Table A.3-1 POLCA-T Results for the NEACRP Benchmark HZP Case C1 ..... A-14

Table A.3-2 POLCA7 and POLCA-T Axial Power Mean Deviation (MD) and RMS A-15

Table A.3-3 POLCA-T Radial Power MD and RMS Error A-18

Table A.3-4 Time and Value of Peak Fission Power TT2 ..... A-22

Table A.3-5 PB2 TT1 and TT2 Tests Measured and Calculated Sequence of Events A-23

Table A.3-6 Summary of POLCA-T Results For Three SPERT-III Tests A-28

Table A.3-7 Initial Conditions for CRDA Cases A-29

Table A.3-8 Comparison of POLCA-T and RAMONA-3 Results for CRDA Analyses A-30

Table A.4-1 Operating Conditions Used In Step 1 ..... A-39

Table A.4-2 List of Selected Candidates for the Limiting Control Rod – CR Worth at Fully Withdrawn Position A-42

Table A.4-3 Control Rod Worth and PPF of the Selected Candidates for the Limiting Rod at Realistic 8 Notches Rod Drop A-43

Table A.4-4 [ ]^{a,b,c} A-46

Table A.4-5 Input Data for the Limiting Initial Condition Cases A-47

Table A.4-6 Typical BWR Scram Insertion in Case Without Significant RPV Pressurization A-47

Table A.4-7 POLCA-T Results for the CRDA Limiting Reactor Initial Conditions Cases A-48

Table A.4-8 POLCA-T Results for the CRDA Energy Deposition in the Fuel – Determination of the Limiting Control Rod A-52

Table A.5-1 Effect of the Doppler Coefficient on the POLCA-T Predicted Peak Fuel Enthalpy A-60

Table A.5-2 Effect of the Delayed Neutron Fraction on the POLCA-T Predicted Peak Fuel Enthalpy A-61

Table A.5-3 Effect of the Pin Peaking Factors on the POLCA-T Predicted Peak Fuel Enthalpy A-62

Table A.5-4 Effect of the Core Inlet Subcooling on the POLCA-T Predicted Peak Fuel Enthalpy A-63

Table A.5-5 Effects of the Core Inlet Subcooling and the RPV Pressure on the POLCA-T Predicted Peak Fuel Enthalpy A-64

Table A.5-6 Effect of the Rate of Reactivity Insertion on the POLCA-T Predicted Peak Fuel Enthalpy A-64

Appendix A

LIST OF TABLES (Cont'd)

Table A.5-7 Effects of the Moderator Density and Void Fraction on the POLCA-T Predicted Peak Fuel Enthalpy A-67

Table A.5-8 Effects of the Core Mass Flow on the POLCA-T Predicted Peak Fuel Enthalpy A-68

Table A.5-9 Conservative Estimates of Uncertainties In Power Predictions by Licensed POLCA7 Code A-75

Table A.5-10 Uncertainties in POLCA-T Predicted Peak Fuel Enthalpy A-76

Table A.5-11 Treatment of Bounding Values and Uncertainties A-76

Appendix A

LIST OF FIGURES

Figure A.3-1 POLCA-T Case C1 Core Axial Power Distribution and Comparison with the Reference Solution (Reference 6) and POLCA7 Code A-15

Figure A.3-2 POLCA-T Case C1 Power Time History and Comparison with PANTHER Reference Solutions (References 6 and 7) A-16

Figure A.3-3 POLCA-T Case C1 Radial Power Distribution at Axial Layer 13: a) at Initial State and b) at Power Peak A-17

Figure A.3-4 POLCA-T Core Average Axial Power Profile Obtained by Different Cross-Section Data at EOC2 State Prior to TT2. (Comparison versus plant data (P1 edit Reference 8)) A-20

Figure A.3-5 POLCA7 and POLCA-T Core Average Axial Power Profile for State Prior to TT1 (a) and TT3 (b) tests. (Comparison versus Plant Data (P1 edit Reference 8)) A-21

Figure A.3-6 Comparison of POLCA-T TT2 Fission Power Time History Obtained by Different XS Data Versus PB2 Measured Data A-24

Figure A.3-7 Comparison of POLCA-T TT1 Fission Power Time History vs. PB2 Measured Data A-24

Figure A.3-8 TT1 Transient LPRM Response for String 5 ..... A-25

Figure A.3-9 TT1 Transient LPRM Response for String 13 ..... A-25

Figure A.3-10 Comparison of POLCA-T Predicted and Measured Fission Power for Cold Cases 43 and 49 ..... A-28

Figure A.3-11 Comparison of POLCA-T and RAMONA-3 Predicted Core Power for CZP Case 1 ..... A-32

Figure A.3-12 Comparison of POLCA-T and RAMONA-3 Predicted Maximum Fuel Enthalpy for CZP Case 1 ..... A-32

Figure A.3-13 Comparison of POLCA-T and RAMONA-3 Predicted Core Power for Hot Case A-33

Figure A.3-14. Comparison of POLCA-T and RAMONA-3 Predicted Maximum Fuel Enthalpy for Hot Case A-33

Figure A.4-1 Group Assignment for the A Sequence A-40

Figure A.4-2 Total Reactivity Worths for Sample BWR/6 Withdrawal Sequence A A-41

Figure A.4-3 Relative Maximum Nodal Peak Power as a Function of the Dropped CR Worth A-41

Figure A.4-4 Control Rods Patterns at Steps 113 and 114 with Selected Candidates for the Limiting Control Rod A-42

Figure A.4-5 [ ]^{a,c} A-46

Appendix A

LIST OF FIGURES (Cont'd)

Figure A.4-6 POLCA-T Predicted Reactor Power Time Histories for CRDA Limiting Initial Conditions Cases A-50

Figure A.4-7 POLCA-T Predicted Peak Fuel Enthalpy Time Histories for CRDA Limiting Initial Conditions Cases A-51

Figure A.4-8 [ ]^{a,c} A-52

Figure A.4-9 POLCA-T Predicted Reactor Power Time Histories for the Candidate Limiting CRs A-53

Figure A.4-10 POLCA-T Predicted Peak Fuel Enthalpy Time Histories for the Candidate Limiting CRs in Step 113 ..... A-54

Figure A.4-11 POLCA-T Predicted Peak Fuel Enthalpy Time Histories for the Candidate Limiting CRs in Step 114 ..... A-54

Figure A.4-12 Strategy for Cycle-Specific Evaluations A-57

Figure A.5-1 POLCA-T Predicted Peak Fuel Enthalpy Versus Total CR Reactivity Worth A-59

Figure A.5-2 POLCA-T Predicted Peak Fuel Enthalpy Versus Doppler Coefficient Multiplier A-61

Figure A.5-3 POLCA-T Predicted Peak Fuel Enthalpy Versus Pin Peaking Factor A-62

Figure A.5-4 POLCA-T Predicted Fission Power Time Histories at Different Reactivity Insertion Rates A-65

FigureA.5-5 POLCA-T Predicted Peak Fuel Enthalpy Time Histories at Different Reactivity Insertion Rates A-65

Figure A.5-6 POLCA-T Predicted Maximum Hot Fuel Rod Temperature Time Histories at Different Reactivity Insertion Rates A-66

Figure A.5-7 POLCA-T Predicted Maximum Fuel Centerline Rod Temperature Time Histories at Different Reactivity Insertion Rates A-66

Figure A.5-8 POLCA-T Predicted Peak Fuel Enthalpy Time Histories at Different Core Mass Flows A-69

Figure A.5-9 Linear Least Square Fit of POLCA-T Predicted Peak Fuel Enthalpy Versus Total CR Reactivity Worth A-74

Appendix A

ABBREVIATIONS

APRM	average power range monitor
ASME	American Society of Mechanical Engineers
B&W	black and white
BE	best estimate
BOC	beginning of cycle
BOP	balance of plant
BPWS	banked position withdrawal sequence
BNL	Brookhaven National Laboratories
BWR	boiling water reactor
CFR	Code of Federal Regulations
CR	control rod
CRDA	control rod drop accident
CZP	cold-zero power
EM	evaluation model
EOC	end of cycle
EPRI	Electric Power Research Institute
FA	fuel assembly
FP	full power
FSAR	Final Safety Analysis Report
GDC	General Design Criterion
GE	General Electric
HZP	hot zero power
LPRM	local power range monitor
LWR	light water reactor
MD	mean absolute deviation
MOC	middle of cycle
msec	milliseconds
MSL	main steam lines
NEA	Nuclear Energy Agency
NK	neutron kinetics
NPP	nuclear power plant
NRC	United States Nuclear Regulatory Commission
NSC	Nuclear Science Committee
OECD	Organization for Economic Co-operation and Development
PB2	Peach Bottom Atomic Power Station Unit 2
pcm	per cent mille (10^{-5})
PIRT	Phenomena Identification and Ranking Table
PPF	power peaking factor
PSU	Pennsylvania State University
PWR	pressurized water reactor
REA	rod ejection accidents
RG	Regulatory Guide

Appendix A

ABBREVIATIONS (Cont'd)

RMS	root mean square
RPCS	rod pattern control system
RPV	reactor pressure vessel
RSCS	rod sequence control system
RWM	rod worth minimizer
sec	seconds
SI	spectrum interaction
SPERT	special power excursion tests
SRP	Standard Review Plan, NUREG-0800
SRV	safety/relief valves
SS	steam separator
TH	thermal-hydraulic
TIP	traveling in-core probe
TSV	turbine stop valve
TT	turbine trip
XS	cross-section
3-D	three dimensional

A.1 SUMMARY AND CONCLUSIONS

A.1.1 Scope

This appendix describes the Westinghouse boiling water reactor (BWR) control rod drop accident (CRDA) methodology and provides qualification information demonstrating that the methodology is adequate for ensuring compliance to General Design Criterion (GDC) 28, "Reactivity Limits," of Appendix A to 10 CFR Part 50 (Reference 1) and the Standard Review Plan (SRP) NUREG-800 (Reference 2). The current Westinghouse analysis methodology for the CRDA is based upon the use of the RAMONA-3 code is described in the Nuclear Regulatory Commission (NRC) approved Topical Report CENPD-284-P-A (Reference 3). The purpose of this report is to present an advanced CRDA methodology for use in performing BWR licensing analysis that is based on the three-dimensional (3-D) dynamic code POLCA-T instead of the RAMONA-3 code.

The Westinghouse methodology for performing CRDA analyses and the systematic cycle-specific strategy utilized by Westinghouse are described in this report.

A complete cycle-specific analysis is fundamentally a two-step approach. The first step involves determination of possible candidates for the control rod that would cause the most severe consequences resulting from a CRDA. [

]^{a,c} The three dimensional steady-state nodal code POLCA7, in conjunction with the lattice physics code PHOENIX4, are utilized for this evaluation. The codes are described in the NRC-approved Topical Report CENPD-390-P-A (Reference 4).

The second step is the simulation of the dynamic response to the identified worst dropped control rod(s) and the subsequent consequences to the fuel. This evaluation is performed with the coupled 3-D neutron kinetics and thermal-hydraulics systems code POLCA-T. The candidates for the worst-case condition established in the first step are simulated in the POLCA-T core model for the dynamic evaluation. The POLCA-T methodology utilizes state-of-the-art phenomenological models, including moderator feedback, to describe the overall transient response of the plant and core in conjunction with the local thermal behavior of the fuel.

The Westinghouse strategy for a cycle-specific evaluation includes systematic review of existing results and the use of bounding calculations to envelope worst-case consequences of the CRDA for the subject cycle.

The qualification basis of the Westinghouse CRDA methodology is described in this report. It is shown that the PHOENIX4/POLCA7 system of codes is qualified for providing adequate local pin power distributions, cross-sections, burnup and void histories, and steady-state control rod worth determinations by reference to the Westinghouse Nuclear Design Methodology in Reference 4. The methodology for steady-state and dynamic evaluation using POLCA-T is applied to the NEACRP-L-335 benchmark (References 5 through 7). The validation presented in Section A.3 of this Appendix demonstrates the adequacy of the methodology for establishing the reactivity and power response resulting from an ejected

control rod and capability in predicting the local power that is crucial for determining the correct fuel enthalpy. In addition, the validation against integral tests such as the Peach Bottom end-of-cycle (EOC) 2 turbine trip (TT) tests (Reference 8) and the SPERT-III-E power excursion tests (Reference 9) demonstrates the POLCA-T capability for the simulation of very fast transients resulting from pressure increase or a dropped control rod. Finally, the comparison of the POLCA-T with the RAMONA-3 code for commercial BWR CRDA analyses illustrates the similarity of the results obtained by tools previously used and the ones presented in this report.

The examples of the Westinghouse CRDA methodology are provided in this appendix. It is demonstrated that the methodology described and justified in this appendix is practical and can be conveniently and accurately utilized for the CRDA evaluation on a cycle-specific or generic basis.

A.1.2 Objectives

The main objective of this appendix is to identify the specific design bases which, if satisfied, assure that all requirements specified in GDC 28 and NUREG-0800 applicable to the CRDA are satisfied. Other objectives of CRDA analysis methodology applying POLCA-T code are:

- Use up-to-date comprehensive methods and models for fuel, core, and plant analyses
- Perform consistent core design and plant safety analyses, that is, steady-state and transient calculations
- Integrate the methods and codes
- Converge to a common methodology for European and U.S. applications

The above objectives also contribute to reducing the risk of human errors in applying the methodology in plant applications.

A.1.3 Not Used

A.1.4 Conclusions

Based on the evaluation in this appendix, it can be concluded that:

1. The design bases and acceptance criteria identified are sufficient to assure that all requirements and guidelines identified in the applicable GDCs and NUREG-0800 for the CRDA will be satisfied.

2. The methodology and strategies described are acceptable for design and licensing purposes. Specifically, they are acceptable for identifying the limiting event and evaluating BWR plant response and subsequent consequences to the fuel systems resulting from a postulated CRDA relative to the design bases acceptance criteria for design and licensing purposes.

3. The methodology described in this appendix can be used to analyze CRDAs for current BWR plant designs and control rod designs.

A.2 CRDA MODEL REQUIREMENTS

A.2.1 Accident Description

The CRDA assumes the decoupling of an inserted rod drive from the control blade. It is postulated that the drive mechanism is withdrawn while the control blade sticks in position and that the blade subsequently falls at its maximum speed to the position of the drive. Since it is assumed that the event can occur in any reactor operating state, consideration must be given to all the control rod configurations that can occur in normal operation as well as those that can occur as a result of equipment malfunction or operator error (such as, the most severe single operator selection of an out-of-sequence control rod).

The accident is most severe when it is assumed to occur at low- or zero-power conditions when the control rod patterns required to establish criticality provide the highest values of incremental (dropped) single control rod worth. Furthermore, the presence of voids in the core at any significant power level will decrease the consequences of the accident through the negative moderator density reactivity (void) coefficient and the enhanced heat transfer to the coolant relative to the cold case. Consequently, large subcooled conditions (such as a startup from cold shutdown) that do not result in significant boiling usually provide the most severe initial states for the event.

For a particular plant, consideration must be given to the hardware employed for rod sequence control and the Technical Specifications concerning inoperable rods in order to determine the limiting incremental rod worth.

For some banked position withdrawal sequence (BPWS) plants, the rod worth minimizer (RWM) is used below a specified power (typically 5 to 20 percent) to enforce the rod withdrawal sequence. To limit the worth of the rod that could be dropped in the group notch class of plants, a group notch rod sequence control system (RSCS) is installed to control the sequence of rod withdrawal. In General Electric (GE) built BWR/6 plants, a rod pattern control system (RPCS) is used to enforce BPWS rules.

The sequence of the accident is as follows:

1. At some time, a fully inserted rod becomes decoupled from its drive and sticks in the fully inserted position.

2. During the startup sequence, rod patterns are employed that are permitted by the constraints on rod movement imposed by the plant Technical Specifications and hardware including the maximum allowable number of bypassed rods. At some time, under critical reactor conditions, a rod pattern exists for which the decoupled rod has the maximum incremental worth from fully inserted to the position of its drive. The rod is assumed to drop at this time.

3. The reactor goes on a positive period, and the initial power burst is terminated by the fuel temperature reactivity feedback.

4. The 120-percent average power range monitor (APRM) power signal scram occurs (no credit is taken for the intermediate range monitor or setdown APRM scram).

5. All withdrawn rods, except the decoupled rod, scram at the Technical Specifications rate.

6. A scram terminates the accident.

A.2.2 Current Analysis Method

The current CRDA analysis method is described in Reference 3 and employs PHOENIX4/POLCA7 (Reference 4) and RAMONA-3 codes. As described in this report, the POLCA-T code replaces RAMONA-3 code. Thus, the steady-state methods are the same as the ones employed in the current CRDA methodology. The code replacement affects only the transient method applied in the dynamic evaluation of CRDA consequences. In general, the POLCA-T code utilizes the same approach as RAMONA-3. However, POLCA-T incorporates advanced neutron kinetics and thermal-hydraulics models and integrates the Westinghouse core design and thermal mechanics methods in its applications.

A.2.3 Design Basis

The licensing requirements for the consequences of the CRDA are established in GDC 28 (Reference 1). According to GDC 28, the effects of postulated reactivity accidents should neither result in damage to the reactor coolant pressure boundary greater than limited local yielding, nor cause sufficient damage to the core, its support structures, or other reactor pressure vessel internals to impair significantly the capacity to cool the core.

In addition, the offsite radiological consequences resulting from the predicted fuel failures during the postulated CRDA should be within the requirements of 10 CFR Part 100, Reactor Site Criteria.

A.2.4 Design Basis Acceptance Criteria

The Westinghouse design bases for the CRDA have been selected to be in compliance with the requirements in subsection A.2.3.

The design basis acceptance criteria against which the consequences of the CRDA are evaluated are given in Reference 2 (NUREG-0800, SRP Section A.15.4.9). The current SRP acceptance criteria are:

1. Reactivity excursions should not result in a radially averaged fuel rod enthalpy greater than 280 calories/gram at any axial location in any fuel rod.

2. The maximum reactor pressure during any portion of the assumed excursion should be less than the value that will cause stresses to exceed the "Service Limit C" as defined in the American Society of Mechanical Engineers (ASME) Code.

3. The number of fuel rods predicted to reach assumed thresholds and associated parameters, such as the mass of fuel reaching melting conditions, will be input to a radiological evaluation. The assumed failure thresholds are a radially averaged fuel rod enthalpy greater than 170 calories/gram at any axial location for zero- or low-power initial conditions, and fuel cladding dryout for rated power initial conditions.

Recent tests of rapid (prompt-critical) reactivity insertion events with highly irradiated fuel have indicated that the current NRC peak fuel enthalpy criterion may not be conservative. Therefore, various new criteria are being proposed by the industry through the Electric Power Research Institute (EPRI) (Reference 11) for the allowable fuel enthalpy increase as a function of the fuel burnup or cladding oxidation. The revised criteria are expected to apply only to the zero- or very-low-power prompt-critical case, and may affect the fuel failure limit as well as the coolability limit.

Revised SRP design basis acceptance criteria are not currently available, but will be adopted by Westinghouse when they become finalized and endorsed by the NRC.

A.2.5 Parameter Sensitivities and PIRT Tables

All processes and phenomena that occur during a CRDA do not equally influence the plant behavior. Phenomena Identification and Ranking Tables (PIRTs) are developed to reduce all candidate phenomena to a sufficient manageable set by identifying and ranking the phenomena with respect to their influence on the critical safety parameters. The ranking is based on the perceived impact of the phenomena on specified critical parameters and the critical parameters depend on the accident scenario.

The CRDA licensing analysis must demonstrate that the design acceptance criteria for the accident as established in subsection A.2.4 have been satisfied. The critical safety parameters will be those that have a strong impact on the radially averaged fuel rod enthalpy and reactor pressure.

The phenomena that are of importance in determining the consequences of a rod ejection accident in a pressurized water reactor (PWR), particularly in high burnup fuel cores, have been identified in the NRC's PIRTs for this accident as described in Reference 12 (NUREG/CR-6742). The phenomena identification and ranking tables presented in this document are based on References 12 through 14, and on the work previously performed and documented in Reference 3 (CENPD-284-P-A).

The PIRTs have also the additional purpose of determining the scope of uncertainty analyses. Uncertainties in the modeling of highly ranked phenomena are carefully evaluated and then combined to determine the total model uncertainty. Sensitivity analyses are used to quantify how individual uncertainties influence the total uncertainty so that the greatest effort can be focused on establishing the uncertainties of those phenomena that have the greatest impact on the critical safety parameters.

A.2.5.1 Rankings

The ranking of the phenomena is done on a scale of "not applicable" to "high importance" using the following categories:

High importance (H):	The phenomenon has a significant impact on the critical safety parameter and should be included in the overall uncertainty evaluation.
Medium importance (M):	The phenomenon has a moderate impact on the critical safety parameter and may be excluded in the overall uncertainty evaluation.
Low importance (L):	The phenomenon has no impact on the critical safety parameter and does not need to be considered in the overall uncertainty evaluation.
Not applicable (NA)	The phenomenon is not applicable to the CRDA event.

A.2.5.2 Critical/Key parameters

The critical/key parameters for the CRDA analyses focus on characterizing the power history during the reactivity pulse and the fuel enthalpy increase during the pulse including the temperature distribution in the fuel rod (pellet, gap, and cladding). The high and medium importance phenomena are shown in Table A.2-1 and have been ranked relative to how they impact these critical parameters for the system analyses.

Table A.2-1. Control Rod Drop Accident Analysis PIRT

Subcategory	Phenomenon	Importance	Affected[1]	Rationale
Calculation of Power History During Pulse (including pulse width)	Control rod worth	High	Yes	Determines the amount of reactivity insertion.
	Rate of reactivity insertion	Medium	No	Within limits, the accident outcome is insensitive to the rate of reactivity insertion.
	Moderator feedback	Medium	Yes	While the moderator coefficient can be up to 30 times larger than the Doppler temperature coefficient, the moderator temperature rise is small. The effect is small, but not negligible.
	Fuel temperature feedback	High	Yes	The fuel temperature feedback causes the power excursion to turn around and essentially limits the energy deposition.
	Delayed neutron fraction	High	Yes	Determines when prompt criticality is reached.
	Reactor trip (scram) reactivity	Low	No	It is important to terminate the accident, but the effect is minor relative to the pulse.
	Fuel Cycle design	High	Yes	Determines the total control rod worth, and it may also affect the high burnup fuel assemblies adjacent to fresh fuel assemblies.
Calculation of Pin Fuel Enthalpy Increase During Pulse (including cladding temperature)	Heat resistance in high burnup fuel, gap, and cladding	Medium	Yes	Per Reference 12, at maximum, 25% of the deposited energy is conducted out and does not contribute to the fuel enthalpy increase.
	Transient cladding-to-coolant heat transfer coefficient	Medium	No	Per Reference 12, at maximum, 25% of the deposited energy is conducted out and does not contribute to the fuel enthalpy increase.
	Fuel and cladding heat capacities	High	No	The enthalpy is the integral of heat capacity and temperature. Enthalpy and enthalpy increase are both highly important.
	Fractional energy deposition in pellet	Low	No	The fraction of the total power deposited in the coolant is small.
	Pellet radial power distribution	Medium	No	This element is rated lower because it is only one part of the total heat transfer audit.
	Pin-peaking factors	High	Yes	Determines how much energy is directed to the peak location.
Initial Conditions	Initial power level	High	No	Affects the inlet subcooling, initial axial power shape, and moderator density feedback.
	Feedwater temperature	High	No	Affects the inlet subcooling, initial axial power shape, and moderator density feedback.
	Total core flow	Medium	No	Fuel enthalpy is relatively insensitive to core flow.
	Steam dome pressure	Medium	No	Affects the moderator properties (assuming constant inlet temperature).

Notes:
1. Affected refers to whether or not the phenomenon can be affected by core design, fuel type or plant type.

A.2.5.2.1 Control Rod Worth

The control rod worth determines the amount of reactivity insertion. The peak fuel enthalpy increases rapidly with increasing total reactivity worth. [

]^{a,c}

The sensitivity of peak fuel enthalpy to total reactivity worth and the clear correlation between the two parameters confirm the usefulness of the total reactivity worth as an indicator of CRDA severity. This sensitivity also illustrates the importance of identifying the startup configurations with the highest total reactivity worth for a specific CRDA evaluation. Therefore, the sensitivity of the peak fuel enthalpy during a CRDA to total reactivity worth and the strong correlation between the two parameters provide both motivation and justification for the Westinghouse two-step process for evaluating the CRDA. The speed and convenience of the 3-D nodal simulator calculations allow a sufficiently broad survey of the startup control rod sequences during the cycle to confidently identify a relatively small number of candidates for the limiting configuration. These candidates then can be evaluated with the POLCA-T dynamic calculations.

A.2.5.2.2 Fuel Temperature Feedback

The Doppler effect is treated by assuming that the nodal fast absorption, removal, and fission cross-sections vary as the square root of the fuel temperature in the POLCA-T calculations. The Doppler effect is, therefore, provided to POLCA-T on a nodal basis and handled as part of the cross-section treatment. The Doppler effect terminates and reverses the initial power excursion. Therefore, the peak fuel enthalpy is generally quite sensitive to the magnitude of the Doppler feedback.

Since the effects of fuel temperature and burnup are accounted for by the cross-section dependence, the impact of these variables on the Doppler feedback is automatically accounted for with the Westinghouse methodology. As discussed in Section A.4, candidates for the most limiting dropped rod are evaluated at a sufficient number of state points throughout the cycle to assure that the most reactive configuration is identified. POLCA-T dynamic calculations are performed with the cross-section, burnup, and void history information from the appropriate state point for which a given candidate was identified. The same nuclear data base that was used for the static 3-D nodal simulator calculations, (that is, core design calculations) is used for the dynamic POLCA-T calculations. Furthermore, the fuel temperature is updated at each time step in the POLCA-T calculations. Therefore, the effects of burnup and fuel temperature are explicitly accounted for.

A.2.5.2.3 Delayed Neutron Fraction

POLCA-T uses the nodal effective delayed neutron fractions obtained by POLCA7, thus their historical and spectral dependencies are accounted for. They are treated in a similar way to the cross-sections (XS) and are updated each time step during the transient simulation to account for their dependence on the instantaneous density, the control rod (CR) presence in the node, and the nodal neutron flux changes. Despite their small impact on the fuel enthalpy, the delayed neutrons precursors constants and neutron velocities are treated in the same way as the delayed neutron fractions.

A.2.5.2.4 Fuel Cycle design

This phenomenon with a high importance ranking is addressed in the first step of methodology selection of the candidates for the limiting CR when the cycle-specific calculations are performed. The methodology is accounting for the core loading pattern and cycle exposure by evaluating the possible CR sequences and out-of-sequence CR at a sufficient number of state points throughout the cycle from the beginning to end of cycle (BOC to EOC). Axial and radial power distribution, CR bank positions, and xenon distribution are also considered in the first step of methodology. POLCA-T dynamic calculations of CRDA for the selected CRs are performed with the cross-section, burnup, void history, xenon, and iodine information from the appropriate state point for which a given candidate was identified.

A.2.5.2.5 Fuel and Cladding Properties and Gas Gap Modeling

Fuel and cladding properties (that is, heat capacity and thermal conductivity), and gas gap model of a licensed fuel performance code (such as, STAV7 of Reference 15) are incorporated into the POLCA-T code and used in the CRDA analysis. In the transient CRDA simulation, [

]^{a,c} The hot fuel rod temperature and properties are used to calculate the peak nodal enthalpy. Thus, the transient CRDA methodology using POLCA-T code applies the same methods and models used in the fuel thermal mechanical design.

A.2.5.2.6 Pin Peaking Factors

The nodal pin peaking factors used in POLCA-T are obtained by incorporated pin power reconstruction model of the core simulator POLCA7 (Reference 4). The local peaking factors are updated at each time step of the transient simulations. [

]^{a,c} Nodal pin peaking factor is accounted for in the enthalpy evaluation of the so-called hot fuel rod in each node as described in subsection A.2.5.2.5.

A.2.5.2.7 Rate of Reactivity Insertion

The rate of reactivity insertion for a given CR worth is determined by the CR drop velocity. The CR drop velocity has minor effect on the power and fuel enthalpy maximum values. It affects mainly the time when these maximum values are observed. The CR drop velocity for a GE-built plant is the same bounding value used in Reference 3 (CENPD-284-P-A) that is, 0.948 m/sec (3.11 ft/sec)[1]. For licensing calculations and in the absence of plant data that would justify the use of a less conservative value, the control rod is assumed to drop at the maximum drop velocity of 0.948 m/sec (3.11 ft/sec) established in Reference 3.

A.2.5.3 Initial Conditions

The initial conditions must be assessed to determine how they impact the plant response to the CRDA. The identified most important initial conditions and their perceived importance ranking on the critical safety parameters are presented in Table A.2-1. Sensitivity studies were then performed to confirm the perceived rankings for these initial conditions. The confirmed ranking was used to select either a bounding or a characterizing range of those high- or medium-importance ranked conditions.

A.2.5.3.1 Initial Power Level

The initial power affects the peak fuel enthalpy through the heat conductivity, moderator density feedback, and initial axial power shape. When the initial power increases, the inlet subcooling is reduced. This, in turn, increases the heat conductivity and moderator density feedback. This results in a reduced peak fuel enthalpy.

The initial power level at cold-zero-power (CZP) condition at a given subcooling does not affect the results of the transient significantly. If the initial power, for example, rises from 40 W to 1 kW, it just implies that the power peak occurs earlier in the transient. The final maximum power level will, therefore, not change significantly. In both cases, a power excursion is generated due to prompt reactivity. The power peak, at a strongly subcooled condition, will mainly be interrupted by the negative reactivity feedback from Doppler. The amount of negative reactivity from Doppler is caused by the same fuel temperature rise in both cases, which implies that the maximum enthalpy is essentially the same.

A.2.5.3.2 Feedwater Temperature

The feedwater temperature determines the core inlet temperature/subcooling. The moderator temperature affects the fuel enthalpy both through the heat conductivity from the fuel rod to the coolant and the moderator density feedback to the core power. For a given reactivity insertion by the dropped control rod, the initial moderator subcooling is an important factor in determining the fluid properties of the moderator during the transient. [

]^{a,c}

1. According to Reference 3, this velocity is justified in the NEDO-10527 report as the maximum rod drop speed that could be achieved allowing for tolerances in physical dimensions at the 3 σ level.

A.2.5.3.3 Steam Dome Pressure

[

]^{a,c}

A.2.5.3.4 Total Core Flow

The peak fuel enthalpy is relatively insensitive to core flow within the range expected during startup. Therefore, the minimum allowed core flow rate is used in present analyses at limiting CZP conditions.

Sensitivities have established that the accident is most severe when it is assumed to occur at low- or zero-power conditions when the CR patterns required to establish criticality provide the highest values of incremental (dropped) single CR worth. Furthermore, the presence of voids in the core at any significant power level will decrease the consequences of the accident through the negative moderator density reactivity (void) coefficient and the relatively low heat conductivity associated with subcooled conditions. Consequently, the evaluation of the accident usually can be limited to highly subcooled conditions and dropped control rod configurations providing relatively large integrated reactivity and high final nodal peaking.

A.3 ASSESSMENT DATA BASE

The validation matrix of POLCA-T ranges from simple available analytical solutions, over small-scale basic and component tests known also as separate effects tests, to full-scale BWR bundle tests, to integral thermal-hydraulic tests, to well accepted international/Organization for Economic Co-operation and Development (OECD) benchmarks, and finally to recorded reactor plant events and transients.

This section contains information to validate that the Westinghouse methodology described in Section A.4 for evaluation of the CRDA is sufficiently accurate and conservative for licensing applications. The validation is provided by systematically addressing the significant components of the methodology that affect the predicted peak fuel enthalpy, which is compared to the design bases. The qualification work is divided in two parts: the first part considers the single parameter confirmation and separate effects, and the second considers the validation against integral effects. Specifically, the following areas are addressed:

1. The capability of the supporting PHOENIX4/POLCA7 system of codes to provide adequate local pin power distributions, cross-sections, burnup, and void histories for POLCA-T is discussed in subsection A.3.1.1. [

]^{a,c}

2. The capability of the POLCA-T code to predict physical phenomena important for the determination of peak fuel enthalpies is addressed in subsection A.3.1.2. Specifically, the adequacy of the methodology for establishing the Doppler temperature feedback, reactivity, and power response resulting from an ejected CR and capability in predicting the local power that is crucial for determining the correct fuel enthalpy are discussed in POLCA-T qualification against the NEACRP-L-335 3-D LWR Core Transient benchmark.

3. The capability of POLCA-T to simulate very fast integral events such as the Turbine Trip event (TT). Specifically, simulations of the Peach Bottom EOC 2 TT tests are provided in subsection A.3.2.1. To our knowledge, these tests provide the best data for directly testing the POLCA-T neutronic (the moderator density feedback), thermal-hydraulic (heat transfer from the fuel rod to the coolant, void fraction formation, and collapse), and fuel rod thermal-mechanic models (fuel, cladding, and gas gap properties) capability to simulate a very fast transient with the same time scale as a CRDA.

4. The capability of POLCA-T to simulate integral tests of a CRDA. Specifically, the results of the simulations of three of the SPERT-III-E power excursion tests are provided in subsection A.3.2.2. These SPERT tests provide the data for directly testing the POLCA-T capability to describe a CRDA.

5. Finally, the comparison of the POLCA-T with the RAMONA-3 code for commercial BWR CRDA analyses illustrating the similarity of the results obtained by previously used tools and the ones described in this report is presented in subsection A.3.2.3.

A.3.1 Single Parameter Confirmation And Separate Effects

A.3.1.1 PHOENIX4 and POLCA7 Qualification

The PHOENIX4 code provides cross-section data to POLCA7 as well as local (pin) power distributions and kinetics parameters, such as delayed neutron fractions and inverse velocities, for the CRDA calculations (see Section A.4). POLCA7 provides burnup and void history distributions and is used to identify candidates for the POLCA-T control rod drop analyses primarily based on calculated total control rod reactivity worths. [

]^{a,c}

Confirmation of the capability of PHOENIX4 and POLCA7 to calculate these quantities with sufficient accuracy to support demonstration by POLCA-T that the CRDA design bases are satisfied is provided in Reference 4. The mentioned reference contains detailed qualification bases for the use of the PHOENIX4/POLCA7 code system for steady-state nuclear design and analyses of BWR cores and was accepted by the NRC for BWR reload design and analysis applications in 2000.

The qualification of POLCA7 is described in details in Reference 4 (Topical Report CENPD-390-P-A), Section A.4. Qualification activities are divided into two categories referred to as verification and validation. Verification involves the testing of individual models or combinations of models to verify that they perform as intended. Validation involves the comparison of POLCA7 predictions with measured data to establish the accuracy of the system operating as a whole.

The POLCA7 verification was performed by comparison with computational benchmarks generated by means of reference calculations as well as by comparison with experimental data suitable for evaluating the individual model being verified. Specifically, the POLCA7 verification effort covers the three areas listed below:

- The neutronics model is verified by comparison with established 2-D analytical benchmarks. Three of the analytical benchmarks involve power calculations without depletion for both PWR and BWR cores. The fourth benchmark provides verification of the POLCA7 depletion models.

- Verification of the thermal-hydraulic model by comparisons with test loop pressure drop measurements and individual channel flow measurements in a Nordic BWR.

- The POLCA7 pin power reconstruction model is verified by comparison with a pin power distribution benchmark. Furthermore, the capability of POLCA7 to predict relative nodal fuel pin and fuel rod power distributions is verified by comparisons with fuel rod gamma scan data.

The POLCA7 validation involves the evaluation of core follow predictions for four reactors as well as comparisons with gamma scan measurements. Specifically, $k_{effective}$ values at hot and cold conditions calculated by POLCA7 are evaluated, and measured in-core detector responses and measured gamma scan data are compared with POLCA7 predictions. The gamma scan, reactivity, and traveling in-core probe (TIP) data were obtained from four BWRs; two Westinghouse-built internal pump reactor and two GE-built plants (a BWR/4 and a BWR/6). For more details see Reference 4.

A.3.1.2 OECD NEACRP 3-D LWR Core Transient Benchmark

The Nuclear Science Committee (NSC) of the Nuclear Energy Agency (NEA)/OECD has released a set of computational benchmark problems for the calculation of reactivity transients in PWRs and BWRs (Reference 5). These benchmark problems verify data exchange in a coupled code system and test the neutronics coupling to fuel transient conduction methodology. Among the benchmark BWR problems, there is none involving fast reactivity initiated transient. Thus, the validation against the PWR rod ejection accidents (REAs) benchmark is aimed at validating the code for the BWR CRDA, as the analyses of both transients require identical phenomena to be modeled.

All six cases of the NEACRP PWR rod ejection transients benchmark have been analyzed by the POLCA-T code. The hot-zero-power (HZP) and full-power realistic problems with symmetrical and asymmetrical rod ejection cover a variety of reactivity excursions from 0.1$ to 1.26$. The obtained results were compared with the reference PANTHER[2] solutions and the published results of RAMONA/POLCA/RIGEL, CORETRAN, RETRAN-3-D, and TRAC-BF1/NEM codes.

2. The Nuclear Energy PANTHER code solves two-group homogeneous neutron diffusion equations in both steady-state and transient form using an analytical nodal method and generalized thermal-hydraulics feedback model for a PWR.

Of the six, problem C1, the HZP full-core asymmetrical case, is the most severe and relevant to the CRDA case. The POLCA-T results of C1 case are summarized and compared to the PANTHER 4x4 reference solution (Reference 7) and the results of Westinghouse PWR 3-D kinetic tools SPNOVA/VIPRE (Reference 14) in Table A.3-1. a,b,c

[ ]

Figure A.3-1 presents the core average axial power distributions predicted by POLCA-T code and their comparison with reference solutions and POLCA7 results for benchmark case C1. POLCA-T and POLCA7 results and reference solutions have been normalized before the comparison. Mean absolute Deviations (MD) and root mean square (RMS) errors have also been calculated and provided in Table A.3-2 for all six benchmark cases[3].

3. The reference axial and radial power distributions are available only from the original 2x2 solution (Reference 6). Thus the comparison is performed against this solution.

a,b,c

Figure A.3-1. POLCA-T Case C1 Core Axial Power Distribution and Comparison with the Reference Solution (Reference 6) and POLCA7 Code

a,b,c

MD and RMS error (standard deviation) were defined by the following formulas

$$MD = \frac{1}{N}\sum_{i=1}^{N}\left|x_i - \hat{x}_i\right|, \text{ and} \tag{3.1}$$

$$RMS = \sqrt{\frac{1}{N}\sum_{i=1}^{N}\left(x_i - \hat{x}_i\right)^2}\ , \tag{3.2}$$

where x_i is the core average axial nodal power calculated by POLCA-T (or POLCA7) code, $\hat{x}_i$ is the reference core average axial nodal power obtained by PANTHER code, N is the number of axial nodes.

[

]^{a,c}

Figure A.3-2 presents the comparison of POLCA-T predicted power time history for benchmark C1 case with reference PANTHER solutions (References 6 and 7). [

]^{a,c}

a,b,c

Figure A.3-2. POLCA-T Case C1 Power Time History and Comparison with PANTHER Reference Solutions (References 6 and 7)

Figure A.3-3 presents local power at axial layer 13 radial power distributions at initial state and at power peak. The comparison of POLCA-T and reference PANTHER solution radial power distribution at initial state, at power peak, and at final state 5 s are summarized in Table A.3-3. Absolute deviations and RMS errors defined by equations (3.1) and (3.2) are [ ]^{a,c} percent and [ ]^{a,c} percent for assembly average power and less than [ ]^{a,c} percent and [ ]^{a,c} percent for local power.

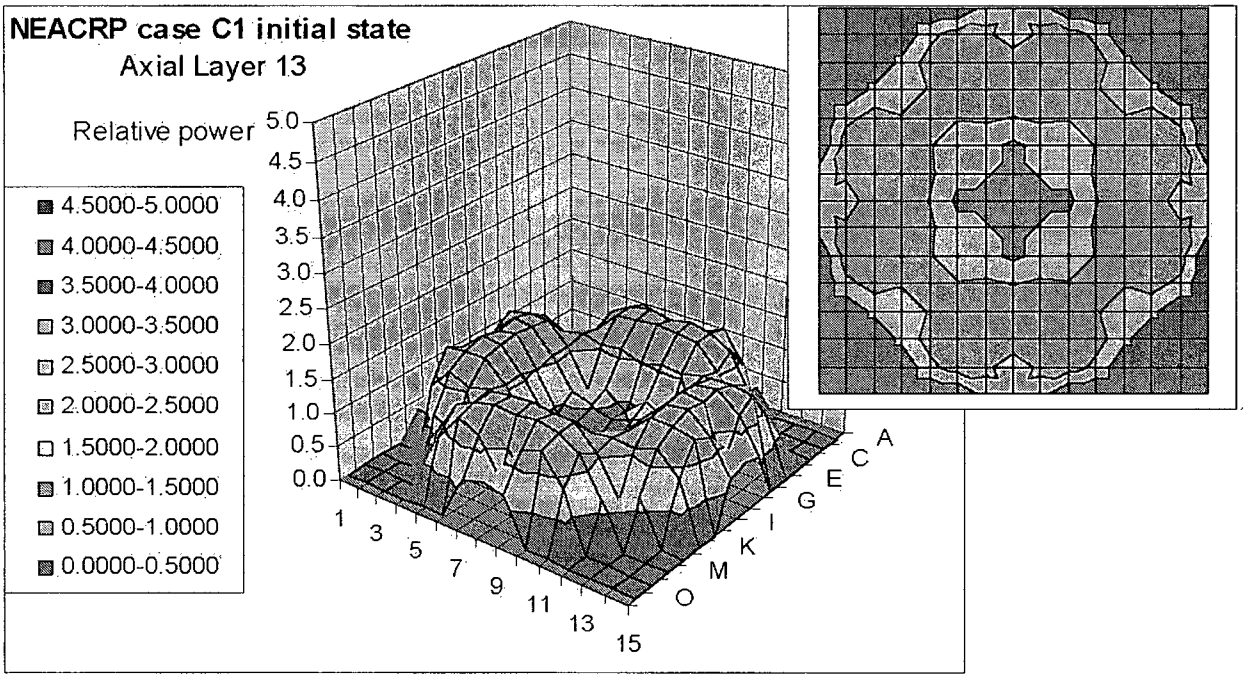

a)

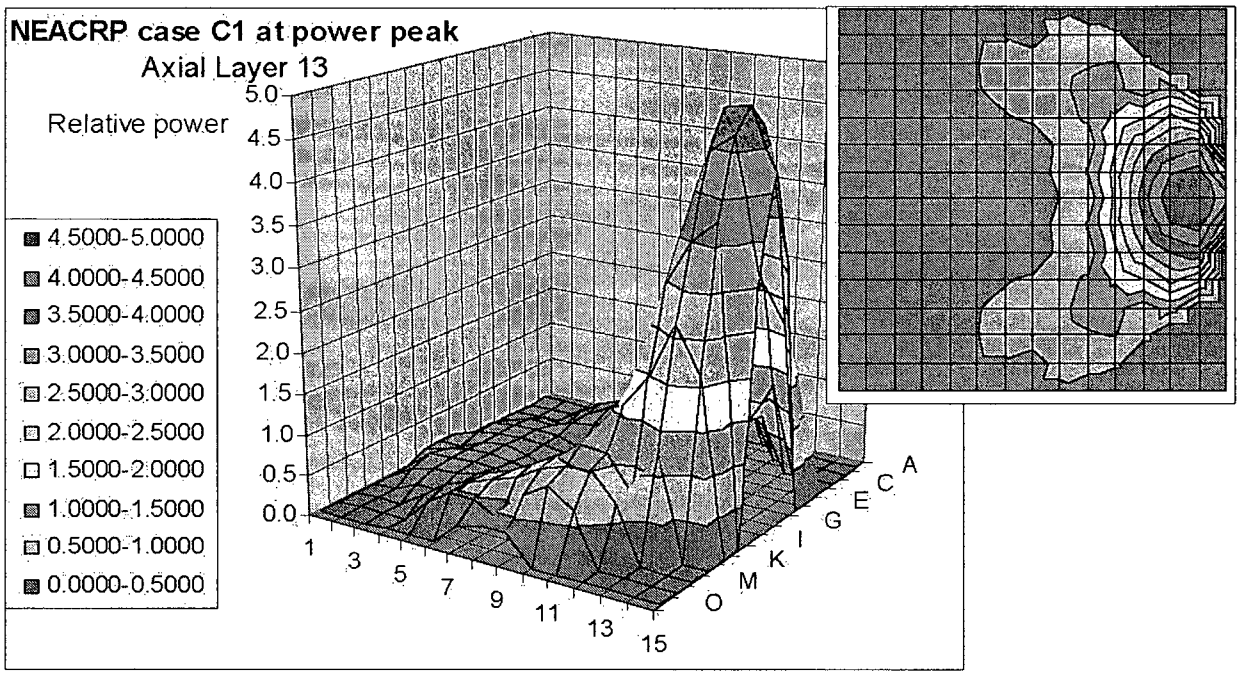

b)

Figure A.3-3. POLCA-T Case C1 Radial Power Distribution at Axial Layer 13: a) at Initial State and b) at Power Peak

a,b,c

Summarizing the POLCA-T results and comparison with the reference solution allows the following observations to be made:

- [ ]^{a,c} The deviation is small and of the same range as other codes.
- POLCA-T predicts the initial power distribution well.
- [ ]^{a,c} The deviation is small and conservative.
- POLCA-T [ ]^{a,c} the fuel temperature increase and the core exit temperature increase.

The following conclusions had to be drawn:

1. POLCA-T initial steady-state results demonstrated excellent agreement in critical boron, CR reactivity worth, and 3-D power distributions with both the reference solution (PANTHER) and the POLCA7 results.

2. POLCA-T transient results are within the spread of the PANTHER reference solution and other state-of art codes for predicted power peak and energy contents. The observed deviations are small for the most severe, and most CRDA relevant, case C1. The POLCA-T transient results demonstrated:

   - Good agreement in transient 3-D power shape with reference PANTHER solution, axially and radially, at time of power peak and in final transient state

   - Good agreement in core average fuel temperature increase and in core outlet coolant temperature

3. POLCA-T gives similar agreements as the NRC-approved Westinghouse PWR transient code SPNOVA/VIPRE.

4. Overall, the above conclusions show that POLCA-T is a state-of-art tool to accurately predict:

   - Inserted reactivity at design basis control rod/assembly initiated accidents
   - Core response to the reactivity insertion
   - The resulting global and local core power transients

Since the local transient power is accurately predicted, the resulting fuel enthalpy increase will also be adequate. Thus the NEA REA benchmark supports that POLCA-T is a state-of-art tool also for BWR CRDA analysis.

A.3.2 Integral Effects

The validation of POLCA-T against integral tests such as the Peach Bottom EOC 2 TT tests (Reference 8) and the SPERT-III-E power excursion tests (Reference 9) and the comparison with the RAMONA-3 code for commercial BWR CRDA analyses are presented in this section.

A.3.2.1 OECD/NRC BWR Turbine Trip Benchmark and Peach Bottom 2 EOC 2 TT Tests

The Peach Bottom 2 (PB2) three TT tests conducted at the EOC 2 has been widely used for validation of system thermal-hydraulic codes. Despite the fact that the turbine trip event is mainly driven by void feedback, the Doppler feedback contributes up to 20 percent of the total reactivity. Turbine trip tests conducted at PB2 at the EOC 2 are of the same time scale as the CRDA, that is, the sharp power increase is observed in the very first second of the transient. Thus, turbine trip tests play an important role in the validation of fuel and core models of coupled codes. In this report, the tests are used to assess the capabilities of the neutron kinetics and thermal-hydraulic code models to correctly predict the plant behavior in a very fast transient.

The first step of POLCA-T validation against PB2 EOC 2 TTs was performed in the frame of OECD/NRC BWR turbine trip benchmark. POLCA-T results had been submitted for all three phases of the benchmark including the extreme scenarios. The code results of exercises 1 and 2 have been published also in the OECD benchmark summary reports References 16 and 17. A summary report on exercise 3, including the extreme scenarios, will be issued by OECD in the near future. However, the benchmark was limited to only one of the turbine trip tests - TT2, although it also required the analyses of challenging extreme cases without scram or/and steam bypass activation, and even without safety/relief valves (SRVs) available. Moreover, some limitations in the benchmark specifications such as using Pennsylvania State University (PSU) cross-section data in specific format, specified fuel properties and models, did not allow the utilization of all POLCA-T features and the validation of Westinghouse BWR methodology for transient analyses. Consequently, additional validation was conducted against all three performed turbine tests TT1, TT2, and TT3 (Reference 19). The work consisted of cross-section data generation using the PHOENIX4 code, core follow calculations for PB2 Cycles 1 and 2 by the POLCA7 code and POLCA-T simulations of TT1, TT2, and TT3 tests.

The accuracy of the PHOENIX4 XS data and core follow calculations was confirmed by good agreement with available TIP measurements at the EOC 2 prior to the conduction of the TT and stability tests.

The comparison of results obtained from steady-state calculations by both the POLCA7 and POLCA-T codes for the state prior to TT2 demonstrated that use of Westinghouse's multi-table cross-section data gives much better agreement with plant data ("P1 edit" in Figure A.3-5) for axial power distribution that the previous results reported in the frame of the benchmark (see Figure A.3-4). This demonstrates the effect of using the PHOENIX4 multiple cross-section table and accounting for historical effects in BWR modeling.

a,b,c

Figure A.3-4. POLCA-T Core Average Axial Power Profile Obtained by Different Cross-Section Data at EOC2 State Prior to TT2. (Comparison versus plant data (P1 edit Reference 8))

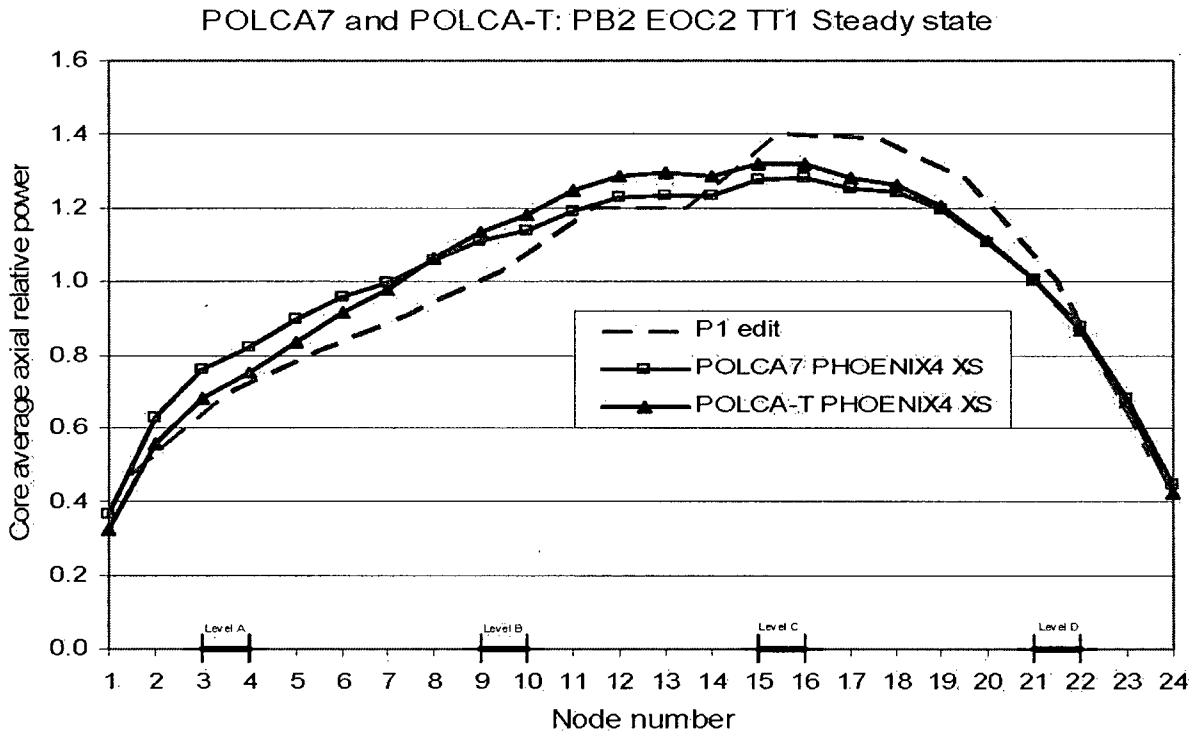

a) TT1 test

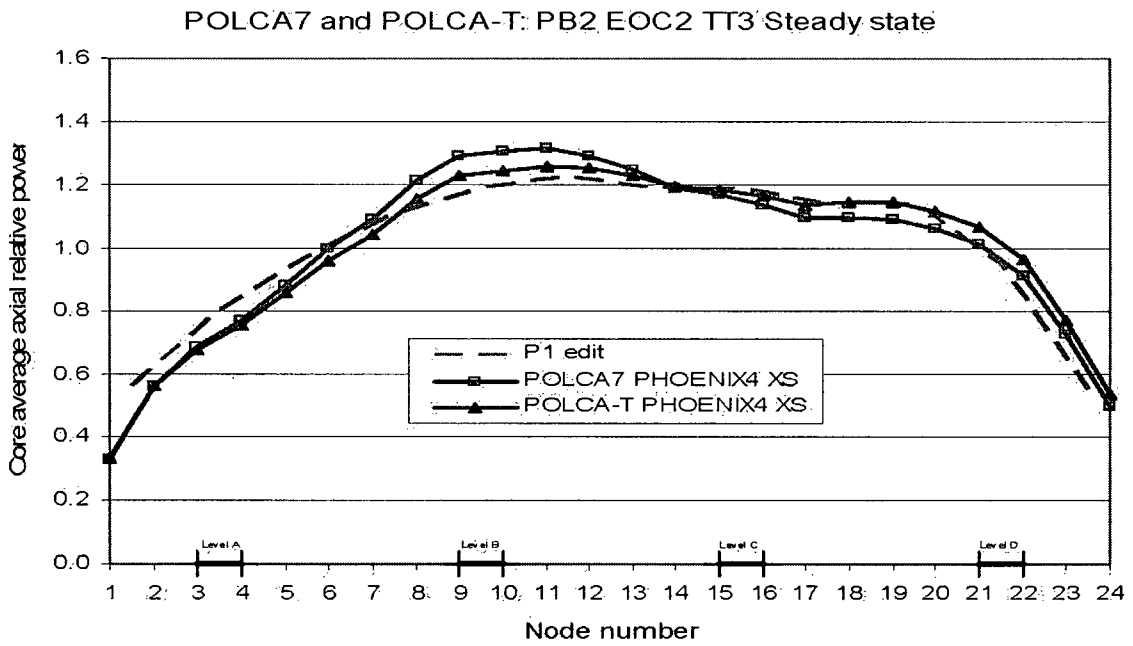

b) TT3 test

Figure A.3-5. POLCA7 and POLCA-T Core Average Axial Power Profile for State Prior to TT1 (a) and TT3 (b) tests. (Comparison versus Plant Data (P1 edit Reference 8))

The 3-D core model was qualified by comparison of core axial power profile with plant data ("P1 edit") for each state prior to TT tests (see Figure A.3-5a for TT1 and Figure A.3-5b for TT3). POLCA-T simulation is performed with PHOENIX4 cross-section data only. POLCA-T local power distributions were compared with available local power range monitor (LPRM) records for all three TT tests. [

]^{a,c}

Two different POLCA-T simulations of the TT2 test have been performed using both sets of cross-section data, that is, the one distributed in the benchmark and the other generated by PHOENIX4. [

]^{a,c} The results with PHOENIX4 cross-section data (both with and without spectral interaction model) showed better agreement with the measured power than the results obtained with the PSU cross-section data. The power peak is slightly underestimated by POLCA-T when using PHOENIX4 cross-section data, and overestimated when using PSU cross-section data (see Table A.3-4). PHOENIX4 XS data improved the agreement to the measured time of the power peak. The results of the POLCA-T TT 2 transient simulations are in good agreement also with measured data for steam dome, core exit, main steam line and turbine inlet pressures, and reactor pressure vessel (RPV) level.

a,b,c

[

]

The sequence of events and peak power values for TT1 and TT2 tests are presented in Table A.3-5. Figure A.3-6 presents the TT2 fission power time history. Figure A.3-7 illustrates POLCA-T predicted fission power time history in the first 5 seconds of the TT1 transient and its zoom 0.5 – 1.0 seconds. Results show that POLCA-T slightly overestimates the power. Comparison of POLCA-T predicted time histories and measured data for integral parameters, (that is, steam dome and core exit pressures, main steam line and turbine inlet pressures, and RPV water level) are in good agreement also.

4. Spectral interaction model is a part of POLCA7 cross-section model incorporated in POLCA-T. It corrects the cross-section for the spectral index, that is, the ratio of the epithermal to thermal neutron fluxes.

a,b,c

[

]

Comparison between measured and calculated transient responses of three selected[5] LPRM strings are shown in Figures A.3-8 and A.3-9 for TT1 and TT2 tests. It is shown that POLCA-T predicts the local power well.

5. Strings 5 (08-49) and 13 (24-41) are selected to represent the core periphery and the core central zone.

a,b,c

Figure A.3-6. Comparison of POLCA-T TT2 Fission Power Time History Obtained by Different XS Data Versus PB2 Measured Data

a,b,c

Figure A.3-7. Comparison of POLCA-T TT1 Fission Power Time History vs. PB2 Measured Data

a,b,c

Figure A.3-8. TT1 Transient LPRM Response for String 5

a,b,c

Figure A.3-9. TT1 Transient LPRM Response for String 13

The validation of POLCA-T against PB2 TT2 tests proved the code capabilities to correctly simulate pressurization transients with very fast power increases. The results obtained for the extreme cases demonstrate the POLCA-T code wide-range capabilities to simulate transients with failure of the scram, steam bypass, and SRV at extremely high reactor pressure and core power. The results of the validation work can be summarized as follow:

1. POLCA-T steady-state results agree well with the measured PB2 steady-state data: TIP, P1 edit, and LPRM.

2. POLCA-T transient simulations of PB2 EOC2 TT tests are in good agreement with measurements: both for integral and local parameters.

3. The results for TT2 that showed better agreement with the measured data where obtained with PHOENIX4 generated cross-section data. This is observed both in the steady-state and transient simulations. [

   ]^{a,c}

4. The power peaks are in good agreement with measured data for TT1 and TT2. [

   ]^{a,c}

5. The predicted pressures for the turbine inlet, main steam line, and steam dome are in good agreement with measurements.

6. Comparison of calculated and measured LPRM signals demonstrated the code capability for both steady-state and transient local power simulation.

The POLCA-T neutronic (the moderator density feedback), thermal-hydraulic (heat transfer from the fuel rod to the coolant, void fraction formation and collapse), and fuel rod thermal-mechanic models (fuel, cladding, and gas gap properties) were validated and qualified for the simulation of a very fast pressurization transients with the same time scale as a control rod accident.

A.3.2.2 SPERT-III-E RIA Experiments

This section presents the results of POLCA-T analyses performed for the code validation against the Special Power Excursion Tests (SPERTs) performed in the 1960s in the SPERT-III E-core (Reference 9). The analyses demonstrate the POLCA-T system code capability to accurately simulate reactivity insertion accidents at CZP conditions. HZP conditions are considered in subsection A.3.1.2.

The SPERT-III-E-core reactor was set up using the IDO-reports that describe the SPERT-III-E-core and the experiments performed. Cross-sections generation, steady-state, and transient analyses have been performed with the PHOENIX4/POLCA-T package. To validate the POLCA-T code against the SPERT-III-E-core experiments, three cold startup tests were selected – Cases 18, 43, and 49.

The SPERT-III-E-core was an experimental facility and is somewhere in between a PWR and a BWR in design. This type of experimental reactors is very different from the commercial reactors normally simulated with the PHOENIX4/POLCA-T code package. It is a very small reactor, approximately 1 by 1 by 1 meter, and it consists of only fresh fuel, which causes a huge leakage compared to commercial reactors. Another difference from commercial reactors is the fuel followers, or the so-called control rods. They contain fuel in the lower section and poison material, borated stainless steel, in the upper section. Additional difficulties in the simulation were caused by the lack of some initial data. For example, the position of control rods of follower types is known for critical conditions with the transient control rod withdrawn, but not at the states prior to the tests. The reactivity inserted is known, but not the position of the control rod that corresponds to that reactivity value. Moreover, the initial power level is known to be somewhere in between 0 and 50W. The reported uncertainties in the SPERT data are 15 percent for reactor power, 4 percent for reactivity insertion, and 17 percent for energy release to time of peak power (Reference 9).

The positions of the fuel followers were, therefore, adjusted to match the peak power value. Then, the time of peak power, inserted reactivity, and energy release were compared to the experimental values. Only the steady-state conditions were adjusted to match the measured peak value, and no adjustments of the transient calculations have been performed.

Table A.3-6 summarizes POLCA-T results and presents the comparison with experimental data (Reference 9). The comparison shows that, with a little less inserted reactivity, POLCA-T predicts a higher than measured peak power and fuel enthalpy. The peak power time predicted by POLCA-T is close to the measured data. Figure A.3-10 presents the comparison of POLCA-T predicted and measured fission power for cold cases 43 and 49. It has to be noted that quite better agreement between POLCA-T predictions and measured data is observed for the prompt critical Case 43 with $1.21 inserted reactivity than in Case 49 with corresponding inserted reactivity of $1.00.

a,b,c

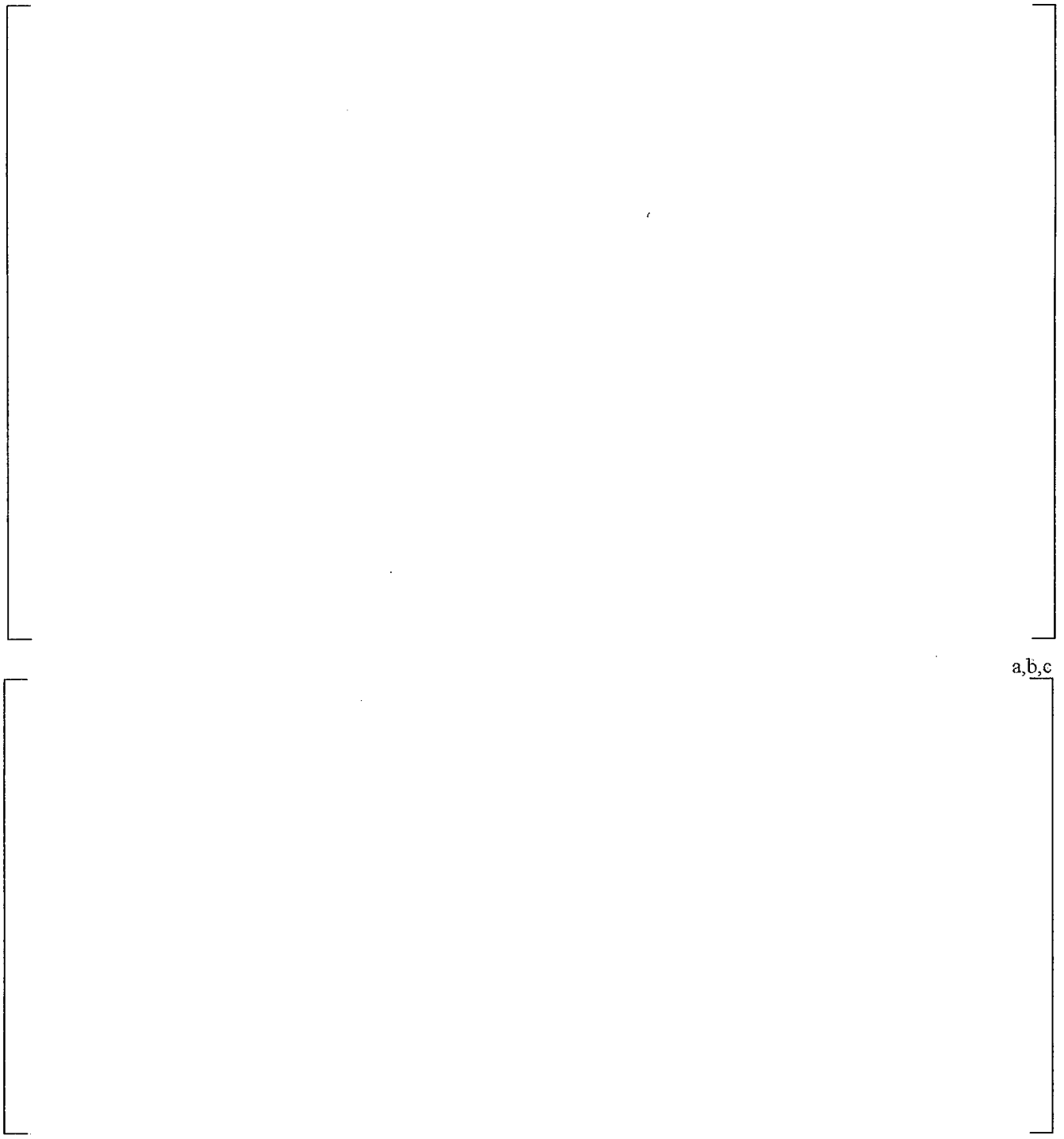

Figure A.3-10. Comparison of POLCA-T Predicted and Measured Fission Power for Cold Cases 43 and 49.

The comparison of POLCA-T simulation predictions with SPERT-III-E power excursion test results demonstrate that, for a peak power consistent with the experimental data, the Westinghouse methodology using POLCA-T predicts resulting values of inserted reactivity, power shape, integrated energy, and time-to-peak power which agree with the experimental values within the experimental uncertainties.

Therefore, it is concluded that the Westinghouse methodology predicts the results of the SPERT-III E-Core tests for which the comparisons were made within the uncertainties in the tests and the uncertainties associated with the information available regarding those tests.

A.3.2.3 POLCA-T Comparison with RAMONA-3

This section presents the results of POLCA-T CRDA comparison with RAMONA-3 for two CZP cases and one hot case at 1 percent initial power[6]. The comparison has been performed for a Westinghouse (former ASEA-ATOM) designed BWR internal pump plant. The considered core is loaded with SVEA-96 Optima2 fuel in an equilibrium cycle.

The analyses were aimed to compare the results of POLCA-T and RAMONA-3 codes application for the CRDA analysis of a commercial BWR. Each code has been run with the normally used CRDA analysis options and models. RAMONA-3 control rod input data were adjusted in order to match the POLCA7 predicted neutron multiplication factor and total incremental steady-state CR worth[7]. The analyzed initial conditions were identical in order to fairly compare the results. Hereafter, the RAMONA-3 and POLCA-T case runs, results, and observations are described.

Table A.3-7 summarizes the initial conditions for the two CZP cases and one hot case at 1 percent of rated initial power.

a,b,c

[ ]

6. The initial power is defined as 1% of rated reactor power

7. The CR cross-sections manipulation by a multiplayer is normally used in CRDA analyses performed by RAMONA-3 to match POLCA7 CR worth. This adjustment is not needed in POLCA-T applications as POLCA7 is fully integrated into POLCA-T and both codes steady-state results are consistent.

The dropped CRs have been defined together with CR checkerboard (black and white) pattern as the ones with the maximum worth rod. The subcooling in the analyzed CZP was selected to make the CRDA more severe and to compare the codes results for prompt critical transients.

The full core is modeled in RAMONA-3 and POLCA-T with one-to-one mapping between thermal-hydraulic channels and neutronic modeling of fuel assemblies.

The selected control rods in all three cases are dropped from fully inserted to fully withdrawn position with a constant acceleration of 7.4 m/s^2 in CZP and 8.0 m/s^2 in the hot case. Positions of dropped CR during the transient are presented in Figure A.3-11 and Figure A.3-13. The dropped control rods are highlighted in the figures.

This section describes and discusses the RAMONA-3 and POLCA-T results for the evaluated CRDA cases. Table A.3-8 presents the summary of the main steady-state and transient parameters. a,b,c

[

]

The adjustment of CR cross-sections in RAMONA-3 is done with certain conservatism and RAMONA-3 over predicts the CR worth by about 40 pcm in CZP cases compared to POLCA-T (see Table A.3-8).

Figures A.3-11 and A.3-13 present a comparison of POLCA-T and RAMONA-3 predicted core power time history for the three analyzed CRDA cases. [

]^{a,c}

Figures A.3-12 and A.3-14 present a comparison of POLCA-T and RAMONA-3 predicted time history of maximum fuel enthalpy. [

]^{a,c} These POLCA-T fuel enthalpy maximum values are observed later than in RAMONA-3 for CZP cases and practically at the same time in the hot case.

The following observations are made from the performed POLCA-T and RAMONA-3 CRDA analyses at CZP and hot conditions:

1. POLCA-T predicted peak power is higher than RAMONA-3 at CZP and lower at hot conditions. POLCA-T predicted time of peak power is later than the one observed in RAMONA-3 results in CZP cases and almost the same as RAMONA-3 at the hot case. [

]^{a,c}

2. POLCA-T predicts higher maximum fuel enthalpy than RAMONA-3 in all cases.

3. POLCA-T also predicts higher maximum fuel centerline temperature in all three cases than RAMONA-3.

The analyses show that while the trends are very similar, POLCA-T predicts generally higher maximum fuel enthalpy values than RAMONA-3. The differences between the two codes are not unexpected, taking into consideration the large differences that exist in models, data, and methodology.

A.3.3 Conclusions

The results in subsections A.3.1 and A.3.2 support the following conclusions:

1. The qualification of the PHOENIX4/POLCA7 system of codes in Reference 4 is sufficient to support their application in the Westinghouse CRDA methodology described in Section A.4. Specifically, the local pin power distributions, cross-sections, burnup, and void histories provided for POLCA-T are calculated with sufficient accuracy to support demonstration by POLCA-T that the CRDA design bases are satisfied. Furthermore, power distributions and void distributions are predicted by POLCA7 with sufficient accuracy to provide an adequate reference point for the corresponding power and void distributions predicted by POLCA-T just prior to the control rod drop. [

]^{a,c} Finally, the control rod worths calculated by POLCA7 are sufficiently accurate to assure that the most limiting configurations are identified and that subsequent evaluation of these configurations by POLCA-T will assure that the CRDA design bases are satisfied.

   It is concluded that the available benchmark data base for the PHOENIX4/POLCA7 code system fully qualifies it for the manner in which it is applied in the Westinghouse CRDA methodology described in Section A.4.

a,b,c

Figure A.3-11. Comparison of POLCA-T and RAMONA-3 Predicted Core Power for CZP Case 1

a,b,c

Figure A.3-12. Comparison of POLCA-T and RAMONA-3 Predicted Maximum Fuel Enthalpy for CZP Case 1

a,b,c

Figure A.3-13. Comparison of POLCA-T and RAMONA-3 Predicted Core Power for Hot Case

a,b,c

Figure A.3-14. Comparison of POLCA-T and RAMONA-3 Predicted Maximum Fuel Enthalpy for Hot Case

2. The POLCA-T neutron kinetic, thermal-hydraulic, and fuel rod performance models predict the time variation of core power, Doppler temperature feedback, moderator density feedback, heat transfer from the pellet to the coolant, and fuel pellet enthalpy with sufficient accuracy to provide reliable predictions of peak fuel enthalpy during the CRDA to confidently demonstrate that the CRDA design bases are satisfied using the Westinghouse methodology described in Section A.4.

3. Comparison of POLCA-T predictions with the PANTHER reference solution for the NEACRP-L-335 3-D LWR Core Transient benchmark show good agreement in transient 3-D power shape, axially and radially, at the time of power peak and the final transient state. Thus it is confirmed that POLCA-T is a state-of-the art tool to accurately predict the inserted reactivity at design basis control rod/assembly initiated accidents, the core response to the reactivity insertion, and the resulting global and local core transient power. Since the local transient power is accurately predicted, the resulting fuel enthalpy increase will also be adequate.

4. Comparison between POLCA-T simulations and PB EOC 2 turbine trip tests recorded data showed good agreement for both integral and local parameters. Thus, POLCA-T neutronic (the moderator density feedback), thermal-hydraulic (heat transfer from the fuel rod to the coolant, void fraction formation and collapse), and fuel rod thermal-mechanic models (fuel, cladding, and gas gap properties) capability to accurately simulate a very fast transient with the same time scale as CRDA was demonstrated.

5. Comparison of POLCA-T predictions with SPERT-III-E power excursion test results shows that the POLCA-T simulations using the Westinghouse CRDA methodology show good agreement with the tests for which the nominal initial conditions quoted appear to reflect the actual situation. The comparisons demonstrate that for a peak power consistent with the experimental data, the Westinghouse methodology using POLCA-T predicts resulting values of the inserted reactivity, power shape, integrated energy, and time-to-peak power that agree with the experimental values within the experimental uncertainties. Therefore, it is concluded that the Westinghouse methodology predicts the results of the SPERT-III E-Core tests for which the comparisons were made within the uncertainties in the tests and the uncertainties associated with the information available regarding those tests.

6. Comparison of the POLCA-T with the RAMONA-3 code for commercial BWR CRDA analyses show that the results of both codes, in general, agree within the code uncertainty established in Reference 3. POLCA-T predicts maximum fuel enthalpy values higher than RAMONA-3.

In summary, the Westinghouse methodology described in Section A.4 for evaluating the CRDA using POLCA-T simulations can predict peak pellet enthalpies during a postulated CRDA, which are sufficiently accurate to demonstrate that the design bases provided in subsection A.2.4 are satisfied.

A.4 WESTINGHOUSE BWR CONTROL ROD DROP ACCIDENT ANALYSIS METHODOLOGY

A.4.1 Introduction

The CRDA is analyzed for commercial BWRs as a design basis accident, which is bounding for all postulated accidents involving additions of prompt reactivity. The method of analysis chosen must be capable of treating the effects of rapidly changing power distributions which are caused by the rapid control rod movement.

This section describes the methodology used by Westinghouse to determine the most limiting dropped control rod configuration and to evaluate the consequences of a CRDA in BWRs of any design, containing fuel and control rods of Westinghouse or other vendors' designs. The methodology is illustrated with typical results including uncertainty treatment described in Section A.5.

A.4.2 Overview

The results of a CRDA are highly dependent of the control rod worth of the dropped rod, which in turn, are dependent on the core loading and fuel design (see Section A.2). This implies that the consequences of the CRDA may be addressed on a cycle-specific basis or in a generic, bounding analysis. The strategy for the cycle-specific evaluation is provided in Section 4.6. The PHOENIX4, POLCA7, and POLCA-T computer codes are used to evaluate the CRDA. The Westinghouse methodology for a CRDA evaluation is discussed in Sections 4.3 through 4.6.

The consequences of the accident relative to the design bases are evaluated for the most limiting time in the cycle and the most limiting reactor conditions.

Any control rod in the startup sequence may be subjected to a CRDA at any time in the cycle. Thus, the CRDA must be analyzed for the most limiting control rod at the most limiting time in cycle. Furthermore, the analyses must be bounding for the most limiting reactor condition defined in subsection A.4.4.2.

The Westinghouse methodology for a complete analysis of the CRDA is fundamentally a two-step approach and is briefly described hereafter.

A.4.2.1 Methodology Step 1 – Steady-State Evaluations

The aim of step 1 is to find the most limiting control rods in the core with respect to CRDA with a steady-state method. The analyses are performed for CZP condition at the most limiting reactor conditions defined in subsection A.4.4.2. The primary parameter that is utilized to determine the most limiting rod drop positions or candidates is the dropped control rod incremental reactivity worth. [

]^{a,c}

[

]^{a,c} An NRC-approved three-dimensional static nodal code, such as POLCA7, in conjunction with the cross-section generator code PHOENIX4, is utilized for this evaluation. The screening of the core is as follows:

1. [

]^{a,c}

2. [

]^{a,c}

3. The analyzed cases encompass a sufficient number of state points during the cycle.

In reality, a control rod cannot drop longer than to the position of its drive. [

]^{a,c} Several candidates with the highest incremental reactivity are selected for the further transient analyses in step 2 of the methodology, and are described in following section.

A.4.2.2 Methodology Step 2 - Dynamic Evaluations

Having established the potential candidates for the most limiting dropped control rods within the cycle, the second step is analysis of the dynamic response to those dropped control rods and the subsequent consequences to the fuel. This evaluation is performed with POLCA-T. [

]^{a,c} The dynamic calculations are as follows:

1. [

]^{a,c}

2. The rod is assumed to drop from a fully inserted position to a banked position giving the highest incremental reactivity.

3. [

]^{a,c}

4. The dynamic analyses are performed taking into account the uncertainty treatment described in Section A.5.

5. The maximum local enthalpies are compared to the acceptance criteria.

The two steps of the methodology are described in detail in subsections A.4.3 and A.4.4.

A.4.3 Determination of Candidates for the Limiting Control Rod

A.4.3.1 Analysis Methodology

[

]^{a,c} The total reactivity worth of a given rod is defined for this application as:

$$\text{Total Reactivity Worth, } CR_{worth} = \frac{k_{eff}^{out} - k_{eff}^{in}}{k_{eff}^{out} \cdot k_{eff}^{in}}$$

where:

k_{eff}^{in} Core $k_{effective}$ with the control rod is fully inserted, and
k_{eff}^{out} Core $k_{effective}$ with the control rod withdrawn to its final position.

[

]^{a,c}

Discussion:

The incremental reactivity insertion as a function of position as the control rod drops is referred to as "the reactivity shape function." [

1.

2.

]^{a,c}

Since it must be assumed that the reactor can be shut down and restarted at any time during the cycle, the possibility of a control rod drop in this operating range must be considered throughout the cycle. The parameters to which the severity of the accident is sensitive can change throughout the cycle. For example, the Doppler coefficient typically tends to get somewhat more negative with the exposure, while the delayed neutron fraction typically tends to decrease with increasing exposure, which tends to make the accident more severe.

The 3-D core simulator POLCA7 is used to simulate the control rod withdrawals observing the restrictions imposed by the plant Technical Specifications. The two most common rod withdrawal sequences specified for U.S. Plants are the BPWS and the group notch sequence. These control rod programs are used to withdraw the control rods in a manner which will mitigate the severity of the CRDA.

[

]^{a,c}

A.4.3.2 Example of a Scoping Calculation

This section provides an illustration of the Westinghouse methodology for establishing candidates for the core conditions and dropped control rods that will result in the most limiting control rod worths for a given cycle.

The illustrative calculations were performed for a 648 fuel assemblies BWR/6 core. The rated core thermal power and flow rate are 3,600 MWt and 11,511 kg/s, respectively. An equilibrium, reload core of Westinghouse SVEA-96 Optima 2 assemblies designed for 12-month cycle application was utilized for this illustration. The most limiting reactor condition according to subsection A.4.4.2 is selected for the evaluations. Three cycle exposures are analyzed; BOC, middle-of-cycle (MOC), and EOC. Initial operating conditions are specified in Table A.4-1.

The control rod patterns are defined by adherence to the startup sequence A. The locations of the different control rod groups are shown in Figure A.4-1. All control rod patterns from cold global criticality to 97 percent of all control rods withdrawn are covered by the analysis. At each step in the startup sequence, all withdrawn control rods are analyzed with respect to rod drop, the rod drops from a fully inserted to a fully withdrawn position.

Table A.4-1. Operating Conditions Used In Step 1

Parameter	Value
Core Power, relative to rated	10^{-8}
Core Flow, kg/s	3,112
Reactor Pressure, MPa	1.0
Inlet Temperature, °C	100
Inlet Subcooling, °C	80

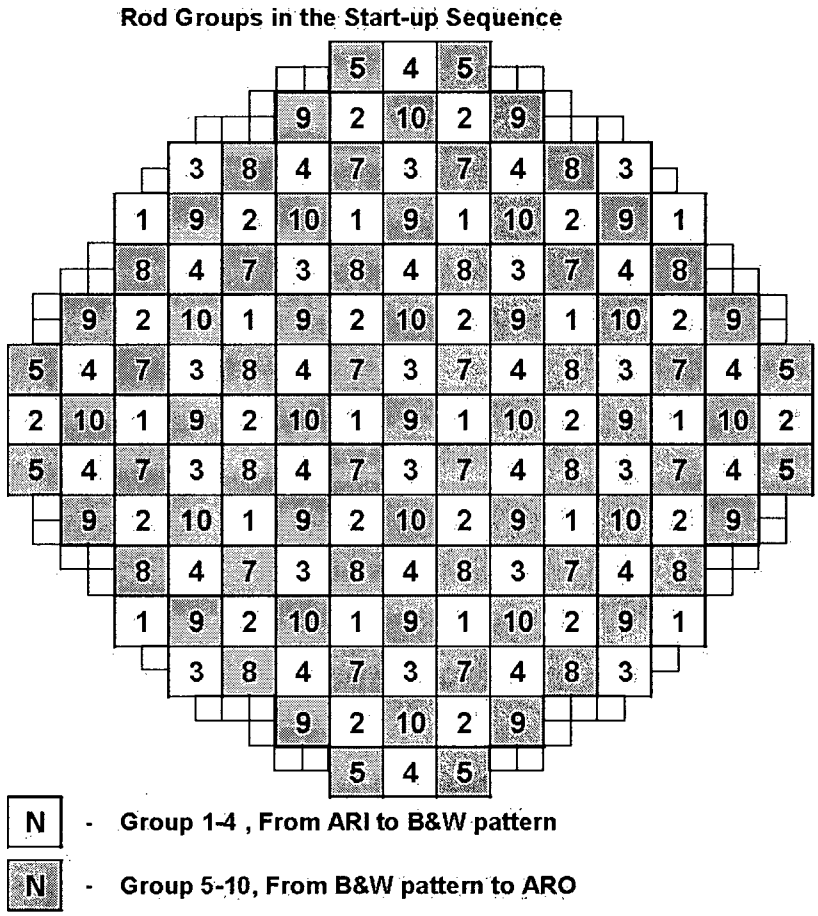

Figure A.4-1. Group Assignment for the A Sequence

Groups 1-4 are withdrawn in the consecutive order Group 1(5 steps) => Group 2 (33 steps) => Group 3 (32 steps) => Group 4 (36 steps). Groups 5-10 are withdrawn in 135 steps in non-consecutive order.

The obtained incremental reactivity versus the sum of the total withdrawn control rods in percent is provided in Figure A.4-2. Figure A.4-3 displays the relation between the maximum nodal power and the incremental reactivity. Eight control rods have an incremental worth at the EOC that is at least 400 pcm higher than the corresponding worth of the each of remaining rods at BOC and MOC states. [

]^{a,c}

a,b,c

Figure A.4-2. Total Reactivity Worths for Sample BWR/6 Withdrawal Sequence A

a,b,c

Figure A.4-3. Relative Maximum Nodal Peak Power as a Function of the Dropped CR Worth

a,b,c

a,b,c

Figure A.4-4. Control Rods Patterns at Steps 113 and 114 with Selected Candidates for the Limiting Control Rod

In this example, in order to include total reactivity worths which would envelope those which we expect for a typical plant and cycle specific-evaluation, the 3-D nodal simulator calculations to determine possible candidates for the control rod(s) which would cause the most severe consequences from a CRDA were performed assuming worst-case conditions. [

]^{a,c}

In the dynamic analyses, a realistic drop of the control rod is considered. Table A.4-3 presents the control rod worth and [ ]^{a,c} of the selected candidates for the limiting rod at a realistic 8 notches drop. In the limiting case a drop of the control rod from a fully inserted position to a banked position of 8 notches gives in this case a highest incremental reactivity of [ ]^{a,c} pcm for CR number 85. The other control rods in the same group as the dropped rod belongs, are withdrawn to the banked position 4 notches. a,b,c

The determination of the actual cases to simulate in the transient calculations is done on a [

]^{a,c}

The selected candidates are utilized in Section A.4.4 in order to define the limiting control rod.

A.4.4 Dynamic Analysis To Determine Energy Deposition in Fuel

A.4.4.1 Analysis Methodology

The dynamic analysis is performed with the POLCA-T code for each of the CR candidates identified in the three-dimensional nodal simulator scoping evaluation as described in subsection A.4.3. The calculations are performed at the limiting reactor initial conditions. [

]^{a,c}

The initial conditions, such as core power, flow rate, inlet temperature, control rod pattern, and RPV pressure are the same as the conditions in the corresponding three-dimensional nodal simulator scoping evaluation.

The data required for CR drop and reactor trip simulation are taken from plant Technical Specifications. In the absence of plant-specific data, the control rod is assumed to drop at the maximum drop velocity of 0.948 m/sec (3.11 ft/second) established in Reference 3. [

]^{a,c}

Discussion:

The core nodalization is exactly the same as in the steady-state evaluations performed with the POLCA7 three-dimensional nuclear simulator code. Full-core calculations are performed with one-to-one neutronics to the thermal-hydraulic mapping scheme. Thus the possible asymmetric effects in the single control rod drop simulation are accounted for. The two-group cross-sections, kinetics data (delayed neutron fractions, precursor's constants, and inverse velocities), and local pin peaking factors are generated by PHOENIX4 for each fuel composition and saved in a standard POLCA7 representation form (Reference 4). They are treated on nodal base by the POLCA7 standard cross-sections and homogenization models. The nodal burnup and void history for each specific case are provided by the POLCA7 code. The instantaneous moderator density, fuel temperature, and control rod dependences at discrete burnup, and density history state points are accounted by the POLCA7 standard cross-sections model. The cross-sections, kinetics data, and local pin peaking factors are updated at each time step during the POLCA-T transient simulations using standard POLCA7 models.

The fuel peak enthalpies are calculated in each node using the nodal powers from the dynamic POLCA-T calculation and the local pin peaking factor calculated for that node. [

]^{a,c}

[

]^{a,c}

Uncertainty treatment and conservatisms included by assuming bounding input parameters are described in Section A.5.3.

A.4.4.2 Example of a Determination of the Limiting Initial Conditions

In this section, the limiting reactor condition to be utilized in the upcoming CDRA analyses is determined. This determination is generic and does not have to be carried out cycle-specific since it is related to the reactor startup procedures.

The following section illustrates the procedure and provides an example of the limiting reactor initial conditions determination as a still conservative base case for POLCA-T CRDA applications.

A.4.4.2.1 [ ]^{a,c}

[

]^{a,c}

a,b,c

Figure A.4-5. [

]^{a,c}

a,b,c

A.4.4.2.2 [

][a,c]

[

]a,c

Table A.4-5. Input Data for the Limiting Initial Condition Cases	
Parameter	**Value**
Initial Power, relative to rated	10^{-8}
Cycle Exposure	EOC
CR Step	113 and 114
Dropped CR	# 85 and # 14
Dropped CR Speed, m/s	0.948
Dropped CR Speed, ft/sec	3.111
Scram delay from 120% trip, s	[ ]a,b,c

The dropped control rod was assumed to drop from the fully inserted to the position of its drive by 8 notches.

A scram is activated with [ ]a,c The scram insertion position is specified according to the typical BWR/6 plant Technical Specifications and is provided in Table A.4-6. Technical Specifications place limits on the scram rate in the form of maximum times for control rods reaching 5, 20, 50, and 90 percent of insertion. Therefore, the effectiveness of the scram is conservatively underestimated.

a,b,c

[

]

The results are summarized in Table A.4-7. For CRs number 14 and number 85 that have the highest and the lowest reactivity worth, the case at [ ]^{a,c} inlet temperature provides the limiting initial conditions that lead to highest peak enthalpy. It has to be noted that these conditions and the ones at [ ]^{a,c} inlet temperature produce both closer values to the values obtained at 1 bar or 70 bar pressure and 20°C inlet temperature. The results obtained for CR number 85 confirm the same trends as the ones observed in CR number 14 results.

a,b,c

[

]

Figures A.4-6 and A.4-7 illustrate the POLCA-T predicted reactor power and peak fuel enthalpy time histories for the CRDA limiting initial conditions cases for both CR number 14 and number 85. [

]^{a,c}

A.4.4.3 Example of a Dynamic Calculation to Determine the Energy Deposition in the Fuel at Limiting Reactor Initial Conditions

This section illustrates the Westinghouse methodology for performing the dynamic CRDA evaluation. The results are shown for the same BWR/6 equilibrium SVEA-96 Optima2 core for which the steady-state evaluation was presented in subsection A.4.3.2. The example dynamic evaluation of CRDA is performed at the limiting initial conditions of [ ]^{a,c}, which in subsection A.4.3.2 was found to lead to the highest peak enthalpy.

The very same plant model and input data described in subsection A.4.4.2 are used in the dynamic calculations presented in this section. The dropped control rod was assumed to drop from fully inserted to the position of its drive by 8 notches. Table A.4-8 presents the summary of the obtained results for the peak power, maximum energy deposited in the fuel and maximum hot rod fuel temperature as well as the timing of observed peak values for all selected CR candidates. [

]^{a,c} Thus the CR number 85 is determined to be the limiting control rod for the considered BWR/6 plant loaded with SVEA-96 Optima2 equilibrium core.

a,b,c

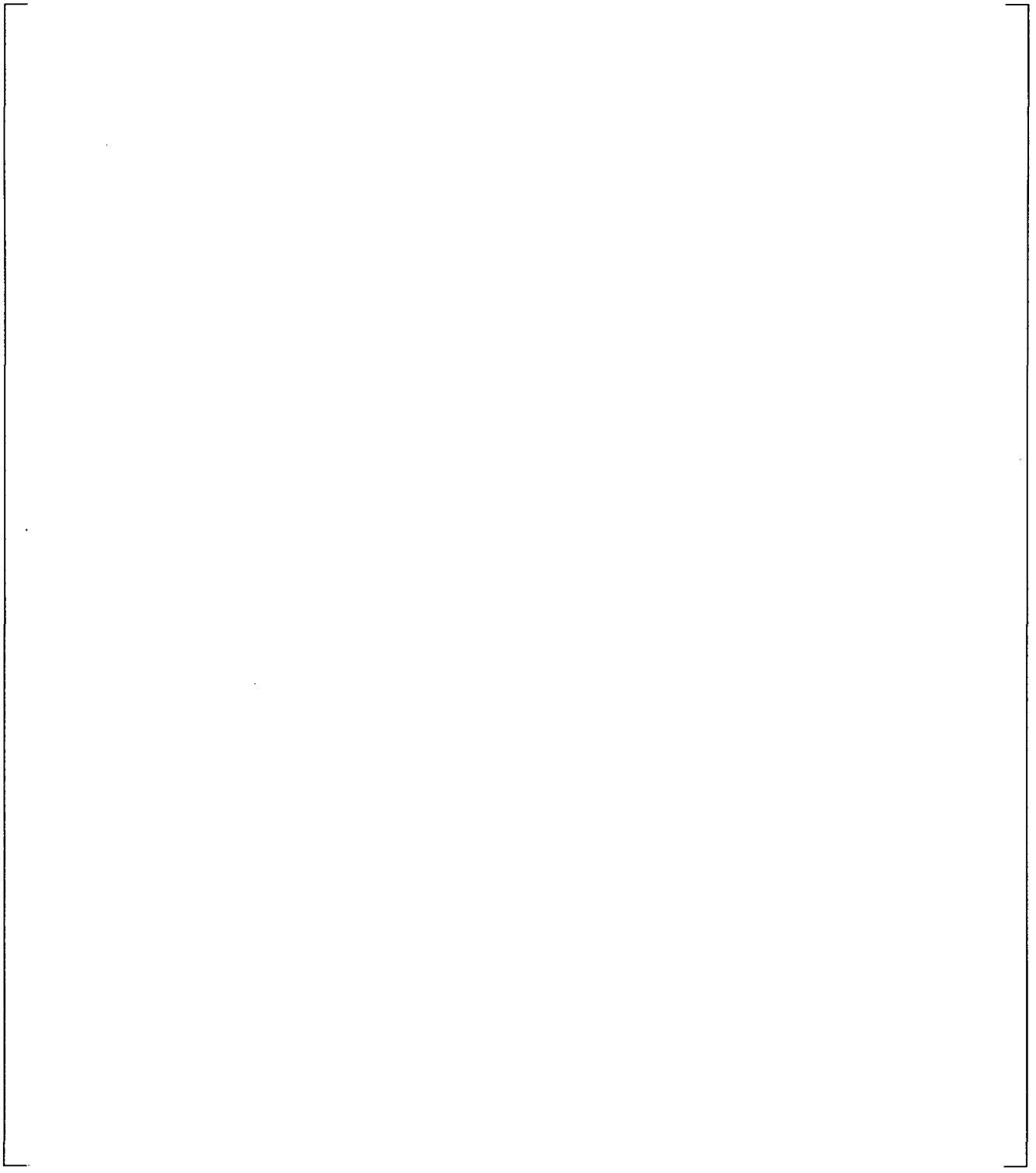

Figure A.4-6. POLCA-T Predicted Reactor Power Time Histories for CRDA Limiting Initial Conditions Cases

a,b,c

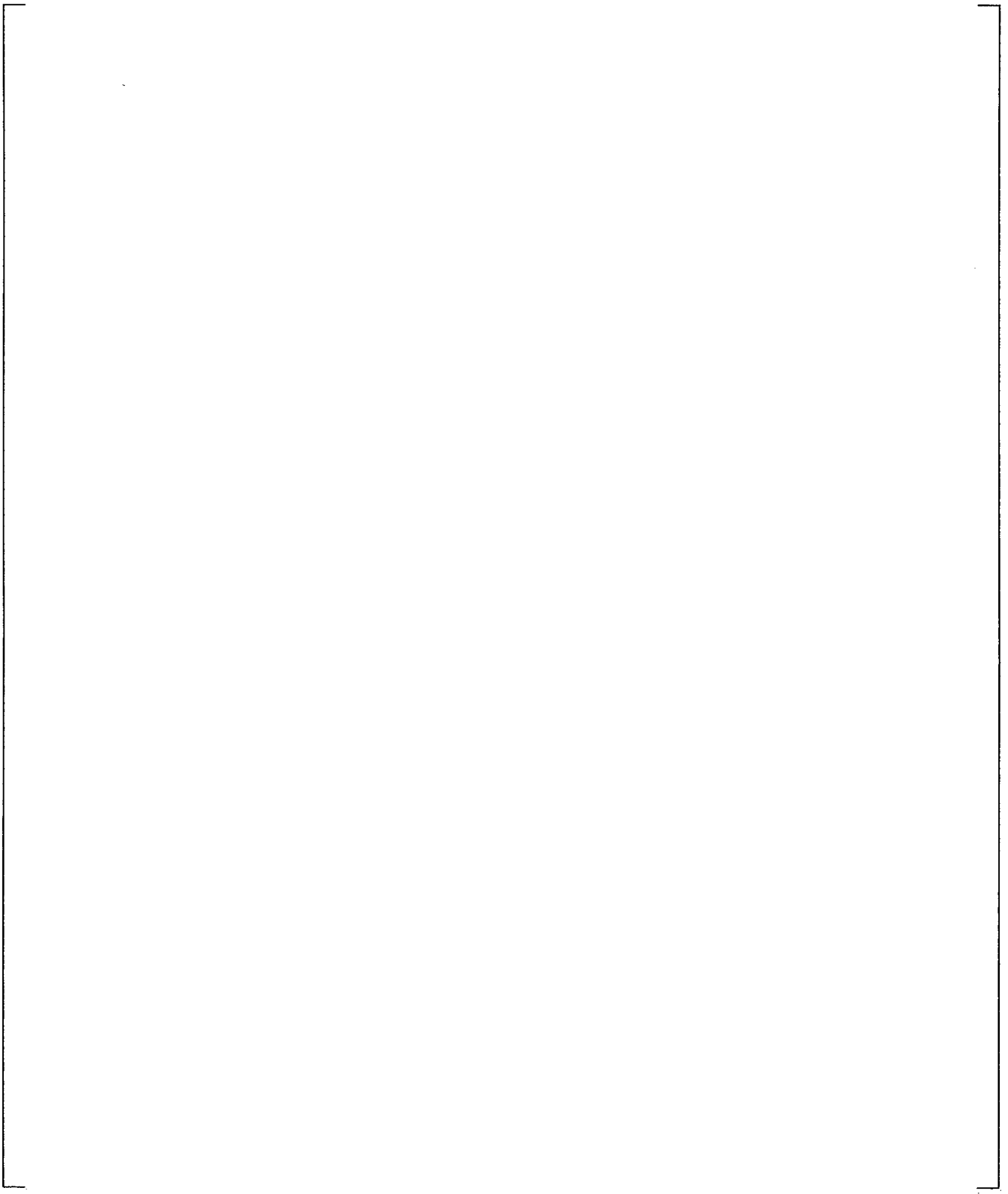

Figure A.4-7. POLCA-T Predicted Peak Fuel Enthalpy Time Histories for CRDA Limiting Initial Conditions Cases

a,b,c

Figure A.4-8. [
]^{a,c}

a,b,c

Insight into the transient is provided by examining the core power response, reactivity, power shapes, fuel enthalpy, and temperature as a function of time for limiting case calculation summarized in Table A.4-8. Figure A.4-9 shows the core power as a function of time for all candidate control rods. Figure A.4-10 and Figure A.4-11 present the POLCA-T predicted peak fuel enthalpy time histories for the candidate limiting control rods in the sequence steps 113 and 114, respectively.

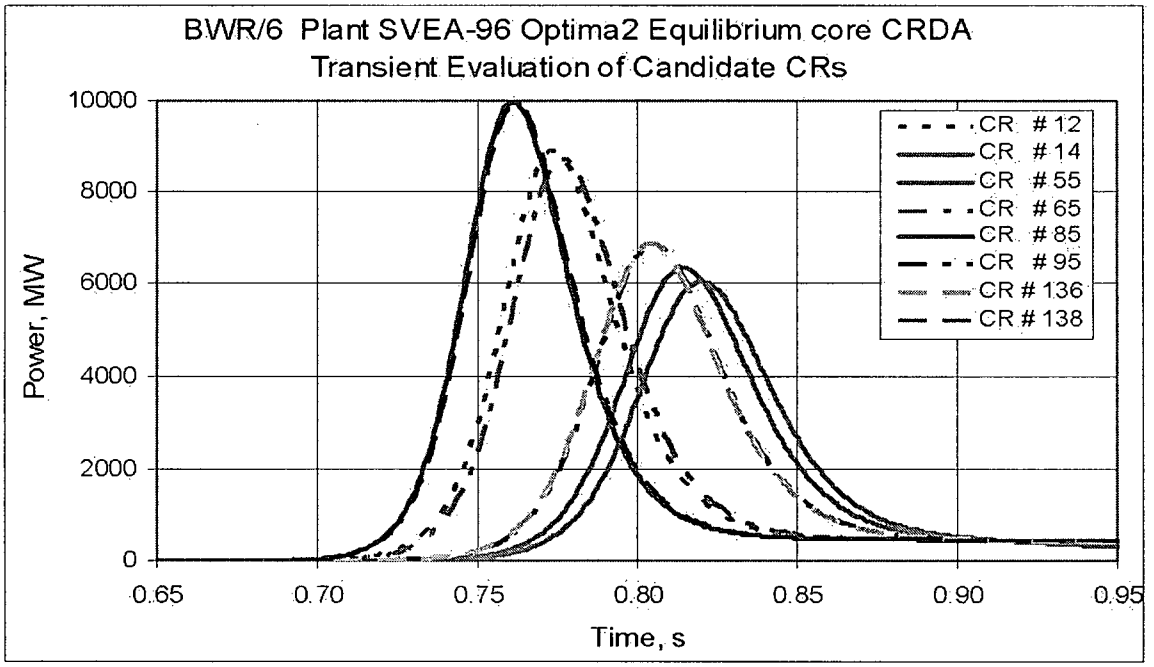

Figure A.4-9. POLCA-T Predicted Reactor Power Time Histories for the Candidate Limiting CRs

[

]^{a,c}

a.b.c

Figure A.4-10. POLCA-T Predicted Peak Fuel Enthalpy Time Histories for the Candidate Limiting CRs in Step 113

a.b.c

Figure A.4-11. POLCA-T Predicted Peak Fuel Enthalpy Time Histories for the Candidate Limiting CRs in Step 114

A.4.4.4 Summary and Conclusions

Summary and conclusions from the limiting case determination and transient evaluation evaluations can be summarized as follows:

1. [

2.

3.

4.

]^{a,c}

A.4.5 Evaluation of Peak System Pressure During the Transient Methodology

[

]^{a,c}

Discussion:

The system pressure increase during a CRDA analyses is calculated by the POLCA-T code. As an example, the selected base case, with a maximum enthalpy of [ ]^{a,c} calories/gram, resulted in a pressure increase of only [ ]^{a,c} MPa, which must be considered as an insignificant pressure increase. The system pressure is not expected to increase significantly higher even if the cladding failure limit is reached.

[

]^{a,c}

[

]^{a,c}

A.4.6 Cycle-Specific Evaluations Methodology

Sections 4.3 and 4.4, respectively, described the Westinghouse methodology for performing CRDA analyses and provided an application example of those methods to a BWR/6 reactor. This section describes the type of strategy which Westinghouse intends to use for applying these methods to cycle-specific licensing evaluations of the CRDA.

[

]^{a,c}

Figure A.4-12 illustrates the procedure followed for the cycle-specific CRDA evaluations.

A.4.7 Comparison of Analysis Results with Evaluation Criteria

A reload design is acceptable only if it conforms to the design criteria in Section A.2.4. [

]^{a,c}

Peak fuel enthalpies are confirmed to be less than the peak enthalpy limit for fuel dispersal.

If the peak enthalpy exceeds the limit for fuel failure, the number of rods exceeding this value at any axial level is calculated from the pin power distributions. The radiological consequences of the number of failed rods is demonstrated to be bounded by the Final Safety Analysis Report (FSAR) radiological evaluation or new values are established and confirmed to be below the acceptance criteria specified in Section 2.4.

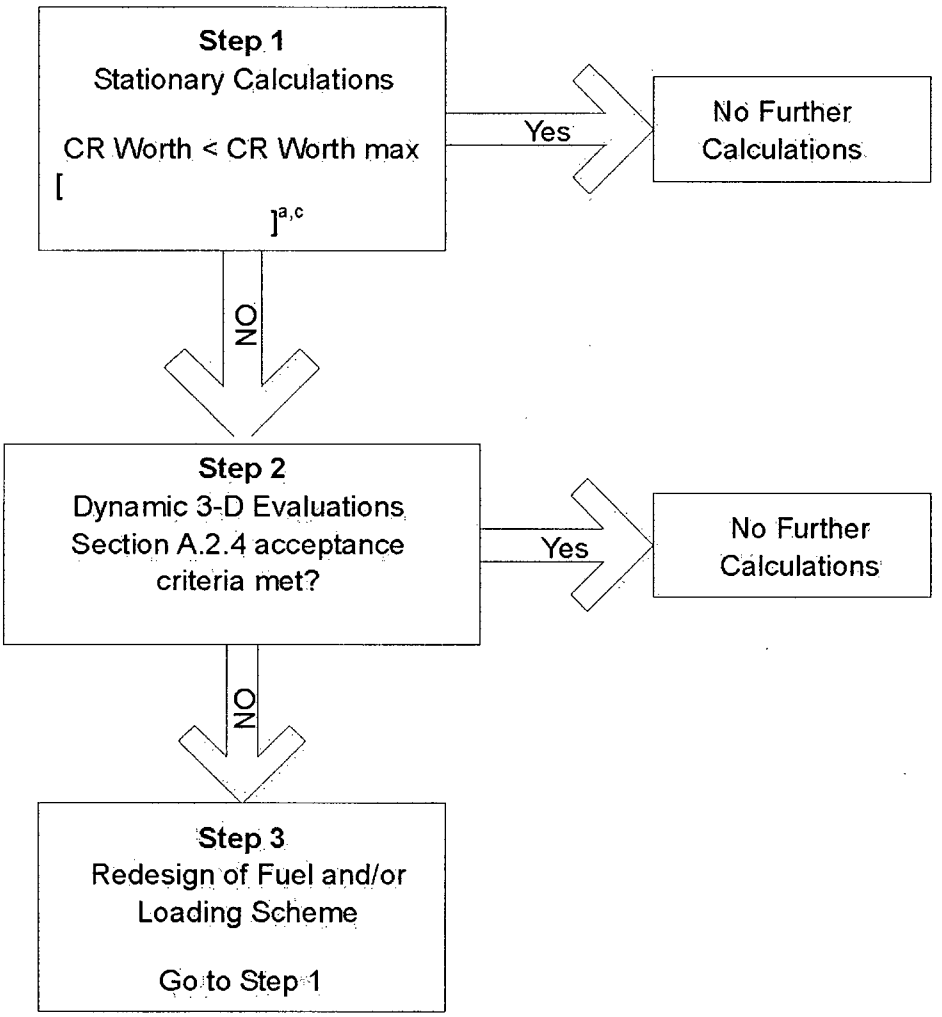

Figure A.4-12. Strategy for Cycle-Specific Evaluations

A.5 EVALUATION MODEL ASSESSMENT

This section describes the assessment of the adequacy of the Westinghouse CRDA evaluation model that utilizes PHOENIX4/POLCA7/POLCA-T code system. Based on the PIRT of Section 2.5, the assessment of the POLCA-T code sensitivities have been investigated and the results are presented. Uncertainties in the parameters with high ranked importance for the fuel enthalpy evaluation are established as a part of Westinghouse CRDA methodology.

A.5.1 POLCA-T Sensitivity Studies

POLCA-T code sensitivity studies are based on the CRDA PIRT described in Section A.2.5. Many reports and papers are available in the literature, which contain discussion of the mechanics of the accident, and parametric studies of the consequences as function of control rod patterns, fuel type, and exposure. These reports and papers are generically applicable and cover a large number of input variables including different fuel types and core designs at different exposures and initial conditions. We have augmented these existing sensitivity studies with our own calculations of BWR/6 and ASEA-ATOM designed BWRs utilizing the POLCA-T code. The critical/key parameters for the CRDA analyses focus on characterizing the power history during the reactivity pulse and the fuel enthalpy increase during the pulse including the temperature distribution in the fuel rod (pellet, gap, and cladding). The phenomena in Table A.2-1 have been ranked relative to how they impact these critical parameters for the system analyses. Hereafter, the sensitivities on the key parameters are presented and discussed.

Sensitivities of the peak fuel enthalpy reached during the accident to the following parameters are discussed in this section:

- [
-
-
-
-
-
-
-
-
-]^{a,c}

A.5.1.1 Total Control Rod Worth

[

]^{a,c}

[

]^{a,c}

a,b,c

[

]

Figure A.5-1. POLCA-T Predicted Peak Fuel Enthalpy Versus Total CR Reactivity Worth

A.5.1.2 Doppler Temperature Feedback

The Doppler effect is treated in the POLCA7 calculations by assuming that the nodal cross-sections vary as the square root of the average nodal fuel temperature. The Doppler effect is, therefore, provided to POLCA-T on a nodal basis and handled as part of the cross-section treatment. The Doppler effect terminates and reverses the initial power excursion. Therefore, the peak fuel enthalpy is generally quite sensitive to the magnitude of the Doppler feedback.

[

]^{a,c}

The effect of Doppler feedback when the fuel temperature change from T_1 to T_2 can be evaluated by the Doppler coefficient C_D defined as

$$C_D = \frac{k_\infty(T_2) - k_\infty(T_1)}{\sqrt{T_2} - \sqrt{T_1}},$$

where the k_∞ values are the nodal eigenvalues calculated by PHOENIX4 code.

The Doppler coefficient also varies with nodal exposure, typically, for example, decreasing with increasing exposure for low exposures.

[

]^{a,c}

a.b.c

]

A.5.1.3 Delayed Neutron Fraction

POLCA-T treats the effective delayed neutron fractions on a nodal basis similar to the way of treatment of the cross-section data. [

]^{a,c}

a,b,c

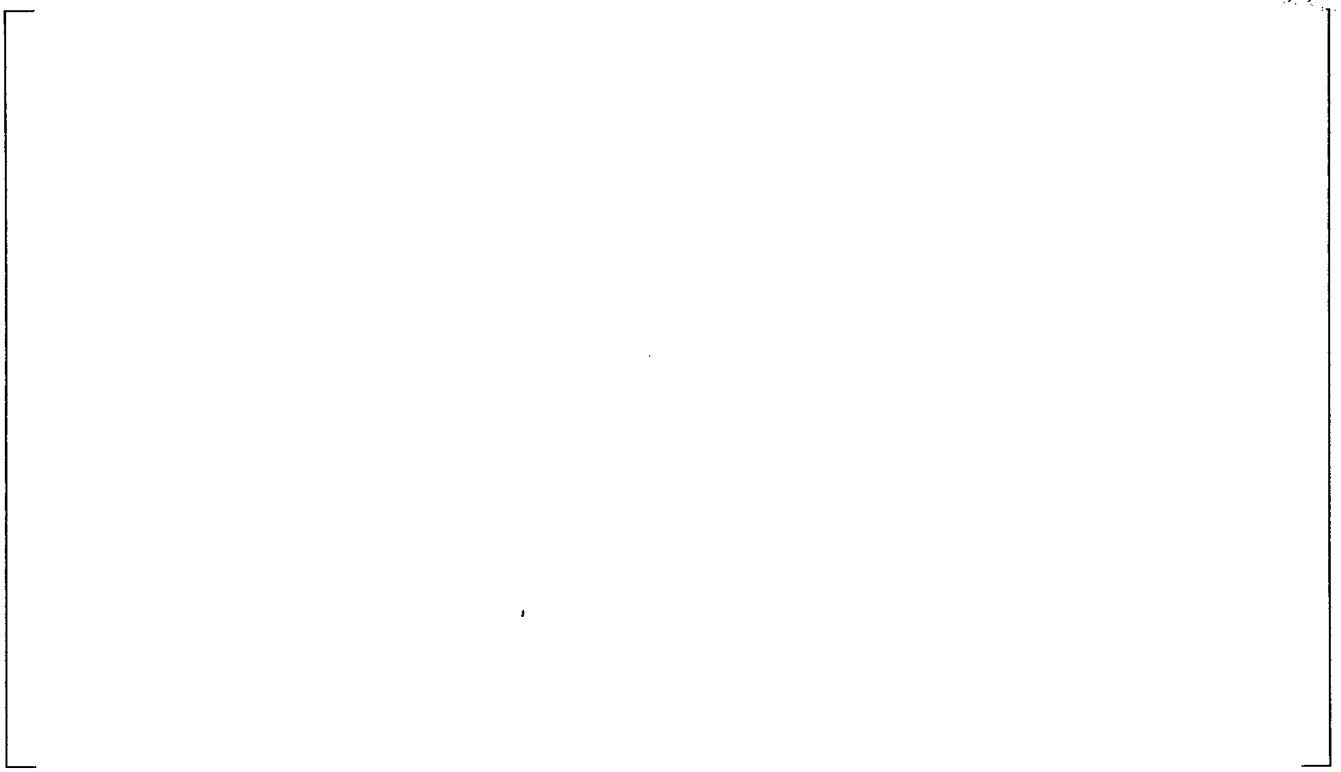

Figure A.5-2. POLCA-T Predicted Peak Fuel Enthalpy Versus Doppler Coefficient Multiplier

a.b.c

A.5.1.4 Pin Peaking Factors

In this study, the nodal pin peaking factors were varied by 5 percent or 10 percent using a multiplayer option built into the POLCA-T code. The option allows one to multiply the pin peaking factor in every fuel node by the user-specified input number. In order to investigate the effect and fairly compare the peak enthalpy, however, a constant in time pin power peaking factor was used in the calculations presented in this section. These nodal peaking factors had been obtained by POLCA7 calculations of the steady-state with dropped control rod. The calculations were performed for given core loading at certain state of the fuel cycle and starting from the very same initial condition in all four simulations which results are provided in Table A.5-3 and Figure A.5-3. [

]^{a,c}

[

]a,c

a,b,c

a,b,c

Figure A.5-3. POLCA-T Predicted Peak Fuel Enthalpy Versus Pin Peaking Factor

A.5.1.5 Initial Power Level

The impact of the core power from which the CRDA is initiated was investigated for ASEA-ATOM designed BWRs utilizing the POLCA-T code. [

]a,c

[

]^{a,c} The amount of negative reactivity from Doppler is caused by the same fuel temperature rise in both cases, which imply that the maximum enthalpy practically will be the same.

A.5.1.6 Feedwater Temperature (Core Inlet Temperature/Subcooling)

The moderator temperature affects the fuel enthalpy both through the heat transfer from the fuel rod to the coolant and the moderator density feedback to the core power. For a given reactivity insertion by the dropped control rod, the initial moderator subcooling is an important factor in determining the fluid properties of the moderator during the transient.

The effect of the moderator subcooling on peak fuel enthalpy was evaluated by running both CZP and HZP sets of the dropped control rod cases. The results are summarized in Table A.5-4. [

]^{a,c}

a,b,c

[

]

The effect of the moderator subcooling on peak fuel enthalpy at a constant core inlet temperature was evaluated in separate study at low-pressure cases presented in Table A.5-5. The results show that the moderator subcooling increase leads to increased peak fuel enthalpy. [

]^{a,c}

a.b.c

[

]

A.5.1.7 Rate of Reactivity Insertion

The effect of accident reactivity insertion rate was examined in this study by control rod drop calculations in which the dropped control rod velocity was varied. The CR drop velocity of 0.948 m/sec (3.11 ft/sec) is justified in Reference 3 as the maximum rod drop speed that could be achieved allowing for tolerances in physical dimensions at the 3 σ level. This is the licensing basis for this accident in many BWR plants and is utilized as the base case velocity in the referenced work. The same velocity is used in the current study. The effect of dropped control rod velocity for a given total reactivity worth was investigated by repeating the calculations for control rod drop velocities of 0.57 m/sec and 1.53 m/sec (1.86 ft/s and 5.00 ft/s), and constant acceleration of 7.4 m/s^2. Table A.5-6 shows the summary of obtained results.
[

]^{a,c} Figures A.5-4 through A.5-7 present the fission power, peak fuel enthalpy, maximum hot rod fuel temperature and maximum fuel centerline temperature time histories. [

]^{a,c}

a.b.c

[

]

a,b,c

Figure A.5-4. POLCA-T Predicted Fission Power Time Histories at Different Reactivity Insertion Rates

a,b,c

FigureA.5-5. POLCA-T Predicted Peak Fuel Enthalpy Time Histories at Different Reactivity Insertion Rates

a,b,c

Figure A.5-6. POLCA-T Predicted Maximum Hot Fuel Rod Temperature Time Histories at Different Reactivity Insertion Rates

a,b,c

Figure A.5-7. POLCA-T Predicted Maximum Fuel Centerline Rod Temperature Time Histories at Different Reactivity Insertion Rates

A.5.1.8 Moderator Density and Void Fraction Feedback

The fact that the moderator feedback to the power does not contribute substantially to the reversal of the initial power burst at CZP is widely described in the literature. Evidently, the Doppler reactivity feedback provides the large initial negative reactivity component that terminates and reverses the initial steep power burst. The moderator density and void fraction feedbacks come into the picture later in the transient when the coolant approaches the saturation conditions. Even at CZP cases with high initial subcooling of about 80°C, some local voiding occurs in the nodes with highest energy release. [

]^{a,c}

[

]^{a,c}

]^{a,c}

a,b,c

[

]

A.5.1.9 Steam Dome Pressure

The effect of the RPV pressure on peak fuel enthalpy at constant core inlet temperature was evaluated in a separate study at low pressure cases presented above in Table A.5-5. [

]^{a,c}

A.5.1.10 Total Core Mass Flow

The effect on the peak fuel enthalpy of the core mass flow was investigated at CZP conditions and is illustrated in Table A.5-8 and Figure A.5-8. [

]^{a,c}

a.b.c

[

]

a,b,c

Figure A.5-8. POLCA-T Predicted Peak Fuel Enthalpy Time Histories at Different Core Mass Flows

A.5.1.11 Fraction of the Energy Deposited in the Fuel

Direct energy deposition in the moderator due to neutrons slowing down and gamma radiation reduces the fraction of the energy deposited in the fuel. The time constant of this phenomena is very short and it has a potential to affect the peak fuel enthalpy observed during the CRDA. [

]^{a,c}

A.5.1.12 Summary on the Sensitivities Studies

The results of performed sensitivity evaluations using POLCA-T code can be summarized as follows:

1. The POLCA-T results presented in Section A.4.4 are consistent with conclusions and sensitivities provided in this section and previous POLCA-T and RAMONA-3 works. The sensitivities observed utilizing POLCA-T code for CRDA analysis agrees with the reported in the literature sensitivities of the peak fuel enthalpy to the considered parameters.

2. [

]^{a,c}

3. [

4.

5.

6.

7.

8.

]a,c

9. [

]a,c

A.5.2 Peak Fuel Enthalpy

Based on the present and previous sensitivity evaluations performed by POLCA-T code, the following parameters have the greatest impact on peak fuel enthalpy in the fuel rods:

- [
-
-
-
-
-]a,c

These parameters depend on such variables as the control rod pattern, the core hydraulic conditions, the core burnup and burnup distribution, and type of fuel in the core. Therefore, analysis of a cycle for the most limiting situation requires, in principle, a large matrix of core conditions and burnups. However, as

noted above, the range of evaluation of the accident can usually be limited to a range from cold critical to hot standby. Furthermore, as described in Section A.4.6, the cycle-specific strategy utilizes a systematic approach based on existing sensitivities to reduce the scope of repetitive cycle-specific evaluation, which can increase error-like situations.

A.5.3 Establishment of the POLCA-T Uncertainty

This section describes the treatment of bounding values and uncertainties in the POLCA-T CRDA analysis. Uncertainties in the modeling of highly ranked phenomena are carefully evaluated and then combined to determine the total model uncertainty. Sensitivity analyses are used to quantify how individual uncertainties influence the total uncertainty so that the greatest effort can be focused on establishing the uncertainties of those phenomena that have the greatest impact on the critical safety parameters.

[

]^{a,c}

An uncertainty analysis is used to address the effect on peak fuel enthalpy of the variation in parameters relative to their nominal values for which bounding values have not been utilized in the nominal POLCA-T calculations. Bounding values are typically used for parameters for which the assignment of a bounding value is practical. For example, utilization of a bounding value of the velocity with which the dropped control rod exits the core is usually practical.

[

]^{a,c}

[

]^{a,c}

An example of the application of this uncertainty analysis approach to the corresponding limiting CR number 85 case described in subsection A.4.4.3 and Table A.4-8 of Section A.4 is provided in this section. In this case the uncertainty, ΔH_{Total}, is intended to provide an upper limit for the 95 percent confidence level.

[

]^{a,c}

A.5.3.1 Total Control Rod Worth

[

]^{a,c}

a,b,c

Figure A.5-9. Linear Least Square Fit of POLCA-T Predicted Peak Fuel Enthalpy Versus Total CR Reactivity Worth

A.5.3.2 [ ]^{a,c}

[

]^{a,c}

A.5.3.3 [ ]^{a,c}

[

]^{a,c}

A.5.3.4 [ ]^{a,c}

[

]^{a,c} [

]a,c

[a,b,c]

A.5.3.5 Fuel and Cladding Heat Capacities and Thermal Conductivity

[

]a,c

A.5.3.6 Gas Gap Heat Transfer Coefficient

[

]a,c

A.5.3.7 [ ]a,c

[

]a,c

a,b,c

a,b,c

A.5.4 Conservatism in POLCA-T CRDA Methodology

Conservative assumptions in POLCA-T CRDA methodology are summarized as follow:

1. **Initial conditions for the CRDA analysis:** [

]^{a,c}

2. **Scram set point:** [

]^{a,c}

3. **Scram time delay and speed:** The value of [ ]^{a,c} seconds delay is based on a specific BWR/6 plant Technical specifications, that is, from input data for safety analyses that are conservative. The specific plant data will be used whenever available. The assumed scram speed is based also on typical Technical Specifications that place limits on scram rate in the form of maximum times from de-energization of the scram solenoid valve for control rods reaching 5, 20, 50, and 90 percent of insertion. Therefore, the effectiveness of the scram is conservatively underestimated.

4. **Scram reactivity insertion:** [

]^{a,c}

5. **Fuel and cladding heat capacities and thermal conductivity:** [

]^{a,c}

6. **Gas gap heat transfer coefficient:** [

]^{a,c}

A.5.5 [

]^{a,c}

[

]^{a,c}

A.6 REFERENCES

1. 10 CFR Part 50, Appendix A, General Design Criteria 28, "Reactivity Limits."

2. NUREG-0800, Standard Review Plan 15.4.9 Spectrum of Rod Drop Accidents (BWR), U.S. Nuclear Regulatory Commission, Rev.3 April 1996. Standard Review Plan 15.4.9.A Radiological Consequences of Control of Rod Drop Accident (BWR) Appendix A, U.S. Nuclear Regulatory Commission, Rev.3 April 1996.

3. Control Rod Drop Accident Analysis for Boiling Water Reactors: Summary and Qualification, ABB CE Topical Report CENPD-284-P-A (Proprietary), July 1996.

4. The Advanced PHOENIX4 and POLCA7 Codes for Nuclear Design of for Boiling Water Reactors, ABB CENPD-390-P-A (Proprietary), April 1999.

5. H. Finnemann and A. Galati, "NEACRP 3-D LWR Core Transient Benchmark, Final Specifications," OECD NEACRP-L-335 (Revision 1), October 1991 (January 1992).

6. H. Finnemann, et al., "Results of LWR Core Transient Benchmarks," OECD NEA/NSC/DOC(93) 25 Report, October 1993.

7. M. P. Knight and P. Bryce, "Derivation of a Refined PANTHER Solution to the NEACRP PWR Rod Ejection Transients," Proceedings of the Joint International Conference on Mathematical Methods and Supercomputing for Nuclear Applications, Vol. 1, pp. 302 – 313, Saratoga Springs, October 5-9, 1997.

8. L. A. Carmichael and R. O. Niemi, "Transient and Stability Tests at Peach Bottom Atomic Power Station Unit 2 at End of Cycle 2," EPRI NP-564, Project 1020-1, Topical Report, June 1978.

9. R. K. McCardell, D. Herborn and J. E. Houghtaling, "Reactivity Accident Test Results and Analyses for the SPERT-III E-Core – A Small, Oxide-Fueled, Pressurized-Water Reactor," IDO-17281, U.S. Atomic Energy Commission, March 1969.

10. Not Used.

11. R. Yang, "Topical Report on Reactivity Initiated Accidents: Bases for RIA Fuel Rod Failures and Core Coolability Criteria," EPRI Report 1002865, June 2002.

12. B.E. Boyack et al., "Phenomena Identification and Ranking Tables (PIRTs) for Rod Ejection Accident in Pressurized Water Reactors Containing High Burnup Fuel," NUREG/CR-6742, September 2001.

13. R.O. Meyer, "Implications From the Phenomenon Identification and Ranking Tables (PIRTs) and Suggested Research Activities for High Burnup Fuel," NUREG/CR-1749, September 2001.

14. "Westinghouse Control Rod Ejection Accident Analysis Methodology using Multi-dimensional Kinetics," WCAP-15806-P-A, Revision 0, November 2003.

15. "Fuel Rod Design Methods for Boiling Water Reactors," ABB Topical Report CENPD-285-P-A (proprietary), CENPD-285-NP-A (non-proprietary), July 1996. and "Supplement 1," WCAP-15836-P-A, June 2002.

16. B. Akdeniz, K.N. Ivanov, A.M.Olson "Boiling Water Reactor Turbine Trip (TT) Benchmark Volume II: Summary Results of Exercise 1," NEA/NSC/DOC(2004) June 21, 2005.

17. B. Akdeniz, K.N. Ivanov, A.M.Olson "Boiling Water Reactor Turbine Trip (TT) Benchmark Volume III: Summary Results of Exercise 2." NEA/NSC/DOC(2006) November 23, 2006.

18. D. Panayotov, U. Bredolt, H. Lindgren, "POLCA-T – A Coupled Multi-Physics Tool for Design and Safety Analyses," Proceedings of Mathematics and Computation (M&C 2005) Topical Meeting, Invited paper 272, Avignon, France, September 12-15, 2005.

19. D.J. Diamond, et al., "Uncertainty Analysis for the PWR Rod Ejection Accident," Transactions of the American Nuclear Society and the European Nuclear Society, Volume 83. pp. 416 – 417, November 2000.

APPENDIX B
POLCA-T: APPLICATION FOR STABILITY ANALYSIS

ABSTRACT

This appendix summarizes the work done to validate POLCA-T as a tool for stability applications. The report is based on validations against [ ]^{a,c} stability tests. It also discusses uncertainties in both measured and calculated decay ratios. A sensitivity study is included in order to investigate limitations and to support the uncertainty analysis. Stability methodology is discussed only briefly since it is essentially the same as the earlier approved methodology for RAMONA-3.

TABLE OF CONTENTS

ABSTRACT iii

TABLE OF CONTENTS v

LIST OF TABLES vii

LIST OF FIGURES ix

ACRONYMS xi

B.1 INTRODUCTION B-1
B.2 SUMMARY AND CONCLUSIONS B-1
B.3 STABILITY ANALYSIS PROCESS B-2
B.4 POLCA-T CORE STABILITY QUALIFICATION – GLOBAL MODE OSCILLATIONS B-4
B.4.1 [ ]^{a,c} CYCLE 7, 10, 13, AND 19 STABILITY TESTS B-4
B.4.2 [ ]^{a,c} CYCLE 14, 15, 16, AND 17 STABILITY TESTS B-19
B.4.3 [ ]^{a,c} CYCLES 19 AND 20 STABILITY TESTS B-32
B.5 POLCA-T CORE STABILITY QUALIFICATION – REGIONAL MODE OSCILLATONS .. B-38
B.5.1 TEST DATA B-38
B.6 POLCA-T CORE STABILITY QUALIFICATION – CHANNEL MODE OSCILLATONS ... B-41
B.6.1 SVEA-96 OPTIMA2 STABILITY TESTS B-43
B.7 POLCA-T CORE STABILITY UNCERTAINTY B-45
B.7.1 MEASUREMENT UNCERTAINTY B-45
B.7.2 SIMULATION UNCERTAINTY B-48
B.8 SENSITIVITY STUDIES B-51
B.9 STABILITY METHODOLOGY B-54
B.10 REFERENCES B-57

LIST OF TABLES

Table B.4-1 [ ]^{a,c} Plant Characteristics B-5
Table B.4-2 [ ]^{a,c} Cycle 7 Core Composition B-5
Table B.4-3 [ ]^{a,c} Cycle 10 Core Composition B-5
Table B.4-4 [ ]^{a,c} Cycle 13 Core Composition B-5
Table B.4-5 [ ]^{a,c} Cycle 19 Core Composition B-6
Table B.4-6 [ ]^{a,c} Cycle 7 Test Conditions B-7
Table B.4-7 [ ]^{a,c} Cycle 7 Measurement Results B-7
Table B.4-8 [ ]^{a,c} Cycle 7 Simulation Results B-9
Table B.4-9 [ ]^{a,c} Cycle 10 Test Conditions B-11
Table B.4-10 [ ]^{a,c} Cycle 10 Measurement Results B-11
Table B.4-11 [ ]^{a,c} Cycle 10 Simulation Results B-12
Table B.4-12 [ ]^{a,c} Cycle 13 Test Conditions B-14
Table B.4-13 [ ]^{a,c} Cycle 13 Measurement Results B-14
Table B.4-14 [ ]^{a,c} Cycle 13 Simulation Results B-15
Table B.4-15 [ ]^{a,c} Cycle 19 Test Conditions B-17
Table B.4-16 [ ]^{a,c} Cycle 19 Measurement Results B-17
Table B.4-17 [ ]^{a,c} Cycle 19 Simulation Results B-18
Table B.4-18 [ ]^{a,c} Plant Characteristics B-20
Table B.4-19 [ ]^{a,c} Cycle 14 Core Composition B-20
Table B.4-20 [ ]^{a,c} Cycle 15 Core Composition B-20
Table B.4-21 [ ]^{a,c} Cycle 16 Core Composition B-21
Table B.4-22 [ ]^{a,c} Cycle 17 Core Composition B-21
Table B.4-23 [ ]^{a,c} Cycle 14 Test Conditions B-22
Table B.4-24 [ ]^{a,c} Cycle 14 Measurement Results B-22
Table B.4-25 [ ]^{a,c} Cycle 14 Simulation Results B-23
Table B.4-26 [ ]^{a,c} Cycle 15 Test Conditions B-25
Table B.4-27 [ ]^{a,c} Cycle 15 Measurement Results B-25
Table B.4-28 [ ]^{a,c} Cycle 15 Simulation Results B-26
Table B.4-29 [ ]^{a,c} Cycle 16 Test Conditions B-27

LIST OF TABLES (Cont'd)

Table B.4-30 [ ]^{a,c} Cycle 16 Measurement Results B-27

Table B.4-31 [ ]^{a,c} Cycle 16 Simulation Results B-28

Table B.4-32 [ ]^{a,c} Cycle 17 Test Conditions B-29

Table B.4-33 [ ]^{a,c} Cycle 17 Measurement Results B-30

Table B.4-34 [ ]^{a,c} Cycle 17 Simulation Results B-30

Table B.4-35 [ ]^{a,c} Plant Characteristics B-32

Table B.4-36 [ ]^{a,c} Cycle 19 Core Composition B-32

Table B.4-37 [ ]^{a,c} Cycle 20 Core Composition B-33

Table B.4-38 [ ]^{a,c} Cycle 19 Test Conditions B-33

Table B.4-39 [ ]^{a,c} Cycle 19 Measurement Results B-33

Table B.4-40 [ ]^{a,c} Cycle 19 Simulation Results B-34

Table B.4-41 [ ]^{a,c} Cycle 20 Test Conditions B-35

Table B.4-42 [ ]^{a,c} Cycle 20 Measurement Results B-36

Table B.4-43 [ ]^{a,c} Cycle 20 Simulation Results B-36

Table B.5-1 [ ]^{a,c} Cycle 7 Test Conditions B-38

Table B.5-2 [ ]^{a,c} Cycle 7 Measurement Results B-38

Table B.5-3 [ ]^{a,c} Cycle 7 Simulation Results B-39

Table B.6-1 Steady-State Properties and Instability Threshold Comparison for Two SVEA-96 Optima2 Cases with Different Axial Power Distributions B-43

Table B.8-1 Sensitivity Study Decay Ratio Results B-51

LIST OF FIGURES

Figure B.4-1 [ ]^{a,c} Core Power Transient During Cycle 7 Stability Measurements. B-8

Figure B.4-2 Comparison of [ ]^{a,c} Cycles 7 10, 13, and 19 POLCA-T Calculations with Global Mode Oscillation Measurements B-19

Figure B.4-3 Comparison of [ ]^{a,c} Cycle 14 POLCA-T Calculations with Measurements B-24

Figure B.4-4 Comparison of [ ]^{a,c} Cycle 15 POLCA-T Calculations with Measurements B-26

Figure B.4-5 Comparison of [ ]^{a,c} Cycle 16 POLCA-T Calculations with Measurements B-29

Figure B.4-6 Comparison of [ ]^{a,c} Cycle 17 POLCA-T Calculations with Measurements B-31

Figure B.4-7 Comparison of [ ]^{a,c} Cycles 19 and 20 POLCA-T Calculations with Measurements B-37

Figure B.5-1 Selected LPRM Signals from the Simulation of Record 5 Cycle 7. ..... B-40

Figure B.5-2 Inserted Control Rods (+) and Detectors (o) Recorded During Record 5 ..... B-40

Figure B.6-1 Flow Diagram of the FRIGG-Loop B-42

Figure B.6-2 Developing Channel Instability POLCA-T Calculation B-44

Figure B.7-1 Variation in Deduced Measured Decay Ratio – Different Methods (M*i*) According to the OECD Benchmark (Reference 8) B-47

Figure B.7-2 Overall Comparison of POLCA-T Simulation Decay Ratio with Plant Measurement Database B-48

Figure B.7-3 Overall Comparison of POLCA-T Simulation Core Resonance Frequency with Plant Measurement Database B-49

Figure B.8-1 Results of Input Sensitivity Study B-53

ACRONYMS

APRM	average power range monitor
AR	auto-regressive method
ARMA	auto-regressive moving average method
BOC	beginning of cycle
BWR	boiling water reactor
BWROG	Boiling Water Reactor Owners Group
CM2	Core Master 2, Westinghouse BWR core engineering tool
COSMOS	core on-line stability monitoring system
DR	decay ratio
EFPH	effective full-power hours
[ ]^{a,c}	[ ]^{a,c}
GE	General Electric
GETARS	[ ]^{a,c} data acquisition system
[ ]^{a,c}	[ ]^{a,c}
LPRM	local power range monitor
MCPR	minimum critical power ratio
MEOD	maximum extended operating domain
MOC	middle of cycle
NEA	Nuclear Energy Agency
OECD	Organization for Economic Co-operation and Development
[ ]^{a,c}	[ ]^{a,c}
SADL	specified acceptable fuel design limit
SRI	select rod insert

B.1 INTRODUCTION

The purpose of this appendix is to describe the validation of POLCA-T as a tool for reactor stability analysis. The code qualification against plant stability measurement demonstrates the capability of performing stability analyses in support of plant-specific applications, such as reload licensing evaluations.

The Westinghouse methodology for performing reload stability analyses using the POLCA-T code is essentially the same compared to the earlier approved methodology using the RAMONA-3 code (Reference 1). Additional features compared to the RAMONA-3 methodology are presented in Section B.9.

B.2 SUMMARY AND CONCLUSIONS

This report demonstrates the ability of the POLCA-T code to predict the margin to the plant instability limit.

The features of the POLCA-T code that make it an excellent tool for stability calculations include:

1. The ability to represent the entire core configuration. This allows explicit modeling of the thermal-hydraulic, neutronic, and fuel thermo-dynamic behavior for each fuel assembly.

2. The ability to describe in detail the entire reactor and plant, including all relevant systems, components, and controllers.

3. The ability to perform a fully coupled three-dimensional transient thermal-hydraulics and neutronics calculation.

Based on the information contained in this report, specific conclusions that can be made regarding the use of the POLCA-T stability methods are:

1. POLCA-T can accurately predict the onset of global (core-wide) and azimuthal (regional) limit cycle oscillations.

2. POLCA-T can accurately predict global decay ratios for damped oscillations.

3. POLCA-T can accurately predict oscillation frequencies for damped oscillations.

4. Mixed core configurations can be explicitly simulated, eliminating modeling uncertainties due to grouping of fuel types and averaging of the three-dimensional power distribution.

5. POLCA-T comparisons with 70 plant data measurements of global oscillations show full consistency by applying the evaluated simulation uncertainty.

Therefore, the overall conclusion is that POLCA-T as described in this report can be used to reliably predict the margin to the plant instability limit. Furthermore, the thorough benchmarking of the code provides good definition of the code uncertainties. The methodology for applying the code and the application of the code uncertainties for reload applications is further discussed in Section B.9.

[
]^{a,c}. Thus, POLCA-T is applicable to existing reactors and fuel designs. Dependencies on core state variables are consistent with earlier approved codes and no additional limitations on POLCA-T applicability exists.

B.3 STABILITY ANALYSIS PROCESS

This section describes the general Westinghouse process for performing a stability calculation with POLCA-T. The general process is used in the plant measurement qualification calculations presented in Sections B.4 and B.5, and is provided primarily to clarify the discussion in those sections. As discussed in Section B.9, a similar process is used for reload design and licensing analyses.

The general steps for performing a stability calculation with POLCA-T can be summarized as follows:

- Set up a plant vessel model:

  1. [
  2.]^{a,c}

- Set up the core configuration:

  3. [
  4.
  5.
  6.]^{a,c}

- Set up the core statepoint:

  7. [

]^{a,c}

- Establish the initial conditions for the reactor state of interest:

  8. [

  9.

  10.

  11.]^{a,c}

- Perform the reactor stability evaluation:

  12. [

  13.

  14.

  15.]^{a,c}

The general layout of the flow-loop model is similar to those of standard one-dimensional system analysis models (such as, RETRAN, BISON, GOBLIN). The number of nodes in each section is, however, normally higher and the description is more detailed. Channel geometry, core layout, and control rod pattern are generally based on three-dimensional steady-state simulator models (such as POLCA7). Steam lines, pressure controller, or feedwater flow controller models are generally not included because of their limited impact on the stability margin evaluation.

The nuclear data library is based on data generated with a two-dimensional lattice physics code (such as, PHOENIX, CASMO, or PARAGON). These data are used in exactly the same way as in POLCA7.

Historical data (such as, burnup, density history, etc), xenon and iodine distributions are read directly from the three-dimensional steady-state core simulator distribution file.

As discussed above, steady-state results are used to confirm that the POLCA-T model is consistent with three-dimensional steady-state simulator results and plant core supervision recordings.

The dynamic behavior of the reactor is simulated by POLCA-T starting from the appropriate initial conditions. The response of the system is evaluated by imposing a suitable perturbation (typically control rod movement) and observing the evolution in time, after the effect of the initial perturbation has died out.

This evolution determines the rate at which oscillations will decay or grow, thereby determining the decay ratio. The perturbation is typically imposed for a period of about one second.

The perturbation should be chosen so that it has no influence on the asymptotic behavior of the system. That is, after the effects of the perturbation have disappeared, the system will oscillate at its own characteristic frequency and will exhibit decaying oscillations if the system is damped or growing oscillations if the system is undamped. Controlled perturbations are preferable also for unstable systems since it helps to identify the limiting oscillation mode (global/regional) and to create proper oscillation amplitudes for the evaluation purposes. In such cases, oscillations will grow even in the absence of an initial perturbation. However, the evaluation might become more difficult and calculation time will be longer.

B.4 POLCA-T CORE STABILITY QUALIFICATION – GLOBAL MODE OSCILLATIONS

To date, a large database has been assembled for qualification of POLCA-T for stability evaluations. The core stability measurement database includes numerous tests conducted in European plants. The data cover a large range of flow and power conditions, and a variety of fuel designs and power distributions.

The POLCA-T qualification effort against core stability measurements is an ongoing process as new data become available. This section provides an assessment of the reliability of POLCA-T to simulate boiling water reactor (BWR) instabilities based on comparisons of code predictions against data from stability tests using the Westinghouse stability analysis process described in Section B.3. The qualification cases presented here are:

- [ ]^{a,c} Cycles 7, 10, 13, and 19 stability tests
- [ ]^{a,c} Cycles 14, 15, 16, and 17 stability tests
- [ ]^{a,c} Cycles 19 and 20 stability tests

These qualification cases comprise 70 individual POLCA-T simulations of measured stability data.

B.4.1 [ ]^{A,C} CYCLE 7, 10, 13, AND 19 STABILITY TESTS

B.4.1.1 Plant Description

The [ ]^{a,c} nuclear power plant is a General Electric (GE) designed BWR located in the [ ]^{a,c}. The principal plant characteristics are listed in Table B.4-1.

Core stability tests were conducted at [ ]^{a,c} in the beginning of the seventh, tenth, thirteenth, and nineteenth cycles of operation. The core composition for Cycle 7 is shown in Table B.4-2. The core consisted primarily of GE 8x8 open lattice fuel. The core composition for Cycle 10 is shown in Table B.4-3. The core dominant fuel was SVEA-96 (10x10) water-cross fuel with the remainder consisting of GE 8x8 fuel. The core composition in Cycle 13 is shown in Table B.4-4, the core is almost entirely SVEA-96. In Cycle 19, a large fraction of the core consisted of fuel with part length rods. The composition is shown in Table B.4-5.

Table B.4-1 [ ]^{a,c} Plant Characteristics			
Parameter	**Value**		
	(Original)	**(Uprate 1)**	**(Uprate2)**
Plant Manufacturer	General Electric		
Product Line	BWR/6		
Commercial Operation Date	1984	1996	2002
Rated Thermal Power	3,138 MW_{th}	3,515 MW_{th}	3,600 MW_{th}
Nominal Core Flow (100 percent)	11,151 kg/sec (88.5 Mlb/hr)		
Number Fuel Assemblies	648		
Recirculation System	20 Jet Pumps		
Core Power Density	54.7 kW/liter	61.3 kW/liter	62.8 kw/liter

Table B.4-2 [ ]^{a,c} Cycle 7 Core Composition		
Bundle Type	**Assembly Description**	**Number of Assemblies**
1	GE8x8-2	532
2	GE8x8-4	108
3	KWU 9x9-LTA	4
4	SVEA-64-LTA	4
Total		648

Table B.4-3 [ ]^{a,c} Cycle 10 Core Composition		
Bundle Type	**Assembly Description**	**Number of Assemblies**
1	GE8x8-2	170
2	GE8x8-4	144
3	SVEA-96	330
4	GE11-LTA	4
Total		648

Table B.4-4 [ ]^{a,c} Cycle 13 Core Composition		
Bundle Type	**Assembly Description**	**Number of Assemblies**
1	SVEA-96	414
2	SVEA-96+	232
3	GE11-LTA	2
Total		648

c

[

]

B.4.1.2 [ ]^{a,c} Cycle 7 Tests

B.4.1.2.1 Cycle 7 Description

A core stability test was conducted at [ ]^{a,c} in the beginning of the seventh operating season during the power ascension phase (Reference 2). The test served three purposes, namely:

- Investigate the stability characteristics of the core in various regions of the power/flow map, with special emphasis on the low-flow region
- Qualify the core on-line stability monitoring system (COSMOS)
- Collect a database for future reactor operations

B.4.1.2.1.1 Testing Sequence

After an initial recording (Record 1) at 61.4-percent power and 76.1-percent flow (performed primarily to check that the recording system was functioning properly and that the recording procedures were satisfactory), the recirculation pumps were switched from high to low speed and the drive flow control valves were opened fully. The core power was about 34 percent. About an hour later, withdrawal of control rods commenced.

A second recording (Record 2) was initiated shortly after completion of a control rod withdrawal campaign. The core power was 55.2 percent and core coolant flow was 36.5 percent.

The power increase was completed by withdrawing peripheral control rods, which resulted in a bowl-shaped radial power distribution, with high power in the peripheral region and low power in the central region. Also, the peripheral region experienced a gradual downward tilt of its axial power shape throughout the power ascension. High-power, bottom-peaked peripheral regions were created to promote the occurrence of out-of-phase oscillations.

The third recording (Record 3) was conducted while a control rod withdrawal campaign was in progress. During the recording, the core power rose from about 53 percent to 56.9 percent for a core flow of 36.6 percent flow.

The next core performance log printout showed a core power of 58.6 percent and a core flow of 36.7 percent. The fourth signal recording (Record 4) was initiated shortly after this core performance log. Minor control rod withdrawals of the central rods were effected on two occasions while this recording was in progress. These rod withdrawals caused a gradual increase of the LPRM signal oscillation amplitudes - which continued until an alarm was triggered and the operator promptly reinserted some control rods. By the time the recording was completed, the power had dropped to 55.9 percent and the core flow to 36.6 percent, according to the next core performance log.

A final recording session (Record 5) was conducted during which the core power was raised fairly rapidly from about 48 percent to the vicinity of the stability limit that had been established during the previous recording. The core power was then 58 percent and the coolant flow was 36.4 percent. The reactor was left for a few minutes at this operating condition and then control rods were inserted to reduce power. The stability test was then terminated.

B.4.1.2.1.2 Test Data

Only Record 2 was used in the comparison with POLCA-T calculations for the global mode evaluation. Conditions for the measurement point that was used in the simulations are given in Table B.4-6. The analysis times correspond to the time on the P-1 performance log printouts (see Figure B.4-1). Values for power, coolant flow, and steam pressure were taken from the P-1 logs. Feed water temperature was derived from subcooling data using POLCA7 calculations.

The evaluation of the collected data was made using noise analysis techniques. Results from the evaluation are given in Table B.4-7.

Table B.4-6 [ ]^{a,c} Cycle 7 Test Conditions

Case	Power (%)	Core Flow (kg/sec)	Feedwater Temperature (°C)	Steam Dome Press (bar)
Record 2 (21:35)	55.2	4,071	186.9	69.65

Table B.4-7 [ ]^{a,c} Cycle 7 Measurement Results

Case	Decay Ratio	Frequency (Hz)	Mode	Comments
Record 2	0.65	0.49	Global	Based on APRM. Control rod movement during measurement

a,b,c

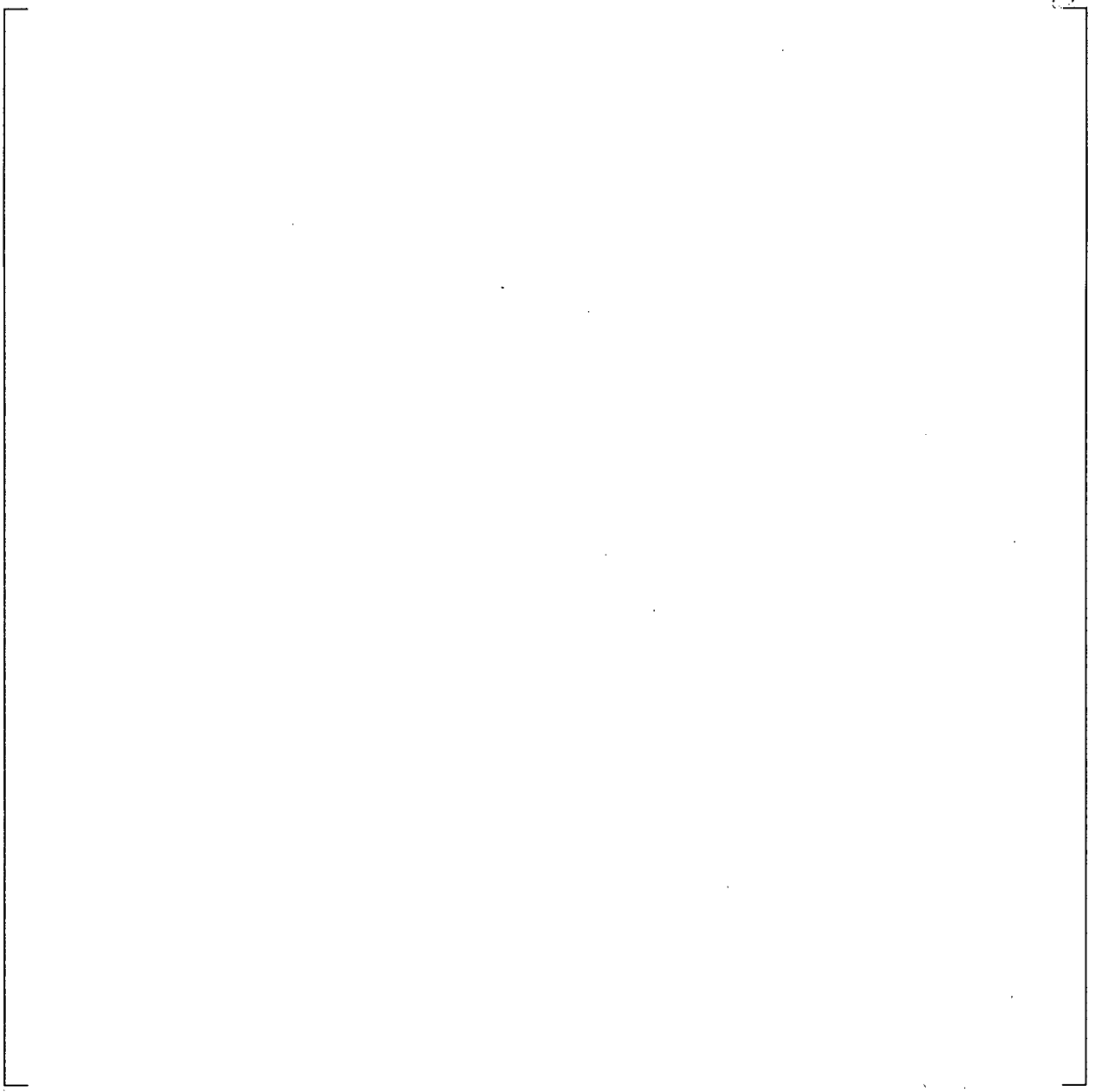

Figure B.4-1. [ ]^{a,c} Core Power Transient During Cycle 7 Stability Measurements.
(The symbols O marks the times when P-1 core performance maps were printed, and the corresponding powers. Time periods covered by recordings 2 through 5 are indicated).

B.4.1.2.2 Cycle 7 Model Description

A POLCA-T model was developed for [ ]^{a,c}. Both plant-specific data and Cycle 7 specific data are described in this section.

The 648-bundle core is represented in full-core geometry, with each bundle represented as a hydraulic channel and 25 axial nodes. An extra hydraulic channel models all internal and common bypass flows.

The geometry of the loop outside the core is modeled according to a detailed description provided by [ ]^{a,c}. The two recirculation loops are lumped into one, and the 20 jet pumps are represented by one pump. One short steam line is modeled and used for applying boundary condition. The pressure controller is not modeled. A simple feedwater controller that only affects the steady-state calculation is used.

LPRM assignments are explicitly represented in accordance with their location in the core. The total number of LPRMs is 35. The LPRM signals are calculated according to POLCA7.

The nuclear data input to POLCA-T includes cross-sections and kinetics parameters. Cross-section data and kinetics parameters are the same as used in the POLCA7 core follow calculations for Cycle 7.

B.4.1.2.3 Cycle 7 Test Simulations

Before the dynamic simulations were started, static calculations were made to assure that the dynamic simulations started from the proper operating point. Results from the steady-state runs were compared to corresponding results from POLCA7. Axial and radial power distributions, core inlet subcooling, k_{eff} and bypass flow fraction were included in the comparison.

The transient calculation was started by introducing a triangular control rod position disturbance. Typically, the stability characteristics of the in-phase oscillation mode were determined from the first 15 to 20 simulation seconds. Decay ratio and resonance frequency were determined based on the calculated power trace.

The results of the calculations are summarized in Table B.4-8 and Figure B.4-2. The measured and calculated stability parameters for the record have large uncertainties associated with them. The transient state of the reactor prior to the measurement period resulted in: (1) larger than the normal uncertainties in the deduced decay ratio and frequency, and; (2) large uncertainty in the state parameters recorded at the plant.

a,b,c

[

]

The uncertainties in input for this record are large and the results are therefore acceptable.

B.4.1.3 [ ]^{a,c} Cycle 10 Tests

B.4.1.3.1 Cycle 10 Test Description

A core stability test was conducted at [ ]^{a,c} in the beginning of its tenth operating cycle. When the test was performed, the reactor had been operating at full power for a few days (after a restart upon completion of its annual refueling and maintenance shutdown period). The core composition for Cycle 10 was shown in Table B.4-3.

There are two regions in the [ ]^{a,c} power flow map in which stability related operating restrictions apply. These two regions are referred to as "Exclusion Region 1" and "Exclusion Region 2" and are characterized as follows:

- Exclusion Region 1: no operation is allowed above the 80-percent load line with coolant flows below 40 percent. The region may be entered temporarily only with permission from the Safety Authorities.

- Exclusion Region 2: the region between 40-percent and 45-percent flow and above the 80-percent load line may not be entered, unless there is active surveillance based on APRM/LPRM signals or the on-line stability monitoring system COSMOS, and the operator takes appropriate action if the core stability limit is approached.

The objectives of the Cycle 10 stability test was to evaluate core stability performance for a number of low-flow conditions, investigate the characteristics of a mixed core of GE 8x8-4 and SVEA-96 (10x10-4), and to study the onset of power oscillations and their suppression with a manual select rod insertion (SRI). All test points were performed with both recirculation pumps running at:

- The upper flow border of Exclusion Region 2

- The flow border between Exclusion Region 1 and Exclusion Region 2

- The highest and lowest coolant flows with recirculation pumps running at minimum speed, within Exclusion Region 1

B.4.1.3.1.1 Testing Sequence

The test procedure for this cycle differed significantly from that of the previous stability test at [ ]^{a,c}, which was conducted during Cycle 7. The Cycle 10 test was initiated after the plant had been running at full power for a sufficiently long time for xenon equilibrium conditions to be established. The power/flow areas of interest for stability testing were then approached using controlled reduction of core coolant flow in combination with power increases via control rod withdrawals. Throughout the test, the decay ratio was monitored by COSMOS and LPRM recordings were conducted by GETARS (a [ ]^{a,c} data acquisition system). A total of 10 signal recordings were made during the test. A description of the test recordings is given below.

The power was reduced by the combined effect of control rod insertion to the 100-percent rod line and recirculation flow rundown to 45-percent core coolant flow. At the constant core flow of 45 percent, the power was increased by careful control rod withdrawal until the minimum critical power ratio (MCPR) operating limit was reached. At this point recording number 4 was taken at 67.8-percent power. The axial power shape was bottom peaked and the radial power distribution was flat.

From the previous test point, the thermal power was reduced by control rod insertion to the 100-percent rod line and recirculation flow reduction to 40 percent core flow. The core flow was then kept constant at 40 percent and the power was increased by careful rod withdrawal to 61 percent, until the MCPR operating limit was reached (Record 6).

The thermal power was then reduced by control rod insertion to the 80-percent rod line. A core flow of 35 percent was established by switching the pump speed from high to low and by fully opening the flow control valves. When steady conditions were obtained a recording was performed (Record 8). With constant core flow of 35 percent, power was increased by rod withdrawal until the MCPR operating limit was again reached. The power at this point was 59 percent (Record 9). The thermal power was reduced by control rod insertion to 80-percent rod line. The pump speed was kept low and both flow control valves were fully closed. The core flow reached was 27 percent. The power was then increased and at 43.5-percent power oscillations in the LPRMs appeared (Record 10). After a period the oscillations amplitude reached about 4-percent peak-to-average.

The SRI was triggered when the oscillations reached the amplitude of 4 percent. The SRI promptly reduced the core thermal power by about 9 percent and the power oscillations were successfully suppressed.

The test demonstrated that the Cycle 10 core design had excellent stability performance and that the use of SRI effectively suppressed power oscillations.

B.4.1.3.1.2 Test Data

During the stability measurements, only global oscillations were present. No regional oscillations were observed. Table B.4-9 shows the plant conditions for Recordings 4, 6, 8, 9, and 10. Table B.4-10 shows results from the noise analysis of these five measurements.

Table B.4-9 [ ]^{a,c} Cycle 10 Test Conditions

Case	Power (%)	Core Flow (kg/sec)	Feedwater Temperature (°C)	Steam Dome Press. (bar)
Record 4 (15:36)	67.7	5,064	196.5	70.35
Record 6 (17:19)	61.3	4,462	191.9	69.99
Record 8 (19:12)	51.6	3,999	183.5	69.42
Record 9 (19:47)	58.6	4,007	188.9	69.81
Record 10 (21:07)	43.0	3,161	175.7	68.98

Table B.4-10 [ ]^{a,c} Cycle 10 Measurement Results

Case	Decay Ratio	Frequency (Hz)	Mode	Comments
Record 4	0.44	0.60	Global	-
Record 6	0.53	0.54	Global	-
Record 8	0.45	0.48	Global	-
Record 9	0.65	0.50	Global	-
Record 10	0.97	0.47	Global	natural circulation

B.4.1.3.2 Cycle 10 Model Description

The plant-specific [ ]^{a,c} model is identical to that used for Cycle 7 (see subsection B.4.1.2.2). The core model was in the same way as for Cycle 7 extracted from the CM2 database.

B.4.1.3.3 Cycle 10 Test Simulation

During the test, 10 recordings of selected signals were made. Each recording lasted 10 minutes. Qualification of POLCA-T code was performed for five of the [ ]^{a,c} Cycle 10 tests. Table B.4-9 shows the conditions for the selected measurement points. The time chosen for the analyses is three minutes after recording initiation. The values for power, core coolant flow, steam Dome Pressure, reactor water level, and feedwater temperature are taken from CM-PRESTO, the three-dimensional core supervision code used at [ ]^{a,c}.

Steady-state POLCA-T calculations were first performed and the results compared to results from POLCA7. This was done to assure that the dynamic simulations start from the proper operating point. Axial and radial power distributions, bypass flow fraction and k_{eff} were compared.

The transient calculations were initiated by introducing a control rod disturbance. From about 8 to 20 seconds after the initial disturbance, decay constants and resonance frequencies were determined based on the oscillation time plots. The results of the analyses are given with comparisons to measured data in Table B.4-11 and in Figure B.4-2. a,b,c

[

]

As can be seen from the table there is good agreement between the measured and calculated decay ratios and frequencies.

B.4.1.4 [ ]^{a,c} Cycle 13 Tests

B.4.1.4.1 Cycle 13 Test Description

A core stability test was conducted at [ ]^{a,c} in the beginning of its thirteenth operating Cycle. When the test was performed, the reactor had been operating at full power for a number of days, after a restart upon completion of its annual refueling and maintenance shutdown period. The core composition for Cycle 13 is shown in Table B.4-4. The core consisted of about 64-percent SVEA-96 fuel and 36-percent SVEA-96+ fuel.

The objectives of the Cycle 13 stability test were to evaluate core stability performance for a number of low-flow conditions, and to investigate the characteristics of the core after the introduction of SVEA-96+ fuel. The tests were a part of a program that aimed to increase the core power to 112 percent. All tests were performed with both recirculation pumps running at:

- Above the upper flow border of Exclusion Region 2
- At the upper flow border of Exclusion Region 2

B.4.1.4.1.1 Testing Sequence

The test procedure for this cycle was rather similar to the stability test at [ ]^{a,c} during Cycle 10. The Cycle 13 test was initiated after the plant had been running at full power for a sufficiently long time for xenon equilibrium conditions to be established. The power/flow areas of interest for stability testing were then approached using controlled reduction of core coolant flow in combination with power increases via control rod withdrawals. Throughout the test, the decay ratio was monitored by COSMOS and LPRM recordings were conducted by GETARS. A total of eight signal recordings were made during the test. A description of the test recordings conducted following rod withdrawal campaigns is given below.

The power was reduced by the combined effect of control rod insertion to the 100-percent rod line and recirculation flow rundown to 55-percent core coolant flow. At the constant core flow of 55 percent, the power was increased by careful control rod withdrawal until the 3,138 MW_{th} maximum extended operating domain (MEOD) operating limit was reached. At this point recording number 2 was performed at 79.7-percent power. The axial power shape was bottom peaked and the radial power distribution was flat.

From the previous test point, the thermal power was reduced by control rod insertion to 100 percent rod line and recirculation flow reduction to 50-percent core flow. The core flow was then kept constant at 50 percent and the power was increased by careful rod withdrawal to 74.0 percent, until the 3,138 MW_{th} MEOD operating limit was reached (Record 4).

The thermal power was then reduced by control rod insertion to 100-percent rod line. A core flow of 45 percent was established. When steady conditions were obtained a recording was performed (Record 5). With a constant core flow of 45 percent, power was increased by rod withdrawal approaching the 3,138 MW_{th} MEOD operating limit. Three recordings (6a, 6b, and 7) were performed at power levels 66.0, 66.8, and 68.2 percent.

B.4.1.4.1.2 Test Data

During the stability measurements, only global oscillations were present. No regional oscillations were observed. Table B.4-12 shows the plant conditions for Recordings 2, 4, 6a, 6b, and 7. Table B.4-13 shows results from the noise analysis of these five measurements.

Table B.4-12 [ ]^{a,c} Cycle 13 Test Conditions				
Case	**Power (%)**	**Core Flow (kg/sec)**	**Feedwater Temperature (°C)**	**Steam Dome Press. (bar)**
Record 2 (19:10)	79.7	6,077	205.9	72.94
Record 4 (20:07)	74.0	5,539	202.4	72.69
Record 6a (20:58)	66.0	5,002	197.3	72.36
Record 6b (21:08)	64.8	4,982	198.0	72.32
Record 7 (21:34)	68.2	4,990	198.8	72.47

Table B.4-13 [ ]^{a,c} Cycle 13 Measurement Results			
Case	**Decay Ratio**	**Frequency (Hz)**	**Mode**
Record 2	0.34	0.61	Global
Record 3	0.45	0.58	Global
Record 6a	0.44	0.51	Global
Record 6b	0.46	0.55	Global
Record 7	0.46	0.55	Global

B.4.1.4.1.3 Cycle 13 Model Description

The plant-specific [ ]^{a,c} model is identical to that used for Cycle 7 (see subsection B.4.1.2.2) and Cycle 10. The core model was in the same way as for Cycles 7 and 10 extracted from the CM2 database.

B.4.1.4.1.4 Cycle 13 Test Simulation

During the test, 8 recordings of selected signals were made. Each recording lasted 10 minutes. Qualification of the POLCA-T code was performed for five of the [ ]^{a,c} Cycle 13 tests. Table B.4-12 shows the conditions for the selected measurement points. The time chosen for the simulation is the starting time for the recording. The values for power, core coolant flow, steam dome pressure, reactor water level and feedwater temperature are taken from CM-PRESTO registrations approximately at the starting time for the recording. CM-PRESTO is the three-dimensional core supervision code used at [ ]^{a,c}.

Steady-state POLCA-T calculations were first performed and the results compared to results from POLCA7. This was done to assure that the dynamic simulations start from the proper operating point. Axial and radial power distributions, bypass flow fraction and k_{eff} were compared.

The transient calculations were initiated by introducing a control rod disturbance. From about 8 to 20 seconds after the initial disturbance, decay constants and resonance frequencies were determined based on the oscillation time plots. The results of the analyses are given with comparisons to measured data in Table B.4-14 and in Figure B.4-2. As can be seen from the table and figure, there is good agreement between the measured and calculated decay ratios and frequencies. a,b,c

[

]

B.4.1.5 [ ]^{a,c} Cycle 19 Tests

B.4.1.5.1.1 Cycle 19 Test Description

A core stability test was conducted at [ ]^{a,c} in the beginning of its nineteenth operating Cycle. When the test was performed, the reactor had been operating at full power for a number of days, after a restart upon completion of its annual refueling and maintenance shutdown period. The core composition for Cycle 19 is shown in Table B.4-5. [

]^{a,c}

The objective of the Cycle 19 stability test was to evaluate core stability performance for a number of low-flow conditions and to investigate the characteristics of the core. The tests were the last part of a program that aimed to increase the core power to 115 percent of the original design. The nominal power had already before the cycle start been redefined such that 3,600MW_{th} was 100 percent. The exclusion regions had already from the previous power upgrade been extended. A second region consisting of the flow regime between 45 and 50 percent, and power above the 3,138 MW_{th} MEOD line had been added to exclusion region 2. Exclusion region 1 had been extended with the region below 45 percent and power above the 3,138 MW_{th} MEOD line.

All test points were performed with both recirculation pumps running at:

- Above the upper flow border of Exclusion Region 2
- Different flows within both Exclusion Regions 1 and 2, with the recirculation pumps running at high speed
- [

]^{c}

B.4.1.5.1.2 Testing Sequence

The test procedure for this cycle was similar to the stability test in [ ]^{a,c} during Cycles 10 and 13. The Cycle 19 test was initiated after the plant had been running at full power for a sufficiently long time for xenon equilibrium conditions to be established. The power/flow areas of interest for stability testing were then approached using controlled reduction of core coolant flow in combination with power increases via control rod withdrawals. Throughout the test, the decay ratio was monitored by COSMOS and LPRM recordings were conducted by GETARS. A total of eleven signal recordings were made during the test. Description of the test recordings conducted following a rod withdrawal campaign is given below.

a,c

[

]

All data except Record 2 are of good quality and could be useful for comparison with calculations. There were some problems with the data collection system during the second recording and the collected data are, therefore, not useful for validation purposes.

B.4.1.5.1.3 Test Data

During the stability measurements, only global oscillations were present. No regional oscillations were observed. Table B.4-15 shows the plant conditions for Recordings 1 and 3 through 11. Table B.4-16 shows results from the noise analysis of these ten measurements.

a,b,c

[

]

B.4.1.5.2 Cycle 19 Model Description

The plant-specific [ ]^{a,c} model is identical to that used for the other cycles (see subsection B.4.1.2.2). The core model was in the same way as for the previous cycles extracted from the CM2 database.

B.4.1.5.3 Cycle 19 Test Simulation

During the test, 11 recordings of selected signals were made. Each recording lasted 10 minutes. Qualification of POLCA-T code was performed for ten of the [ ]^{a,c} Cycle 19 tests. Table B.4-15 shows the conditions for the selected measurement points. The time chosen for the simulation is the

starting time for the recording. The values for power, core coolant flow, steam dome pressure, reactor water level, and feedwater temperature are the average values obtained from the GETARS data.

Steady-state POLCA-T calculations were first performed and the results compared to results from POLCA7. This was done to assure that the dynamic simulations start from the proper operating point. Axial and radial power distributions, bypass flow fraction and k_{eff} were compared.

The transient calculations were initiated by introducing a control rod disturbance. From about 8 to 20 seconds after the initial disturbance, decay constants and resonance frequencies were determined based on the oscillation time plots. The results of the analyses are given with comparisons to measured data in Table B.4-17 and in Figure B.4-2. As can be seen from the table and figure, there is acceptable agreement between the measured and calculated decay ratios and frequencies.

a,b,c

[

]

a,b,c

Figure B.4-2. Comparison of [ ]^{a,c} Cycles 7 10, 13, and 19 POLCA-T Calculations with Global Mode Oscillation Measurements

B.4.2 [ ]^{A,C} CYCLE 14, 15, 16, AND 17 STABILITY TESTS

B.4.2.1 Plant Description

[ ]^{a,c} is an ASEA-ATOM designed BWR located on the [ ]^{a,c}. [ ]^{a,c} is an external recirculation loop design BWR that went into commercial operation in 1977. In 1989, the plant was uprated from its original rated power of 2,270 MW_{th} to 2,500 MW_{th}. Plant characteristics for [ ]^{a,c} are summarized in Table B.4-18.

Table B.4-18 [ ]^{a,c} Plant Characteristics		
Parameter	**Value**	
	(Original)	**(Uprate)**
Plant Manufacturer	ASEA-ATOM	
Product Line	External Pump Design	
Commercial Operation Date	1977	1989
Rated Thermal Power	2,270 MW_{th}	2,500 MW_{th}
Rated Core Flow	9,400 kg/seconds (74.6 Mlb/hr)	
Number Fuel Assemblies	648	
Recirculation System	6 External Pumps	
Core Power Density	40.8 kW/liter	44.9 kW/liter

[ ]^{a,c} plant utility, performed extensive stability measurements during Cycles 14, 15, 16, and 17. For all these cycles, the core was comprised almost exclusively of the ABB SVEA-64 water-cross fuel. The core compositions for these four cycles are shown in Table B.4-19 through Table B.4-22.

Table B.4-19 [ ]^{a,c} Cycle 14 Core Composition		
Bundle Type	**Assembly Description**	**Number of Assemblies**
1	ASEA-ATOM 8x8-1	145
2	ASEA-ATOM SVEA-64-1	183
3	ASEA-ATOM SVEA-64	320
Total		648

Table B.4-20 [ ]^{a,c} Cycle 15 Core Composition		
Bundle Type	**Assembly Description**	**Number of Assemblies**
1	ASEA-ATOM 8x8-1	126
2	ASEA-ATOM SVEA-64-1	124
3	ASEA-ATOM SVEA-64	398
Total		648

Table B.4-21 [ ]^{a,c} Cycle 16 Core Composition		
Bundle Type	**Assembly Description**	**Number of Assemblies**
1	ASEA-ATOM 8x8-1	112
2	ASEA-ATOM SVEA-64-1	74
3	ASEA-ATOM SVEA-64	458
4	ASEA-ATOM SVEA-100	4
Total		648

Table B.4-22 [ ]^{a,c} Cycle 17 Core Composition		
Bundle Type	**Assembly Description**	**Number of Assemblies**
1	ASEA-ATOM 8x8-1	76
2	ASEA-ATOM SVEA-64-1	40
3	ASEA-ATOM SVEA-64	528
4	ASEA-ATOM SVEA-100	4
Total		648

The [ ]^{a,c} tests for these Cycles have earlier been selected by the nuclear committee of the OECD/NEA to provide a benchmark problem for stability calculations (Reference 3). Because of this benchmark, it is relevant to include these data in a validation even if the core content is not representative for a modern core.

B.4.2.2 [ ]^{a,c} Cycle 14 Tests

B.4.2.2.1.1 Cycle 14 Test Description

Noise measurements were performed by [ ]^{a,c} plant personnel at the beginning of Cycle 14 during power ascension after refueling in September 1990. The recordings were made at points arranged in a grid layout in the high power/low-flow region of the operating range.

The most important process parameters (APRM, LPRM on Levels 2 and 4 from the top, core flow, steam flow, feedwater flow and temperature, reactor pressure, reactor water level) were measured with a data scanner at ten operating states, as described in Table B.4-23.

Table B.4-23 [ ]^{a,c} Cycle 14 Test Conditions			
Case	**Power (%)**	**Core Flow (kg/sec)**	**Feedwater Temperature (C)**
1 (A)	65.0	4,105	157.7
3 (C)	65.0	3,666	157.6
4 (D)	70.0	3,657	160.3
5 (E)	70.0	3,868	160.3
6 (F)	70.2	4,126	160.4
8 (H)	75.1	3,884	162.0
9 (G)	72.6	3,694	161.2
10 (I)	77.7	4,104	162.8

The recording order follows the alphabetic identifiers shown in Table B.4-23. No oscillations were observed in the readings for the operational points 1 to 6. After measurement 6, the core flow was reduced to minimum flow and control rods were withdrawn. At about 72-percent power (Record 9), the LPRM instruments started to oscillate. Oscillations were suppressed by gradual insertion of control rods. The oscillations stopped after two steps in the control rod insertion sequence. The flow was then slightly increased from the flow limit line, and the last two points (Records 8 and 10) were measured under stable conditions.

The recorded data were analyzed several times by [ ]^{a,c} and ASEA-ATOM (today Westinghouse) to evaluate the quality of the measured signals, resonance frequencies, decay ratios and phase shift between LPRM detector signals (see Section B.7.1). The result of the latest data analyses are shown in Table B.4-24.

Table B.4-24 [ ]^{a,c} Cycle 14 Measurement Results				
Case	**Decay Ratio**	**Frequency (Hz)**	**Mode**	**Comments**
1 (A)	0.30	0.43	global	-
3 (C)	0.69	0.43	global	-
4 (D)	0.79	0.55	global	-
5 (E)	0.67	0.51	global	-
6 (F)	0.64	0.52	global	-
8 (H)	0.78	0.52	global	-
9 (G)	0.80	0.56	global	APRM signal measurement
10 (I)	0.71	0.50	global	-

B.4.2.2.1.2 Cycle 14 Model Description

The reactor core was modeled in full symmetry. This avoids any symmetry assumption and is necessary when regional oscillations are to be studied. The core consists of 648 channels. All channels have been treated explicitly in the neutronic and hydraulic calculations. An independent hydraulic channel represents common bypass and leakage flows. The total size of the model is:

- Number of neutronic channels: 648
- Number of hydraulic channels: 649
- Number of axial nodes: 25

A new model for the recirculation flow loop was developed. The model follows the outline used for the BISON model of [ ]^{a,c}. All data used for the BISON model have been reviewed against original drawings. The steam lines were not modeled. A simple control system for the feedwater flow has been applied.

Cross-section data were extracted from the CM2 system. The CM2 system has also been used for core follow (burnup) calculations and detailed xenon tracking.

B.4.2.2.1.3 Cycle 14 Test Simulation

The analysis procedure is the same as that outlined for the [ ]^{a,c} simulations. Results from the POLCA-T calculations for Cycle 14 are shown in Table B.4-25.

a,b,c

[ ]

Figure B.4-3 shows measured and calculated decay ratios for all the analyzed Cycle 14 tests. The agreement is acceptable even if there is a systematic under prediction.

a,b,c

Figure B.4-3. Comparison of [ ]^{a,c} Cycle 14 POLCA-T Calculations with Measurements

B.4.2.3 [ ]^{a,c} Cycle 15 Tests

B.4.2.3.1.1 Cycle Test Description

Stability measurements were made at the beginning of Cycle 15 (September 10-11, 1991) following a procedure similar to that performed for Cycle 14 (see subsection B.4.2.2.1.1). The test state points used for stability evaluation are shown in Table B.4-26. The deduced stability parameters for each test point are given in Table B.4-27. In all measurements, the in-phase (global) oscillation mode dominated.

Table B.4-26 [ ]^{a,c} Cycle 15 Test Conditions			
Case	**Power (%)**	**Core Flow (kg/sec)**	**Feedwater Temperature (°C)**
1	64.7	4,138	159.2
2	65.2	3,881	159.2
3	65.1	3,649	158.8
4	70.1	4,165	161.4
5	70.1	3,945	161.4
6	70.3	3,775	161.3
8	75.2	3,994	163.5
9	71.1	3,633	162.0
10	77.3	4,216	163.4

Table B.4-27 [ ]^{a,c} Cycle 15 Measurement Results				
Case	**Decay Ratio**	**Frequency (Hz)**	**Mode**	**Comments**
1	0.23	0.44	global	-
2	0.24	0.42	global	-
3	0.21	0.43	global	-
4	0.33	0.44	global	-
5	0.43	0.44	global	-
6	0.59	0.47	global	-
8	0.77	0.55	global	-
9	0.67	0.53	global	-
10	0.60	0.54	global	-

B.4.2.3.1.2 Cycle 15 Model Description

The POLCA-T (plant) model developed for [ ]^{a,c} Cycle 14 was used. Cross-section data and historical data including xenon were extracted from the CM2 system using the same procedure as for Cycle 14.

B.4.2.3.1.3 Cycle 15 Test Simulation

As with the Cycle 14 tests, POLCA-T simulations were performed for each measurement point in Table B.4-26. Results from the POLCA-T calculations for Cycle 15 are shown in Table B.4-28.

a,b,c

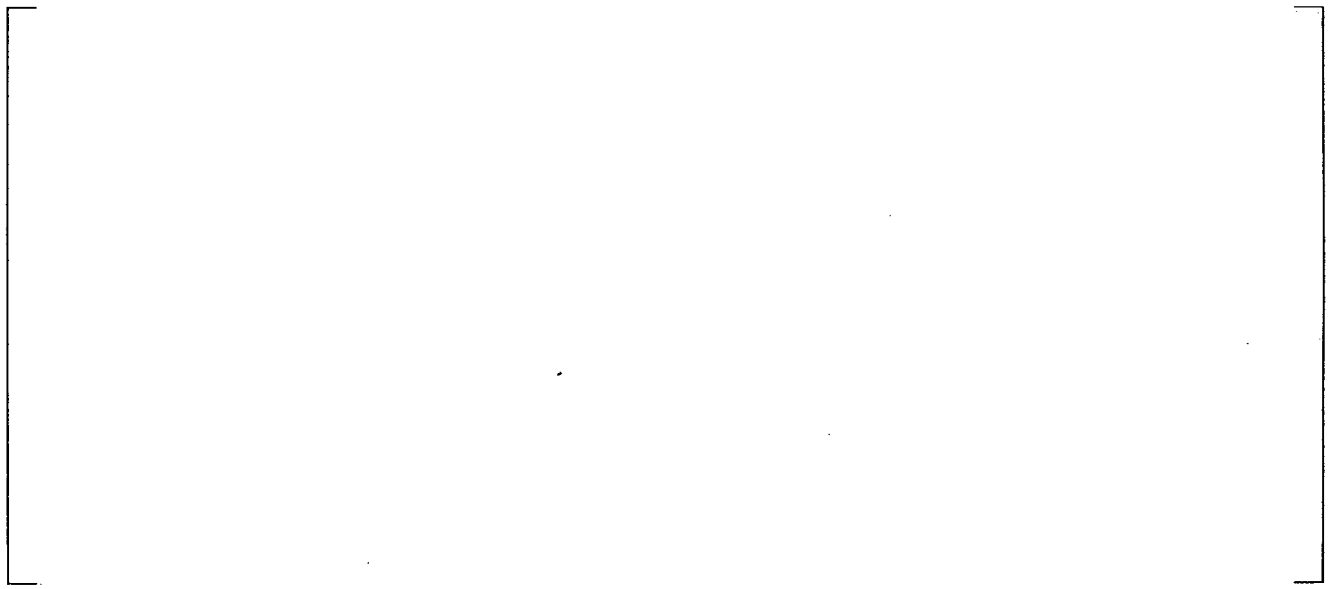

Figure B.4-4 also shows measured and calculated decay ratios for all the analyzed Cycle 15 tests. The agreement is fairly good.

a,b,c

Figure B.4-4. Comparison of [ ]^{a,c} Cycle 15 POLCA-T Calculations with Measurements

B.4.2.4 [ ]^{a,c} Cycle 16 Tests

B.4.2.4.1.1 Cycle 16 Test Description

Stability measurements again were made at the beginning of Cycle 16 (February 11-27, 1993) and also about six months later (July 24, 1993) during Cycle operation. The measurements followed the same procedure as that performed for Cycles 14 and 15 (see subsection B.4.2.2.1.1). The test state points used for stability evaluation are shown in Table B.4-29. The deduced stability parameters for each test point are given in Table B.4-30. In all measurements, the in-phase (global) oscillation mode dominated.

Table B.4-29 [ ]^{a,c} Cycle 16 Test Conditions

Case	Power (%)	Core flow (kg/seconds)	Feedwater temp (C)
1	64.3	4,112	157.6
2	64.6	3,925	157.4
3	64.6	3,698	157.6
4	70.2	4,165	159.6
5	69.9	3,932	159.5
6	69.5	3,673	159.5
7	74.4	4,081	162.0
8	74.9	3,907	162.0
9	74.6	3,678	162.2
10	76.0	4,217	162.7
11	66.1	3,653	158.3
moc1	77.4	6,588	163.6
moc2	75.6	6,034	162.4
moc4	57.5	3,815	155.0

Table B.4-30 [ ]^{a,c} Cycle 16 Measurement Results

Case	Decay Ratio	Frequency (Hz)	Mode	Comments
1	0.54	0.48	global	measurement at beginning of cycle
2	0.54	0.48	global	measurement at beginning of cycle
3	0.69	0.47	global	measurement at beginning of cycle
4	0.71	0.52	global	measurement at beginning of cycle
5	0.67	0.49	global	measurement at beginning of cycle
6	0.79	0.49	global	measurement at beginning of cycle
7	0.72	0.50	global	measurement at beginning of cycle
8	0.82	0.49	global	measurement at beginning of cycle
9	0.87	0.48	global	measurement at beginning of cycle

Table B.4-30 [ ]^{a,c} Cycle 16 Measurement Results (cont.)				
Case	**Decay Ratio**	**Frequency (Hz)**	**Mode**	**Comments**
10	0.65	0.50	global	measurement at beginning of cycle
11	0.66	0.48	global	measurement at beginning of cycle
moc1	0.35	0.68	global	measurement during cycle
moc2	0.33	0.61	global	measurement during cycle
moc4	0.73	0.51	global	measurement during cycle

B.4.2.4.1.2 Cycle 16 Model Description

The POLCA-T (plant) model developed for [ ]^{a,c} Cycle 14 was used. Cross-section data and historical data including xenon were extracted from the CM2 system using the same procedure as for Cycles 14 and 15.

B.4.2.4.1.2 Cycle 16 Test Simulations

As with the Cycles 14 and 15 tests, POLCA-T simulations were performed for each measurement point in Table B.4-29. Results from the POLCA-T calculations for Cycle 16 are shown in Table B.4-31.

a,b,c

[ ]

Figure B.4-5 also shows measured and calculated decay ratios for all the analyzed Cycle 16 tests. Better agreement was obtained for the beginning-of-cycle tests compared to Cycles 14 and 15. The middle-of-cycle tests showed similar agreement as the previous cycles.

a,b,c

Figure B.4-5. Comparison of [ ]^{a,c} Cycle 16 POLCA-T Calculations with Measurements

B.4.2.5 [ ]^{a,c} Cycle 17 Tests

B.4.2.5.1 Cycle 17 Tests Description

Stability measurements again were made at the beginning of Cycle 17 (November 17, 1993). The measurements followed the same procedure as that performed for Cycles 14, 15, and 16 (see subsection B.4.2.2.1.1). The test state points used for stability evaluation are shown in Table B.4-32. The deduced stability parameters for each test point are given in Table B.4-33. In all measurements, the in-phase (global) oscillation mode dominated.

Table B.4-32 [ ]^{a,c} Cycle 17 Test Conditions

Case	Power (%)	Core Flow (kg/sec)	Feedwater Temperature (°C)
2	65.6	3,954	158.6
3	65.6	3,680	158.6
4	69.5	4,166	160.3
5	69.9	4,015	159.8

Table B.4-32 [ ]^{a,c} Cycle 17 Test Conditions (cont.)			
Case	Power (%)	Core flow (kg/seconds)	Feedwater Temperature (°C)
6	69.7	3,758	156.4
7	74.9	4,140	162.6
8	75.1	4,020	162.5
9	75.4	3,739	162.5
10	78.1	4,058	163.8

Table B.4-33 [ ]^{a,c} Cycle 17 Measurement Results				
Case	Decay Ratio	Frequency (Hz)	Mode	Comments
2	0.24	0.46	global	-
3	0.22	0.44	global	-
4	0.32	0.46	global	-
5	0.28	0.42	global	-
6	0.34	0.46	global	-
7	0.33	0.46	global	-
8	0.41	0.48	global	-
9	0.57	0.47	global	-
10	0.49	0.49	global	-

B.4.2.5.2 Cycle 17 Model Description

The POLCA-T (plant) model developed for [ ]^{a,c} Cycle 14 was used. Cross-section data and historical data including xenon were extracted from the CM2 system using the same procedure as for the previous cycles.

B.4.2.5.2 Cycle 17 Test Simulation

As with the previous Cycle tests, POLCA-T simulations were performed for each measurement point in Table B.4-32. Results from the POLCA-T calculations for Cycle 17 are shown in Table B.4-34. a,b,c

[

]

a,b,c

[ ]

Figure B.4-6 also shows measured and calculated decay ratios for all the analyzed Cycle 17 tests. The agreement for these tests was good, even if the decay ratios are slightly over estimated.

a,b,c

[ ]

Figure B.4-6. Comparison of [ ]^{a,c} Cycle 17 POLCA-T Calculations with Measurements

B.4.3 [ ]^{A,C} CYCLES 19 AND 20 STABILITY TESTS

B.4.3.1 Plant Description

[ ]^{a,c} is an ASEA-ATOM designed BWR located on the [ ]^{a,c}. [ ]^{a,c} went into commercial operation in 1981. The original rated core thermal power was 2,711 MW_{th}. In 1987 it was uprated to operate at 108.0 percent of rated power (2,928 MW_{th}). The original rating of 2,711 MW_{th} maintained as 100-percent nominal power following the uprate. Plant characteristics for [ ]^{a,c} are summarized in Table B.4-35.

Table B.4-35 [ ]^{a,c} Plant Characteristics

Parameter	Value	
	(Original)	(Uprate)
Plant Manufacturer	ASEA-ATOM	
Product Line	BWR 75	
Commercial Operation Date	1981	1987
Rated Thermal Power	2,711 MW_{th}	2,928 MW_{th}
Rated Core Flow	11,000 kg/seconds (87.3 Mlb/hr)	
Number Fuel Assemblies	676	
Recirculation System	8 internal pumps	
Core Power Density	46.1 kW/liter	49.8 kW/liter

Stability tests are performed every cycle at [ ]^{a,c}. Traditionally, one measurement has been performed at beginning of cycle and one at middle of cycle. The main purpose of the tests is to verify prior calculations and to confirm the exclusion region. During Cycles 19 and 20, a larger number of measurements have been performed to investigate the sensitivity to different state points (power and recirculation flow).

Cycle 19 is divided into the subcycles 19a and 19b (and 19c) due to a short outage to remove a leaking assembly (and the symmetry assembly). The leaking assembly and the symmetry assembly were replaced with assemblies of the same type. The core composition for Cycles 19 and 20 are shown in Tables B.4-36 and B.4-37, respectively. The core content is dominated by SVEA-100 and SVEA-96 assemblies. A small number of SVEA96 Optima2 lead test assemblies with part length rods are also present in the two cycles.

Table B.4-36 [ ]^{a,c} Cycle 19 Core Composition

Bundle Type	Assembly Description	Number of Assemblies
1	ABB SVEA-100	524
2	ABB SVEA-96	146
3	ABB SVEA-96 Optima2	6
Total		676

Table B.4-37 [ ]^{a,c} Cycle 20 Core Composition		
Bundle Type	**Assembly Description**	**Number of Assemblies**
1	ABB SVEA-100	392
2	ABB SVEA-96	278
3	ABB SVEA-96 Optima2	6
Total		676

B.4.3.2 [ ]^{a,c} Cycle 19a Tests

B.4.3.2.1 Cycle 19a Test Description

During Cycle 19a in [ ]^{a,c}, four stability measurements were conducted three at the beginning of the Cycle and one in the middle. The three measurements performed at beginning of cycle (BOC) were performed during power ascension. The fourth recording was carried out in connection with the periodic main steam isolation valve test on October 31, 2000 (see Table B.4-38).

Table B.4-38 [ ]^{a,c} Cycle 19 Test Conditions			
Case	**Power (%)**	**Core Flow (kg/sec)**	**Core Inlet Temperature (°C)**
C19a-1	59.2	3,783	263.1
C19a-2	64.9	4,139	263.8
C19a-3	69.9	4,940	266.4
C19a-4	65.0	4,491	265.2
C19b-5	61.5	4,901	267.9
C19b-6	65.5	5,304	268.3

The recording of measured parameters during each state point was done after steady-state conditions were obtained. Each recording took approximately 10 minutes. The decay ratio and core resonance frequency were determined using parametric identification methods (see subsection B.7.1.1). The deduced decay ratios and core resonance frequencies are shown in Table B.4-39. The in-phase (global) oscillation mode dominated for all measurements.

Table B.4-39 [ ]^{a,c} Cycle 19 Measurement Results				
Case	**Decay Ratio**	**Frequency (Hz)**	**Mode**	**Comments**
C19a-1	0.76	0.46	Global	Beginning of Cycle measurement
C19a-2	0.75	0.50	Global	Beginning of Cycle measurement
C19a-3	0.59	0.54	Global	Beginning of Cycle measurement
C19a-4	0.78	0.54	Global	Middle of Cycle measurement
C19b-5	0.77	0.55	Global	Middle of Cycle measurement
C19b-6	0.50	0.55	Global	Middle of Cycle measurement

B.4.3.2.2 Cycle 19a Model Description

The full reactor core was modeled. This avoids any symmetry assumption and is necessary if regional oscillations are to be studied. The core consists of 676 channels. All channels have been treated explicitly in the neutronic and hydraulic calculations. An independent hydraulic channel represents common bypass and leakage flows. The total size of the model is:

- Number of neutronic channels: 676
- Number of hydraulic channels: 677
- Number of axial nodes: 25

A new POLCA-T model for the recirculation flow loop was developed. The model follows the outline used for the BISON model of [ ]^{a,c}. All data used for the BISON model have been reviewed against original drawings. The steam lines were not modeled. A simple control system for the feedwater flow has been applied. The internal recirculation pumps are lumped into one equivalent pump.

Cross-section data and historical data (burnup, etc.) were extracted from the CM2 system. The CM2 system has also been used for core follow (burnup) calculations and the detailed xenon tracking calculations were performed with "stand-alone" POLCA7.

B.4.3.2.3 Cycle 19a Test Simulation

Before the dynamic simulations were started, static calculations were made to assure that the dynamic simulations started from the proper operating point. Results from the static runs were compared to corresponding results from POLCA7. Axial power distributions, core inlet subcooling, core average void and k_{eff} were included in the comparison.

The transient calculation was started by introducing a triangular control rod disturbance. Typically, the stability characteristics of the in-phase oscillation mode were determined from the first 8 to 15 simulation seconds. Decay ratio and resonance frequency were determined based on the calculated power trace.

The results of the calculations are summarized in Table B.4-40 and in Figure B.4-7. The frequencies calculated with POLCA-T are slightly over predicted while the decay ratios agree well with measured data.

a,b,c

[ ]

B.4.3.3 [ ]^{a,c} Cycle 19b Tests

B.4.3.3.1 Cycle 19b Test Description

During Cycle 19b in [ ]^{a,c}, two stability measurements were conducted. Both were conducted during the power ascension after the short outage to remove a leaking assembly. Two different state points were analyzed (Table B.4-38).

The recordings were conducted in the same way as in Cycle 19a. The deduced decay ratio and core resonance frequency are shown in Table B.4-39. The in-phase (global) oscillation mode dominated both measurements.

B.4.3.3.2 Cycle 19b Model Description

The plant-specific [ ]^{a,c} model is identical to that used for Cycle 19a (see subsection B.4.3.2.2). The core model was also identical to Cycle 19a with exception of four assemblies due to the removal of a leaking assembly. Historical data were extracted from CM2 according to the standard technique.

B.4.3.3.3 Cycle 19b Test Simulation

The simulations were performed in exactly the same way as for Cycle 19a. The results of the calculations are summarized in Table B.4-40 and in Figure B.4-7. The frequencies calculated with POLCA-T are slightly over predicted while the decay ratio does not show any trend.

B.4.3.4 [ ]^{a,c} Cycle 20 Tests

B.4.3.3.3 Cycle 20 Test Description

During Cycle 20 in [ ]^{a,c}, three stability measurements were conducted. One measurement was conducted during power ascension after the outage and the other two at different state points in the middle of the cycle. The latter two were conducted in connection with the periodic main steam isolation valve test on January 11, 2002 (see Table B.4-41).

Table B.4-41 [ ]^{a,c} Cycle 20 Test Conditions

Case	Power (%)	Core Flow (kg/seconds)	Core Inlet Temperature (°C)
C20-1	64.8	4,333	262.8
C20-2	64.2	4,444	264.9
C20-3	64.4	4,618	265.7

The recordings were performed the same way as in Cycle 19. That is, performed under steady-state conditions and data were recorded for approximately 10 minutes. The decay ratio and core resonance frequency were determined using parametric identification methods. The deduced decay ratios and core resonance frequencies are shown in Table B.4-42.

Table B.4-42 [ ]^{a,c} Cycle 20 Measurement Results				
Case	**Decay Ratio**	**Frequency (Hz)**	**Mode**	**Comments**
C20-1	0.72	0.55	Global	Beginning of cycle measurement
C20-2	0.72	0.48	Global	Middle of cycle measurement
C20-3	0.66	0.49	Global	Middle of cycle measurement

B.4.3.4.2 Cycle 20 Model Description

The POLCA-T plant model developed for [ ]^{a,c} Cycle 19 was also used for Cycle 20. The cycle-specific core model for Cycle 20 was obtained by extracting data from CM2. The core composition is given in Table B.4-37. The nuclear cross-section data were extracted from CM2 using the standard technique. Detailed xenon-tracking calculations were used to obtain the correct xenon and iodine concentrations at the different state points.

B.4.3.4.3 Cycle 20 Test Simulation

For Cycle 20, the transient calculation was started by introducing a triangular control rod disturbance. Decay ratio and resonance frequency were determined based on the extremes of the calculated power trace.

The results of the calculations are summarized in Table B.4-43 and in Figure B.4-7. The decay ratios for the MOC recordings are in excellent agreement with the measurement. For the BOC recording, the decay ratio is under predicted. The frequencies for the two middle-of-cycle (MOC) recordings are slightly over predicted, while the BOC recording shows excellent agreement. a,b,c

[ ]

a,b,c

Figure B.4-7. Comparison of [ ]^{a,c} Cycles 19 and 20 POLCA-T Calculations with Measurements

B.5 POLCA-T CORE STABILITY QUALIFICATION – REGIONAL MODE OSCILLATONS

To date, only a limited number of measurements of regional mode oscillations exist for qualification of POLCA-T for stability evaluations. The qualification will be based on the [ ]^{a,c} Cycle 7 measurements, where recording 5 showed the typical signs of a regional mode oscillation.

The general description of the reactor (see subsection B.4.1.1) the core loading (see subsection B.4.1.1) and the testing sequence (see subsection B.4.1.2.1.1) are given above.

B.5.1 TEST DATA

Record 2 has been used for the validation of the global oscillation mode calculations (see subsection B.4.1.2.3). Record 5 is analyzed in this section for the qualification of the regional mode calculations with POLCA-T.

Conditions for the measurement point that was used in the simulations are given in Table B.5-1. The analysis time corresponds to the time on the performance log printout (see Figure B.4-1). Values for power, coolant flow and steam pressure were taken from the log. Feedwater temperature was derived from subcooling data using POLCA7 calculations.

The evaluation of the collected data was made using noise analysis techniques. Results from the noise evaluation of Record 5 are given in Table B.5-2. Recording 5 exhibited out-of-phase (regional) oscillations during portions of the measurement, with the boundary between the oscillating regions rotating with time.

Table B.5-1 [ ]^{a,c} Cycle 7 Test Conditions

Case	Power (%)	Core flow (kg/sec)	Feedwater Temperature (°C)	Steam dome press. (bar)
Record 5 (23:55)	58.0	4,066	188.3	69.68

Table B.5-2 [ ]^{a,c} Cycle 7 Measurement Results

Case	Decay Ratio	Frequency (Hz)	Mode	Comments
Record 5	0.97-0.99	0.58	Regional	Based on LPRM. Control rod movement during measurement

a,b,c

[

]

There are large uncertainties in the definition of the operating conditions during the Cycle 7 recordings. The measurements were conducted in transitory conditions (xenon buildup, control rod movements, power level changes, and changes in the recirculation loop and feedwater conditions). The POLCA-T evaluation did not account for these phenomena, and therefore could not reproduce all the transitions between modes and variations observed. [

]^{a,c}

The results are shown in Table B.5-3. The simulation shows that limit cycle out-of-phase oscillations were obtained for Record 5. A comparison of three different LPRMs is shown in Figure B.5-1. The oscillation amplitudes are in good agreement with what was observed during the test. The phase shift between LPRM 16-41 A and 40-17 A in the two opposite halves of the core can clearly be seen in Figure B.5-1, confirming that it is an out-of-phase oscillation. The positions of the detectors in the core are shown in Figure B.5-2. The global mode may disturb both the calculation and the analysis of the measurement. However, the analysis of LPRM 16-17 A shows that the impact in the simulation is very limited (see Figure B.5-1).

a,b,c

Figure B.5-1. Selected LPRM Signals from the Simulation of Record 5 Cycle 7.
(The LPRMs are normalized against core power, which is different from the plant normalization).

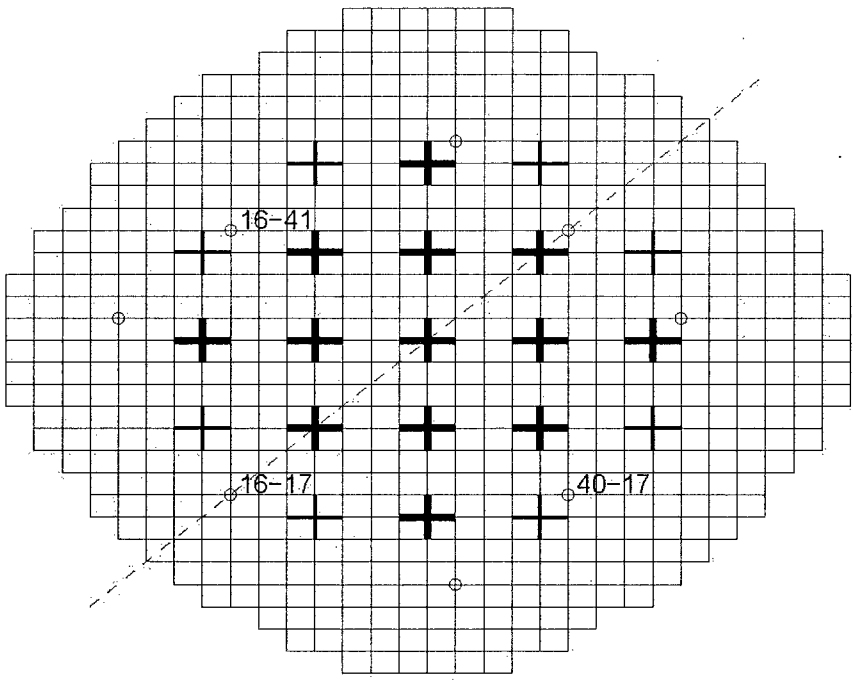

Figure B.5-2. Inserted Control Rods (+) and Detectors (o) Recorded During Record 5.
(Eight shallow controls rods are marked with thinner lines than the deeply inserted control rods. An approximate position of the symmetry line is shown by the dashed line (--).)

B.6 POLCA-T CORE STABILITY QUALIFICATION – CHANNEL MODE OSCILLATONS

Qualification against plant measurements provides a measure of the code capability to capture the effects of density wave oscillations combined with the effect of power feedback and fuel thermodynamics. This is discussed in Sections B.4 and B.5. Qualification against thermal-hydraulic loop test data measures the capability to predict the onset of density-wave oscillations for a single channel (that is, fuel assembly) operating at constant power. These comparisons, therefore, represent a separate effects test in the sense that the nuclear feedback is not included.

Measurements of thermal-hydraulic oscillations have been performed on a variety of assembly designs at the Westinghouse's test loop FRIGG. This section provides a demonstration of POLCA-T calculations for the SVEA-96 Optima2 design. Description of the SVEA-96 Optima2 fuel design is provided in Section 2 of Reference 4.

The general purpose of the FRIGG stability tests is to demonstrate and evaluate the stability properties of a new fuel design. The measurements also provide data for code validation.

The FRIGG loop test vessel (Figure B.6-1) consists of an electrically heated test section and lower and upper plenum. The two-phase flow enters through the riser section up to the part-wise perforated chimney, that is, the steam separator. The steam is transported to the condenser, the condenser hot water is cooled in the heat exchangers, and fed back to the test loop. The condenser and heat exchange system are not shown in Figure B.6-1. Saturated water, from the steam separator, and subcooled feedwater is mixed in the downcomer before the main circulation pump. The subcooling of the feedwater controls the test section inlet temperature. The water level is controlled by a spray system within the bulk water volume.

Stability tests are performed by establishing the desired hydraulic conditions, at constant pump speed, and increasing the bundle power step-wise until flow oscillations occur.

Due to the thermal-hydraulic stability properties of the SVEA-96 Optima2 design and the test loop characteristics, it is not possible to reach instability at 70 bars pressure without first getting dryout in the test assembly. Therefore the pressure was decreased, and the power-step-procedure was repeated, until instability occurred. For the SVEA-96 Optima2 measurements, instabilities were reached at about [ ]^{a,c}.

a,c

[

]

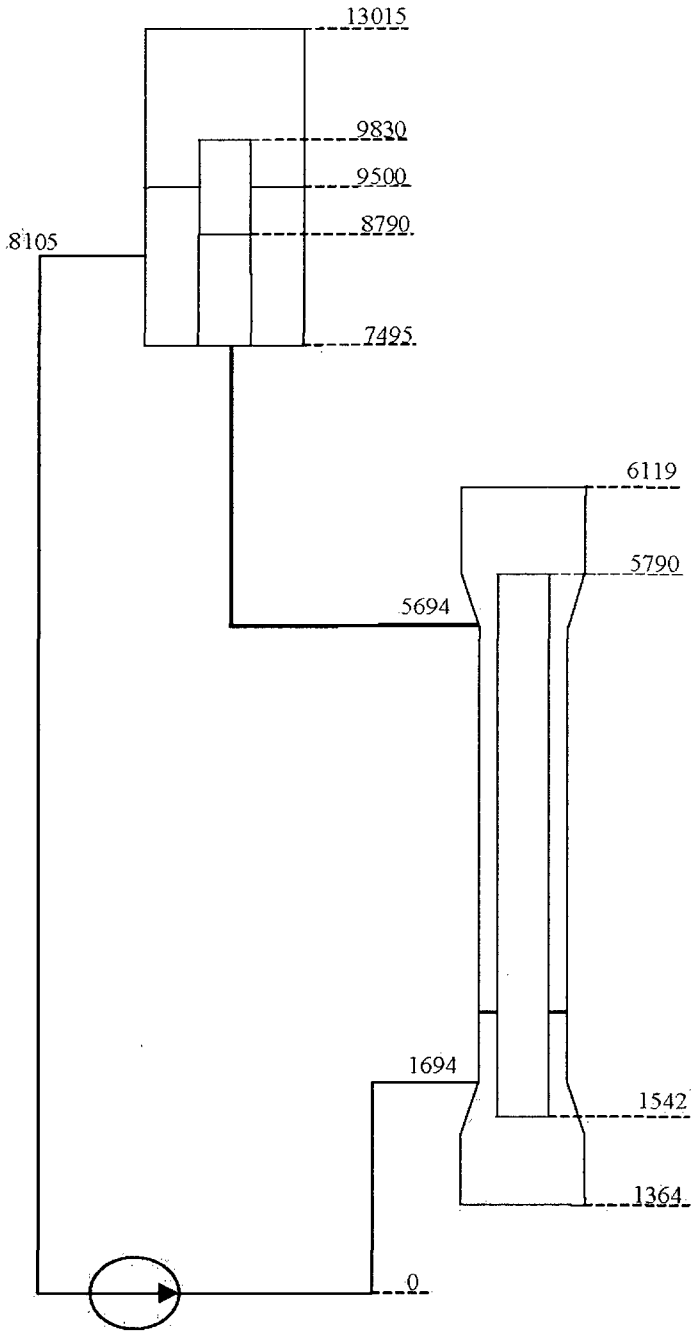

Figure B.6-1. Flow Diagram of the FRIGG-Loop

B.6.1 SVEA-96 OPTIMA2 STABILITY TESTS

The SVEA-96 Optima2 sub-bundle used in the FRIGG loop test consists of 24 electrically heated rods of three different types: [ ]^{a,c}. The flow area and hydraulic diameter thus vary along the sub-bundle. Nominal dimension heater rods, fuel channel, and spacers were used to create correct flow conditions in the test assembly.

The selected measurements are performed at [ ]^{a,c} in the SVEA-96 Optima2 test series. In Table B.6-1, the measured and calculated steady-state values are compared.

a,b,c

[

]

Pump speed, axial power distribution, bundle power, inlet temperature and inlet pressure are boundary conditions in the calculations. The pressure drops and inlet flow are calculated values.

Table B.6-1 shows that the [ ]^{a,c}. It can thus be expected that POLCA-T would predict the instability onset [ ]^{a,c}.

[

]^{a,c}

a,b,c

Figure B.6-2. Developing Channel Instability POLCA-T Calculation

[

]a,c

B.7 POLCA-T CORE STABILITY UNCERTAINTY

To estimate the uncertainty associated with determining the accuracy of decay ratio predictions using POLCA-T, two sources of uncertainty must be considered in examining the benchmark results:

- Measured decay ratio uncertainties
- Simulation uncertainties

Measurement uncertainties are associated with the accuracy to which a decay ratio can be deduced from the APRM or LPRM signals. Contributing factors are:

- Sample rate and length of the recording
- Relative magnitude of the signal to background noise
- Accuracy of the method used to transform time signals into decay ratios and oscillation frequencies

The POLCA-T simulation uncertainties can be attributed to the following:

a,c

[ ]

The above uncertainty elements are discussed in more detail below. Section B.7.1 discusses measurement uncertainty. Section B.7.2 discusses simulation uncertainties and associated studies performed to understand specific stability predictions.

B.7.1 MEASUREMENT UNCERTAINTY

B.7.1.1 Data Evaluation

The concept of the decay ratio is often used to measure the stability of BWRs. The decay ratio is the ratio between two consecutive maxima of the impulse response. For a second order system, this ratio is constant for any two consecutive maxima. For higher order systems, the impulse response is formed by contributions of all the poles and the ratio between consecutive peaks is not constant, but it converges to an asymptotic value associated with the least stable pair of poles (Reference 5).

In the data reduction of the plant measurements, two methods have been commonly used:

- The autocovariance function (Reference 5)
- Parameter identification methods based on auto-regressive (AR) or auto-regressive moving average (ARMA) modeling of the neutron noise (Reference 6).

The autocovariance function of a signal from an oscillatory system has similar properties regarding decay ratio and resonance frequency as the impulse response. That is, the "asymptotic" "decay ratio from the autocovariance function is used to quantify the stability of the system, and the "apparent" decay ratio is not a good indicator of the system's stability margin. Parameter identification methods applied to the neutron detector signals have been used exclusively for the measurements described in this report.

The neutron flux signal is modeled as an ARMA process:

$$y(t) + a_1y(t-1) + a_2y(t-2) +....+ a_{na}y(t-na) =$$

$$c_0e(t) + c_1e(t-1) +. \ . \ .+ c_{nc}e(t-nc) \qquad (7\text{-}1)$$

where:

y is the measured output signal,
e is the white noise, and
t is the discrete time values from the measurement.

The identification process consists of determining the coefficients a and c given a selected model order. Once the coefficients are determined, the stability characteristics of the system can be readily derived, either from the impulse response of the model or preferably, from the model coefficients directly. The model given above is the ARMA model.

B.7.1.2 Evaluation Method Uncertainties

The uncertainty associated with the measured decay ratio depends on the sampling time, the signal-to-noise ratio, and the stability margin of the system. For a given recording quality, the uncertainty in deducing a decay ratio value from Equation 7-1 contains:

- [ ]^{a,c}
-

The uncertainty due to model order is larger for low decay ratios because of the low signal-to-noise ratio.
[

]^{a,c}

[ ]^{a,c} (7-2)

[

]^{a,c}

B.7.1.3 Evaluation Differences

Evaluation uncertainties have also been the subject for an Organization for Economic Co-Operation/Nuclear Energy Agency (OECD/NE) benchmark (Reference 8). About 10 different institutes and companies contributed and in total 15 different evaluations for each record were performed. One of the test cases consisted of 14 different noise recordings from [ ]^{a,c} from dedicated stability tests performed under controlled conditions. The decay ratios varied between about 0.4 and 0.8.

In Figure B.7-1, selected data from the benchmark study are shown. The base for the selection of data is to include methods similar to those applied for the measured data referenced in this report[1]. This means that AR and ARMA methods deducing the decay ratio from the dominating poles of the identified model have been included. The figure also shows the one sigma uncertainty band according to Equation 7-2[2]. A comparison of the data sample in Figure B.7-1 with the uncertainty band shows that they are fully consistent.

a,b,c

Figure B.7-1. Variation in Deduced Measured Decay Ratio – Different Methods (*Mi*) According to the OECD Benchmark (Reference 8)

1. Westinghouse/ABB Atom [ ]^{a,c} and [ ]^{a,c} have used the ARMA method in the evaluations.

2. The samples in the OECD benchmark contained only 4,000 samples and scaling factor $1/\sqrt{2}$ have been applied to Equation 7-2.

B.7.2 SIMULATION UNCERTAINTY

Simulation uncertainty includes:

a,c

[

]

The simulation uncertainty has been estimated to be [ ]^{a,b,c}. This uncertainty includes [ ]^{a,c}, which is appropriate for a validation. For a predictive calculation, the plant state data are [ ]^{a,c} therefore conservative for predictive calculations.

Figure B.7-2 shows the complete qualification database and the combined evaluation and simulation uncertainty band (one sigma). The figure shows that the data are fully consistent with the applied uncertainties.

a,b,c

[

]

Figure B.7-2. Overall Comparison of POLCA-T Simulation Decay Ratio with Plant Measurement Database

Measured versus calculated core resonance frequencies are shown in Figure B.7-3. POLCA-T predicts the resonance frequencies for all plant measurements quite well. [ ]^{a,c} Some characteristics of the POLCA-T simulation database are discussed in the following subsections. The data set gives an overall uncertainty of [ ]^{a,b,c} Hz with a bias of [ ]^{a,b,c} Hz (calculated minus measured).

a,b,c

Figure B.7-3. Overall Comparison of POLCA-T Simulation Core Resonance Frequency with Plant Measurement Database

B.7.2.1 Qualification Database Studies

The stability database used in qualification of POLCA-T spans a wide range of conditions:

- Core power (~ 1,300 to 2,700 MW_{th})
- Core flows (~ 3,200 to 6,100 kg/s)
- Fuel designs (e.g., open lattice 8x8, water rod 8x8, water-cross 8x8, water-cross 10x10, water-cross 10x10 with part length rods)

- Combinations between fuel designs (see fuel composition tables in Section B.4)
- Core power distributions

However, the POLCA-T code and methodology instability analysis could be applied to other core power and core flow ranges provided appropriate benchmarks are performed to demonstrate their acceptability.

B.7.2.2 Cycle-to Cycle-Data Studies

The POLCA-T qualification database contains a number of data measurements following similar test procedures in consecutive cycles, but performed for different core fuel compositions and configurations. Specifically, POLCA-T simulations have been made for:

- [ ]^{a,c} – Cycles 14, 15, 16, and 17
- [ ]^{a,c} – Cycles 19 and 20.

Examination of the POLCA-T predictions of these cycle-to-cycle tests shows fully consistent results for [ ]^{a,c} (see Figure B.4-7). For [ ]^{a,c}, a trend in the data comparison can be observed (compare Figure B.4-3 through Figure B.4-6). In Cycle 14, [

]^{a,c}.

B.8 SENSITIVITY STUDIES

The sensitivity analysis intends to cover both uncertainties related to the state parameters as well as more general dependencies. The state parameters included in the analysis are the core power, the core coolant flow, and the core inlet temperature. The choice of state parameters follows the standard PIRT table concept (see for example Reference 9). The more general dependencies include reactor type, fuel design, cycle burnup, and stability characteristics (that is, nominal decay ratio).

Record 9 from [ ]^{a,c} Cycle 10 has been chosen as a reference case. The decay ratio is relatively high, that is, it is of about the same magnitude as would be expected for limiting cases in a core design analysis. Further, the calculated decay ratio shows good agreement with the measured one. Because of the content of the database, it is possible to perform studies of general parameters. This is possible since measurements with varying conditions have been performed at the same reactor with different core compositions. The core composition is also similar to the cycles analyzed for [ ]^{a,c}, which makes reactor type dependent studies possible. The state parameters have been varied [ ]^{a,c}. The nominal results are summarized in Table B.8-1 together with the results from the following sensitivity analysis. [ ]^{a,c} It should be kept in mind the variations applied in this section are examples, and the magnitude of the variations in a reload analysis must be based on plant-specific data.

a,b,c

[

]

In order to investigate if the response is dependent on the magnitude of the decay ratio Record 4 from [ ]^{a,c}, Cycle 10 was chosen. The nominal decay ratio is 0.44 and is significantly lower than for the reference case. [

]^{a,c}

3. [ ]^{a,c}

To investigate the dependence on fuel design Record 10 from [ ]^{a,c}, Cycle 19 was chosen. [

]^{a,c}

Record 1 from Cycle 20 at [ ]^{a,c} illustrates the dependency on reactor type, an ASEA-ATOM internal pump design compared to the GE BWR/6 in the reference case. [

]^{a,c}

Finally, the effect on cycle burnup is investigated by comparing Record 2 with Record 1 for [ ]^{a,c} Cycle 20. The former measurement is performed at 4,534 effective full-power hours (EFPH) (MOC) and the latter at BOC in a 12-month cycle (9,097 EFPH). The comparison of the two [ ]^{a,c} cases shows that the responses are very similar.

In Figure B.8-1, the results of the sensitivity study is summarized. The relative change in decay ratio is plotted for the five different cases. From the figure, the above conclusions are obvious, (that is, that the responses in respective variable are comparable for the five cases with the [

]^{a,c}

[

]^{a,c} The dependencies on core state variables are consistent with earlier approved code and impose no additional limitations on POLCA-T applicability.

a,b,c

Figure B.8-1. Results of Input Sensitivity Study

B.9 STABILITY METHODOLOGY

The proposed stability methodology using POLCA-T as a tool is essentially the same as the RAMONA-methodology earlier licensed (Reference 1). As RAMONA, POLCA-T is a three-dimensional coupled neutronic-thermal-hydraulic time domain code.

The Westinghouse core stability methodology can be summarized as follows:

1. Establishes acceptance limits for demonstrating acceptable stability performance

2. Identifies the stability analysis methods that are used to demonstrate compliance with the acceptance limits

3. Establishes the process for identifying the limiting plant conditions to be evaluated

4. Identifies the process of relating the calculated limits of acceptable stability performance to a domain of acceptable plant operation

Westinghouse stability analysis methodology for licensing safety evaluation, reload fuel applications, or plant operation modifications falls within the already accepted non-vendor specific U.S. Boiling Water Reactor Owners Group (BWROG) methodologies (Reference 10).

The stability solutions were developed to comply with the requirements of 10 CFR 50 Appendix A, "General Design Criteria for Nuclear Power Plant". The Appendix A criteria related to stability are:

Criterion 10: The reactor core and associated coolant, control and protection systems shall be designed with appropriate margin to ensure that specific acceptable fuel design limits are not exceeded during any conditions of normal operation, including the effects of anticipated occurrences.

Criterion 12: The reactor core and associated coolant, control and protection systems shall be designed to ensure that power oscillations which can result in conditions exceeding specified acceptable fuel design limits are not possible or can be reliably and readily detected and suppressed.

These criteria form the design basis and are implemented in different ways for different utilities. The Westinghouse stability safety analysis process is performed as required by the plant specific stability licensing basis, either it follows the Option I, II, or III solutions (References 10 and 11).

The fundamental approaches to provide protection against reactor power-flow oscillations are:

1. An acceptable approach is to reduce the operating domain by defining an exclusion region where the reactor is not allowed to operate. The exclusion region, defined by the area in the operating map where stability criteria are not met, should be enforced automatically. In addition to the exclusion region, this approach defines a larger buffer region, which is enforced with administrative controls. The buffer region minimizes challenges to the reactor protection system.

2. An alternative acceptable approach is to readily detect and suppress unstable power oscillations by scramming the reactor before specified acceptable fuel design limits (SAFDLs) are violated. An approved detect and suppress solution, which relies on calculations of the reduction in critical power ratio margin for oscillations of a given magnitude, should be implemented. The approach defined in Reference 11 is an approved-detect-and suppress methodology.

All stability solutions should have backup options in case the licensing solution is declared inoperable. Backup options in effect for short periods may rely on administrative controls and manual operator actions only if operator actions required to prevent violation of the SAFDLs can be reasonably prompt. Backup solution exclusion regions should be confirmed for specific Cycles.

As indicated above, the second approach requires coupling of power-flow oscillations to limiting fuel design criteria such as the minimum critical power ratio (MCPR). The approved methodology for performing these calculations is prescribed in Reference 11 and is not covered in this document.

The anticipated power-flow (also called density waves) oscillatory modes in a BWR are:

1. Global (core-wide), when the power and flow of all core channels oscillate in phase

2. Regional, when the power and flow of half the core channels oscillate out-of-phase with the other half, and neutron kinetics excite the first azimuthal neutron flux mode resulting in fuel channels in one region oscillating out-of-phase with fuel channels in another region in the core. The regional mode symmetry line[4] (or plane) separates the core regions oscillating out-of-phase.

3. Single channel, when the flow in a single channel oscillates accompanied by small power oscillations.

Decay ratios and oscillation frequencies, describing the stability properties of the power-flow oscillations, are evaluated from plant stability measurements in order to validate the method and evaluate the associated uncertainties.

The decay ratio is defined as the ratio between consecutive oscillation amplitudes. The value of decay ratio is 1.0 at the instability boundary. The decay ratio for increasing amplitudes (unstable system) is higher than 1.0 and for decreasing amplitudes (stable system) less than 1.0.

Oscillation frequency is characteristic for the system and set mainly by the thermal-mechanical and hydraulic properties of the fuel and core. Oscillation frequency is an important parameter for stability monitoring and detection but of limited importance with regard to fuel integrity.

For global (core-wide) oscillations, the decay ratio is calculated using the transient reactor power oscillations, or APRM signal. For regional oscillations, the decay ratio is calculated using the transient local power, or LPRM signal. For channel oscillations, the channel inlet flow is used to determine the decay ratio.

[4] The symmetry plane may also rotate due to simultaneous excitation of two neutron flux azimuthal harmonics.

A limitation of time domain codes is that they can only predict the decay ratio of the dominating oscillation mode, that is, the global or the regional but not both at the same time. A symmetric control rod perturbation is introduced to excite the global mode. An asymmetric control rod perturbation is introduced to excite the regional mode. However, one must search for the phase shift and the core symmetry line to ensure that the regional mode has been excited. A perturbation in for example channel power is used to excite the channel instability mode.

The reactor is considered stable if the calculated decay ratio (DR) for all three common stability modes (global, regional, and channel) satisfies the criterion:

[ ]

The prediction uncertainty is tool specific and evaluated from the validation against actual plant measurements. In a best-estimate methodology, a common way to define prediction uncertainty is by using the simulation uncertainty. The evaluated simulation uncertainty for POLCA-T is [ ]^{a,b,c} (see Section B.7.2).

[ ]^{a,c}

B.10 REFERENCES

1. "Thermal-hydraulic Stability Methodology for Boiling Water Reactors" CENPD-295-P-A (Proprietary), CENPD-295-NP-A (Non Proprietary), July 1996.

2. J. Blomstrand, "Operational Experience of Core Stability in KKL Gained from Tests Conducted in 1990 and 1993," Janhrestagung Kerntechnick 1994, 17-19 May, 1994, Stuttgart, Germany.

3. "Ringhals 1 Stability Benchmark," OECD/NEA report NEA/NSC/DOC(1996)22.

4. WCAP-15942-P-A, "Fuel Assembly Mechanical Design Methodology for Boiling Water Reactors, Supplement 1 to CENPD-287-P-A," March 2006.

5. J. March-Leuba, and W. T. King, "Development of a Real-Time Stability Measurement System for Boiling Water Reactors," Transactions of the American Nuclear Society, Vol. 54, p.370.

6. B. R. Upadhyaya and M. Kitamura, "Stability Monitoring of Boiling Water Reactors by Time-Series Analysis of Neutron Noise," Nuclear Science and Engineering, Vol. 77, P.480, 1981.

7. C. Rotander, "Methods to identify stability properties for a thermohydraulic channel and from reactor noise measurements," TRITA-S3-REG-9901, ISSN 0347-1071.

8. "Forsmark 1 & 2 Boiling Water Reactor Stability Benchmark, Time Series Analysis Methods for Oscillations During BWR Operation," OECD/NEA Report NEA/NSC/DOC(2001)2.

9. Letter, D. W. Newkirk to BWROG Detect and Suppress Methodology Committee, "Plant-Specific DIVOM Procedure Guideline," OG05-0136-260, June 2, 2005.

10. "BWR Owners Group. Long Term Stability Solutions. Licensing Methodology," NEDO-31960.

11. "Reactor Stability Detect and Suppress Solutions. Licensing Basis Methodology for Reload Applications," NEDO-32465.